



Investigation of non-classical light and its application in ultrasensitive measurements

Janousek, Jirí

Publication date:
2008

[Link back to DTU Orbit](#)

Citation (APA):
Janousek, J. (2008). *Investigation of non-classical light and its application in ultrasensitive measurements*.
http://optics.upol.cz/janousek/Quantum_imaging/PhD_final/Thesis_Janousek.pdf

General rights

Copyright and moral rights for the publications made accessible in the public portal are retained by the authors and/or other copyright owners and it is a condition of accessing publications that users recognise and abide by the legal requirements associated with these rights.

- Users may download and print one copy of any publication from the public portal for the purpose of private study or research.
- You may not further distribute the material or use it for any profit-making activity or commercial gain
- You may freely distribute the URL identifying the publication in the public portal

If you believe that this document breaches copyright please contact us providing details, and we will remove access to the work immediately and investigate your claim.



Department of Physics
Technical University of Denmark

**Investigation of non-classical light
and its application in ultrasensitive
measurements**

Jiri Janousek

Supervisor:
Prof. Preben Buchhave

*Submitted in partial fulfilment of the requirements
for the degree of Doctor of Philosophy in Physics
at the Technical University of Denmark*

December, 2007

Abstract

Recent advances in quantum optics and quantum information science have opened the possibility of entirely new methods for forming optical images with unprecedented sensitivity and resolution. This new field of research, known as quantum imaging, has led to other breakthroughs as well, such as the possibility of making spatial measurements of displacement and tilt of a laser beam below the quantum noise limit. In addition, quantum imaging offers significant opportunities within the fields of quantum communication and quantum information processing as it allows a secure two-dimensional information transfer and teleportation. Understanding the spatial aspects of quantum fluctuations and quantum correlations provides a great potential for further technological applications within this field.

For investigating the basics of the spatial quantum effects, we require a multi-mode squeezed light, where the light beam displays nonclassical spatial properties in the transverse direction. Such a source of squeezed spatial light can be based on optical parametric amplifiers, widely used in quantum optics experiments for generating amplitude or phase squeezed light. The first attempt for achieving the goal is to generate squeezing in the higher-order Hermite-Gauss modes, in particular in the TEM_{10} spatial mode, which form an optimum basis for measurements of displacement and tilt of a laser beam. This requires understanding of mode coupling between the different transverse modes in a nonlinear device; in our case via the second-order nonlinear interaction.

In our work we have studied the second-order nonlinear interaction between the higher-order Hermite-Gauss modes via second harmonic generation in a PPKTP nonlinear medium, and applied these results in reverse to generate a squeezed light in the TEM_{10} higher-order spatial mode utilizing an optical parametric amplifier. Our primary objective was to design an efficient squeezing source operating in this particular spatial mode. We generated vacuum squeezed light and observed a noise suppression of -2.9 dB below the quantum noise limit. We studied further optimization of the nonlinear gain of the amplifier in order to achieve higher degrees of squeezing in the TEM_{10} mode. This in effect promises higher sensitivity for measurements of displacement and tilt of a laser beam below the quantum noise limit.

We have experimentally demonstrated the generation of optical squeezing in multiple longitudinal modes and transverse Hermite-Gauss modes of an optical parametric amplifier. We present measurements of approximately -3 dB squeezing at baseband, 1.7 GHz, 3.4 GHz and 5.1 GHz, which correspond to the first, second and third resonances of the amplifier. We show that both the magnitude and the bandwidth of the squeezing in the higher longitudinal modes are greater than can be observed at baseband. The squeezing observed is the highest frequency squeezing reported to date.

In addition to squeezed light, the so-called entangled beams or EPR-beams are of great interest. Entangled beams give us the opportunity to investigate fundamental quantum properties of twin light beams, such as non-locality and entanglement. These quantum properties are presently seen as fundamental to future technological

applications such as quantum communication and quantum computing. The output of two squeezed laser beams, operating in the same mode, can be combined to a pair of entangled modes. This is well established for Gaussian beam and has been used in many applications, such as dense coding and teleportation. We can now extend this to spatial systems, where the entangled properties are for example displacement and tilt, or rather position and momentum, of a bright laser beam. Such an experiment would verify the original concept of position-momentum entanglement, termed here as spatial entanglement, proposed by Einstein, Podolsky and Rosen.

To prove the concept of spatial entanglement, we have built a unique apparatus for the generation of a pair of beams entangled in position and momentum. This experiment involves two identical squeezing sources operating in the TEM_{10} mode. Both squeezers delivered constantly -3.2 dB of a dim amplitude squeezed light. We generated a position-squeezed beam by mixing one of the TEM_{10} squeezed fields with a bright TEM_{00} carrier field, which makes a reference in the system for position and momentum. Mixing this multi-mode spatially squeezed beam with the other TEM_{10} squeezed field on a 50/50 beamsplitter then allows to entangle an information about position and momentum of the bright reference beam into the pair of output beams.

We characterized the strength of entanglement using the inseparability criterion and the EPR paradox criterion, and we measured their degrees in the frequency range 3.2 – 4.2 MHz to be $\mathcal{I} = 0.51 \pm 0.01$ and $\mathcal{E} = 0.78 \pm 0.01$, respectively. The presented results show the first demonstration of entanglement between position and momentum of a bright optical beam in the continuous variable regime as originally considered by Einstein, Podolsky and Rosen. Moreover, this system allows demonstration of quantum imaging protocols such as spatial teleportation and dense coding. We could also demonstrate using this setup the capability of a quantum communication system with several degrees of freedom by encoding and detecting modulation onto squeezing into different degrees of freedom. This gives us also the opportunity to explore techniques for the modulation, transmission and detection of complex quantum states.

Dansk Resumé

I dette arbejde har vi undersøgt anden ordens ulineære vekselvirkninger mellem højere ordens Hermite-Gauss modes (svingningstilstande) gennem studiet af anden harmonisk generering i en PPKTP optisk ulineær krystal, og vi har derefter anvendt disse resultater til at generere såkaldt squeezed lys (lys med fluktuationer under standard kvantestøjgrænsen) i en TEM_{10} rumlig mode ved brug af en optisk parametriske forstærker. Vores primære mål var at designe en effektiv kilde for squeezed lys i denne særlige rumlige mode. Vi fremstillede squeezed vacuum og observerede en støjundertrykkelse på -2.9 dB under kvantestøjgrænsen. Videre studerede vi optimering af den ulineære forstærkning i den parametriske forstærker med det formål at opnå bedre squeezing i en TEM_{10} mode. En videre konsekvens af dette er muligheden for større følsomhed ved målinger af forskydning og vinkelændring af en laserstråle, en følsomhed som kan blive bedre end kvantestøjgrænsen.

Ud over fænomenet squeezed lys har de såkaldte ”entangled beams” (stråler med særlige kvantekorrelationer) eller EPR-stråler stor interesse. For at eftervise fænomenet rumligt entanglement har vi bygget et enestående udstyr, som kan fremstille et par laserstråler, hvis position og impuls er entangled. Forsøget involverer to identiske kilder for squeezed laserstråler i TEM_{10} mode. Begge squeezere producerede konstant -3.2 dB squeezing i en svag amplitude squeezed stråle. Vi genererede en positions-squeezed stråle ved at blande en af de to TEM_{10} squeezed stråler med en kraftig TEM_{00} stråle, som udgjorde en reference i systemet for både position og impuls. Ved derefter at blande denne multi-mode rumligt squeezed stråle med den tilsvarende squeezed stråle fra den anden halvdel af opstillingen i en 50/50 beamsplitter opnåedes entanglement af informationen om position og impuls fra den kraftige stråle nu i de to TEM_{10} squeezed stråler.

Vi karakteriserede styrken af entanglement ved at bruge et inseparability kriteriet, \mathcal{I} , og EPR paradox kriteriet, \mathcal{E} , og vi målte graden af entanglement i frekvensområdet 3.2–4.2 MHz til at være henholdsvis $\mathcal{I} = 0.51 \pm 0.01$ og $\mathcal{E} = 0.78 \pm 0.01$. Disse resultater udgør den første demonstration af entanglement mellem position og impuls af en kraftig optisk stråle i det kontinuerte variable regime på en måde som oprindeligt overvejet af Einstein, Podolsky og Rosen. Yderligere tillader dette system en demonstration af kvante-afbildings protokoller som f.eks. teleportation og dense coding. Med denne opstilling kunne vi også eftervise kapaciteten af et rumligt kvante-kommunikations system ved at indkode og detektere modulation i flere frihedsgrader med squeezing. Dette giver mulighed for videre undersøgelser af modulation, transmission og detektion af komplekse kvantetilstande.

Acknowledgements

This thesis is an account of research undertaken between January 2005 and December 2007 at the Department of Physics, Technical University of Denmark (DTU), Lyngby, Denmark, and at the ARC Centre of Excellence for Quantum-Atom Optics, Department of Physics, Australian National University (ANU), Canberra, Australia, under the supervision of Prof. Preben Buchhave from DTU. This PhD project was funded by DTU, Center for Biomedical Optics and New Laser Systems (BIOP), and the ARC Centre of Excellence for Quantum-Atom Optics, ANU.

The research presented in this thesis was undertaken in the Optics Group at DTU and the Quantum Imaging Group at ANU, where I have had the opportunity to work with many talented and bright people. The close and productive collaboration between the two groups, even though separated by 16.000 km, was a source of great experience and motivation for my work, and I greatly appreciate the opportunity to gain knowledge and experimental tricks from both parts.

My first warm thanks go to my supervisor Preben Buchhave, who gave me a great insight into the field of quantum optics. I am extremely grateful for his kindness, patience and most for the support he gave me during the whole course of my PhD, especially when I was traveling so much time around the whole World. I would also like to thank Ulrik L. Andersen for motivating scientific discussions, and giving me all his trust in building the super-squeezer in his lab. I appreciate Peter Tidemand-Lichtenberg for passing on me some of his brilliant knowledge about nonlinear systems. My special thanks go to all my PhD fellows for their fruitful comments and help with my research; Alex, for organizing the best bike trip ever, Metin, for the great time in the lab and all the jokes, Mikael, giving me the honour in rebuilding all his squeezers, and Martin, the Optics Group party man. I must extend my warmest thanks to the workshop guys (and guyettes), without their help the research would not be possible; Karin, for working hard on all the mechanical parts for the squeezer, and Anders, for building all kind of electronics for the experiments. I greatly appreciate Søren for his technical assistance in the lab. His ability to construct scientific gadgets from couple of screws and unused components lying in and mostly out of the lab is amazing. I will never forget the high-tech lab temperature sensor.

During the course of my PhD, I have had the opportunity to spend together 13 months in Australia and undertake research in the Quantum Imaging Group at ANU. Here I would like to express my warmest thanks to Hans Bacher for providing me a wonderful environment to do science, for his guidance in the research, and his remarkable ability to explain complicated stuff simple so that even I could understand it. Thank you for your support in all circumstances, and also for introducing me into the Australian life and nature. I thank to all my ANU fellows, I learnt so much from each of you; Kate, for the endless evenings with the entanglement machine, Magnus,

for teaching me all kind of swear-words which should know every successful researcher, Hongxin, for the after-lunch relaxing discussions, Vincent, for the fantastic time and being my best beach volleyball mate, Oliver, for the perfect outdoor trips, Gabriel, Nicolai and Roger, for sharing with me their experimental experience. I appreciate Ping Koy Lam and Charles Harb for their inspiring approach to research and fruitful scientific discussions. I thank the ANU workshop guys for providing me plenty of mechanical parts required for such a complex system as the spatial entanglement machine is, and Shane with Neil, for building electronics for the experiment and repairing all the burned gadgets. My thanks go also to Ruth Wilson for helping me with all the administrative stuff and arranging accommodation while staying in Canberra.

My last and the warmest acknowledgements go to my parents and family, who always encouraged me in all circumstances. Sorry for being so much abroad out of all of you. Most importantly, I thank my partner, Jana, for her constant encouragement, and loving support, wherever we were together around the World.



Jiri Janousek

1 February 2008

Publications

During the course of this project, a number of public presentations have been made which are based on the work presented in this thesis. They are listed here for reference.

- *Observation of a comb of optical squeezing over many gigahertz of bandwidth*
R. J. Senior, G. N. Milford, J. Janousek, A. E. Dunlop, K. Wagner, H-A. Bachor, T. C. Ralph, E. H. Huntington, and C. C. Harb
Optics Express, vol. 15, no. 9, pp. 5310 (2007)
- *Tools for spatial multi-mode quantum information: modulation, detection and quantum correlations*
M. Lassen, V. Delaubert, J. Janousek, K. Wagner, H-A. Bachor, P. K. Lam, N. Treps, P. Buchhave, C. Fabre, and C. C. Harb
Phys. Rev. Lett. 98, 083602 (2007)
- *Experimental realization of spatial entanglement for bright optical beams*
J. Janousek, V. Delaubert, K. Wagner, H. Zou, C. C. Harb, P. K. Lam, and H-A. Bachor
- Oral presentation, AQIS 2007, Kyoto, Japan
- Oral presentation IF2-2-TUE, CLEO/IQEC 2007, Munich, Germany
- Poster WC0654, AIP 2006, Brisbane, Australia
- *Entangling the spatial properties of laser beams*
J. Janousek, K. Wagner, V. Delaubert, H. Zou, C. C. Harb, N. Treps, P. K. Lam, and H-A. Bachor
To be submitted to Nature Physics (2008)

Contents

I	The basics	1
1	Introduction	3
2	Theoretical quantum optics	7
2.1	Quadrature operators	7
2.1.1	Linearizing the operators	9
2.2	Gaussian quantum states of light	10
2.2.1	Vacuum states	10
2.2.2	Coherent states	10
2.2.3	Squeezed states	11
2.3	Representation of the squeezed light	11
2.3.1	Classical phase and amplitude modulation	12
2.3.2	Quantum sidebands	12
2.3.3	Wigner function	13
2.4	The quantum Langevin equation	14
2.5	The Hermite-Gauss basis	15
2.6	Summary	17
3	Experimental techniques	19
3.1	Detection of quantum states of light	20
3.1.1	Beamsplitter	20
3.1.2	Balanced homodyne detection	21
3.1.3	Optical attenuation	22
3.1.4	Power spectral density	23
3.2	Optical cavities	23
3.3	Stabilizing the optical resonators	27

3.3.1	Pound-Drever-Hall locking	27
3.3.2	Dither locking	28
3.4	The laser	29
3.5	Mode cleaning cavity	30
3.6	Generation of higher-order modes	32
3.6.1	Cavity response of higher-order modes	33
3.6.2	Optimizing generation of the TEM_{10} and TEM_{20} modes	35
3.7	Summary	36
II	OPA squeezing of higher-order modes	37
4	SHG of higher-order modes	39
4.1	Second-order nonlinear interaction	40
4.1.1	Nonlinear polarization	40
4.1.2	Energy conservation and phase-matching condition	40
4.2	Multi-mode second harmonic generation	42
4.2.1	Single pass SHG experiment	43
4.2.2	Generalized Boyd-Kleinman coefficients	44
4.2.3	Influence of the phase-matching temperature	47
4.2.4	Optimizing TEM_{10} conversion	49
4.3	Summary	50
5	OPA squeezing	51
5.1	Theory of OPA	53
5.1.1	Classical description	54
5.1.2	Quantum description	55
5.1.3	Squeezing trace	57
5.2	Generation of squeezed vacuum states	59
5.2.1	Experimental setup	59
5.2.2	Regenerative gain	62
5.2.3	TEM_{00} and TEM_{10} squeezing generation	64
5.2.4	Influence of the pump noise on squeezing generation	67
5.2.5	Optimizing the output coupler transmission	69

5.3	Summary	70
6	High-frequency squeezing	71
III	Spatial entanglement	79
7	Theory and experimental realization of spatial entanglement	81
7.1	Entangled states	83
7.1.1	Continuous variable entanglement	83
7.1.2	Inseparability criterion	85
7.1.3	EPR paradox criterion	86
7.2	Displacement and tilt	87
7.2.1	Classical description	87
7.2.2	Quantum operators	89
7.2.3	Heisenberg inequality relation	90
7.2.4	Spatial entanglement	90
7.3	Experimental setup	92
7.3.1	The squeezing sources	95
7.3.2	Generation of position and momentum squeezed states	97
7.3.3	Generation and detection of entangled states	100
7.4	Experimental results	101
7.4.1	Regenerative gain and squeezing	101
7.4.2	Measurements of the position-squeezed states	104
7.4.3	Measurements of entanglement	105
7.4.4	Characterization of the entangled states	107
7.4.5	Summary	111
8	Conclusions and outlook	113
A	Spatial entanglement setup	115
B	Picture gallery	117

List of Figures

2.1	Graphical representation and the Wigner function of a coherent state, displaced amplitude squeezed state and displaced phase squeezed state .	13
2.2	Normalized one dimensional representation of the thirst three Hermite-Gauss modes in the transverse plane	16
3.1	A schematic diagram of a beamsplitter with reflectivity ρ	20
3.2	A schematic diagram of the homodyne detection system	21
3.3	A schematics of an optical cavity coupled to the environment	24
3.4	Frequency response of a high finesse cavity for the reflected and transmitted fields	25
3.5	Spectral filtering effect of a high finesse cavity	26
3.6	Experimentally generated error signal and the imaginary component of the cavity response	28
3.7	Principle of dither locking	29
3.8	Frequency spectra of a 9 mW infrared field exiting the laser	30
3.9	Schematic design of the mode cleaning cavity used to improve the spectral and spatial mode quality of the infrared laser beam	31
3.10	Frequency spectra of a 9 mW infrared laser field before and after transmission through the MCC	32
3.11	Measurements of the transmitted field through a high finesse optical cavity with the corresponding PDH error signals used to lock the cavity	33
3.12	The rate of power coupled from the fundamental mode into the TEM ₁₀ and TEM ₂₀ modes as a function of the beam displacement	34
3.13	Phase profiles of flipped modes with corresponding Hermite-Gauss modes	35
3.14	Conversion efficiency for the TEM ₁₀ and TEM ₂₀ modes in an optical cavity utilizing flipped modes, as a function of the incident beam waist radius	36

4.1	Three wave mixing processes: SHG and OPA	41
4.2	The effect of phase mismatch on the efficiency of the nonlinear process for 10 mm long PPKTP and 10 mm long MgO:LiNbO ₃	42
4.3	Scheme of the single pass SHG experiment	43
4.4	SHG conversion efficiency as a function of the focusing parameter ξ for TEM ₀₀ , TEM ₁₀ and TEM ₂₀ pump modes	45
4.5	Modal decomposition of the SH field into the TEM _{<i>n0</i>} H-G basis as a function of the focusing parameter ξ for TEM ₁₀ and TEM ₂₀ pump modes	46
4.6	SHG conversion efficiency measurements and theoretical fits as a func- tion of the phase-matching temperature for TEM ₀₀ , TEM ₁₀ and TEM ₂₀ pump modes, and the decomposition of the SH field into the TEM _{<i>n0</i>} H-G basis	47
4.7	3D profiles and transverse cross-sections of the generated SH field for three different phase-matching temperatures for TEM ₁₀ and TEM ₂₀ pump modes	48
4.8	Modal decomposition of the SH field into the TEM ₀₀ and TEM ₂₀ modes as a function of the phase-matching temperature and the focusing param- eter ξ , when the nonlinear crystal is pumped by the TEM ₁₀ fundamental field	50
5.1	Schematic of an optical parametric amplifier	54
5.2	Amplitude squeezing generated by a back seeded OPA operating in the deamplification regime as a function of frequency and nonlinear gain	56
5.3	Squeezing traces analyzed in a homodyne detector with swept local os- cillator phase, for three different values of the nonlinear gain and optical attenuation	58
5.4	Output variance as a function of the ratio s_1/s_2 , shown for different detection efficiencies	59
5.5	Schematics of the experimental setup used to generate vacuum squeezing in the TEM ₀₀ and TEM ₁₀ modes utilizing the PPKTP OPA	60
5.6	Schematics of a bow-tie cavity OPA based on a PPKTP nonlinear material	61
5.7	Amplitude frequency spectra of a 3.5 mW SH field before and after transmission through the SH field MCC	62
5.8	Measurements and theoretical simulations of the regenerative gain of the PPKTP OPA as a function of pump power	63
5.9	Measurements of squeezing traces of TEM ₀₀ and TEM ₁₀ modes, when pumped by 350 mW of SH power in the TEM ₀₀ mode	65

5.10	Measurements and theoretically predicted variances of the vacuum squeezed states generated by the PPKTP OPA as a function of pump power . . .	66
5.11	Degradation of squeezing by an excess amplitude noise of the pump field	67
5.12	Predicted measured squeezing as a function of antisqueezing for different values of total detection efficiency and influence of phase jitter on observed squeezing	68
5.13	Optimization of the squeezed variance in the TEM_{10} mode in terms of the output coupler transmission, considering the pump field being in the TEM_{00} or TEM_{20} mode	69
6.1	Schematic of the experimental setup for squeezing generation at very high frequencies	73
6.2	High frequency TEM_{00} mode power spectrum of squeezing, normalized to the quantum noise limit	75
6.3	High frequency TEM_{10} mode power spectrum of squeezing, normalized to the quantum noise limit	76
7.1	Schematics of the quadrature entanglement experiment	84
7.2	Representation of ideal EPR states in Fresnel plane	85
7.3	EPR paradox criterion and inseparability criterion as a function of detection efficiency η_{tot}	87
7.4	Displacement and tilt of a TEM_{00} Gaussian beam relative to the propagation axis	88
7.5	Representation of a position and momentum squeezed state in the position-momentum Fresnel diagram	90
7.6	Fresnel representation of x-p entanglement and spatial entanglement . .	92
7.7	Scheme for position-momentum entanglement for a bright TEM_{00} carrier field generated by mixing a position-squeezed beam with a dim amplitude squeezed beam on a 50/50 beamsplitter	93
7.8	Schematics of the experimental setup used to demonstrate spatial entanglement	94
7.9	Schematics of the $\text{MgO}:\text{LiNbO}_3$ based OPA	96
7.10	Schematics of the beamsplitter mode combiner and the nonsymmetric Mach-Zehnder interferometer mode combiner	98
7.11	Split-detector locking	99
7.12	Electronic layout of the HD systems used to lock the system to produce a pair of entangled fields, and to perform measurements of their properties	101

7.13	Measurements of regenerative gain of the MgO:LiNbO ₃ OPAs as a function of pump power, and theoretically predicted gain	102
7.14	Measurements of locked squeezing and antisqueezing spectra produced by OPA ₁ operating in the TEM ₀₀ and TEM ₁₀ spatial modes	103
7.15	Measurements and theoretically predicted variances of the TEM ₁₀ squeezed states generated by the MgO:LiNbO ₃ based OPAs as a function of pump power	104
7.16	Squeezing and antisqueezing noise spectra of a multi-mode position-squeezed beam, compared to a TEM ₁₀ squeezed beam	105
7.17	Measured frequency spectra of the amplitude and phase quadrature variances of the individual entangled fields x and y , normalized to the QNL	106
7.18	Measured frequency spectra of the minimum of amplitude and phase quadrature sum and difference variances between the position-momentum entangled beams x and y	107
7.19	Frequency spectra of the amplitude and phase quadrature conditional variances of the beam x (y) given a measurement of that properties on the beam y (x)	108
7.20	Frequency spectra of the degree of EPR paradox between position and momentum of the entangled beams x and y	109
7.21	Frequency spectra of the degree of inseparability \mathcal{I} and EPR paradox \mathcal{E} between position and momentum of the entangled beams x and y	110
A.1	Detailed schematics of the experimental setup used to demonstrate spatial entanglement	115
B.1	Diabolo laser - dual output solid-state monolithic ring-cavity laser based on Nd:YAG material with an internal frequency doubler	117
B.2	Bow-tie cavity OPA based on a PPKTP nonlinear material	118
B.3	Experimental setup for generation of vacuum squeezing in the TEM ₀₀ and TEM ₁₀ spatial modes utilizing a PPKTP OPA	118
B.4	MgO:LiNbO ₃ based OPA serving as a TEM ₁₀ squeezing source for the spatial entanglement experiment	119
B.5	Experimental setup used to generate a pair of entangled beams in position and momentum	119

List of Tables

5.1	Parameters used for theoretical simulations of the PPKTP and MgO:LiNbO ₃ OPAs	57
6.1	Parameters used to fit the theoretical simulations to the measured high frequency squeezing results	77

Symbols and acronyms

Term	Definition
$\hat{\mathcal{O}}$	Arbitrary operator
$\bar{\mathcal{O}}$	Expectation value of operator $\hat{\mathcal{O}}$
$\delta\hat{\mathcal{O}}$	Expectation fluctuations of operator $\hat{\mathcal{O}}$
$\Delta\hat{\mathcal{O}}$	Standard deviation of operator $\hat{\mathcal{O}}$
$\Delta^2\hat{\mathcal{O}}, V_{\mathcal{O}}$	Variance of operator $\hat{\mathcal{O}}$
$\Delta_{x\pm y}^2\hat{\mathcal{O}}$	Sum and difference variance of operator $\hat{\mathcal{O}}$ between sub-systems x and y
$\Delta_{x y}^2\hat{\mathcal{O}}$	Conditional variance of operator $\hat{\mathcal{O}}$ in sub-system x after measurement of the operator in sub-system y
\hat{a}	Field annihilation operator
\hat{a}^\dagger	Field creation operator
\hat{A}	Field operator (units of $\text{s}^{-1/2}$)
c	Speed of light in vacuum
d	Nonlinear coefficient; Cavity round trip path length; Beam displacement
$\hat{\mathcal{D}}$	Displacement operator
e	Electron charge
\mathcal{E}	Degree of EPR paradox
$\hat{\mathcal{E}}$	Electric field operator
\mathcal{E}_0	Electric field amplitude
f	Lens focal length
F	Finesse
\hat{F}_a	Noise operator
g	Nonlinear gain
g_r	Regenerative gain of an OPA
g_D	Gain of the detection process
\hbar	Dirac's constant
H	Hamiltonian
H_n	Hermite polynomials
i	Photocurrent
I	Optical intensity
\mathcal{I}	Degree of inseparability
\vec{k}	Wave vector of the field

L	Length of a nonlinear crystal
\hat{n}	Photon number operator
n	Refractive index
p	Transverse momentum of the beam
\hat{p}	Momentum operator
P	Optical power; Polarization
r	Squeeze parameter
R	Radius of curvature; Mirror reflectivity
s	Transverse position parameter
S	Power spectrum
\hat{S}	Squeezing operator
T	Crystal temperature
u_{nm}	Transverse spatial mode profile
w_0	Beam waist radius
\mathcal{W}	Wigner function
\hat{x}	Position operator
\hat{X}^+	Amplitude quadrature operator
\hat{X}^-	Phase quadrature operator
\hat{X}^ϕ	Arbitrary quadrature operator
z_R	Rayleigh range of a beam
α	Coherent amplitude of \hat{a}
γ	Cavity decay rate; Cavity coupling rate
δ	Modulation depth; Kronecker delta function
δl	Cavity linewidth
Δk	Phase mismatch
ϵ	Nonlinear interaction strength
ϵ_0	Electric permittivity in free space
λ	Wavelength of light
Λ	Classical nonlinear strength
Λ_{qpm}	Poling period of a QPM nonlinear device
η	Quantum or conversion efficiency; Mirror transmissivity
θ	Tilt of a beam
ϕ	Relative phase between optical beams; Phase delay
ϕ_G	Gouy phase shift
ρ	Mirror reflectivity
ν	Visibility
ξ	Focusing parameter
τ	Round-trip time; Normalized longitudinal position
$\chi^{(2)}$	The second order susceptibility
ω	Optical carrier frequency
Ω	Sideband frequency
$\Omega_m, \Omega_{\text{PDH}}$	Modulation frequency

Term	Definition
AM	Amplitude modulation
ANU	Australian National University
BS	Beamsplitter
CV	Continuous variable
DTU	Technical University of Denmark
EM	Electro-magnetic
EOM	Electro-optic modulator
EPR	Einstein, Podolsky and Rosen
FSR	Free spectral range
FWHM	Full width at half maximum
GRIIRA	Green induced infrared absorption
HD	Homodyne detection
H-G	Hermite-Gauss
HR	High reflecting
HV	High voltage amplifier
ISO	Optical isolator
LN	Lithium Niobate
LO	Local oscillator
MC	Mode combiner
MCC	Mode cleaning cavity
MTC	Mode transferring cavity
MZI	Mach-Zehnder interferometer
OC	Output coupler
OPA	Optical parametric amplification
OPO	Optical parametric oscillation
PDH	Pound-Drever-Hall
PID	A proportional-integral-derivative controller
PM	Phase modulation
PPKTP	Periodically poled Potassium Titanyl Phosphate
PZT	Piezo ceramic transducer
QNL	Quantum noise limit
QPM	Quasi-phase matching
RBW	Resolution bandwidth
SH	Second harmonic
SHG	Second harmonic generation
VBW	Video bandwidth

Part I

The basics

Chapter 1

Introduction

Since the first experimental realization of the laser source [1], lasers became widely used in a variety of applications ranging from devices used in our daily life to novel technological and research applications in all areas of physics, chemistry and biology. One of the important applications of lasers is the optical measurement of physical parameters of a sample, such as the size of the object, its movement and velocity, changes in orientation, optical properties. The sensitivity of measurements relies on the properties of the laser light used, i.e. its wavelength, optical power, and noise statistics. In particular, using the approximation of wave optics the wavelength of light defines the ultimate limit on the minimum size of the optical measurement performed on a sample. This is defined by the Rayleigh criterion [2].

However, in order to accurately measure the spatial properties of the sample, the quantum nature of light has to be taken into account. This is relevant even though we use bright optical beams with a large photon flux for these measurements. This noise limit is a consequence of the randomness in the photon flux. The time arrival of the photons on a detection device is random, and this is the origin of *quantum fluctuations* of the optical field. This, in effect, puts an ultimate limit on the resolution of optical measurements when all other sources of noise, i.e. mechanical, acoustic, thermal and electronic, have been canceled, and is called the *standard quantum noise limit* (QNL). In other words, the quantum noise of a laser is a consequence of the Heisenberg uncertainty relation, and can not be removed.

The relative sensitivity of an optical measurement, given by the QNL, is improved with increasing photon flux of the probe laser field. When the optical power is limited, for example due to existence of a damage threshold of the sample to be measured, the only possible improvement of the sensitivity is to alter the noise properties of the laser. Overcoming this fundamental bound for the sensitivity is only possible, for particular operations of the probe laser field, using quantum optics and nonlinear processes. Recent progress in quantum optics and laser science allows generation of *squeezed states* of light, whose quantum fluctuations in a certain quadrature (variable) are reduced below the QNL, at the cost of increase of quantum fluctuations in its conjugate quadrature. This is possible as the Heisenberg uncertainty relation bounds the product of the variances of the two conjugated quadratures only, and it does not impose any restrictions to the value of individual variances. Such manipulations of the quantum fluctuations can only be achieved via an interaction of the laser light with a nonlinear medium. In this way quantum correlations are generated between the different variables of the electromagnetic light field. Experimentally, squeezed states can be generated utilizing a variety of nonlinear processes including optical parametric amplification [3, 4],

second harmonic generation [5], Kerr effect [6, 7], and other. In particular, optical parametric amplification has consistently generated the best quadrature squeezing results [8, 9, 10, 11].

Using squeezed light in optical measurements that are limited by the QNL will improve the signal-to-noise ratio. Information, which is masked by the quantum noise, can therefore be extracted. Thus squeezed light can be used for ultra-sensitive applications including sub-shot-noise spectroscopy [12, 13], or for detection of gravitational waves using large scale interferometers [14]. These applications require single spatial modes of light, and the squeezed light is matched to the mode in the sensor. However, a spatial sensor or image detection inherently requires several spatial modes. In order to improve the spatial resolution within an optical image, we require squeezed light with a specific spatial mode. For each degree of freedom of the image or the sensor we will require an additional mode and an additional source of squeezed light. Such a multi-mode spatially squeezed state can in principle be generated in transverse degenerate cavities, in which all transverse modes can be simultaneously resonant [15, 16]. These cavities, however, are unstable and require a large pump power, and are hence difficult to operate.

Things can get simpler, if we want to extract from the measurement of the object only a particular information. It has been shown that simple spatial measurements, for example of the displacement and tilt of a Gaussian beam, can be simply described with Hermite-Gauss modes [17]. Squeezed light of the required mode can be used to measure these parameters with an increased level of accuracy even below the QNL [18, 19, 20]. This is of great interest in ultra-sensitive image measurement for which quantum noise is a limiting factor, nanometer scale laser beam displacement measurements in gravitational wave detectors [21], or atomic force microscopes [22]. The detection of small displacements and tilts of a Gaussian beam below the QNL requires a multi-mode beam which combines a bright coherent TEM_{00} beam, called the *carrier* or *reference beam*, with a squeezed vacuum field of the TEM_{10} spatial profile [23].

One of the main topics of this thesis is to investigate the efficient generation of optical squeezing in the TEM_{10} mode utilizing an optical parametric amplifier, as require measurements of displacement and tilt of a laser beam below the QNL. To achieve squeezing in this particular mode requires an understanding of mode coupling of the optical fields in the second-order nonlinear media. In chapter 4, we introduce the theoretical model for the multi-mode second harmonic generation process, recently developed by Delaubert *et al.* [24, 25]. Next we test the basic principles of the nonlinear process in a periodically poled nonlinear medium PPKTP, which allows the optimization of the nonlinear gain of an optical parametric amplifier operating in a selected higher-order mode. In chapter 5, we describe in detail the experimental arrangement used to generate vacuum squeezed states in the TEM_{00} and TEM_{10} modes, employing a bow-tie resonator around the PPKTP crystal to enhance the parametric amplification, and use it as a squeezing source. We experimentally characterize the level of squeezing, measuring up to -5.5 dB of squeezing in the TEM_{00} mode and -3.1 dB of squeezing in the TEM_{10} mode, after correction for the electronic noise. We also discuss an optimization of the current system for the efficient generation of squeezing in the TEM_{10} spatial mode, promising -5.2 dB of noise suppression. In chapter 6, we experimentally demonstrate the generation of optical squeezing in multiple longitudinal modes and transverse Hermite-Gauss modes of an optical parametric amplifier. We present measurements of approximately -3 dB squeezing at baseband, 1.7 GHz, 3.4 GHz and 5.1 GHz which correspond to the first, second and third resonances of the amplifier. We show that both the magnitude and the bandwidth of the squeezing in the higher longitudinal modes is greater than can be observed at baseband.

Besides the ultra-sensitive measurements, the multi-mode spatially squeezed states can be utilized in the field of parallel quantum information communication and processing. Quantum information science is a new and rapidly expanding field of research, which combines the techniques developed in quantum optics with those of information science. Laser beams are widely used to send and process quantum information, and this has been done with the information encoded into one mode. However, multiple orthogonal spatial modes can also provide advantages with regard to the complexity of quantum information protocols, and can allow parallel transfer of quantum information through an optical network [26]. Moreover combination of the spatially squeezed states on a 50/50 beamsplitter allows production of entangled optical beams or *EPR states*, i.e. states entangled in position and momentum, in the continuous variable regime [27], as originally proposed by Einstein, Podolsky and Rosen in 1935 [28]. The EPR paradox is a quantum mechanical phenomenon in which the states of two or more objects have to be described with reference to each other (inseparability), even though the different objects may be spatially separated (non-locality). Position-momentum entangled beams give us the opportunity to investigate fundamental quantum properties of twin light beams, i.e. non-locality and entanglement, in the spatial domain. These quantum properties are the tools required for future applications such as spatial quantum communication and computing.

In chapter 7, we introduce the concept of spatial entanglement. We detail the experimental arrangement used to generate a pair of entangled beams in position and momentum. The experiment is based on a pair of OPAs each delivering -3.2 dB of locked squeezing in the TEM_{10} spatial mode. The experimental results are presented showing strong quantum correlations in the frequency range 3.2 – 4.2 MHz between the spatial properties of the two entangled fields. These results show the first demonstration of entanglement between position and momentum of a bright optical beam in the continuous variable regime as originally considered by Einstein, Podolsky and Rosen. This novel system has the potential to demonstrate quantum imaging protocols such as teleportation and dense coding in the spatial domain. We could also demonstrate a quantum communication system with several degrees of freedom by encoding and detecting modulation onto squeezing into different degrees of freedom and give us the opportunity to explore techniques for the modulation, transmission and detection of complex quantum states.

Chapter 2

Theoretical quantum optics

Contents

2.1	Quadrature operators	7
2.1.1	Linearizing the operators	9
2.2	Gaussian quantum states of light	10
2.2.1	Vacuum states	10
2.2.2	Coherent states	10
2.2.3	Squeezed states	11
2.3	Representation of the squeezed light	11
2.3.1	Classical phase and amplitude modulation	12
2.3.2	Quantum sidebands	12
2.3.3	Wigner function	13
2.4	The quantum Langevin equation	14
2.5	The Hermite-Gauss basis	15
2.6	Summary	17

In this chapter, we introduce the basic theory required for this thesis. We introduce the amplitude and phase quadrature operators and define the Heisenberg uncertainty principle. We show the method of linearizing quantum operators, which significantly simplifies an analysis of different problems in quantum optics. We introduce the Gaussian quantum states of light, i.e. the vacuum state, the coherent state and the squeezed state, and define the displacement and squeezing operators. The classical phase and amplitude modulation is detailed. We describe two pictures for visualizing squeezed states: the quantum sideband picture and the graphical representation utilizing the Wigner function. We introduce the quantum Langevin equation, employed in this thesis for modeling optical cavities and optical parametric amplifiers. Finally, we define the Hermite-Gauss basis used to describe the transverse profile of optical beams.

2.1 Quadrature operators

The quantization of the electromagnetic field represents one of the differences between a classical field, which can have any energy value, and a quantum field of discrete energy values. The quantization of the field is carried out by considering the field as an ensemble of harmonic oscillators. In the Heisenberg picture of quantum mechanics an electromagnetic oscillation at frequency ω is represented by the field annihilation

operator $\hat{a}(\omega)$, which together with its conjugate, the field creation operator $\hat{a}^\dagger(\omega)$, satisfy the boson commutation relations [29]

$$[\hat{a}(\omega), \hat{a}^\dagger(\omega')] = \delta(\omega - \omega'), \quad (2.1)$$

$$[\hat{a}(\omega), \hat{a}(\omega')] = [\hat{a}^\dagger(\omega), \hat{a}^\dagger(\omega')] = 0, \quad (2.2)$$

where $\delta(\omega)$ is the Kronecker delta function. Note that the commutation relations in the time domain are defined similarly to their frequency domain counterparts. In the following, we will suppress for simplicity the notation of frequency dependence and all the operators will be also assumed to be the frequency domain operators.

Any optical field and its evolution can be described by the creation and annihilation operators¹. The two operators are non-Hermitian and therefore nonmeasurable. On the other hand, their real and imaginary parts, the amplitude quadrature of the field \hat{X}^+ and the phase quadrature of the field \hat{X}^- , respectively, are Hermitian and it is the properties of these operators that are typically measured in quantum optics experiments. These operators are defined as

$$\hat{X}^+ = \hat{a}^\dagger + \hat{a}, \quad (2.4)$$

$$\hat{X}^- = i(\hat{a}^\dagger - \hat{a}). \quad (2.5)$$

An arbitrary quadrature operator \hat{X}^ϕ Hermitian for all ϕ values can also be defined as a linear combination of amplitude and phase quadratures by

$$\hat{X}^\phi = \hat{a}e^{-i\phi} + \hat{a}^\dagger e^{i\phi} = \hat{X}^+ \cos \phi + \hat{X}^- \sin \phi. \quad (2.6)$$

The two quadrature operators \hat{X}^+ and \hat{X}^- are related to the amplitude and phase of the optical field, respectively, and obey the following commutation relation

$$[\hat{X}^+, \hat{X}^-] = 2i. \quad (2.7)$$

The Heisenberg uncertainty principle states [30] that it is impossible to simultaneously obtain precise knowledge of two non-commuting observables. That is, given the commutation relation between two arbitrary operators $\hat{\mathcal{A}}$ and $\hat{\mathcal{B}}$

$$[\hat{\mathcal{A}}, \hat{\mathcal{B}}] = \mathcal{C}, \quad (2.8)$$

where \mathcal{C} is a complex number, the product of the uncertainties of simultaneous measurements on the observables is bounded by

$$\Delta\hat{\mathcal{A}}\Delta\hat{\mathcal{B}} \geq \frac{1}{2}|\mathcal{C}|, \quad (2.9)$$

where $\Delta\hat{\mathcal{O}}$ is the standard deviation² of measurements of an operator $\hat{\mathcal{O}}$ performed on an ensemble of identically prepared systems. This is a consequence of the quantization

¹The electric field envelope $\hat{\mathcal{E}}(\vec{r}, t)$ of an electromagnetic radiation polarized in direction \vec{e} can be expressed using the creation and annihilation operators as

$$\hat{\mathcal{E}}(\vec{r}, t) = \mathcal{E}_0 \vec{e} \left(u_{nm}(\vec{r}) \hat{a} e^{-i(\omega t - \vec{k} \cdot \vec{r})} + u_{nm}^*(\vec{r}) \hat{a}^\dagger e^{i(\omega t - \vec{k} \cdot \vec{r})} \right), \quad (2.3)$$

where \mathcal{E}_0 is the field amplitude, $u_{nm}(\vec{r})$ is the transverse spatial mode profile introduced in sec. 2.5, \vec{r} describes the spatial position and \vec{k} is the wave-vector of the field.

²The standard deviation is related to the variance $\Delta^2\hat{\mathcal{O}}$ and expectation values by

$$\Delta^2\hat{\mathcal{O}} = \langle \hat{\mathcal{O}}^2 \rangle - \langle \hat{\mathcal{O}} \rangle^2. \quad (2.10)$$

of the electromagnetic field. The result is that there is an uncertainty relation between the phase and amplitude quadratures of the electromagnetic field and is given by

$$\Delta\hat{X}^+\Delta\hat{X}^- \geq 1. \quad (2.11)$$

A state of light that satisfies $\Delta\hat{X}^+\Delta\hat{X}^- = 1$ is termed *minimum uncertainty state*³. The majority of the work presented in this thesis is aimed at manipulating this uncertainty relation, that is enhancing the measurement precision of one quadrature at the cost of other, and is termed *squeezing*. The quantum fluctuations in the measurement of each quadrature are referred to as the *quantum noise* of the electromagnetic field.

2.1.1 Linearizing the operators

The most common method of generating analytic results in quantum optics is to expand the operators about their steady state values and then linearize the resulting expressions to first order in the fluctuation terms [31]. Assuming that the fluctuations of the electromagnetic field are much smaller than the steady state amplitudes, the creation and annihilation operators can be written in the linearized form as

$$\hat{a} = \alpha + \delta\hat{a}, \quad \hat{a}^\dagger = \alpha^* + \delta\hat{a}^\dagger, \quad (2.12)$$

where α is the (complex) expectation value $\langle\hat{a}\rangle$, and $\delta\hat{a}$ is the fluctuation operator with the mean value $\langle\delta\hat{a}\rangle = 0$. Similarly, $\langle\hat{a}^\dagger\rangle = \alpha^*$ and $\langle\delta\hat{a}^\dagger\rangle = 0$. Linearizing the operators greatly simplifies the analysis of different problems in quantum optics. Using the equa. 2.12, the quantum fluctuations in the quadrature ϕ of the mode are described by the operator

$$\delta\hat{X}^\phi = \delta\hat{a}e^{-i\phi} + \delta\hat{a}^\dagger e^{i\phi}, \quad (2.13)$$

which has a zero mean value $\langle\delta\hat{X}^\phi\rangle = 0$. The variance of the arbitrary quadrature operator \hat{X}^ϕ is therefore given by

$$\Delta^2\hat{X}^\phi = \langle(\delta\hat{X}^\phi)^2\rangle - \langle\delta\hat{X}^\phi\rangle^2 = \langle(\delta\hat{X}^\phi)^2\rangle \quad (2.14)$$

and can be obtained by evaluating a single expectation value. To validate the linearization of the operators, we can calculate the variance of the photon number. The photon number $\hat{n} = \hat{a}^\dagger\hat{a}$ for a field in the coherent state is after linearization given by

$$\hat{n} \approx |\alpha|^2 + |\alpha|\delta\hat{X}^+. \quad (2.15)$$

The expectation value of the photon number is then $\bar{n} = \langle\hat{n}\rangle = |\alpha|^2$, since $\langle\delta\hat{X}^+\rangle = 0$, which is a result expected from exact theory. The linearized variance of photon number can be found as

$$\Delta^2\hat{n} = |\alpha|^2\langle(\delta\hat{X}^+)^2\rangle. \quad (2.16)$$

Calculating the variance of the coherent state using the equa. 2.16 gives $\Delta^2\hat{n} = |\alpha|^2$, whereas calculating exact variance results in $\Delta^2\hat{n} = |\alpha|^2 + 1$. Hence the linearization is valid provided the extra '1' can be ignored. This will always be the case for bright coherent beams, where $|\alpha|^2 \approx 10^{17}$ assuming 1 mW of light at 1064 nm, and the method of linearizing operators can therefore be safely adapted throughout this thesis.

³The parameter used to characterize how close a state is from a minimum uncertainty state is called *purity* \mathcal{P} . For a pure state $\mathcal{P} = 1$, whereas for a mixed state $\mathcal{P} < 1$.

2.2 Gaussian quantum states of light

In this thesis, we limit ourselves to the analysis of the quantum states relevant to quantum optics experiments in the continuous variable (CV) regime⁴: the Gaussian quantum states. We will introduce in the following the fundamental quantum states, i.e. the vacuum states and the coherent states, together with the squeezed states which are the non-classical states of light generated and used in the experiments throughout this thesis. The entangled states, which are obtained by combination of two squeezed states in quadrature on a 50/50 beamsplitter, will be introduced in sec. 7.1.

2.2.1 Vacuum states

The vacuum state $|0\rangle$ is the ground state of the electromagnetic field with the average number of photons to be zero. Recalling the Heisenberg inequality relation 2.11, we can say that the electromagnetic field of a vacuum state still fluctuates, even though it has no photons. In fact, the fluctuations of the amplitude and phase quadratures of a vacuum state are equal, i.e. $\Delta\hat{X}^+ = \Delta\hat{X}^- = 1$. Thus processes such as optical loss that couple vacuum states, or *vacuum noise*, to a system will have the unavoidable consequence of also introducing fluctuations to the system amplitude and phase quadratures. We will show modeling of optical loss using a beamsplitter in sec. 3.1.3. The fluctuations of a vacuum state pose a limit to the accuracy of most optical measurement devices. The vacuum noise is also referred to as *quantum noise* or *shot noise*. A variance which is measured to be less than the noise of the vacuum state is referred to as sub-shot noise or being below the quantum noise limit (QNL).

2.2.2 Coherent states

The coherent state of light $|\alpha\rangle$ is a minimum uncertainty state with the average number of photons $\bar{n} = |\alpha|^2$ and quadrature variances identical to those of the vacuum state, i.e. equal to 1 and uncorrelated. The coherent state can be written in terms of the Fock states $|n\rangle$ as [29]

$$|\alpha\rangle = \sum_n |n\rangle \langle n|\alpha\rangle = e^{-|\alpha|^2/2} \sum_n \frac{\alpha^n}{\sqrt{n!}} |n\rangle, \quad (2.17)$$

which is the Poissonian distribution⁵ of the Fock states $|n\rangle$, or rather the electromagnetic oscillation states that contain exactly n photons, and α is the coherent amplitude of the field at frequency ω , $\alpha = \langle \hat{a} \rangle$. A coherent state may be generated from a vacuum state by using the *displacement operator* $\hat{\mathcal{D}}$, i.e. $|\alpha\rangle = \hat{\mathcal{D}}|0\rangle$, defined as

$$\hat{\mathcal{D}}(\alpha) = \text{Exp}\left[-\frac{1}{2}|\alpha|^2 + \alpha\hat{a}^\dagger - \alpha^*\hat{a}\right]. \quad (2.18)$$

Note that the coherent state describes approximately the output of a single frequency laser well above the lasing threshold.

⁴CV regime corresponds to large photon flux as opposed to the photon counting regime.

⁵Since any truly random system exhibits Poissonian statistics the photon number distribution of a coherent state is therefore entirely random. For bright coherent states the Poissonian distribution is well approximated by the Gaussian distribution.

2.2.3 Squeezed states

The squeezed state is a non-classical state of light that has noise properties different from the vacuum state. Although the Heisenberg inequality 2.11 defines a minimum value to the product of the variances of the two conjugated quadratures, it does not impose any restrictions to the value of individual variances. It is therefore possible to produce states for which the variance of one quadrature is reduced below the QNL, so either $\Delta\hat{X}^+ < 1$ or $\Delta\hat{X}^- < 1$, at the cost of increasing the variance of the conjugate quadrature. In this section we will assume a minimum uncertainty squeezed state which requires that $\Delta\hat{X}^+\Delta\hat{X}^- = 1$ ⁶.

The squeezed state can be derived from the vacuum state by applying the unitary *squeezing operator* $\hat{\mathcal{S}}$ and the displacement operator $\hat{\mathcal{D}}$. The squeezing operator is defined in terms of the squeeze parameter r as

$$\hat{\mathcal{S}}(r, \phi) = \text{Exp}\left[\frac{1}{2}(r^*e^{-i\phi}\hat{a}^2 - re^{i\phi}\hat{a}^{\dagger 2})\right], \quad (2.19)$$

where ϕ defines the quadrature of the squeezing relative to some local oscillator (LO). The squeezing parameter is assumed to be positive, i.e. $r \geq 0$. If $r = 0$ we obtain a coherent state; however for infinite squeezing $r \rightarrow \infty$ we get a perfectly squeezed state. The pure squeezed state $|\alpha, \phi, r\rangle$ is constructed from the vacuum state as

$$|\alpha, \phi, r\rangle = \hat{\mathcal{D}}(\alpha)\hat{\mathcal{S}}(r, \phi)|0\rangle \quad (2.20)$$

and its average number of photons \bar{n} is found to be $\bar{n} = \sinh^2 r + |\alpha|^2$. The quadrature standard deviations $\Delta\hat{X}^\phi$ are for the squeezed quadrature e^{-r} and for the non-squeezed quadrature e^r defined relative to LO. By applying the squeezing operator directly on a vacuum state, we obtain a *squeezed vacuum* state which is not actually a vacuum state as it contains some photons, since $\bar{n} = \sinh^2 r$. The greater degree of squeezing, the more photons in the beam. On the other hand, a squeezed state with a large coherent amplitude is called a *bright squeezed* state. Experimentally, the squeezed states can be obtained via a nonlinear interaction such as optical parametric amplification (OPA) [3, 4], second harmonic generation (SHG) [32, 33], Kerr effect [6, 7] and other. In the experiments throughout this thesis, we generated the squeezed states via OPA, which is a parametric down conversion process and is introduced in sec. 5.1.

2.3 Representation of the squeezed light

In previous section we derived the operators and expressions used to describe a squeezed state of light. This, however does not provide an intuitive picture of the state itself. For our work it will be sufficient using two pictures: the quantum sideband picture and the graphical representation using the Wigner function. In the quantum sideband picture, we can understand squeezing as having correlations between the upper and lower sidebands at a particular frequency, centered around the carrier field frequency. This picture is analogous to the classical phase and amplitude modulation, which is also introduced in the following. It is also useful to visualize a quantum state in a graphical representation using the Wigner function, which completely defines all the parameters of a quantum state.

⁶In fact, due to the optical loss in any real experiment, the product $\Delta\hat{X}^+\Delta\hat{X}^-$ is always greater than unity.

2.3.1 Classical phase and amplitude modulation

Phase modulation (PM) can be produced by modulating the length of an optical path of a propagating field. This can be done simply by varying the position of a mirror mounted on a PZT actuator. However, for higher modulation frequencies the response of a PZT actuator is not linear over its cross section, which results in distortion of the modulated signal. Therefore for high speed modulation it is more convenient to utilize the electro-optic effect [34] of certain crystals, e.g. lithium niobate. The effect is the change in refractive index of the material exposed to the modulating electric field. Regardless of the method of production, the desired result is a time varying change in the phase of the field. Mathematically, the PM beam at frequency Ω_m can be represented for a small modulation depth $\delta \ll 1$ by

$$\mathcal{E}_{PM} = \mathcal{E}_0 e^{i\omega t} \left(1 + i\delta \cos(\Omega_m t) \right) = \mathcal{E}_0 e^{i\omega t} \left(1 + i\frac{\delta}{2} e^{i\Omega_m t} + i\frac{\delta}{2} e^{-i\Omega_m t} \right), \quad (2.21)$$

where $\mathcal{E}_0 e^{i\omega t}$ is the field prior to modulation, referred to as the *carrier field*. The modulation gives rise to two additional *sidebands* offset from the carrier in frequency by $\pm\Omega_m$. The two sidebands are of equal magnitude with relative phase shift of π . Larger modulation depths introduce onto the beam higher order sidebands at harmonics of Ω_m , which are undesirable in practical experiments.

Amplitude modulation (AM) can be introduced onto the beam using acousto-optic effect [35, 36, 37], which is based on diffraction of a light field on a grating formed by sound waves in a material. Alternatively, AM can be produced through modulations of the attenuation experienced by the beam. This can be done by first passing a circularly polarized light through an electro-optic crystal, where the phase of only the vertically polarized component of the field is modulated, resulting in the polarization modulation of the output field. In the second stage we select one of the components of the output field with a polarizing beamsplitter. The final field is purely AM field, but attenuated by 50% compared to the power of the original field. The AM field is given by

$$\mathcal{E}_{AM} = \mathcal{E}_0 e^{i\omega t} \left(1 + \delta \cos(\Omega_m t) \right) = \mathcal{E}_0 e^{i\omega t} \left(1 + \frac{\delta}{2} e^{i\Omega_m t} + \frac{\delta}{2} e^{-i\Omega_m t} \right). \quad (2.22)$$

Note that AM field has always two sidebands at frequencies $\pm\Omega_m$ regardless how large the modulation depth δ is.

2.3.2 Quantum sidebands

Results of classical PM and AM can help us to understand noise origin of quantum states. Quantum noise can be thought of as sidebands created by beating the carrier field with the vacuum field, which results in white amplitude and phase noise. The quantum sidebands are all equal size and exist along both sides of the carrier field frequency. In the case of coherent state, phases of all the quantum sideband pairs are completely uncorrelated so the quantum noise is distributed equally between the amplitude and phase quadratures. This results in an intensity noise spectrum that is flat.

Squeezing is the reduction of the amplitude or phase noise below the QNL. We can imagine that this is due to the creation of correlations between the upper $+\Omega_m$ and lower $-\Omega_m$ sidebands. At the frequencies where squeezing occurs, the sidebands become synchronized with one another rather than being fully random. Giving an example, amplitude squeezing at sideband frequency Ω_m occurs when the random quantum side-

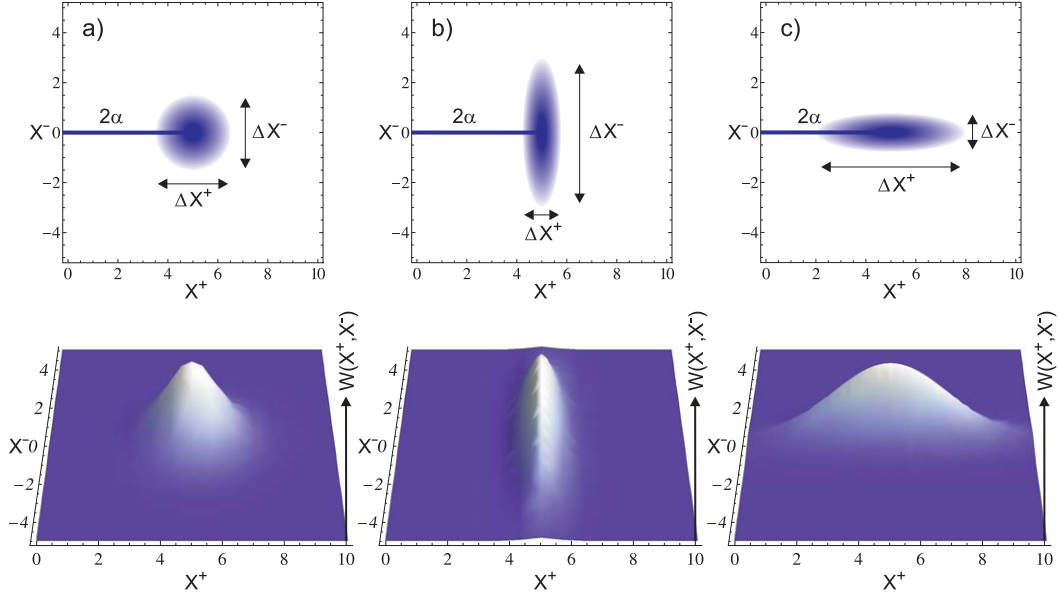


Figure 2.1: Graphical representation and the Wigner function of a) coherent state, b) displaced amplitude squeezed state and c) displaced phase squeezed state. Every state is characterized by its coherent amplitude α and the standard deviation of the quadratures $\Delta\hat{X}^\pm$. Parameters used: $\alpha = 2.5$, $\Delta\hat{X}^\pm = 0.5$ for the squeezed quadrature, $\Delta\hat{X}^\pm = 2$ for the antisqueezed quadrature.

bands at this frequency are converted to phase sidebands. This results in an increase of phase noise, but also means that the amplitude noise will be squeezed. Detailed description of the quantum optics of optical sidebands can be found in reference [38].

2.3.3 Wigner function

Any quantum state can be fully characterized by its density matrix. As we are dealing in this thesis with CV states of light containing typically 10^{17} photons, the density matrix is of infinite dimension. Furthermore, the density matrix does not provide a particularly intuitive representation of the state. It is therefore convenient for us to describe quantum states using a quasi-probability distribution such as the Wigner function [39].

A classical electromagnetic oscillation can be represented by its coherent amplitude α as a point in the phase space - the two-dimensional space with the amplitude quadrature X^+ and the phase quadrature X^- as dimensions. The coherent amplitude may fluctuate in some manner and this fluctuation can then be represented as a joint-probability distribution for the real and imaginary parts of the coherent amplitude, such that at any given time the oscillation exists with well defined amplitude and phase quadratures. This certainly does not hold in quantum mechanics due to the Heisenberg uncertainty principle. Instead, the Wigner quasi-probability distribution plays an analogous role.

Considering that the states have a Gaussian statistics the Wigner function is equivalent to a classical probability distribution, and is a two-dimensional Gaussian. The Wigner function of a displaced Gaussian state with coherent amplitude $\alpha = \alpha^+ + i\alpha^-$ is given in the amplitude and phase quadrature space by [40]

$$\mathcal{W}(X^+, X^-) = \frac{2}{\pi\Delta\hat{X}^+\Delta\hat{X}^-} \text{Exp}\left[-\frac{(X^+ - 2\alpha^+)^2}{2\Delta^2\hat{X}^+} - \frac{(X^- - 2\alpha^-)^2}{2\Delta^2\hat{X}^-}\right]. \quad (2.23)$$

The Wigner function of any Gaussian state can be completely defined by its standard deviation contour and a stick representing the coherent amplitude of the state. Fig. 2.1 shows the Wigner function and the *graphical representation* of a coherent state, displaced amplitude and phase squeezed states. The Wigner function of a Gaussian state may be fully characterized by its coherent amplitude α , and by the width of the standard deviation contour along its semimajor and semiminor axes, which for a squeezed state correspond to the standard deviations of the antisqueezed and squeezed quadratures, respectively. So by measuring the three parameters α , $\Delta\hat{X}^+$ and $\Delta\hat{X}^-$, we can achieve a complete characterization of quantum states.

2.4 The quantum Langevin equation

In previous sections, we introduced the quantum states of light and basic tools used to characterize them. The quantum states are produced in certain optical systems and their properties are directly linked in reverse to properties of these systems. In order to investigate the evolution of these states of light in an optical system, we introduce here the quantum Langevin equation, which is particularly important to model behavior of optical cavities. In this thesis, we will use this equation to model the mode cleaning cavity (sec. 3.5) and the optical parametric amplifier (sec. 5.1), where placing a nonlinear medium inside an optical cavity has the effect of enhancing the nonlinear interaction.

In general, any real system exchanges its energy irreversibly with the environment, and is termed as an *open system*. For optical systems this has the consequence that photons will leak out of the system into the environment, while quantum fluctuations will flow into the system from the environment. This is opposed to the *closed system*, which exchanges no energy with the rest of the universe.

Any physical system can be mathematically described by the Heisenberg equation of motion [29]. For a closed quantum system with Hamiltonian H_{rev} , the equation of motion of the system operator \hat{a}_{sys} is given by

$$\dot{\hat{a}}_{sys} = \frac{1}{i\hbar} [\hat{a}_{sys}, H_{rev}]. \quad (2.24)$$

Because this system is closed the Hamiltonian is reversible, hence the name H_{rev} . In open systems however, fields from the environment interact with the system, and equation of motion becomes more complex as extra terms must be included to describe the exchange of energy with the rest of the universe. It has been shown [41] that if the environment interacts irreversibly with the system operator of interest \hat{a}_{sys} , its effect on the equation of motion of the operator can be modeled by adding a correction term to equa. 2.24. This statement holds assuming that the coupling of the system to the environment γ is independent of frequency. The equation of motion is then

$$\dot{\hat{a}}_{sys} = \frac{1}{i\hbar} [\hat{a}_{sys}, H_{rev}] - [\hat{a}_{sys}, \hat{a}^\dagger] (\gamma \hat{a} - \sqrt{2\gamma} \delta \hat{a}_{env}) + (\gamma \hat{a}^\dagger - \sqrt{2\gamma} \delta \hat{a}_{env}^\dagger) [\hat{a}_{sys}, \hat{a}], \quad (2.25)$$

where $\delta \hat{a}_{env}$ is the time domain annihilation operator describing the environment and \hat{a} is the system operator coupled to the environment. This is known as the *quantum Langevin equation*. The first part of equa. 2.25 is the equation of motion of the closed, reversible system; the two other terms are due to the irreversible interaction of the system with the universe, which is modeled as a reservoir with an infinite number of modes [29].

We will be mainly interested in the evolution of the optical field in a cavity, which is modeled as a harmonic oscillator with Hamiltonian $H_{rev} = -\omega\hbar\hat{a}^\dagger\hat{a}$. Choosing a frame rotating at frequency ω , we make the substitutions $\hat{a} = \hat{a}e^{-i\omega t}$ and $\delta\hat{a}_{env} = \delta\hat{a}_{env}e^{-i\omega t}$ and the equation of motion is then found to be

$$\dot{\hat{a}} = -\gamma\hat{a} + \hat{F}_a, \quad (2.26)$$

where \hat{F}_a is the *noise operator* describing the coupling of quantum fluctuations from the environment into the system. The noise operator depends on the reservoir variables and is given as $\hat{F}_a = \sqrt{2\gamma}\delta\hat{a}_{env}$ with the expectation value $\langle\hat{F}_a\rangle = 0$. Note that the presence of the noise operator in equa. 2.26 is necessary to preserve the time domain commutation relation 2.1 at all times. In the absence of noise term, i.e. $\hat{F}_a = 0$, the equation of motion 2.26 can be easily solved and using these results, the commutation relation of the field creation and annihilation operators becomes

$$[\hat{a}, \hat{a}^\dagger] = \text{Exp}[-2\gamma t], \quad (2.27)$$

which clearly represents violation of the commutation relation. The noise operator with appropriate correlation properties helps to maintain the commutation relation 2.1 at all times. Moreover, the presence of the noise term \hat{F}_a along with the damping term in equa. 2.26 is a manifestation of the fluctuation-dissipation theorem of statistical mechanics, which states that dissipation is always accompanied by fluctuations.

2.5 The Hermite-Gauss basis

In this section, we introduce a mathematical formalism of the Hermite-Gauss (H-G) basis, which will be used throughout this thesis to describe the spatial profile of optical beams. The H-G basis is commonly used to describe the transverse distribution of optical fields propagating in a medium of rectangular symmetry, typically an optical cavity. H-G modes, denoted here as u_{nm} or TEM_{nm} , are solutions of the paraxial field propagation equation and are therefore limited to the description of beams whose propagation direction remains within a small angle with respect to the propagation axis z . Their expression is composed of the Hermite polynomials H_n multiplied by a Gaussian function. Their general normalized expression is [42]

$$u_{nm}(x, y, z) = \frac{C_{nm}}{w(z)} H_n\left(\frac{\sqrt{2}x}{w(z)}\right) H_m\left(\frac{\sqrt{2}y}{w(z)}\right) e^{-\frac{x^2+y^2}{w(z)^2}} e^{+ik\frac{x^2+y^2}{2R(z)}} e^{+ikz} e^{-i(n+m+1)\phi_G(z)}, \quad (2.28)$$

where we have introduced parameters

$$C_{nm} = \frac{1}{\sqrt{\pi 2^{n+m+1} n! m!}}, \quad (2.29)$$

$$w(z) = w_0 \sqrt{1 + \left(\frac{z}{z_R}\right)^2}, \quad (2.30)$$

$$R(z) = z + \frac{z^2}{z_R}, \quad (2.31)$$

$$\phi_G(z) = \arctan\left(\frac{z}{z_R}\right). \quad (2.32)$$

Here λ is the wavelength of light, w_0 is the beam waist radius, $z_R = \frac{\pi w_0^2}{\lambda}$ is the beam Rayleigh range, $R(z)$ is the radius of curvature, and $\phi_G(z)$ is the Gouy phase shift [42, 43], which will play a particularly important role in our work.

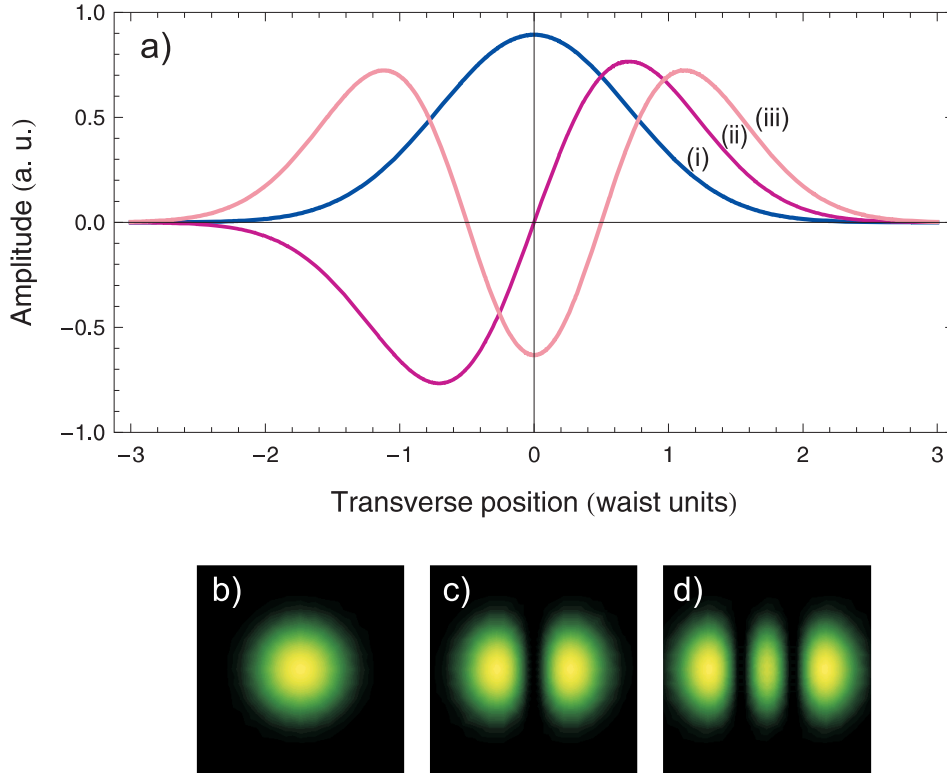


Figure 2.2: a) Normalized one dimensional representation of the first three Hermite-Gauss modes in the transverse plane: (i) TEM_{00} , (ii) TEM_{10} and (iii) TEM_{20} . Two-dimensional intensity distribution of H-G modes: b) TEM_{00} , c) TEM_{10} and d) TEM_{20} .

The quantity $w(z)$ is independent of n and m , but does not correspond to the beam radius for higher order modes. Indeed, the spatial extension of the modes increases with the order of the mode. A TEM_{nm} mode has n and m zeros on the x and y axis, and therefore $n + 1$ and $m + 1$ lobes along the same axis, respectively. As shown by equa. 2.28, spatial modes of different order n and m can be present on each transverse direction. However, in our case of interest, we will consider the variations of the field along a single transverse axis, namely x . For the sake of simplicity, we will thus denote the one dimensional H-G modes by $u_n(x, z)$ and knowing that the dependence along the y axis will always be a simple Gaussian in our experiments, these modes will be related to the two dimensional ones by the relation

$$u_n(x, z) = \int_{-\infty}^{\infty} u_{n0}(x, y, z) dy. \quad (2.33)$$

We will be primarily concerned with the first three one-dimensional H-G modes, which are represented in fig. 2.2. We can see that the spatial extension along the transverse axis increases with the order of the mode, as previously discussed, and their expressions are

$$u_0(x, z) = \left(\frac{2}{\pi w^2(z)} \right)^{\frac{1}{4}} e^{-\frac{x^2}{w(z)^2}} e^{ik \frac{x^2}{2R(z)}} e^{ikz} e^{-i\phi_G(z)}, \quad (2.34)$$

$$u_1(x, z) = \left(\frac{2}{\pi w^2(z)} \right)^{\frac{1}{4}} \frac{2x}{w(z)} e^{-\frac{x^2}{w(z)^2}} e^{ik \frac{x^2}{2R(z)}} e^{ikz} e^{-2i\phi_G(z)}, \quad (2.35)$$

$$u_2(x, z) = \left(\frac{2}{\pi w^2(z)} \right)^{\frac{1}{4}} \frac{1}{\sqrt{2}} \left(\frac{4x^2}{w^2(z)} - 1 \right) e^{-\frac{x^2}{w(z)^2}} e^{ik \frac{x^2}{2R(z)}} e^{ikz} e^{-3i\phi_G(z)}. \quad (2.36)$$

The higher order H-G modes are particularly interesting as they are directly related to simple spatial properties of Gaussian beams [44, 45]. For our work, we will focus on the displacement and tilt of a propagating TEM₀₀ carrier beam, where the information about the change in transverse position δd and tilt $\delta\theta$ is encoded respectively as a real and imaginary parts of the TEM₁₀ mode propagating along with the carrier beam [46]. This feature can be utilized in generation of a position-momentum entanglement, as detailed in chapter 7. Moreover the real and imaginary parts of the TEM₂₀ mode are directly related to the waist size mismatch δw and a waist size position mismatch δz along the propagation axis z [25].

2.6 Summary

In summary, we introduced the basic theory required for the thesis. This includes amplitude and phase quadrature operators, which are related to the amplitude and phase of the optical field, and we showed how these two quantities are bounded by Heisenberg uncertainty principle. We introduced the method of linearizing the operators and proved that this approximation is always valid for bright optical beams, which is the case in our experiments. We introduced the Gaussian quantum states of light, i.e. the vacuum state, the coherent state and the squeezed state, and defined the displacement and squeezing operators. We discussed the classical phase and amplitude modulation, which will be particularly important for implementing locking schemes into an optical system. We showed how squeezing can be visualized using the quantum sideband picture and the graphical representation utilizing the Wigner function. We introduced the quantum Langevin equation, which will be particularly important for modeling optical cavities and optical parametric amplifiers. Finally, we introduced a mathematical formalism of the Hermite-Gauss basis used in this thesis to describe the transverse profile of optical beams.

Chapter 3

Experimental techniques

Contents

3.1	Detection of quantum states of light	20
3.1.1	Beamsplitter	20
3.1.2	Balanced homodyne detection	21
3.1.3	Optical attenuation	22
3.1.4	Power spectral density	23
3.2	Optical cavities	23
3.3	Stabilizing the optical resonators	27
3.3.1	Pound-Drever-Hall locking	27
3.3.2	Dither locking	28
3.4	The laser	29
3.5	Mode cleaning cavity	30
3.6	Generation of higher-order modes	32
3.6.1	Cavity response of higher-order modes	33
3.6.2	Optimizing generation of the TEM ₁₀ and TEM ₂₀ modes	35
3.7	Summary	36

In this chapter, we introduce basic tools required for quantum optics related experiments. First, we detail techniques used to accurately measure the quantum states of light. These employ the beamsplitter, the most powerful tool in quantum optics experiments, which makes possible the homodyne detection scheme to work. Besides detection of quantum states of light, we show how the beamsplitter can be used to model inefficient processes. We introduce methods to model optical cavities and show their spectral filtering effect. We detail two frequently used techniques for controlling length of optical resonators.

We introduce the laser source used in all experiments throughout this thesis, and present a design of a mode cleaning cavity employed for spectral and spatial filtering of the coherent light. We discuss methods for converting a mode of a certain spatial profile into any desired higher-order Hermite-Gauss mode. We show that an optical cavity can serve as a selective mode converter, and we address limits of this device for power conversion of the fundamental mode into any desired Hermite-Gauss mode.

3.1 Detection of quantum states of light

The measurement of the noise properties of the optical field is not directly performed at the optical frequency ω , as a real photodetector¹ cannot follow such fast oscillations of the optical field, which is in the order of 10^{15} Hz. Instead the measurement is done at some optical sideband frequencies $\omega + \Omega$, where Ω is within the photodetector bandwidth $\Delta\Omega$ ². The photo detection can be described by the photoelectric effect, the process where electrons are liberated from material under the action of radiant energy. The number of generated electrons is proportional to the number of photons in the beam to be detected. As a result the photocurrent is a measure of the optical power of the detected field, and is given by

$$i = \eta_{det} e \frac{P}{\hbar\omega}, \quad (3.1)$$

where P is the incident optical power of a beam of frequency ω , η_{det} is the quantum efficiency of the photodiode and e is the charge of the electron. The generated electronic signals are classical signals. Nevertheless it reflects the quantum properties of the detected light field. In quantum optics, one is highly concerned about losses and therefore also about the quantum efficiency η_{det} of the photodiodes³.

3.1.1 Beamsplitter

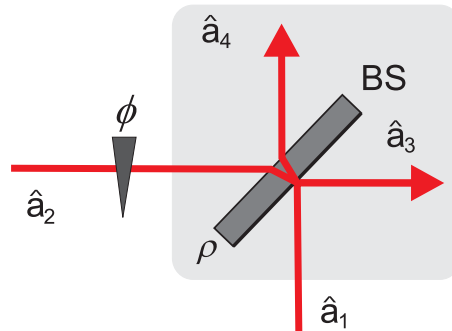


Figure 3.1: A schematic diagram of a beamsplitter with reflectivity ρ . The incident fields are \hat{a}_1 and \hat{a}_2 , the exiting fields are \hat{a}_3 and \hat{a}_4 .

The beamsplitter (BS) is one of the most powerful and simple tools in quantum optics and is the key element for detection of quantum states of light. The schematic diagram of a BS is shown in fig. 3.1. The relationship between the two input fields \hat{a}_1 and \hat{a}_2 with a relative phase of ϕ between them and the exiting fields \hat{a}_3 and \hat{a}_4 is given by conservation of energy

$$\hat{a}_3 = \sqrt{\rho}\hat{a}_1 + \sqrt{1-\rho}e^{i\phi}\hat{a}_2, \quad (3.2)$$

$$\hat{a}_4 = \sqrt{1-\rho}\hat{a}_1 - \sqrt{\rho}e^{i\phi}\hat{a}_2. \quad (3.3)$$

¹The photodetectors are made of different photodiodes depending on the wavelength to be detected. Silicon photodiodes are used for detection of the optical field in the range from 200–1100 nm, depending on the design of the photodetector. InGaAs photodiodes are sensitive in the range 900–1700 nm.

²The bandwidth of the detector is set by frequency range, in which the photocurrent response is proportional to the incident optical power. Typically, the bandwidth of the detectors used for the experiments was around 20 MHz.

³The quantum efficiency of the Si and InGaAs detectors specially designed for our experiments were typically $90 \pm 5\%$ and $95 \pm 3\%$, respectively.

On transmission the phase of each field remains unchanged, on reflection from a hard surface the phase is shifted by π . We can see that the BS couples the incident fields \hat{a}_1 and \hat{a}_2 with a coupling strength dependent on the BS power reflectivity ρ . Equas. 3.2 and 3.3 are identical for both time and frequency domain operators.

3.1.2 Balanced homodyne detection

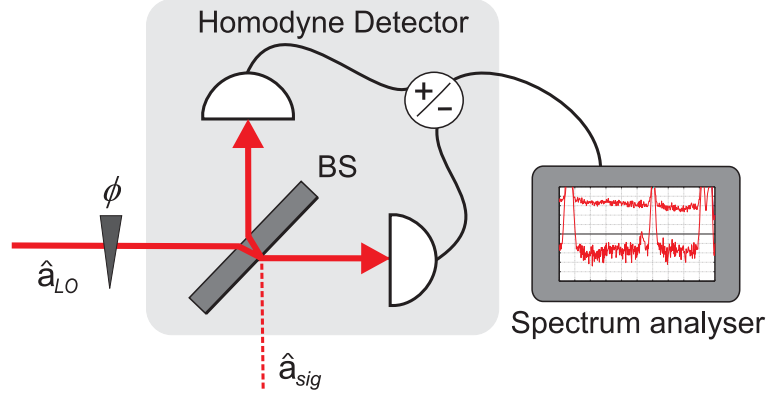


Figure 3.2: A schematic diagram of the homodyne detection system.

The generation of squeezed light depends on the relative phase between the interacting light fields. We therefore need a phase-sensitive measurement of the squeezed quadratures of the light field [47]. This is provided by a homodyne detection (HD) system, and is described in the following. The schematics of HD is shown in fig. 3.2.

To find the variance of the arbitrary frequency dependant quadrature operator \hat{X}_{sig}^ϕ of the signal field, we interfere the signal beam \hat{a}_{sig} with a bright local oscillator (LO) beam \hat{a}_{LO} with a relative phase ϕ between the two fields. The outputs from the BS are then sent to a pair of photodetectors, and the sum and difference of the photocurrents are recorded. Assuming that the power of LO is much higher than of the signal beam, the effect of LO is to rotate the coherent amplitudes of the two BS outputs allowing the homodyne detector to measure an arbitrary quadrature of the input state.

Assuming the LO beam sidebands are shot noise limited at frequencies $\omega \pm \Omega$, the ratio of the difference and sum photocurrent frequency dependant variances gives [38]

$$\frac{V_{diff}}{V_{sum}} = V_{sig}^\phi, \quad (3.4)$$

which is a calibrated measurement of the variance of an arbitrary quadrature of the input state defined by V_{sig}^ϕ . Setting the phase difference between the signal and LO beam $\phi = 0$ and $\phi = \pi$ allows the calibrated measurement of the amplitude, \hat{X}_{sig}^+ , and phase, \hat{X}_{sig}^- , quadratures, respectively⁴.

Of course, we must be careful to ensure that the LO field is shot noise limited at the frequencies we are interested in. An alternative approach using the same apparatus is to always measure V_{diff} and to block the input state (but not the LO beam) to provide the normalization. In this case, since there is no optical power entering the BS input port, we can be sure that the input becomes a vacuum state, and hence that

⁴If the beam entering the HD is a strong bright squeezed beam and one port is left empty then the sum and the difference of the photocurrents yield directly the noise suppression value (squeezing) and the QNL, respectively. This kind of HD is called self-homodyne detection [47].

$V_{sig|blocked}^\phi = 1$ for any ϕ and any sideband frequency Ω . The ratio of the difference current variances with the input unblocked and blocked is given by

$$\frac{V_{diff|unblocked}}{V_{diff|blocked}} = V_{sig}^\phi, \quad (3.5)$$

which also provides a calibrated measurement of V_{sig}^ϕ . This technique was adopted through the majority of this thesis, because it does not necessarily require the LO beam to be perfectly shot noise limited at the detection frequency as the classical noise of the LO beam gets subtracted in this measurement.

3.1.3 Optical attenuation

In an ideal optical detection, there is a one-to-one correspondence between the number of incident photons and the number of electrons in the photodiode current. If some of the photons are lost due to lossy optical environment or inefficient photodetector, then the electrical statistics will not correspond to the ideal representation of the photon statistics. We can model the optical loss as having an inefficient detector represented by a BS with transmission η , followed by an ideal detector. The effect of BS is to introduce quantum vacuum \hat{a}_v into the quantum state. Using the BS equations 3.2 and 3.3 and neglecting the phase term $e^{i\phi}$ as this has no meaning for the vacuum state, we find the output state \hat{a}_{out} measured by an ideal detector to be

$$\hat{a}_{out} = \sqrt{\eta}\hat{a}_{sig} + \sqrt{1-\eta}\hat{a}_v. \quad (3.6)$$

Then for the degraded variance of an arbitrary quadrature of the input state V_{out}^ϕ normalized to the QNL we can obtain [47]

$$V_{out}^\phi = \eta V_{sig}^\phi + (1-\eta), \quad (3.7)$$

where again V_{out}^ϕ is the variance of an arbitrary quadrature of the light field incident on the ideal detector. This equation describes any situation, where the optical field is attenuated by a lossy optical component or detected by a real detector. To see the effect of loss on squeezing, we can assume a perfectly amplitude squeezed state, i.e. $V_{sig}^+ \rightarrow 0$. Then the detected intensity noise spectrum is $V_{out}^+ \rightarrow (1-\eta)$ showing that any kind of loss has a strong negative influence on squeezing. It is therefore desirable to minimize inefficiencies in any quantum optical experiment.

We have assumed in our calculations that the signal beam and the LO beam are perfectly mode-matched⁵. However, in practical situations the total detection efficiency is limited by homodyne visibility along with the optical loss η_{opt} and the efficiency of the detectors⁶ η_{det} itself. The homodyne fringe visibility ν_{vis} is defined as

$$\nu_{vis} = \frac{P_{max} - P_{min}}{P_{max} + P_{min}}, \quad (3.8)$$

⁵In the case of self-homodyne detection, the vacuum is always perfectly mode-matched to the signal beam.

⁶The detector and signal processing units introduce into the measurement also uncorrelated electronic noise. It is therefore desirable to operate the detectors at high power, so the electronic noise is well below the QNL and such does not reduce the measured amount of squeezing. To subtract the electronic noise V_{el} from measured data V_{meas} we used for correcting the data following relation $V_{corr} = 10\log(10^{V_{meas}/10} - 10^{V_{el}/10})$. We designed our detectors to operate typically 10 – 14 dBm above its electronic noise level.

where P_{max} and P_{min} correspond to the maximum and minimum power in the fringe, respectively. The total detection efficiency is then given by $\eta_{tot} = \nu_{vis}^2 \eta_{det} \eta_{opt}$. In our experiments, we balanced the power of the two input beams and characterized the visibility of interference to determine the mode-matching efficiency. Typically, we achieved mode-matching efficiencies in the range 0.93 to 0.98. The efficiencies were usually limited not by focussing, alignment, or polarization of the optical fields, but rather by variations from a perfect Gaussian transverse mode shape.

3.1.4 Power spectral density

Experimentally, the most common tool for evaluating the noise properties of a beam of light incident on a detector is using an electronic spectrum analyzer. Spectrum analyzer measures the power spectrum S_{meas} of the fluctuations of the field in some bandwidth $\Delta\Omega$ around the optical carrier frequency ω . This bandwidth should be chosen so that the spectrum includes all noise details of the optical field. Experimentally, this bandwidth is chosen by the resolution bandwidth (RBW) of the spectrum analyzer. On the other hand, the video bandwidth (VBW) is basically a smoothing filter with a bandwidth equal to the RBW. VBW essentially reduces the noise displayed, making the power levels easier to see. The normalized power spectrum of the fluctuations of the analyzed beam is given by [48]

$$S = \frac{S_{meas}}{RBW} = \langle |\delta\hat{X}\phi|^2 \rangle, \quad (3.9)$$

which gives the information about the noise spectrum of the optical field with respect to the QNL. For the vacuum noise, equa. 3.9 gives $S = 1$. As a simple example, we may find the power spectrum S_n of a directly detected laser beam. The linearized frequency domain fluctuation operator for the photon number is given by $\bar{A}\delta\hat{X}^+$, where \bar{A} is the average field amplitude. Then the spectrum can be found to be

$$S_n = \bar{A}^2 V^+. \quad (3.10)$$

In other words, frequency domain detection of the photon number gives the spectrum of the amplitude quadrature of the beam scaled by the optical power in the beam. In the case of detecting a coherent beam, i.e. $V^\pm = 1$, equa. 3.10 gives $S_n = \bar{A}^2$, which is the quantum noise limit.

3.2 Optical cavities

An optical cavity is one of the key elements involved in the experiments throughout this thesis. We used optical cavities to improve the spatial and spectral properties of a laser beam, see sec. 3.5, or to enhance the effective nonlinearity of nonlinear systems such as an optical parametric amplifier (OPA), see sec. 5.1. In this section, we will model a passive resonator and demonstrate its spectral and spatial mode cleaning properties. Since a crucial aspect of optical resonators is the interference of the internal and external fields, precise control of the length of the resonator is important. In sec. 3.3, we describe how error signals can be generated allowing an active control of the resonator length.

A schematics of an optical cavity is shown in fig. 3.3. The resonator mirrors, which we term here the input (subscript ic) and output (subscript oc) couplers, have some transmissivity η_{ic} and η_{oc} , respectively, and the intra-cavity mode \hat{a} experiences some

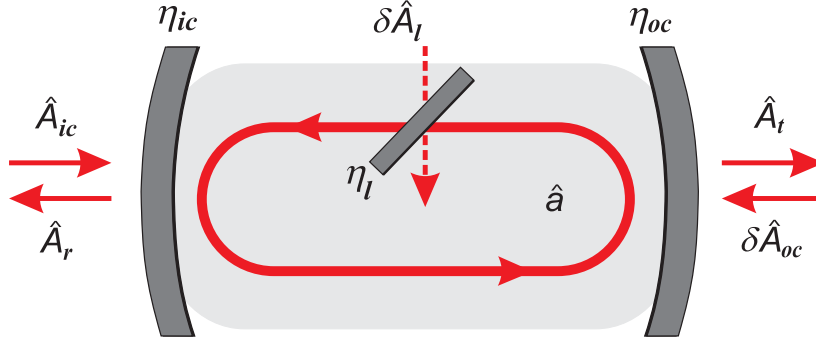


Figure 3.3: A schematics of an optical cavity coupled to the environment. \hat{a} : intra-cavity field, \hat{A}_{ic} : incident field onto the cavity, \hat{A}_r : reflected field, \hat{A}_t : transmitted field, $\delta\hat{A}_{oc}$: vacuum mode entering the cavity through the output mirror, $\delta\hat{A}_l$: vacuum mode coupled to the cavity by intra-cavity loss, η_{ic} : input coupler transmissivity, η_{oc} : output coupler transmissivity, η_l : round-trip loss.

round-trip loss η_l , which can be modeled using a BS as explained in sec. 3.1.3. Since optical cavities are not isolated systems, each of these properties couples the cavity modes with the environment. This coupling is responsible for the leaking of photons from the cavity and also for the introduction of vacuum noise fluctuations into the cavity. Starting from the quantum Langevin equation 2.26, it can be shown that the equation of motion for an empty cavity is given by [38]

$$\dot{\hat{a}} = -(\gamma + i\Delta)\hat{a} + \sqrt{2\gamma_{ic}}\hat{A}_{ic} + \sqrt{2\gamma_{oc}}\delta\hat{A}_{oc} + \sqrt{2\gamma_l}\delta\hat{A}_l, \quad (3.11)$$

where \hat{A}_{ic} is the pump field with frequency ω_p , which may be different from the cavity frequency ω_c . The term $\Delta = \omega_p - \omega_c$ describes the detuning between the cavity and pump field. $\delta\hat{A}_{oc}$ is the vacuum mode at the output mirror and $\delta\hat{A}_l$ is the vacuum mode coupled in by intra-cavity loss. γ is the total cavity damping rate given by $\gamma = \gamma_l + \gamma_{ic} + \gamma_{oc}$, where γ_l corresponds to the coupling rate of the cavity mode due to intra-cavity loss, γ_{ic} is the coupling rate through the input mirror and γ_{oc} is the coupling rate through the output mirror. Each of these coupling rates has a corresponding transmissivity $\eta_{(ic,oc,l)}$. In the case of high finesse cavities, i.e. $\eta_{(ic,oc,l)} \ll 1$, the damping rates may be expressed in terms of the transmissivity of the mirrors and loss elements in the cavity as $\gamma_{(ic,oc,l)} = \eta_{(ic,oc,l)}/\tau$, where τ is the round-trip time. The units of the capitalized fields are $s^{-1/2}$ to give the photon number of these fields ($\hat{A}^\dagger\hat{A}$) in units of s^{-1} . These are traveling waves and are therefore measured in photons per second. The lower case mode \hat{a} is dimensionless because it is a mode in a cavity and the operator ($\hat{a}^\dagger\hat{a}$) just counts the number of photons in the cavity.

Assuming a perfect resonance between the cavity and pump fields so that $\Delta = 0$, and taking the Fourier transform of equa. 3.11, i.e. $\mathbb{F}(\dot{\hat{a}}) = i\Omega\tilde{a}$, with the input-output relations for the open system⁷, we can calculate the reflected, \tilde{A}_r , and transmitted, \tilde{A}_t , fields in the frequency domain as

$$\tilde{A}_r = \frac{(2\gamma_{ic} - \gamma - i\Omega)\tilde{A}_{ic} + 2\sqrt{\gamma_{ic}\gamma_{oc}}\delta\tilde{A}_{oc} + 2\sqrt{\gamma_{ic}\gamma_l}\delta\tilde{A}_l}{i\Omega + \gamma}, \quad (3.13)$$

$$\tilde{A}_t = \frac{2\sqrt{\gamma_{ic}\gamma_{oc}}\tilde{A}_{ic} + (2\gamma_{oc} - \gamma - i\Omega)\delta\tilde{A}_{oc} + 2\sqrt{\gamma_{oc}\gamma_l}\delta\tilde{A}_l}{i\Omega + \gamma}, \quad (3.14)$$

⁷The input and output coupler boundary conditions [41] are given for our system as

$$\hat{A}_r = \sqrt{2\gamma_{ic}}\hat{a} - \hat{A}_{ic} \quad \text{and} \quad \hat{A}_t = \sqrt{2\gamma_{oc}}\hat{a} - \delta\hat{A}_{oc}. \quad (3.12)$$

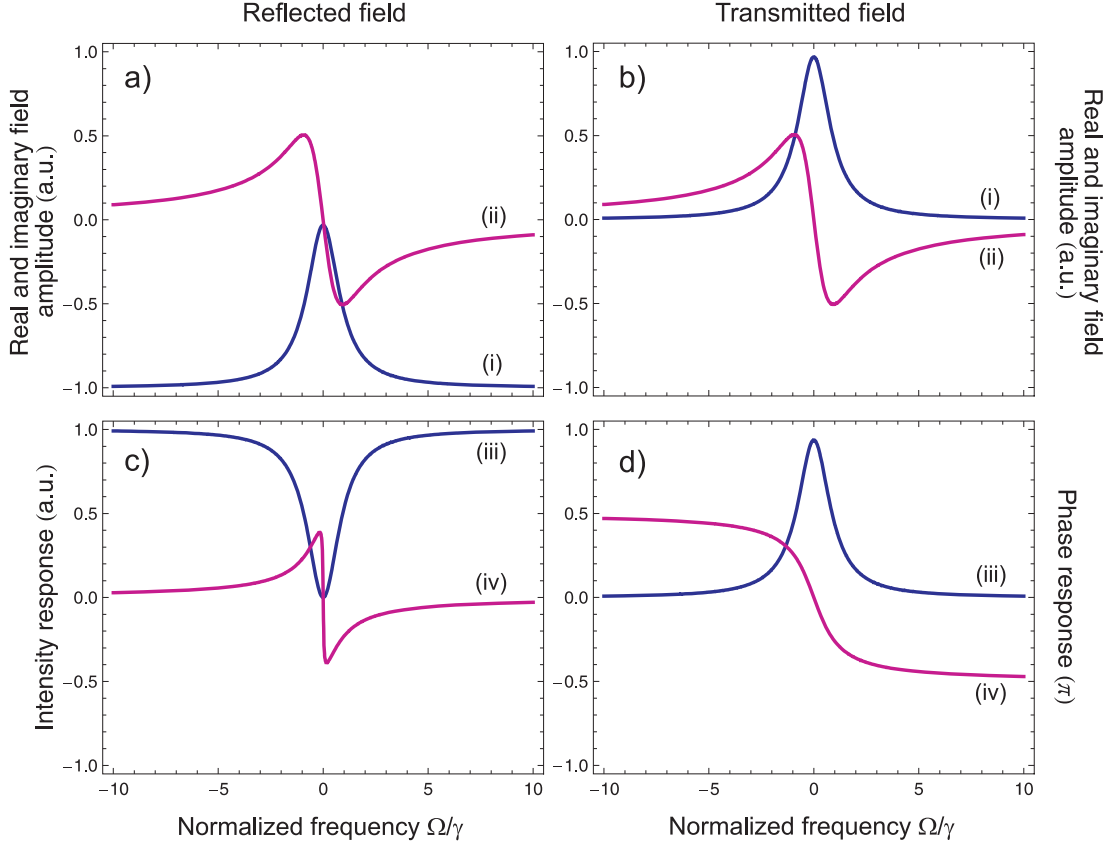


Figure 3.4: Frequency response of a high finesse cavity: a,b) the amplitude (i) and phase (ii) of the reflected and transmitted fields; c,d) the mean power \tilde{P} (iii) and the mean phase delay $\tilde{\phi}$ (iv) of the two fields. Parameters used: $d = 50$ cm, $\eta_{ic} = \eta_{oc} = 0.0015$, $\eta_l = 0.0001$, $F = 2000$.

where the fields denoted with tilde are to the end of this section frequency domain operators. Fig. 3.4 shows the response of a high finesse cavity. Here we consider a specific example of relevance to this thesis. That of a resonator with equal input and output coupler decay rates $\gamma_{ic} = \gamma_{oc}$, with a bright field incident on the input coupler of amplitude \tilde{A}_{ic} , and assuming the fields entering the resonator through the output coupler and through loss to be in vacuum state. Figs. 3.4 a) and b) show the phase and amplitude of the reflected and transmitted fields, respectively, to be strongly dependant on the frequency of the field relative to the resonant frequency of the cavity.

The frequency response of the mean power, \tilde{P} , and the mean phase delay, $\tilde{\phi}$ ⁸, of the two fields are shown in figs. 3.4 c) and d). The maximum power is transmitted when the field is on resonance with the cavity, i.e. $\Omega = 0$. Moreover no phase delay is experienced by the fields reflected off and transmitted through the resonator. In both cases the phase varies linearly with Ω around $\Omega = 0$, but as $\Omega/\gamma \rightarrow \pm\infty$ the mean resonator phase delay asymptotes to $\tilde{\phi}_r = 0$ for the reflected field and to $\tilde{\phi}_t = \pm\pi/2$ for the transmitted field. As we will see in the next section, this behavior allows generation of error signals for controlling the length of an optical cavity.

⁸The resonator mean phase delay $\tilde{\phi}$ is defined as

$$\tilde{\phi} = \arcsin\left(\frac{\langle \text{Im}\{\tilde{A}\} \rangle}{\sqrt{\tilde{P}}}\right), \quad \text{where} \quad \tilde{P} = \hbar\omega\langle \tilde{A}^\dagger \tilde{A} \rangle. \quad (3.15)$$

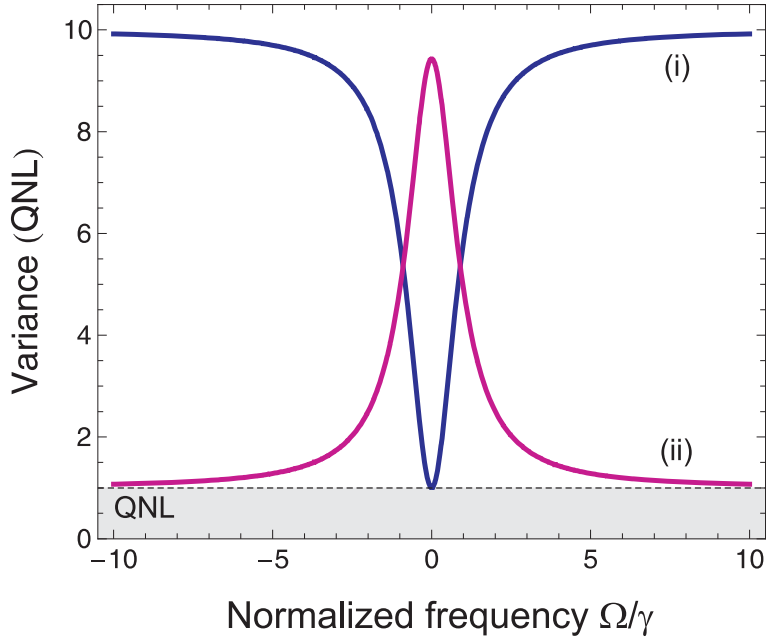


Figure 3.5: Spectral filtering effect of a high finesse cavity. (i) reflected field, (ii) transmitted field. Parameters used: $V^\pm = 10$, $d = 50$ cm, $\eta_{ic} = \eta_{oc} = 0.0015$, $\eta_l = 0.0001$, $F = 2000$.

Assuming that the fields entering the resonator through the output coupler and loss are vacuum states, we can find the field spectra V^\pm from equas. 3.13 and 3.14 as

$$V_r^\pm = 1 + \frac{((2\gamma_{ic} - \gamma)^2 + \Omega^2)(V_{Aic}^\pm - 1)}{\Omega^2 + \gamma^2}, \quad (3.16)$$

$$V_t^\pm = 1 + \frac{4\gamma_{ic}\gamma_{oc}(V_{Aic}^\pm - 1)}{\Omega^2 + \gamma^2}. \quad (3.17)$$

The spectral filtering effect of the cavity is shown in fig. 3.5. Here we consider a bright field incident on the input coupler with some classical laser noise of $V^\pm = 10$, and again the fields entering the resonator through the output coupler and through loss being in vacuum state. At frequencies much higher than the total resonator decay rate, i.e. $|\Omega| \gg \gamma$, we find that the transmitted field is at the QNL. We see that the resonator is acting as a low pass filter on the input state, with $\Omega = \gamma$ defining the 3 dB point⁹. This is a feature which has been frequently used to clean the classical noise from the laser. We will demonstrate a design and operation of a mode-cleaning cavity in sec. 3.5.

⁹The linewidth δl of a lossless cavity is defined as the full-width-half maximum of the cavity resonance, and can be calculated classically as [42]

$$\delta l = \frac{\text{FSR}}{F}, \quad (3.18)$$

where the parameters FSR and F are the free spectral range and finesse, respectively, of a cavity of optical round-trip path length d with input/output mirror reflectivities R_{ic} and R_{oc} , and are given by

$$\text{FSR} = \frac{c}{d}, \quad F = \frac{\pi(R_{ic}R_{oc})^{1/4}}{1 - \sqrt{R_{ic}R_{oc}}}. \quad (3.19)$$

3.3 Stabilizing the optical resonators

For practical situations we require to hold the laser field on resonance with an optical cavity. To do this requires a generation of an error signal, which is proportional to the error between the current operating condition and the desired operating condition. This signal has to change its sign as the laser passes through the cavity resonance, so that by looking at the signal we have an information, which way the system should be adjusted to go back to resonance. The error signal is used in the feedback loop to actively control or lock a particular parameter to that desired value. To produce such an error signal, we use techniques which require some kind of optical modulation, see sec. 2.3.1. For locking the optical cavities and interferometers, we employed in our experiments two locking techniques: Pound-Drever-Hall (PDH) locking method [49] and the dither locking method. In the PDH locking method, we first introduce phase modulation¹⁰ (PM) on the input laser field incident onto the cavity. When the cavity is detuned from resonance, the phase shift of the carrier beam converts PM into amplitude modulation (AM), which may be used to derive an error signal. The dither locking method is in principle the same as the PDH method, and the only difference is that we modulate the cavity length, e.g. via a PZT actuator, which generates frequency modulation¹¹ of the intra-cavity field, and hence also of the reflected and transmitted fields.

3.3.1 Pound-Drever-Hall locking

The PDH technique is the most commonly used method to generate a resonator locking error signal. As was already mentioned, the input field to the resonator is PM at the frequency Ω_{PDH} , where we assume for now that the modulation frequency is well outside the cavity bandwidth¹². As the sidebands are so far from resonance, they simply reflect off the input coupler. Looking at figs. 3.4 c) and d), we can see that when the carrier field is on resonance with the cavity, the reflected and transmitted fields will not experience any phase shift. Thus the interaction of the reflected sidebands with the reflected carrier will give a pure PM beam, and an intensity measurement of the reflected light will therefore show no AM at the sideband frequency.

However, when the carrier is slightly away from perfect resonance, it will undergo a linear phase delay $\langle\phi_r\rangle$ relative to the sidebands. The carrier and sidebands will no longer beat to form a pure PM, forming instead a slightly AM field

$$\mathcal{E}_{AM} = \zeta \tilde{P}_r \sin(\Omega_{\text{PDH}} t) \sin\langle\phi_r\rangle, \quad (3.20)$$

where the term $\zeta \tilde{P}_r$ is power in the sidebands and $\sin\langle\phi_r\rangle$ is the amount of AM due to the phase delay described above. The quantity we need to measure is just the phase

¹⁰The phase modulation can be done by using e.g. an external electro-optic modulator (EOM) which phase-modulates its transmitting field via the electro-optic effect [34]; one can also directly modulate the refractive index of the laser crystal via a PZT actuator placed on top of it that mechanically stress the crystal and changes its refractive index. Both of these modulation techniques were used for the experiments.

¹¹Modulation of the cavity length is identical to the laser frequency modulation and this for sinusoidal modulation equals to PM.

¹²In principle, the PDH technique can work for any nonzero modulation frequency. We avoid the low modulation frequencies in real experiments as the modulation itself and its higher harmonics can introduce an excess noise into the detection frequency window. Moreover, any kind of modulation might be a source of the phase jitter in the system, therefore we aim for modulation frequencies as high as experimentally possible. Both of the mentioned factors have a negative influence on the squeezing generation.

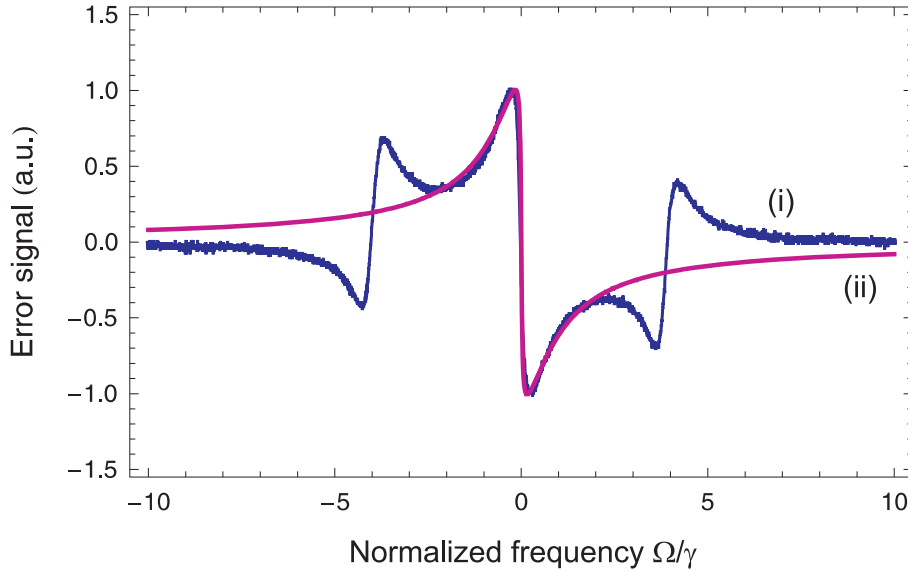


Figure 3.6: (i) Experimentally generated error signal and (ii) the imaginary component of the cavity response.

delay. The error signal can be generated by detecting the reflected field¹³, mixing down the resulting photocurrent at the modulation frequency Ω_{PDH} and low-pass filtering the signal to remove the modulation frequency and its harmonics. The resulting PDH error signal \mathcal{E}_{PDH} is then given by

$$\mathcal{E}_{\text{PDH}} \approx -g_D \zeta \tilde{P}_r \langle \tilde{\phi}_r \rangle, \quad (3.21)$$

where g_D represents the gain of the detection process. The error signal is linear around the cavity resonance and almost a perfect copy of the imaginary component of the cavity response, as shown in fig. 3.6. The difference away from $\langle \tilde{\phi}_r \rangle$ arises from the sidebands approaching resonance and acquiring their own phase shift, thus introducing an extra source of AM. This signal provides an excellent error signal for controlling the cavity resonance position.

3.3.2 Dither locking

As we already mentioned, dither locking is based on the modulation of the resonant frequency of the cavity by changing its length, for example via scanning one of the cavity mirrors mounted on a PZT actuator. We used experimentally the dither locking technique mainly in locking two beam interferometers, which we can think of as low finesse cavities. These include Mach-Zehnder interferometers (MZI), see sec. 7.3.2, or locking the amplitude and phase quadratures of a squeezed beam with the phase of the LO beam, see sec. 7.3.3.

The principle of dither locking technique is shown in fig. 3.7. When the laser field is exactly on resonance, the modulation of the resonant frequency of the cavity gives no AM due to the local flatness of the reflection or transmission response. When the laser is slightly out of resonance, the two fields undergo AM whose sign depends at

¹³Or the transmitted field, but for $\Omega_{\text{PDH}} \gg \gamma$ the transmitted error signal is significantly smaller. To get a stronger error signal, we can in principle place on the input beam phase sidebands, which are within the cavity bandwidth. In this case, the amplitude of one sideband will be attenuated compared to the other as the cavity moves away from resonance. The differential change in sideband intensity leads to AM of both reflected and transmitted fields, which can be used to generate the error signal. As was already mentioned, we tend to avoid the low frequency modulation from technical reasons.

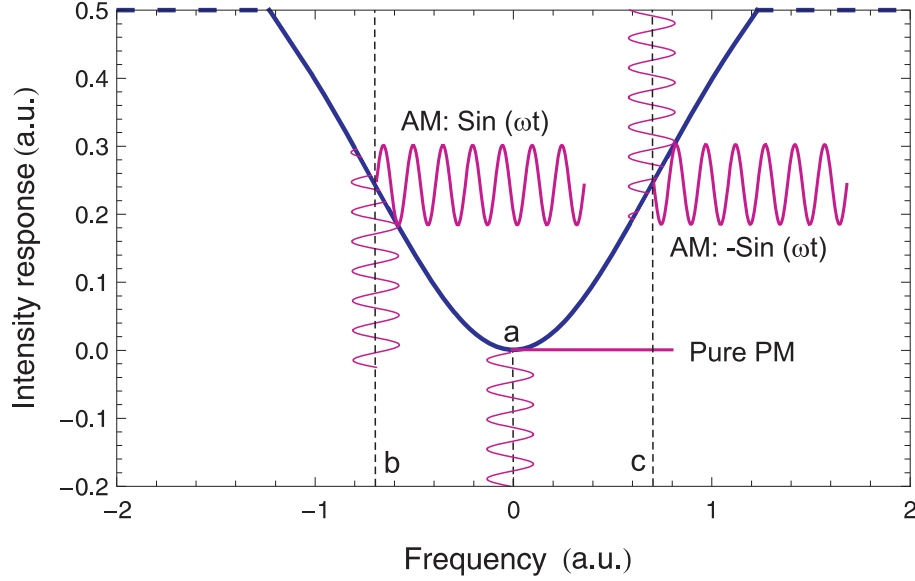


Figure 3.7: Principle of dither locking. a) Laser is exactly on resonance, the modulation of the resonant frequency of the cavity gives no AM; b) and c) Laser is out of resonance, fields undergo AM whose sign depends at which side of the cavity response curve the laser operates.

which side of the cavity response curve the laser operates. This results in generation of the error signal, which can be used for locking. In fact the dither locking technique is identical to the PDH method, where the phase sidebands placed onto the carrier beam are within the cavity bandwidth.

3.4 The laser

As we already mentioned, the experiments presented in this thesis were done at the research labs at DTU and ANU. We used for the experiments at both institutions the Diabolo type [50] ultrastable, continuous-wave single frequency lasers based on Nd:YAG laser material (Innolight GmbH). These all-solid-state, diode-pumped lasers feature monolithic non-planar ring geometry cavity, which provides the output from the laser of extremely stable frequency. The FWHM of the laser output is less than 1 kHz. This together with low noise control electronics makes the laser ideal for quantum optics experiments. The Diabolo lasers used in the experiments were dual-wavelength systems operating at both 1064 nm and its second harmonic (SH) of 532 nm. The SH field is generated in an internal SHG cavity¹⁴, where part of the fundamental field is tapped off and PM at 12 MHz using an electro-optic modulator (EOM) for stabilization of the internal doubler. The output fields are close being diffraction limited with the beam quality parameter m^2 of less than 1.1. The frequency of the laser can be controlled at low frequencies via heating or cooling the laser crystal by the Peltier elements, what in effect changes the length of the resonator.

The output beam can be also internally PM at high frequencies via a PZT actuator that mechanically stress the laser crystal¹⁵, and therefore changes its refractive index. This method was used at the DTU experiments as an EOM was not available at that time. The disadvantage of the direct modulation of the infrared beam via stressing the

¹⁴The output power of the DTU laser is 450 mW at 1064 nm and 800 mW at 532 nm, the ANU version has 180 mW output at 1064 nm and 1 W at the second harmonic

¹⁵It is possible to modulate the beam up to 200 MHz using this method.

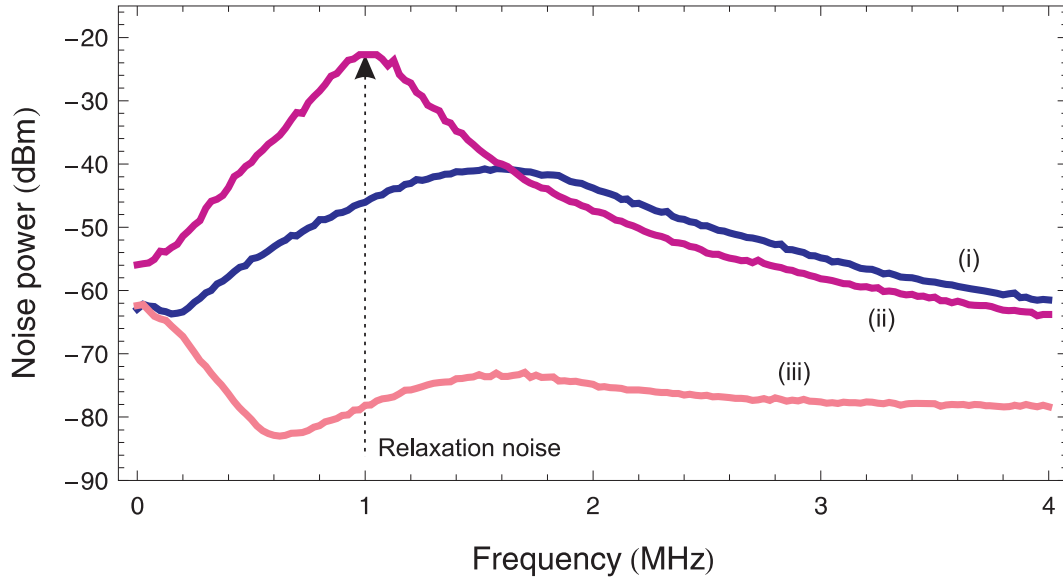


Figure 3.8: Frequency spectra of a 9 mW infrared field exiting the laser with the Noise Eater switched (i) ON and (ii) OFF (sum of the photocurrents); trace (iii) is the QNL (difference of the photocurrents). The electronic noise of the detectors is around 16 dBm below the QNL. RBW: 300 kHz, VBW: 300 Hz.

laser crystal is that this modulation is also coupled via the nonlinear interaction into the SHG field, and so introducing an additional noise on the green beam. As will be discussed in sec. 5.2, an excess noise of the pump field is one of the limiting factors for an efficient generation of sideband squeezing.

The resonant relaxation oscillation of the laser, which couples noise into its power spectrum, has a peak at around 1 MHz. This can be thought of as the atomic cycling frequency from the ground state of the Nd:YAG energy level system to the laser level. Indeed this laser noise is suppressed by 25 dB in Diabolo laser electronically using the function *Noise Eater*. The typical amplitude noise spectra of the infrared field are shown in fig. 3.8. The traces are the sum and difference of the photocurrents measured with the homodyne detectors with a vacuum input in one of the ports of the homodyne BS. We recall that the sum and the difference of the HD photocurrents determines the amplitude noise of the laser beam and the calibration of the QNL¹⁶, respectively.

3.5 Mode cleaning cavity

Squeezing and entanglement related experiments are very sensitive to spectral noise and spatial mode-matching inefficiencies. As was already discussed in sec. 3.2, an optical resonator acts as a low-pass frequency filter, and moreover defines a spatial Gaussian mode of the transmitted field. The spatial properties of the resonator mode depend on the configuration of the cavity mirrors forming the optical cavity and on its length. In order to minimize an excess noise of the laser beam, and to define a perfect Gaussian shape of the beam, we passed the laser field through a high-finesse optical resonator, or rather mode cleaning cavity (MCC). Generally, we used MCCs for spectral and spatial cleaning of the infrared field and for transferring power from the fundamental TEM₀₀ mode into higher-order transverse modes, and vice versa. This technique will be detailed in the next section.

¹⁶For a QNL laser beam the sum and difference of the HD photocurrents will have equal noise power.

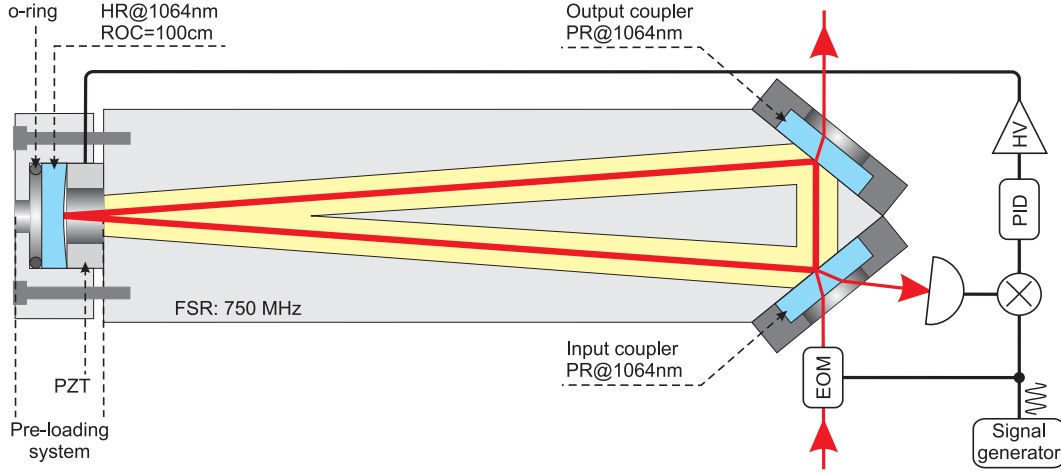


Figure 3.9: Schematic design of the mode cleaning cavity used to improve the spectral and spatial mode quality of the infrared laser beam.

Schematic design of an infrared MCC¹⁷ is shown in fig. 3.9. The ring cavity consists of two flat input/output coupling mirrors angled at 43° and a back curved mirror. This mirror has the radius of curvature 100 cm and is coated for high reflection (HR) at normal incidence (reflectivity 99.997% at 1064 nm). The cavity mirrors are housed in an enclosed solid aluminium block, which enhances the mechanical stability of the cavity, and is also robust against air fluctuations. The length of the resonator is 40 cm and is controlled by a ring PZT actuator (thickness 9 mm, diameter 1 inch), which pushes the back HR curved mirror against a rubber o-ring. This pre-loading system is of great advantage as the resonance frequency and thus the locking bandwidth of the cavity is increased. The PZT and mirror assembly are clamped to increase the tension over the PZT, with a rubber o-ring acting as a spring between the clamp and the mirror. The effect of the pre-loading is simply to increase the spring constant and damping coefficient of the PZT. Of course, these quantities depend on the tension of the clamping, and can be varied by tightening the clamping screws. Typically, the MCCs used for the experiments had the locking bandwidth of around 17 kHz.

The coupling mirrors¹⁸ have different reflectivities at 43° angle of incidence depending on the polarization of the incident infrared field, i.e. 99.94% and 99.27% for the s - and p -polarized input, respectively. Hence it is possible to operate the MCC in two finesse regimes, corresponding respectively to 10.500 and 425, assuming no intra-cavity loss. We operated the MCCs at the lower finesse regime¹⁹, giving the theoretical value of the cavity linewidth $\delta l = 1.8$ MHz, which is sufficient for our experiments. The measured values of the finesse were of around 390²⁰, which well correspond to the theoretical value. Frequency spectra for the intensity noise of a 9 mW infrared laser field before and after transmission through the MCC is shown in fig. 3.10. We can see that the noise of the transmitted field is significantly reduced, and the field is quantum noise limited from 7 MHz.

¹⁷We used the same optical and mechanical design of the MCC in all the experiments detailed in this thesis.

¹⁸Super mirrors with very low loss coated at ATFilms.

¹⁹Locking the cavity into the high finesse regime requires very fast detectors, which were not available for the experiments. Indeed the transmitted power through the cavity would be only fraction of the incident power due to the sharp linewidth of the cavity. Thus operating the cavity in low finesse regime is a reasonable compromise between the transmitted power and spectral noise reduction.

²⁰Over time we observed degradation of the finesse of the MCC used at the DTU, which might be due to high power coupled into the cavity and possible damage of the optical coating.

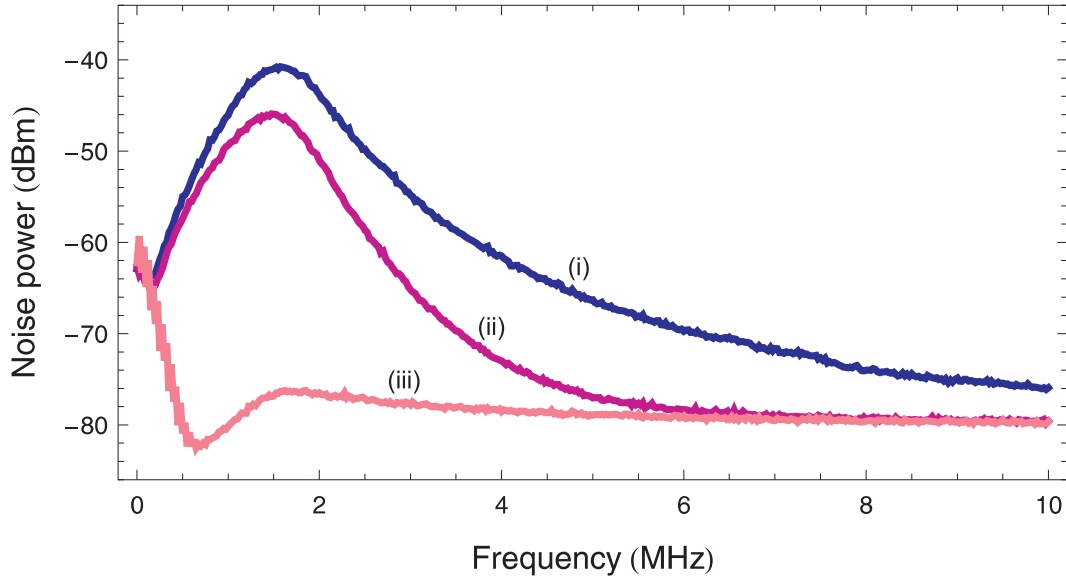


Figure 3.10: Frequency spectra of a 9 mW infrared laser field (i) before and (ii) after transmission through the MCC (sum of the photocurrents); trace (iii) is the QNL (difference of the photocurrents). The electronic noise of the detectors is around 16 dBm below the QNL. RBW: 300 kHz, VBW: 300 Hz.

The cavity was locked on resonance using the PDH locking technique. At DTU, we modulated directly the laser crystal refractive index via the PZT actuator, as described in the previous section, with the modulation frequency of 18.72 MHz, as the exiting infrared beam from the laser is modulation free under normal conditions. The ANU MCC was locked in the same manner, but only using the internal 12 MHz modulation of the infrared laser beam, which is used for locking the internal doubler as well. Typical transmission lines of the laser field passed through the MCC, when scanning the length of the cavity, are together with the generated PDH locking signal shown in fig. 3.11 a). Power transmission through the MCC locked to the TEM_{00} mode was typically 95%.

3.6 Generation of higher-order modes

In our work we are primarily interested in generation of squeezed states in the higher-order modes, particularly in the TEM_{10} mode, which is of key importance for the displacement and tilt measurements below the QNL [18], and for demonstration of spatial entanglement of bright optical beams [27], see chapter 7. For operating these systems, we require both the classical and nonclassical fields to be of specific spatial profiles. In particular, these systems utilize optical fields of higher-order Hermite-Gauss (H-G) modes. In general, we also require the ability of switching between different transverse modes. Thus for operating these systems we would need a universal mode converter, which potentially converts any mode into a desired spatial mode.

Such a device for converting modes could be a simple hologram mask [51]. Its advantages are low cost and the fact that it can be easily duplicated. The drawback of such device is mainly its specificity as one hologram corresponds to a single mode generation for a very particular illumination mode, for which the hologram was processed. Moreover, the transmission loss of the hologram might be the limiting factor for the mode conversion of a non-classical beam. The most flexible universal device is the spatial modulator, although it is a complex device to use and fairly expensive. It consists of an array of micro-controlled mirrors which can be programmed to produce

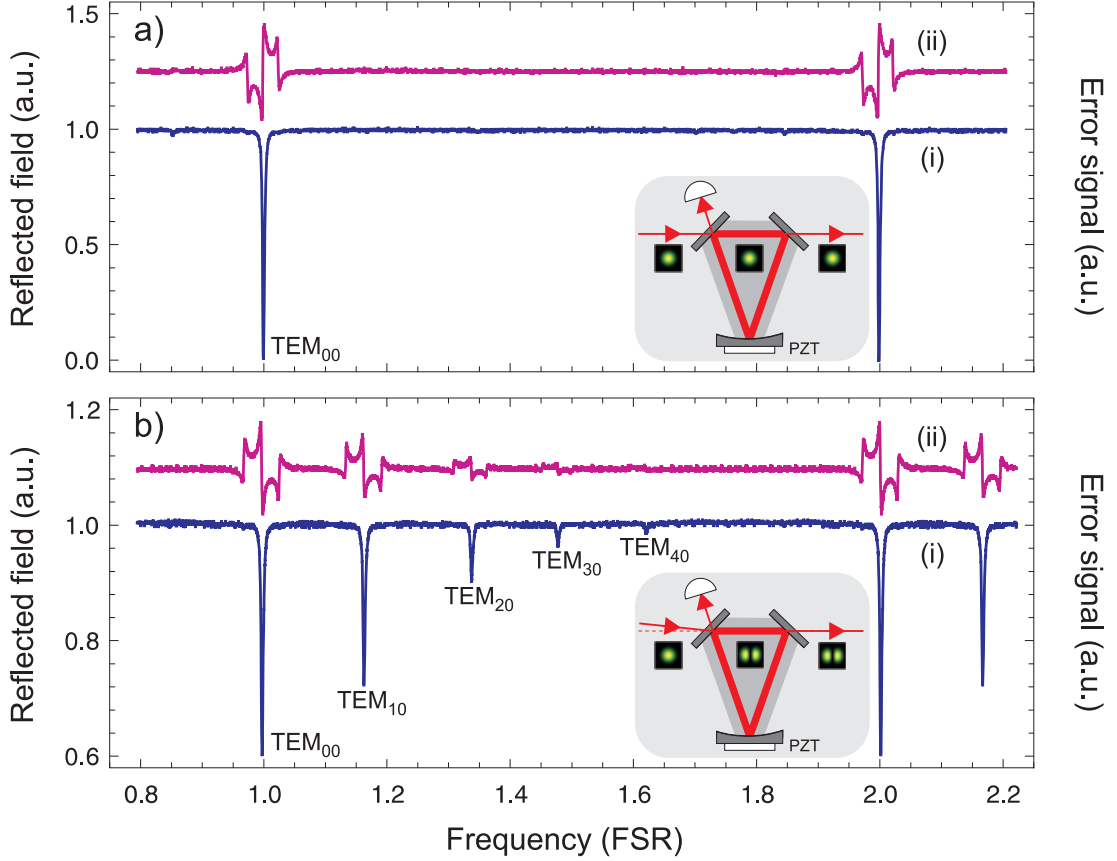


Figure 3.11: Measurements of the transmitted field (i) through a high finesse optical cavity of a) a mode-matched input field and b) a mismatched input field, when scanning the length of the optical cavity. (ii) Measurements of corresponding PDH error signals used to lock the cavity.

any spatial mode. The drawback are high losses, which limit its implementation for quantum imaging applications.

For the experiments throughout this thesis, we utilized for selective generation of H-G modes a simple optical cavity. This scheme, shown in inset of fig. 3.11 b), can be used to convert the TEM_{00} input beam into a pure TEM_{n0} mode, and vice versa. In the following we will concentrate on conversion of the TEM_{00} mode into the TEM_{10} and TEM_{20} modes as these are required for an optical system involving TEM_{10} squeezed states. Here we will address the limits of the power conversion from the fundamental mode into the higher-order modes, and propose schemes for improving the conversion efficiencies.

3.6.1 Cavity response of higher-order modes

An optical resonator can support any higher-order transverse mode, assuming that the resonance condition is satisfied²¹ [42]. Since different higher-order modes accumulate different Gouy phase shift when propagating in an optical medium, their exact resonance inside the optical cavity will be different. By detuning the cavity, e.g. by changing separation of the cavity mirrors, it is possible to selectively obtain resonance for a certain higher-order transverse mode TEM_{nm} . Given that we can efficiently and reliably

²¹The accumulated phase shift of the optical beam inside the cavity is an integer of 2π for one round trip.

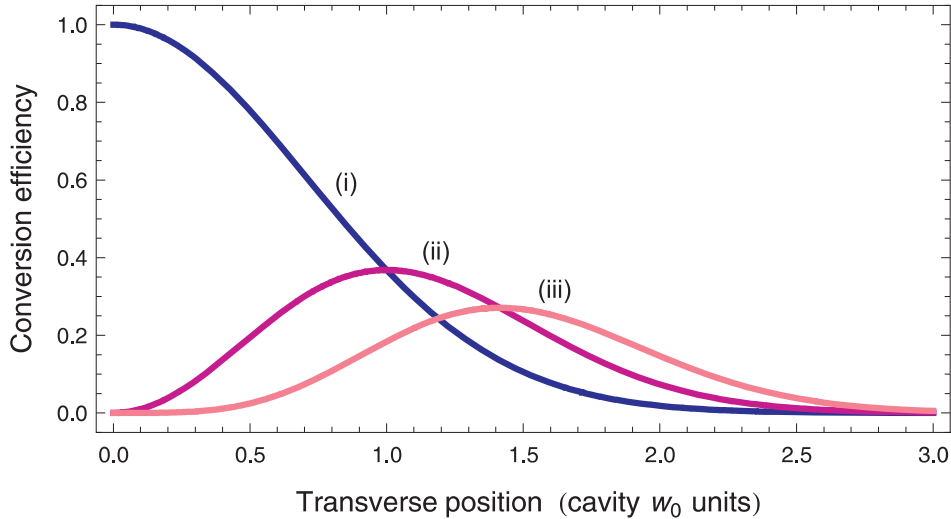


Figure 3.12: The rate of power coupled from the fundamental mode (i) into the TEM_{10} (ii) and TEM_{20} (iii) modes as a function of the beam displacement.

couple power contained in a particular transverse mode into the resonant TEM_{nm} cavity mode, this scheme would be then a universal mode convertor. These issues will be addressed in the following.

For generating higher-order modes experimentally, we utilized a ring optical cavity such as the MCC described in sec. 3.5. The advantages of the mode conversion with a ring cavity are the purity of the output mode, and the reliability of switching between different H-G modes. The propagation axis of the output beam is never modified as it is defined by the cavity axis, thus no realignment is required between the operation of the cavity resonating on different modes. This is important in real applications. When the incident beam of a certain spatial mode is perfectly aligned and mode-matched into a cavity, then the transmission of the cavity can reach in principle 100%. Such an example is for an incident TEM_{00} mode shown in fig. 3.11 a). However, when the beam is misaligned relative to the perfect configuration, the displaced or the tilted beam projects onto several transverse modes of the optical cavity. Hence by misalignment of the incident field to the cavity, we couple some power into the other transverse modes, as shown in fig. 3.11 b). Locking the cavity to the desired mode, one can obtain a selective mode converter, which can be easily operated.

To find the limit of decomposition of the TEM_{00} mode into higher-order modes, we calculate the exact decomposition coefficients in the TEM_{n0} basis as a function of beam displacement d using an overlap integral given by [25, 52]

$$c_n(d) = \int_{-\infty}^{\infty} u_0(x-d)u_n(x)dx. \quad (3.22)$$

The amount of power coupled from the fundamental mode (assuming unity power) into the TEM_{n0} mode is given simply by taking square of the decomposition coefficients $c_n(d)$. The results for TEM_{10} and TEM_{20} conversion are shown in fig. 3.12. We can see that conversion from the fundamental mode into the TEM_{10} and TEM_{20} modes can be only up to 36% and 25% efficient utilizing a proper displacement, respectively. In the case of other H-G modes, the conversion efficiency is rapidly decreasing with increasing their order. Besides low efficiency, such a device produces higher-order modes of very high purity²², which is required for quantum imaging applications. Moreover,

²²If the cavity is designed to prevent any mode degeneracy, the purity can easily exceed 99%.

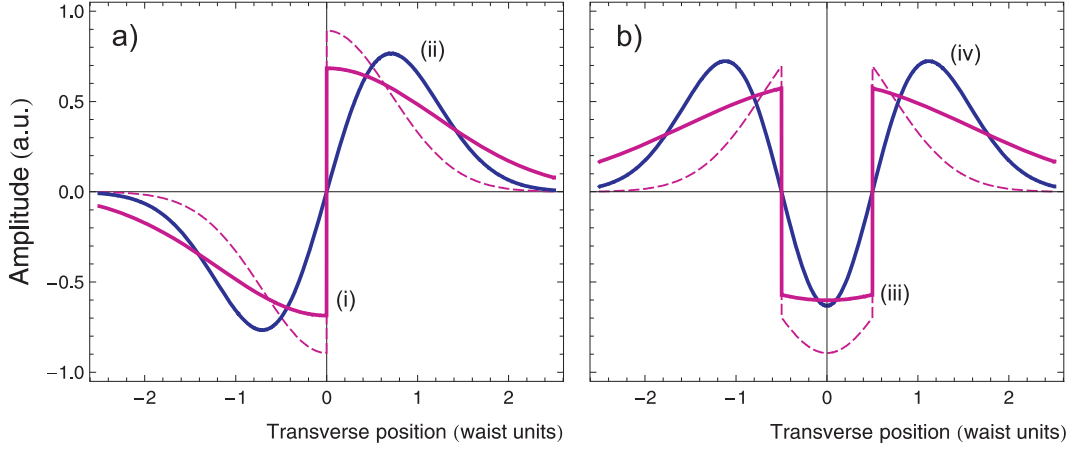


Figure 3.13: Phase profiles of flipped modes (i) and (iii) with the corresponding Hermite-Gauss TEM_{10} (ii) and TEM_{20} (iv) modes, respectively. The flipped modes are shown for optimized mode-conversion (full line) and as a directly converted TEM_{00} cavity mode (dashed line).

conversion efficiencies can be further enhanced, but at the cost of reliability of the mode converting device. In the following, we will propose how to optimize the conversion of a fundamental mode into TEM_{10} and TEM_{20} modes, which are relevant to this thesis.

3.6.2 Optimizing generation of the TEM_{10} and TEM_{20} modes

The conversion efficiencies can be further improved by using a specifically designed phase plate, which can be inserted into the beam path prior coupling the beam into the optical cavity. For an efficient generation of the TEM_{10} mode, we converted in our experiments the fundamental mode into a *flipped mode* [53], which is a TEM_{00} mode with π phase flip in the center of the beam as shown in fig. 3.13 a). Calculating the overlap integral using equa. 3.22, we can find for this particular case the best conversion to be 64% for zero displacement. Experimentally, we achieved efficiencies utilizing the flipped mode of around 60%. This technique was used for converting coherent beams only as the low efficiency does not allow conversion of the nonclassical fields.

As will be clarified in the next chapter, for generating TEM_{10} squeezed states utilizing an OPA we would prefer using a pump beam of the TEM_{20} spatial profile rather than a fundamental mode directly generated by the laser. The reason is higher nonlinear conversion efficiency, which is of key importance for generating quantum states of high degree of squeezing. In similar manner to the TEM_{10} case, we propose here for a TEM_{20} mode conversion a phase plate with the profile shown in fig. 3.13 b). This phase plate can improve the conversion efficiency up to 47% when inserted into the beam path of the TEM_{00} mode prior coupling into the cavity.

Mode conversion efficiencies can be further increased by defocusing the incident flipped mode into the cavity as shown in fig. 3.14. For the TEM_{10} case, mode conversion can be up to 82% efficient in combination of the flipped mode shown in fig. 3.13 a) and by defocusing the incident beam to 1.7 of the size of the cavity-mode beam waist radius w_0 . Similarly, the TEM_{20} mode conversion can be efficient up to 78% when the flipped mode shown in fig. 3.13 b) is defocused to 2.2 of the size of the cavity-mode beam waist radius w_0 . These results can be used in future experiments for a rather efficient generation of high purity TEM_{10} and TEM_{20} spatial modes.

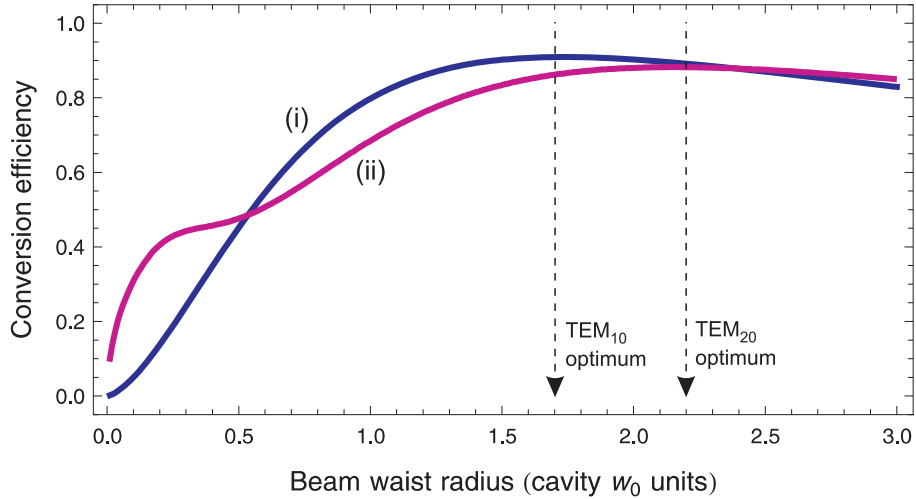


Figure 3.14: Conversion efficiency for the TEM_{10} (i) and TEM_{20} (ii) modes in an optical cavity utilizing flipped modes, as a function of the incident beam waist radius w_0 . An optimum conversion can be achieved for the two modes defocusing the corresponding flipped modes respectively to 1.7 and 2.2 of the size of the cavity-mode beam waist radius w_0 .

3.7 Summary

In summary, we introduced basic tools required for experiments utilizing quantum states of light. In particular, we detailed the beamsplitter, the most powerful tool in quantum optics experiments, together with the balanced homodyne system used to detect quantum states of light. We modeled optical cavities showing their spectral filtering effect and introduced methods for controlling their length. We introduced the laser source used in all experiments throughout this thesis, and presented a design of a mode cleaning cavity employed for spectral and spatial filtering of the coherent light.

We discussed methods for converting a mode of a certain spatial profile into any desired higher-order Hermite-Gauss mode. We showed that an optical cavity can serve as a selective mode converter, and we addressed limits of this device for power conversion of the fundamental mode into any desired higher-order Hermite-Gauss mode. Finally, we proposed schemes for improving conversion efficiencies, when transferring a fundamental mode into the TEM_{10} and TEM_{20} spatial modes. Utilizing flipped modes and defocusing the incident beam into the cavity, this process can be up to 82% and 78% efficient for the TEM_{10} and TEM_{20} mode conversion, respectively.

Part II

OPA squeezing of higher-order modes

Chapter 4

SHG of higher-order modes

Contents

4.1	Second-order nonlinear interaction	40
4.1.1	Nonlinear polarization	40
4.1.2	Energy conservation and phase-matching condition	40
4.2	Multi-mode second harmonic generation	42
4.2.1	Single pass SHG experiment	43
4.2.2	Generalized Boyd-Kleinman coefficients	44
4.2.3	Influence of the phase-matching temperature	47
4.2.4	Optimizing TEM ₁₀ conversion	49
4.3	Summary	50

Second harmonic generation (SHG), also called frequency doubling, is based on the second order susceptibility $\chi^{(2)}$ of nonlinear crystals, where two low energy photons of frequency ω are combined into a high energy photon at frequency 2ω . This phenomenon was first experimentally demonstrated in the optical regime by Franken *et al.* in 1961 [54]. Nowadays, the SHG process is widely used to generate wavelengths from the far UV to the far IR optical region [55, 56], with efficiencies exceeding 80% in the continuous-wave regime [57]. The most common application of SHG is the generation of 532 nm coherent light by frequency doubling of an Nd:YAG laser operating at 1064 nm. In quantum optics, the SHG process can be used for generating bright squeezed light [5, 58, 59], and there are also some attempts to generate harmonic entanglement [60].

In this chapter, we first introduce basic principles of the second-order nonlinear interaction in optical media. This is followed by theory of the multi-mode SHG process recently developed by Delaubert *et al.* [24, 25], who extended the SHG analysis by Boyd and Kleinman [61], relying on the nonlinear interaction of fundamental Gaussian modes, to more general SHG of higher-order Hermite-Gauss modes. We test the principles of the multi-mode SHG in a PPKTP nonlinear medium, which in reverse allows optimization of the nonlinear gain of an optical parametric amplifier (OPA) operating in a particular higher-order mode.

4.1 Second-order nonlinear interaction

4.1.1 Nonlinear polarization

In general, when an electro-magnetic field (EM) is applied to a dielectric medium (of neutral electric charge), a separation of bound charges of the atoms constituting the medium is induced, creating polarized dipole moments. Optical polarization P is the overall effect of these dipole moments and the material becomes polarized as a response to the applied EM field. For a weak EM field the atomic dipoles will oscillate linearly in tune with the oscillation of the applied field. The induced polarization will act as a source term for a re-radiated EM field which has in this case the same frequency as the applied field. When the applied field is intense, i.e. the amplitude of the applied field is of the same order of magnitude as the interatomic fields of the medium, the displacement of the electrons in the material is no longer proportional to the applied field and this results in a nonlinear behavior of the polarization [34], which is responsible for the generation of EM waves at various new combination frequencies. In this case the polarization can be expressed as:

$$P = P^{(1)} + P^{(2)} + P^{(3)} \dots, \quad (4.1)$$

$$P^{(i)} = \varepsilon_0 \chi^{(i)} \underbrace{\mathcal{E} \mathcal{E} \dots \mathcal{E}}_i, \quad i = 1, 2, 3, \dots \quad (4.2)$$

where $\chi^{(i)}$ is the i -th order dielectric response tensor describing the strength with which the crystal material responds to the different exponential powers of the optical driving field \mathcal{E} ; the constant $\varepsilon_0 = 8.85 \times 10^{-12}$ F/m is the electric permittivity in free space. Here we will focus on the second order nonlinearity, which can be used to facilitate SHG and OPA, nonlinear processes which are relevant to this thesis. These processes involve interaction of three photons¹ through the second order susceptibility $\chi^{(2)}$ of a nonlinear medium as shown in fig. 4.1, and are governed by the same fundamental equations [34]. In a SHG process two low energy photons of the same frequencies are combined and form a photon of higher energy, in an OPA process a high energy photon is split into two photons of low energy in the presence of a seed field. By down-converting the high energy photon, we create two fields called signal (ω_a^s) and idler (ω_a^i), and in the case $\omega_a^s = \omega_a^i$ the OPA process is termed *degenerate*.

4.1.2 Energy conservation and phase-matching condition

In the nonlinear processes as well as in all optical loss less processes, both energy and momentum need to be conserved [34]. The energy conservation condition can be written as

$$\omega_b = \omega_a + \omega'_a \quad (4.3)$$

and momentum conservation is achieved by satisfying the phase-matching condition

$$\Delta \vec{k} = \vec{k}_b - \vec{k}_a - \vec{k}'_a = 0, \quad (4.4)$$

where $|\vec{k}_i| = n_i \omega_i / c$; n_i is the refractive index of the nonlinear medium experienced by the photon of frequency ω_i and c is the speed of light in vacuum. The phase mismatch Δk is used to quantify the degree of mismatch in a nonlinear system. What frequency or wavelength will be generated in the conversion process is governed by the phase-

¹This is to be opposed to the wave picture, which is viewed as an interaction of three electromagnetic waves [34].

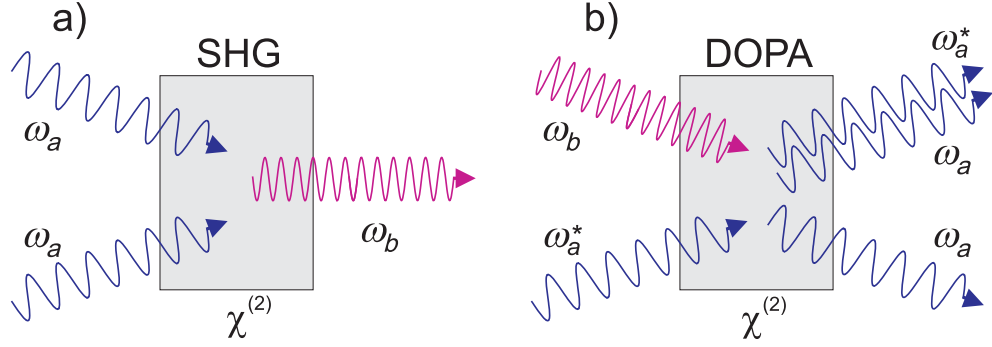


Figure 4.1: Three wave mixing processes: a) SHG: combination of two low energy photons (ω_a) into a high energy photon ($\omega_b = 2\omega_a$); b) degenerate OPA: a high energy photon (ω_b) is split into two low energy photons called signal (ω_a^s) and idler (ω_a^i) in the presence of a seed field ω_a^* . In the case $\omega_a^s = \omega_a^i = \omega_a$ the OPA process is degenerate.

matching and energy conservation conditions given by equas. 4.3 and 4.4, respectively. Assuming SHG and degenerate OPA processes, for which the frequencies of the two co-propagating fields, referred to as the fundamental field (ω_a) and the second harmonic field (ω_b), are governed by $\omega_b = 2\omega_a$, the condition 4.4 results in restriction of the refractive indices $n_a = n_b$ experienced by the interacting fields. This means that in order to have efficient nonlinear process, the generated field has to propagate through the nonlinear crystal with the same phase velocity as the fundamental field, hence the term phase-matching condition.

The phase-matching condition 4.4 cannot be achieved in dielectric media of normal dispersion, where the refractive index of the material increases with increasing wavelength. However, this can be satisfied in birefringent crystals, in which the extraordinary refractive index varies with the orientation of the optical polarization relative to the optical axis [34]. If all polarization directions of the interacting fields are along the crystal axes, the process is termed *non-critically* phase-matched. However, this is not often the case and phase-matching is achieved when the fields propagate in a direction with certain angle relative to the optical axis of the nonlinear crystal, termed as the *critical* phase-matching. In this case the fields experience some *walk-off*, i.e. they spatially separate, when they travel along the medium as a result of its birefringence. This limits the interaction length of certain crystals along which the nonlinear process is efficient and places a constraint on the beam size of interacting fields. We used for some of the experiments MgO doped LiNbO₃ working as the *type I* non-critically phase-matched medium [34], i.e. the second harmonic (SH) field is polarized along the fast axis of the crystal and the fundamental field along its slow axis. It can be non-critically phase-matched by tuning its temperature as the refractive index is strongly temperature dependant.

Another and more promising method to satisfy the momentum conservation is the quasi-phase matching (QPM) method [62]. It relies on periodically poled domains in a nonlinear medium such that at the point, where the SH wave and the fundamental wave are out of phase by $\pi/2$, the direction of crystal axis is flipped resulting in offset of the accumulated phase mismatch. Equa. 4.4 can be written in the case of QPM as

$$\Delta\vec{k} = \vec{k}_b - \vec{k}_a - \vec{k}_a' - \frac{2\pi}{\Lambda_{qpm}} = 0, \quad (4.5)$$

where Λ_{qpm} is the poling period and is typically in the order of few micrometers. A significant advantage of QPM is that any interaction within the transparency range of the material can be non-critically phase-matched at a specific temperature, even

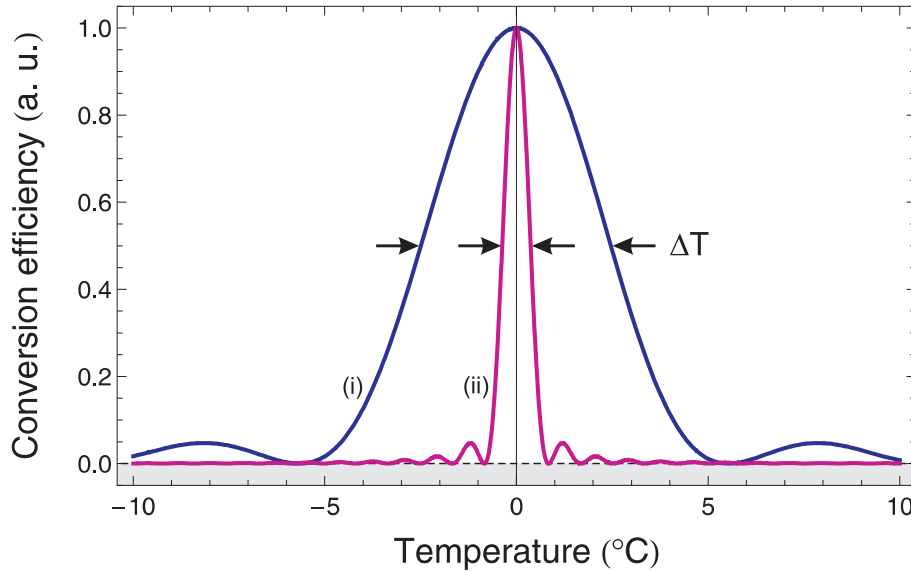


Figure 4.2: The effect of phase mismatch on the efficiency of the nonlinear process for (i) 10 mm long PPKTP, (ii) 10 mm long MgO:LiNbO₃, in terms of crystal temperature $T - T_{pm}$. The phase matching temperature T_{pm} is 27.3°C for PPKTP and 62.1°C for MgO:LiNbO₃.

interactions for which birefringent phase-matching is impossible. Another benefit of QPM is that we can allow the beams to propagate along the optical axis with the highest nonlinear coefficient², typically d_{33} for which all the interacting fields are of the same polarization. The nonlinear coefficient is for the first-order QPM medium given by $d_{qpm} = \frac{2}{\pi}d_{33}$ [34], where the factor $2/\pi$ arises from the mechanism of QPM. For some of the squeezing experiments, we used a periodically poled Potassium Titanyl Phosphate crystal (PPKTP), which has a large optical nonlinear coefficient $d_{33} = 16.9$ pm/V and together with its optical properties is thus an ideal candidate for optical parametric processes. This to be compared with LiNbO₃ material, which has in fact much larger nonlinear coefficient $d_{33} = 34.4$ pm/V. However, for an OPA operating at 1064 nm with type I noncritical phase-matching, we utilize the $d_{31} = 5.95$ pm/V coefficient, which is almost halve the value as for the PPKTP nonlinear medium. In reality it is very difficult to fabricate a poling structure of desired poling period Λ_{qpm} exactly for a certain temperature, and temperature tuning has to be done to satisfy the phase-matching condition.

Fig. 4.2 shows the temperature tuning curves for QPM of 10 mm long PPKTP, and type I phase-matching of 10 mm long MgO:LiNbO₃. The effect of phase mismatch Δk on the efficiency of the nonlinear process η_{nl} is in the plane wave approximation given by $\eta_{nl} \sim \text{sinc}^2(\Delta k L/2)$, where L is the interaction length. The advantage of PPKTP is besides a large nonlinear coefficient also its high temperature bandwidth. Thus the process of phase-matching does not require such precise control of temperature of the nonlinear medium as for e.g. lithium niobate.

4.2 Multi-mode second harmonic generation

For demonstrating the spatial entanglement for bright optical beams, which is the topic of chapter 7, we require squeezed states of light to be generated at higher-order Hermite-Gauss modes (H-G), in this particular case at the TEM₁₀ mode. As was already

²The nonlinear coefficient d is related to the dielectric susceptibility by $d = \frac{1}{2}\chi^{(2)}$.

mentioned in the previous section, the OPA process serving as a principle for generating squeezed states is the parametric down-conversion process, which is reciprocal process to SHG. The important factor for generating states of high degree of squeezing is the nonlinear efficiency of the device used for this purpose. Thus understanding the basic principles of multi-mode SHG will help us to optimize the efficiency of the nonlinear process and in essence maximize the amount of squeezing generated in an OPA.

In the thin crystal approximation, which is valid experimentally as long as the beam is not too strongly focused into a nonlinear crystal, i.e. the Rayleigh range of the interacting fields is much larger than the length of the crystal $z_R \gg L$, a nonlinear process can be described by a simple plane wave theory [34]. However, in the case of strong focusing, i.e. $z_R \approx L$, which is necessary in real applications to achieve a highly efficient nonlinear process, a more detailed description is needed as one has to consider the Gouy phase shift experienced by the interacting beams when propagating through a nonlinear medium. This places a constraint on the optimum focusing of the beams into the nonlinear crystal and is detailed in the study by Boyd and Kleinman [61], who assumed interacting TEM₀₀ Gaussian beams.

The Boyd-Kleinman analysis has been recently extended by Delaubert *et. al.* to higher-order transverse modes [24, 25]. Here we will follow their work on studies of the SHG process with higher order H-G modes. We will test experimentally the same principles using a different and more promising nonlinear material, PPKTP, which is of another type of phase-matching (QPM) than used in their original experiments (type I phase matched MgO:LiNbO₃). Recall that in the case of PPKTP, all the interacting fields are polarized in the same direction.

4.2.1 Single pass SHG experiment

In order to investigate the SH multi-mode generation, we considered a single-pass experiment as shown in fig. 4.3. A diode-pumped monolithic Nd:YAG ring laser operating at 1064 nm (sec. 3.4) served as a pump for the nonlinear conversion. In this experiment we used an optical cavity as a mode converting device for transferring power from the fundamental TEM₀₀ mode delivered by the laser into nearly perfect high purity TEM₀₀, TEM₁₀ and TEM₂₀ Gaussian modes of optical powers 144 mW, 92 mW and 28 mW, respectively. To maximize the TEM₁₀ conversion, we coupled into the mode transferring cavity a flipped mode, as discussed in sec. 3.6.2. The TEM₂₀ mode was generated by misaligning the incident field into the cavity. The resonator was locked to a certain higher-order mode using the PDH locking technique, as detailed in sec. 3.3.1.

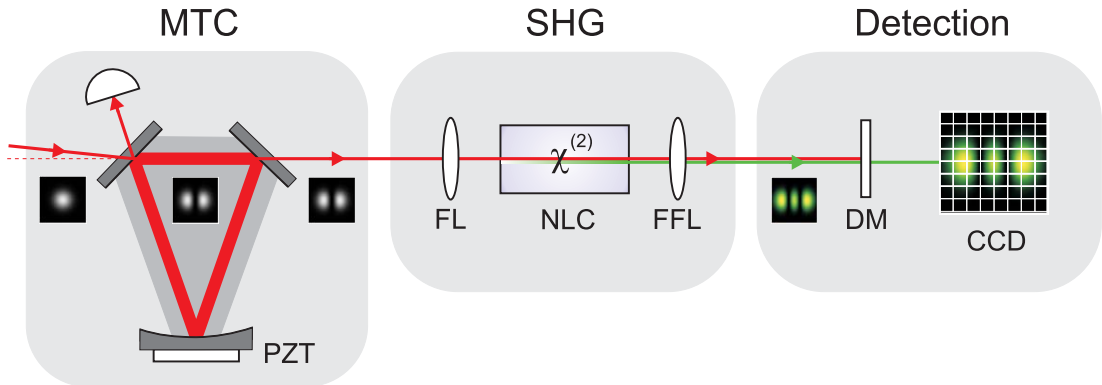


Figure 4.3: Scheme of the single pass SHG experiment. MTC: mode transferring cavity used to generate higher-order H-G modes; FL: focusing lens; NLC: nonlinear crystal; FFL: far field lens; DM: dichroic mirror; CCD: recording camera.

The output from the mode converting device was focused by a $f = 50$ mm lens into a nonlinear medium, which in this case was a PPKTP crystal with dimensions $10 \times 2 \times 0.5$ mm³ (Raicol Crystals Ltd.). The crystal is poled over its entire length in order to satisfy the phase-matching condition. The poling period has been estimated using the Sellmeier equations [63, 64], temperature-dependent dispersion equations [65] and measurements of the phase-matching temperature to be $\Lambda_{qpm} = 8.958$ μ m. The QPM method allows all the interacting waves of the same polarization to travel along the same optical axis and thus experience the highest nonlinear coefficient in the crystal. The nonlinear crystal is housed in an oven and its temperature is controlled by a Peltier element. The focused beam has a beam waist radius of 33 μ m and is located in the center of the crystal. The generated SH field is filtered from the infrared field by a dichroic mirror and its spatial profile is recorded by a CCD camera (far field).

4.2.2 Generalized Boyd-Kleinman coefficients

As the generated field in a SHG process relies on the square of the fundamental field, the spatial transverse profile of the SH mode can be obtained by the decomposition of the square of the fundamental pump mode profile into the SH basis. It is important to note that this statement is valid only as far as the two fundamental photons, which after the nonlinear interaction create the SH photon, are of the same polarization. This is satisfied in type I and QPM, or rather type III, interaction only. As the consequence the SH field is composed of $n + 1$ mode components, which are all even since the TEM _{n 0} pump squared profile is necessarily even. In type II interaction, where the two fundamental photons are of orthogonal polarizations, the spatial profile of the fundamental field is transferred to the SH field without any quadratic effect [66].

Because of the different evolution of each H-G component of the generated SH field, a local field description and a propagation of the SH modes along the crystal length is necessary. Here we will focus on the nonlinear interaction of the first three H-G modes in a nonlinear medium as these are relevant to this thesis. In order to simplify the calculations, we will consider negligible loss in the material for both the fundamental and SH fields. This does not affect the description of the generated SH field. However, optical loss has to be taken into account for squeezing generation as this is one of the limiting factors in generating high degrees of squeezing [67]. We will also consider that the fundamental beam is focused in the center of the nonlinear crystal, which corresponds to the optimized case of a nonlinear interaction, and that the beam is propagating along the optical axis of the crystal, thus we can omit any walk-off effects in the calculations. As was already mentioned, in the case of PPKTP used in the experiments all the interacting fields are polarized in the same direction and propagate along the z axis.

The intensities of the SH field I_{sh}^{n0} generated by the fundamental field of spatial profile TEM _{n 0} can be written along one direction of the transverse plane denoted x as

$$I_{sh}^{00}(s, \xi, \Delta k) = \kappa_I e^{-4s^2} \left[H_{0,0}(\xi, \Delta k) \right]^2, \quad (4.6)$$

$$I_{sh}^{10}(s, \xi, \Delta k) = \kappa_I \frac{e^{-4s^2}}{4} \left[H_{1,0}(\xi, \Delta k) - (8s^2 - 1)H_{1,2}(\xi, \Delta k) \right]^2, \quad (4.7)$$

$$\begin{aligned} I_{sh}^{20}(s, \xi, \Delta k) = & \kappa_I \frac{e^{-4s^2}}{4} \left[\frac{3}{4}H_{2,0}(\xi, \Delta k) - \frac{1}{2}(8s^2 - 1)H_{2,2}(\xi, \Delta k) + \right. \\ & \left. + \frac{1}{4}(64s^4 - 48s^2 + 3)H_{2,4}(\xi, \Delta k) \right]^2, \end{aligned} \quad (4.8)$$

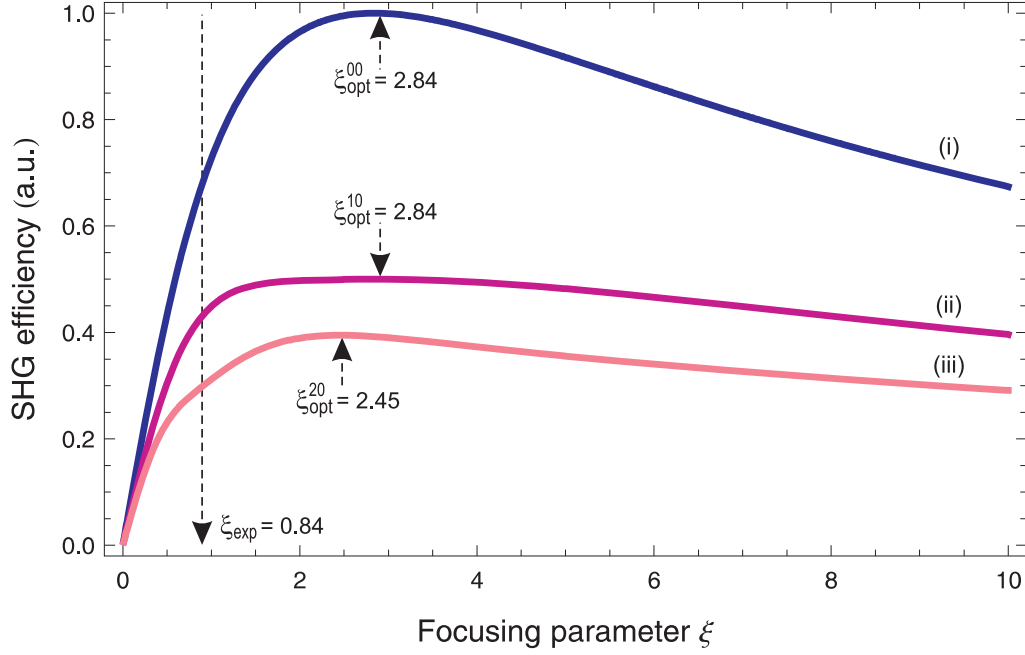


Figure 4.4: SHG conversion efficiency as a function of the focusing parameter ξ for (i) TEM_{00} pump, (ii) TEM_{10} pump and (iii) TEM_{20} pump. For each data point, the SHG efficiency was numerically maximized by adjusting the temperature of the nonlinear crystal. The SHG efficiencies are normalized to the best conversion efficiency for the TEM_{00} pump.

where $\kappa_I = 4\pi K(\frac{P_a k_a}{\tau})^2$; K is the effective coupling constant proportional to the square of the effective nonlinear coefficient d_{eff} and is defined as $K = \frac{128\pi^2 \omega_a^2}{c^3 n_a^2 n_b} d_{\text{eff}}^2$; P_a is the fundamental pump power; $\tau = (z - \frac{L}{2})/z_R$ represents the normalized longitudinal position; L is the length of the nonlinear crystal; z_R is the Rayleigh range; $s = xz_R/w_0z$ is the transverse position parameter; ξ is the focusing parameter given by $\xi = L/2z_R$ and Δk is the phase mismatch given by equa. 4.4. $H_{n,2p}(\xi, \Delta k)$ integrates the nonlinear effects on the crystal length and is defined by [24]

$$H_{n,2p}(\xi, \Delta k) = \frac{1}{2\pi} \int_{-\xi}^{\xi} \frac{(1 - i\tau)^{n-p} e^{-i\frac{L\Delta k\tau}{2\xi}}}{(1 + i\tau)^{n-p+1}} d\tau. \quad (4.9)$$

The indices n and $2p$ refer to the TEM_{n0} pump mode and to the even TEM_{2p0} generated SH mode, respectively. Each term in equas. 4.6-4.8 thus accounts for the contribution of an even SH mode to the total SHG field. Because of the Gouy phase shift, the propagation of the modes strongly depends on the focusing parameter and the phase mismatch experimentally achievable via the change of crystal temperature. Both of these effects are described by the function $H_{n,2p}(\xi, \Delta k)$.

By integrating the intensity distributions I_{sh}^{n0} along the transverse direction, we obtain powers P_{sh}^{n0} of the SH field as

$$P_{sh}^{00}(\xi, \Delta k) = \frac{\kappa P}{\xi} |H_{0,0}(\xi, \Delta k)|^2, \quad (4.10)$$

$$P_{sh}^{10}(\xi, \Delta k) = \frac{\kappa P}{\xi} \left[\frac{1}{4} |H_{1,0}(\xi, \Delta k)|^2 + \frac{1}{2} |H_{1,2}(\xi, \Delta k)|^2 \right], \quad (4.11)$$

$$P_{sh}^{20}(\xi, \Delta k) = \frac{\kappa P}{\xi} \left[\frac{9}{64} |H_{2,0}(\xi, \Delta k)|^2 + \frac{1}{8} |H_{2,2}(\xi, \Delta k)|^2 + \frac{3}{8} |H_{2,4}(\xi, \Delta k)|^2 \right] \quad (4.12)$$

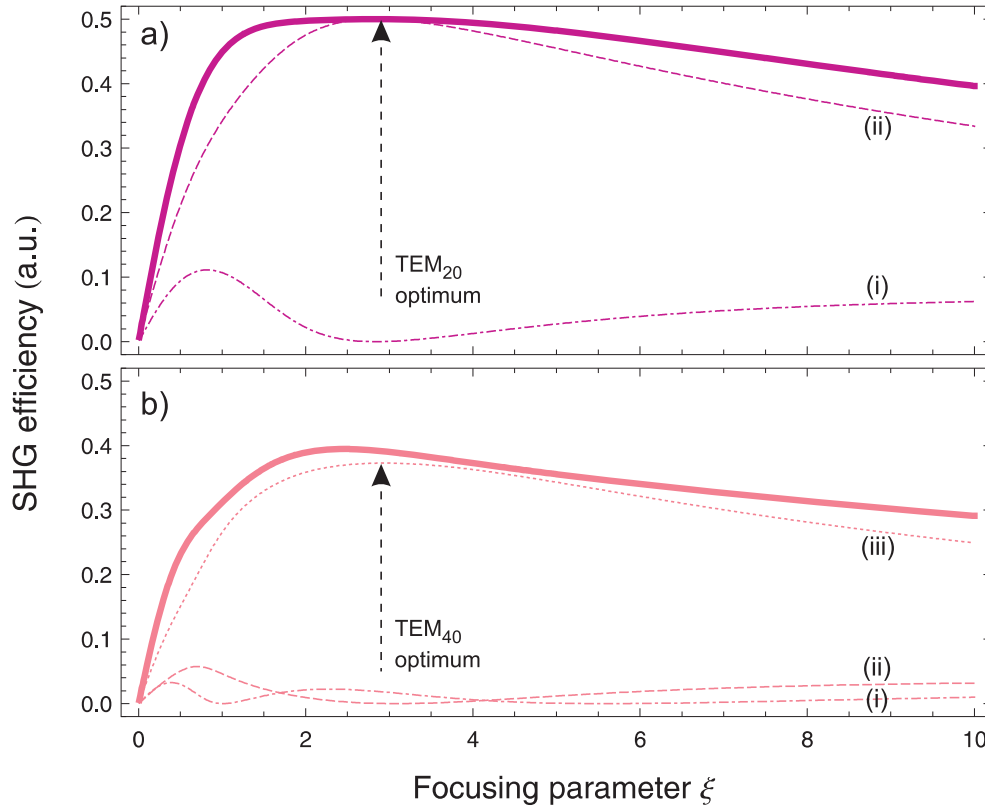


Figure 4.5: Modal decomposition of the SH field into the TEM_{n0} H-G basis where (i) $n = 0$, (ii) $n = 2$ and (iii) $n = 4$, as a function of the focusing parameter ξ for a) TEM_{10} pump and b) TEM_{20} pump mode. The conversion efficiencies are normalized to the best conversion efficiency for the TEM_{00} pump.

where the parameter $\kappa_P = \pi^2 K P_a^2 \kappa_a L$. The fig. 4.4 shows the SHG efficiency for the first three H-G fundamental modes as a function of the focusing parameter ξ , when normalized to the best conversion efficiency for the TEM_{00} pump. Note that the SHG efficiency for a certain focusing parameter was numerically maximized by optimizing the phase mismatch, or rather temperature of the nonlinear crystal. The maximum conversion efficiencies occur for $\xi_{opt}^{00} = 2.84$ as expected from Boyd-Kleinman theory³, $\xi_{opt}^{10} = 2.84$ and $\xi_{opt}^{20} = 2.45$ ⁴. The maximum achievable SHG efficiency is 50% for the case of TEM_{10} pump and 40% for the TEM_{20} pump mode. We can see that the SHG efficiency is a decreasing function of the pump mode order and this is due to the lower local intensity in higher-order modes.

It is clear from equas. 4.10-4.12 that the final SH field is composed of $n + 1$ transverse mode components when the crystal is pumped by a TEM_{n0} fundamental mode.

³By modulating the refractive index of the nonlinear material one can compensate for the Gouy phase shift between the fundamental field and the SH field, when propagate through the nonlinear medium, and in this case the optimum focusing regime becomes for $\xi_{opt}^{00} = 3.32$ [68]. This results in an increase of SHG efficiency by 4.4%. The refractive index can be modulated via the electro-optic effect [34] or via introducing temperature gradients on the crystal. Alternatively we propose in a QPM device a fan poling structure of a specific shape, which can compensate for the Gouy phase shift without any sophisticated external modulation. Another advantage is that such a device works also for the counter propagating wave, which is of great importance when enhancing the nonlinear effect in an optical cavity. Modulating the refractive index can compensate for the Gouy phase shift only for waves propagating in one direction [68].

⁴Note that the optimum focusing parameters for the TEM_{10} and TEM_{20} pump are slightly different than published in the reference [24] as a result of optimization of the phase mismatch for every data point of the SHG efficiency.

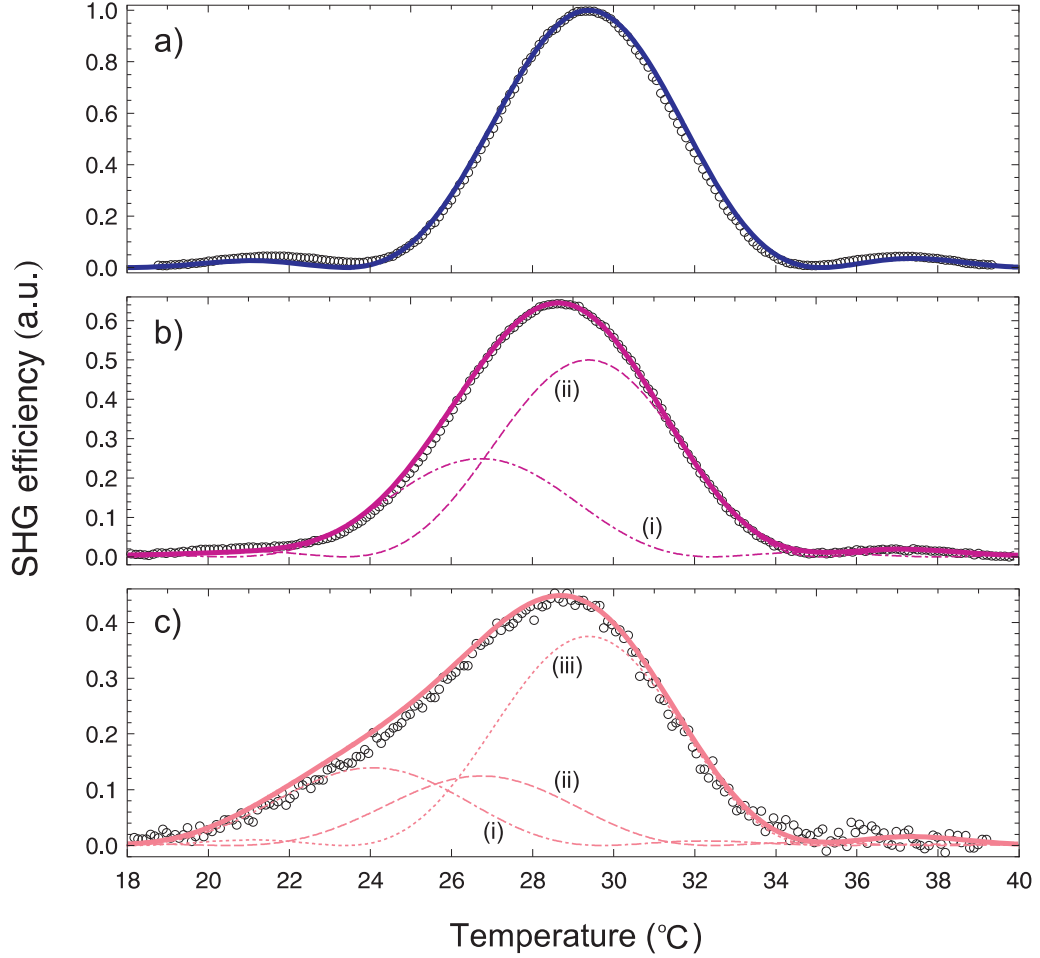


Figure 4.6: SHG conversion efficiency measurements (circles) and theoretical fits (full lines) as a function of the phase-matching temperature for a) TEM₀₀ pump, b) TEM₁₀ pump and c) TEM₂₀ pump mode, and the decomposition of the SH field into the TEM_{*n*0} H-G basis, where (i) $n = 0$, (ii) $n = 2$ and (iii) $n = 4$. The fundamental pump beam focused into a 10 mm long PPKTP nonlinear crystal has a beam waist radius of $33 \mu\text{m}$, which corresponds to $\xi_{exp} = 0.84$. The SHG efficiencies are normalized to the best conversion efficiency for the TEM₀₀ pump.

The evolution of the SH higher-order modal components as a function of the focusing parameter ξ is shown in fig. 4.5. In the case of TEM₁₀ pump, the dominant SH component is just the TEM₂₀ mode having its maximum at $\xi = 2.84$ with corresponding SHG efficiency of 50%. For weaker focusing and/or strong focusing, the TEM₀₀ component is getting noticeable and makes the final SHG efficiency curve broader compared to the case of TEM₀₀ conversion. For the TEM₂₀ pump the dominant SH component is the TEM₄₀ mode peaking again at $\xi = 2.84$ with corresponding SHG efficiency of 37.5%. The TEM₀₀ and TEM₂₀ mode components are again present mainly in the low focusing regime and/or strong focusing regime, but having only poor conversion efficiencies of several percents.

4.2.3 Influence of the phase-matching temperature

The second parameter influencing the SH field composition is the phase mismatch Δk , which is related to the temperature dependance of the refractive index of the nonlinear crystal, described by the Sellmeier equations [63, 64]. Fig. 4.6 shows measurements of the SHG conversion efficiency (circles) again for the first three H-G modes as a function of the phase-matching temperature. Temperature of the PPKTP crystal was changed

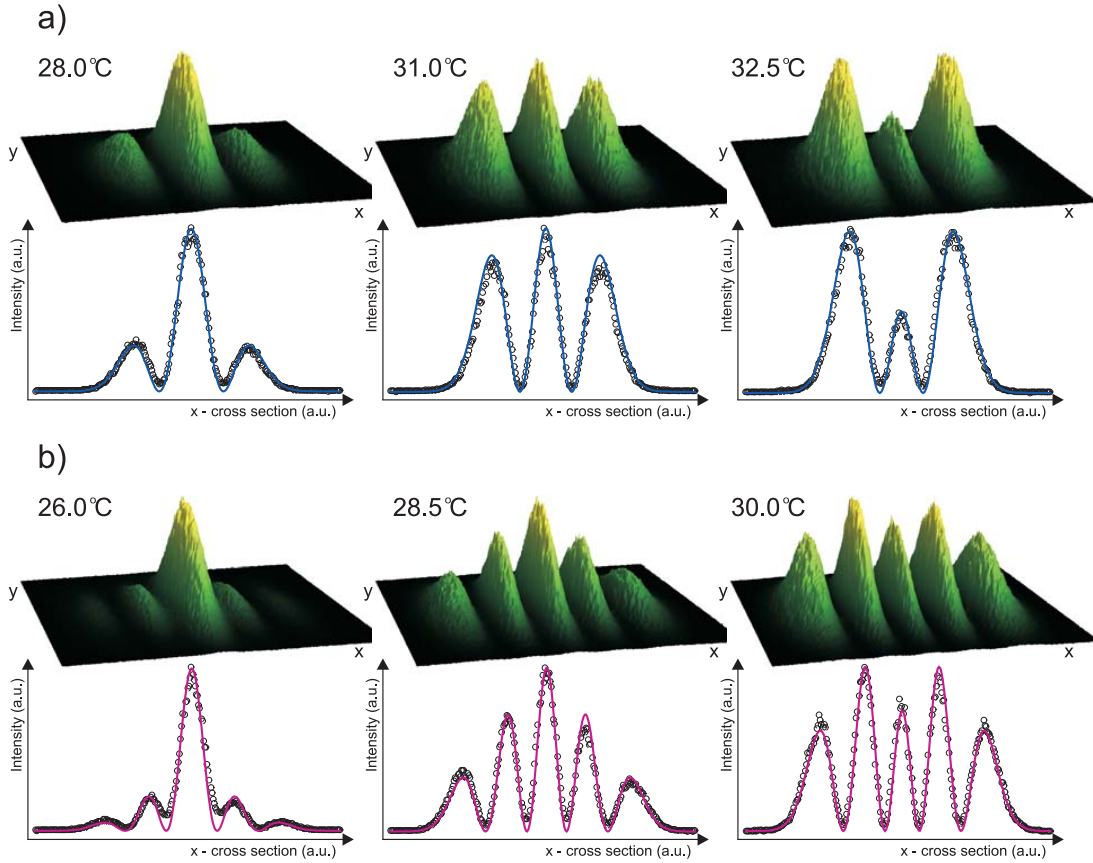


Figure 4.7: 3D profiles and transverse cross-sections of the generated SH field for three different phase-matching temperatures for a) TEM_{10} pump and b) TEM_{20} pump mode. The cross-section graphs show measured data (circles), which are theoretically fitted (lines) using real experimental parameters.

in steps of 0.1°C and each of the plotted data points represents the average value of 5 subsequent measurements in time intervals of 2 seconds at the same temperature. In the case of TEM_{00} conversion, the phase-matching curve is for the relatively weak focusing of the fundamental field into the crystal, which was adopted in this experiment ($\xi_{exp} = 0.84$), almost a perfect sinc function⁵ with the optimum phase-matching temperature of 29.3°C and the temperature bandwidth of 5.1°C . The SHG efficiencies for the maximum TEM_{10} and TEM_{20} conversion are 65% and 44% when normalized to the TEM_{00} conversion, respectively, and these values perfectly match to the predicted efficiencies shown in fig. 4.4 for the experimental focusing parameter $\xi_{exp} = 0.84$.

The interesting feature is that for the higher-order modes the phase-matching distribution is clearly asymmetric and is getting more asymmetric with increasing pump mode order. This is again due to the Gouy phase shift, which leads to different phase-matching conditions for each SH mode as the beam propagates along the crystal length. So the overall phase-matching curve corresponds to sum of shifted phase-matching distributions of each of the modal components. This is clearly visible in figs. 4.6 b) and c), where the theoretically predicted phase-matching distributions of each of the SH field components are shown (non-solid lines). Note that the dominant SH component for particular TEM_{n0} pump mode is again the highest order mode in the decomposition of the overall SH field, i.e. TEM_{2n0} mode, and the maximum of this SH component occurs at the same phase-matching temperature as for the TEM_{00} conversion. The

⁵Note that for stronger focusing the phase matching distribution is getting asymmetric and even the optimum phase matching temperature is changing as a result of the Gouy phase shift.

phase-matching maxima of the supplementary SH field components are shifted to lower temperatures, which has been observed experimentally as well (see sec. 5.2.2). In general, we can see an excellent agreement between the theoretical overall phase-matching curves and the measured data.

The results shown in fig. 4.6 predict a high sensitivity of the beam profile of the SH generated field to the crystal temperature. We therefore expect to see a modification of the SH profile when the crystal temperature is varied. The generated intensity SH profiles normalized to their maximum are for three different temperatures of the crystal shown in figs. 4.7 a) and b) for the case of TEM_{10} and TEM_{20} pump modes, respectively. We can see that by changing the phase-matching temperature, we continuously change the modal composition, and so we find that the SH field is a temperature dependant linear combination of the SH field modal components. This effect might find applications as accurate temperature sensors or can be used for trapping or displacing particles in an optical beam, as was proposed in reference [24]. The cross-section profiles (circles) are fitted using the equas. 4.6-4.8 (solid lines) with the experimental parameters detailed in sec. 4.2.1. We can see again an excellent agreement, which proves that transverse mode coupling can be understood in terms of mode overlaps, and that a full quantitative description can be obtained in the general case.

4.2.4 Optimizing TEM_{10} conversion

As SHG is the reciprocal process of OPA, understanding the higher-order mode conversion in SHG enables the optimization of the SH pump profile in order to pump the OPA cavity efficiently [69]. So by looking at the SH field, we may find the optimum operation of a certain SH modal component, and in essence an optimum spatial profile of the OPA pump field. As we have seen previously, the two parameters, which can be experimentally optimized, are the focusing parameter ξ and the phase-matching temperature. It is therefore straightforward to plot the SHG efficiency as a function of the two parameters, and decompose the final field into its SH modal components. As we are particularly interested in the TEM_{10} squeezing generation, which is the major technique used for demonstrating the spatial entanglement (see chapter 7), we did such a model for the case of the TEM_{10} fundamental pump mode.

Fig. 4.8 shows the nonlinear conversion into the TEM_{00} and TEM_{20} modes. We can see that the optimum conversion from the pump into the two SH modes occurs at completely different experimental conditions. If we desire to use the TEM_{00} mode as a pump of an OPA, the maximum nonlinear interaction is obtained for rather low focusing parameter $\xi = 1.8$ and at the phase-matching temperature $T_{pm} = 23.5^\circ\text{C}$. In this case, the conversion efficiency corresponds to $\eta_{sh}^{00} = 22\%$ when normalized to the best SHG efficiency with fundamental modes. A more promising method is to use the TEM_{20} mode as an OPA pump, ensuring more than twice the nonlinear efficiency, i.e. $\eta_{sh}^{20} = 50\%$, and this occurs for the optimum focusing parameter $\xi = 2.84$ and at the phase-matching temperature $T_{pm} = 27.8^\circ\text{C}$. Thus for an efficient TEM_{10} squeezing generation, we require the OPA pump field to be in the TEM_{20} mode.

As a common frequency doubled laser delivers optical power in the TEM_{00} mode, we need to use an optical cavity to transform this beam into the desired spatial mode, see sec. 3.6. Conversion of the TEM_{00} mode into the TEM_{20} mode can be up to 78% efficient with use of a specially designed wave-plate, and by defocusing the incident beam into the mode converting cavity, as discussed in sec. 3.6.2.

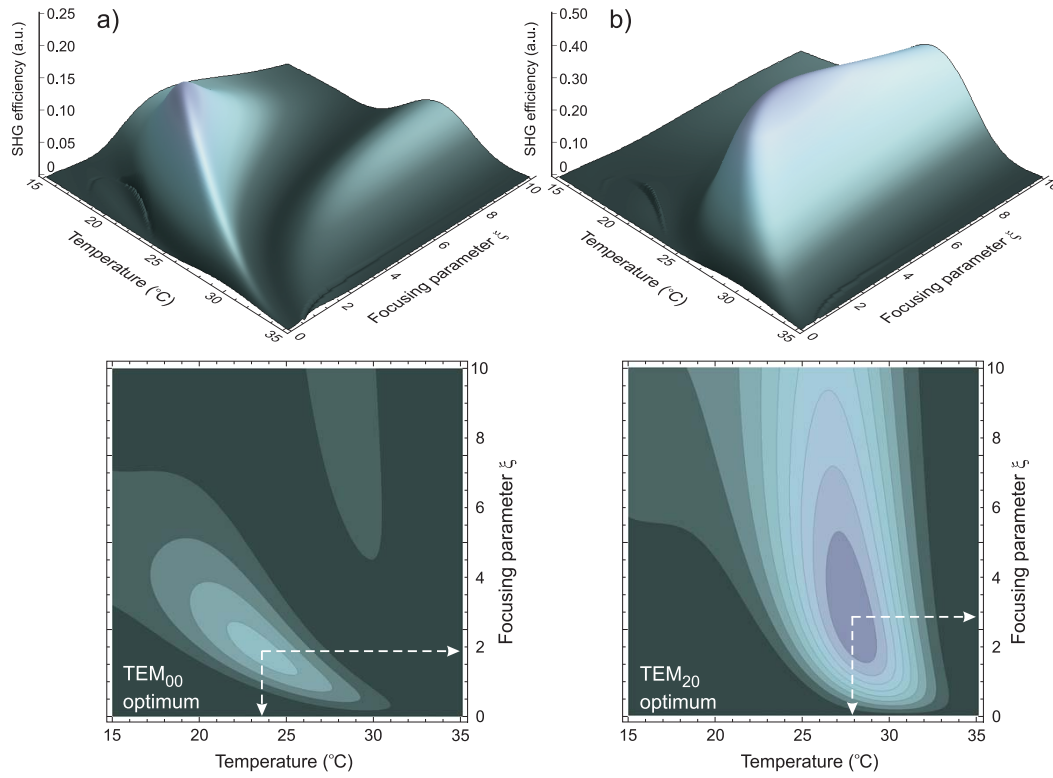


Figure 4.8: Modal decomposition of the SH field into a) TEM_{00} and b) TEM_{20} modes as a function of the phase-matching temperature and the focusing parameter ξ , when the nonlinear crystal is pumped by the TEM_{10} fundamental field. The largest nonlinear conversion of the fundamental TEM_{10} field into the TEM_{00} and TEM_{20} modes occurs for $T = 23.5^\circ\text{C}$, $\xi = 1.8$ and $T = 27.8^\circ\text{C}$, $\xi = 2.84$, respectively, and these correspond to $\eta_{sh}^{00} = 22\%$ and $\eta_{sh}^{20} = 50\%$. The conversion efficiencies are normalized to the best conversion efficiency for the TEM_{00} pump.

4.3 Summary

In summary, we demonstrated the multi-mode SHG in a PPKTP nonlinear medium and conclude that we can use the same principles for describing the evolution of the generated SH field inside a QPM nonlinear device as in the case of a type I phase-matched bulk crystal. The results show that transverse mode coupling of the interacting fields can be understood in terms of mode overlaps, and that the ratio between the generated SH components can be experimentally adjusted via the focusing parameter and crystal temperature.

We can use these results in reverse to optimize a spatial profile of the pump field for an efficient down-conversion process of an OPA operating in higher-order modes. For an OPA operating in the TEM_{n0} mode, the optimum pumping scheme is achieved utilizing a pump beam of TEM_{2n0} spatial profile with the focusing parameter $\xi = 2.84$, and the highest nonlinear gain occurs at the same phase-matching temperature as for the fundamental mode operation. In particular, the nonlinear conversion can be for a TEM_{10} OPA up to 50% efficient using a TEM_{20} pump, and in the case of a TEM_{20} OPA this process can be up to 37.5% efficient using a TEM_{40} pump, relative to the conversion efficiency achieved with fundamental modes. If we desire to use a TEM_{00} pump for an OPA operating in the TEM_{10} spatial mode, the maximum conversion efficiency is 22%, and is obtained for rather low focusing parameter $\xi = 1.8$ and at lower phase-matching temperatures.

Chapter 5

OPA squeezing

Contents

5.1 Theory of OPA	53
5.1.1 Classical description	54
5.1.2 Quantum description	55
5.1.3 Squeezing trace	57
5.2 Generation of squeezed vacuum states	59
5.2.1 Experimental setup	59
5.2.2 Regenerative gain	62
5.2.3 TEM ₀₀ and TEM ₁₀ squeezing generation	64
5.2.4 Influence of the pump noise on squeezing generation	67
5.2.5 Optimizing the output coupler transmission	69
5.3 Summary	70

Squeezing was first demonstrated by Slusher *et al.* in 1985 [70], using a four-wave mixing nonlinear effect in a sodium vapor. Since that time, the squeezed states were successfully produced in other nonlinear systems, based mainly on second-order nonlinear effect in an optical material by employing optical parametric amplification (OPA) and second harmonic generation (SHG) [32, 33], or based on third-order nonlinear effect in optical fibers by employing Kerr effect [6, 7], and other. Squeezing generated with an OPA, which is relevant to this thesis, was first achieved by Wu *et al.* in 1986 [3, 4], and since that time OPAs have consistently generated the best quadrature squeezing results [8, 9, 10, 11], with a recent record of -10 dB noise suppression below the QNL [11]. Squeezing was demonstrated at sideband frequencies down to sub-kHz frequencies [71] and up to the GHz regime [72].

The use of squeezed light in general is restricted to measurements at RF frequencies, because squeezing sources suffer from an excess noise at lower frequencies due to acoustic, thermal and electronic noise present in the system and relaxation oscillation of the laser source used [47]. So working at a quantum noise limit (QNL), squeezed light finds applications in such measurements, for which quantum noise is a limiting factor, and for which the optical power is limited, for example because of the existence of a damage threshold of a sample to be measured. To give an example, using a -3 dB amplitude squeezed light, which is easily experimentally achievable, the amplitude of the quantum fluctuations is reduced by a factor of $\sqrt{2}$ relative to the noise of the coherent light. Such a factor can be of great importance in order to distinguish a very small

signal from the quantum noise. In order to obtain a similar signal-to-noise ratio of a squeezed beam of a certain power, we would require a coherent beam twice as powerful.

Squeezed light can be used for ultra-sensitive applications e.g. in sub-shot-noise high sensitivity spectroscopy [12, 13] or for detection of gravitational waves using large interferometers [14]. Moreover combination of squeezed states allows production of a continuous variable entanglement [73, 74, 75, 76], which can be utilized in the quantum information science [77] for applications such as quantum communication and teleportation [78], dense coding [79] and secret data sharing [80].

The squeezed optical mode was limited until recently to the TEM_{00} mode, until our group demonstrated the first generation of squeezed light in higher-order Hermite-Gauss (H-G) modes [69], which is particularly useful for quantum imaging applications. These include the detection of spatial parameters such as small displacements and tilts below the QNL [18], enhancing the data read-out density of optical discs [81], nanometer scale laser beam displacement measurements in gravitational wave detectors [21], or atomic force microscopes [22]. There has been proposals for more advanced applications such as super-resolution [82] and quantum holography [83]. Moreover, a multi-mode squeezed light can be utilized in generation of position-momentum entanglement of bright optical beams, as will be shown in chapter 7. Spatial entanglement has the potential for use in parallel quantum information processing as it allows teleportation and dense coding of spatial information. In particular, for production of position-momentum entanglement, we require squeezing of the TEM_{10} mode.

In this chapter, we present the quantum theory of an OPA along with possible limitations of squeezing production. Then we describe in detail the experimental setup used to generate vacuum squeezed states in the TEM_{00} and TEM_{10} modes, employing a bow-tie PPKTP based OPA as a squeezing source. We present both classical and squeezing measurements, and these are compared to the results predicted by our model. We experimentally characterize the level of squeezing, measuring at the best -5.5 dB of squeezing in the TEM_{00} mode and -3.1 dB of squeezing in the TEM_{10} mode, after correction for the electronic noise. Finally, we analyze the influence of a pump amplitude noise on generation of squeezing and discuss an optimization of the current setup for an efficient generation of squeezing in the TEM_{10} spatial mode.

5.1 Theory of OPA

The behavior of an OPA can be theoretically investigated using the quantum Langevin equation 2.25. Here the reversible Hamiltonian describing a degenerate second order process $\hat{H}_{\chi(2)}$ is given by [67]

$$\hat{H}_{\chi(2)} = \hbar\omega_a\hat{a}^\dagger\hat{a} + \hbar\omega_b\hat{b}^\dagger\hat{b} + \frac{i\hbar\epsilon}{2}(\hat{a}^{\dagger 2}\hat{b} - \hat{a}^2\hat{b}^\dagger), \quad (5.1)$$

where the first two terms are the energies of the fundamental and SH fields, respectively, and the last term describes the nonlinear interaction between the fields with ϵ being the interaction strength. This quantity is related to the nonlinearity of the material, interaction length, beam focusing and phase mismatch. In experiments, the aim is to maximize the interaction strength and so maximize squeezing generation. In order to access high nonlinearities in the crystal, high field intensities are required as discussed in sec. 4.1. This is achieved for a continuous-wave operation by inserting the nonlinear medium in an optical cavity resonant for the fundamental field, as shown in fig. 5.1. When the cavity is on resonance, the intra-cavity field and thus the nonlinear interaction is strongly enhanced. In the following we will assume a back seeded OPA (seeded through the high reflecting mirror with transmissivity η_{ic}), which is relevant to our work.

Inserting the Hamiltonian $\hat{H}_{\chi(2)}$ into the quantum Langevin equation and assuming that the fundamental field is on resonance, we end up with the equations of motion for the fundamental and SH intra-cavity time dependent fields denoted \hat{a} and \hat{b} , respectively, and these are given as [38, 67]

$$\dot{\hat{a}} = -\gamma_a\hat{a} + \epsilon\hat{a}^\dagger\hat{b} + \sqrt{2\gamma_{ic}^a}\hat{A}_{ic} + \sqrt{2\gamma_{oc}^a}\delta\hat{A}_{oc} + \sqrt{2\gamma_l^a}\delta\hat{A}_l, \quad (5.2)$$

$$\dot{\hat{b}} = -\gamma_b\hat{b} - \frac{\epsilon}{2}\hat{a}^2 + \sqrt{2\gamma_{ic}^b}\hat{B}_{ic} + \sqrt{2\gamma_{oc}^b}\delta\hat{B}_{oc} + \sqrt{2\gamma_l^b}\delta\hat{B}_l. \quad (5.3)$$

We used here the same convention as for the case of the passive resonator described in sec. 3.2, with superscripts a and b referring to the fundamental and SH fields, respectively. The overall system interacts with the environment through the loss terms, and the two fields are coupled via the nonlinear interaction strength ϵ . Note that, for operating the OPA in higher-order H-G modes, the interaction strength has to be multiplied by the efficiency of the multi-mode nonlinear process as outlined in sec. 4.2. This reduced nonlinear strength reflects the fact that the local intensity of the interacting higher-order modes drops as the spatial extension increases with the order of the mode. As a result, the OPO threshold is increased and we expect lower squeezing generation because of a lower nonlinear gain.

In all experiments throughout this thesis the OPA cavities are resonant only for the fundamental field, and the pump field is single-passed¹ through the nonlinear crystal, i.e. $\gamma^a \ll \gamma^b$. In this case the evolution of the SH field will occur rapidly compared to the fundamental field, and we can assume $\dot{\hat{b}} = 0$ [84, 85]. For simplicity, we will assume no coupling of the SH field with the environment, so $\gamma_{oc}^b = \gamma_l^b = 0$ and then $\gamma_b = \gamma_{ic}^b$. As we operate the OPA below its threshold, i.e. $\epsilon|\alpha|^2/2 \ll \sqrt{2\gamma_b}\hat{B}_{ic}$, where \hat{B}_{ic} is the classical amplitude of the pump field, then also the pump depletion can be neglected and the equation of motion for the fundamental field becomes

¹In squeezing experiments with MgO:LiNbO₃ nonlinear crystal (sec. 7.3), the pump field was actually double-passed through the nonlinear crystal as one side of the crystal was coated for high reflection at the pump frequency.

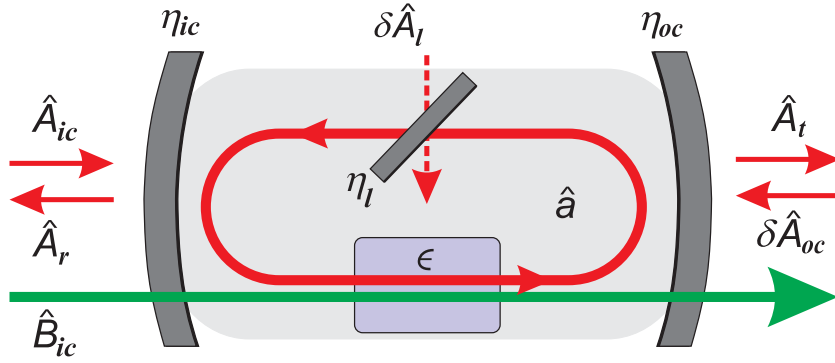


Figure 5.1: Schematic of an optical parametric amplifier. A nonlinear medium is inserted into a resonant cavity for the fundamental field (signal and idler). The cavity consists of input and output couplers of transmissivities η_{ic} and η_{oc} , respectively. The intra-cavity field \hat{a} experiences some round-trip loss η_l through which the quantum fluctuations $\delta\hat{A}_l$ are coupled into the system. The nonlinear crystal is single passed with the pump field \hat{B}_{ic} entering the OPA through the input coupler. The fundamental and SH fields are coupled via the nonlinear interaction strength ϵ . \hat{A}_{ic} : input fundamental (seed) field; \hat{A}_r : reflected field; \hat{A}_t : transmitted field; $\delta\hat{A}_{oc}$: quantum fluctuations entering the system through OC.

$$\dot{\hat{a}} = -\gamma_a \hat{a} + \frac{\epsilon \hat{b}_{in}}{\gamma_b} \hat{a}^\dagger + \hat{a}_{in}, \quad (5.4)$$

where the input fields into the system \hat{a}_{in} and \hat{b}_{in} are

$$\hat{a}_{in} = \sqrt{2\gamma_{ic}^a} \hat{A}_{ic} + \sqrt{2\gamma_{oc}^a} \delta\hat{A}_{oc} + \sqrt{2\gamma_l^a} \delta\hat{A}_l, \quad (5.5)$$

$$\hat{b}_{in} = \sqrt{2\gamma_b} \hat{B}_{ic}. \quad (5.6)$$

5.1.1 Classical description

The classical behavior of an OPA can be analyzed using equa. 5.4 by replacing each operator with its expectation value. In steady state, i.e. $\dot{\hat{a}} = 0$, we then find the intra-cavity fundamental field α as

$$\alpha = \frac{\sqrt{2\gamma_{ic}^a}(1 + g/\gamma_a)}{\gamma_a(1 - |g|^2/\gamma_a^2)} \bar{A}_{ic}. \quad (5.7)$$

Here g is the nonlinear gain defined as $g = \Lambda \bar{B}_{ic} e^{i\phi}$, where the quantity $\Lambda = \sqrt{\frac{2}{\gamma_b}} \epsilon$ is the classical nonlinear strength. We assumed that the classical amplitudes of the seed field, \bar{A}_{ic} , and the pump field, \bar{B}_{ic} , are real and positive with ϕ being a relative phase between the two fields. This phase difference dictates whether the field entering an OPA will be amplified or deamplified. Using the input-output relations 3.12, we find the amplitude of the transmitted field as $\bar{A}_t = \sqrt{2\gamma_{oc}^a} \alpha$, and comparing this with the transmitted amplitude without gain, $\bar{A}_{t|g=0}$, we obtain a relation for the OPA gain. This in terms of optical power is called the *regenerative gain* of an OPA and is given by

$$g_r = \frac{(1 + g/\gamma_a)^2}{(1 - |g|^2/\gamma_a^2)^2}. \quad (5.8)$$

If the pump and seed fields are in phase, the pump power is transferred into the fundamental field. The input field is getting more amplified with increasing nonlinear gain g until the threshold of the optical parametric oscillator (OPO) is reached, i.e.

$|g| = \gamma_a$, which corresponds to $g_r \rightarrow \infty$. Further increase of the nonlinear gain g results in the OPO operation [67], which is not considered here. If the pump and seed fields are out of phase, $\phi = \pi$, the OPA then deamplify the seed field, transferring power from the fundamental into the pump field. The limit for deamplification is 0.25 and occurs as the OPO threshold is approached. This does not place a fundamental limit on the squeezing generation achievable with an OPA as we will see later in this section. For generation of bright squeezing throughout this thesis, we always operate the OPA in the deamplification regime below its OPO threshold, which is for $|g| < \gamma_a$ and $\phi = \pi$. In this regime, the quantum fluctuations in the amplitude quadrature are also deamplified leading to amplitude squeezing. In the case of the OPA amplification regime, the amplitude quadrature fluctuations are amplified, which in essence means that the phase quadrature fluctuations become squeezed. A special case is the vacuum squeezing, see sec. 5.2, where we only refer to squeezed and antisqueezed quadratures, because vacuum has no phase and in this case the amplitude and phase quadratures have therefore no meaning.

5.1.2 Quantum description

To see the effect of an OPA working either in the amplification or deamplification regime on the amplitude and phase quadrature fluctuations, we start again with the simplified equation of motion 5.4. To find the quadrature operators, we need to first expand each of the operators in the equation in terms of its expectation values and fluctuations, $\hat{a} = \alpha + \delta\hat{a}$. Assuming the fluctuations are much smaller than the coherent amplitude, we can neglect the higher order terms in $\delta\hat{a}$. Then the equation of motion for $\delta\hat{a}$ can be rewritten in terms of amplitude and phase quadrature operators $\delta\hat{X}^+$ and $\delta\hat{X}^-$, respectively, and by taking the Fourier transform of these quadrature operator equations of motion and using the boundary condition 3.12, we can find the frequency domain quadrature operators for the transmitted field through the OPA cavity as

$$\hat{X}_t^{a\pm} = \frac{2\sqrt{\gamma_{oc}^a \gamma_{ic}^a} \hat{X}_{ic}^{a\pm} + (2\gamma_{oc}^a - i\Omega - \gamma_a \pm g)\delta\hat{X}_{oc}^{a\pm} + 2\sqrt{\gamma_{oc}^a \gamma_l^a} \delta\hat{X}_l^{a\pm} + \Lambda\alpha\hat{X}_{ic}^{b\pm}}{i\Omega + \gamma_a \mp g}, \quad (5.9)$$

where the information whether the OPA works in the amplification or deamplification regime is contained in the nonlinear gain g . Note that the quadrature operators depend not only on the input fields at the fundamental frequency, but also on those at the SH frequency via the term $\Lambda\alpha\hat{X}_{ic}^{b\pm}$. We can see that noise from the pump beam can be coupled to the fundamental field and thus degrade the amount of squeezing generated. In real experiments, we therefore eliminate this coupling by minimizing the amplitude of the intra-cavity fundamental field.

Using equa. 3.9 and assuming that the fields entering the resonator from the environment as a result of losses are in vacuum states, these quadrature operators lead to the field spectra

$$V_t^{a\pm} = 1 + 4\eta_{esc}\eta_{tot} \frac{\pm g/\gamma_a + \gamma_{in}^a/\gamma_a(V_{ic}^{a\pm} - 1) + \frac{\Lambda^2|\alpha|^2}{4\gamma_a\gamma_{oc}^a}V_{ic}^{b\pm}}{\Omega^2/\gamma_a^2 + (1 \mp g/\gamma_a)^2}, \quad (5.10)$$

where $\eta_{esc} = \gamma_{oc}^a/\gamma_a$ is the escape efficiency determining the efficiency with which the squeezing may exit the cavity, and η_{tot} is the overall detection efficiency². Naturally, we require $\gamma_{oc}^a \gg \gamma_{ic} + \gamma_l$. The escape efficiency is then close to 100%. By making γ_{oc}^a large,

²The overall detection efficiency contains the optical loss experienced by the squeezed beam on the way towards the HD, efficiency of the HD in terms of visibility and the efficiency of the detectors itself.

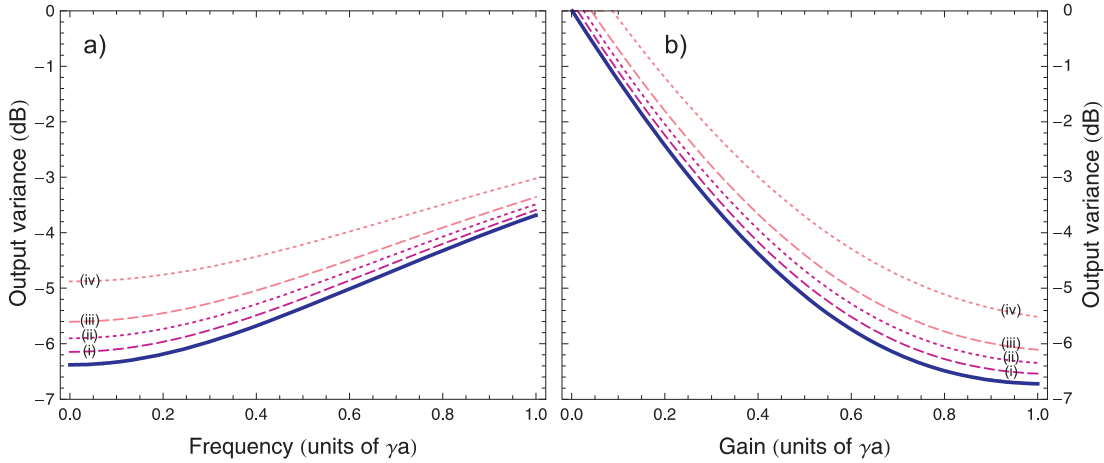


Figure 5.2: Amplitude squeezing (solid line) generated by a back seeded OPA operating in the deamplification regime a) as a function of frequency Ω with nonlinear gain $g = 0.7\gamma_a$; and b) as a function of the nonlinear gain g at detection frequency $\Omega = 0.2\gamma_a$. The effect of the pump field noise is shown for (i) $V_{ic}^{b+} = 10$ and (ii) $V_{ic}^{b+} = 20$; the effect of the seed field noise is for (iii) $V_{ic}^{a+} = 10$ and (iv) $V_{ic}^{a+} = 20$. All calculations were performed for experimental parameters of the bow-tie OPA specified in table 5.1, but assuming here the intra-cavity circulating power of $\hbar\omega_a|\alpha|^2 = 1$ mW.

the total cavity decay rate becomes big and hence the pump power required to generate the nonlinear gain g becomes excessive. There must be trade-off between the output coupler transmission and the pump power needed to create sufficient gain in an OPA. It is therefore more important to minimize intra-cavity losses as much as practically possible. We can see from equa. 5.10 that for coherent input of the fundamental field, i.e. $V_{ic}^{a\pm} = 1$, and assuming vacuum squeezing such as $\alpha = 0$, the best OPA squeezing is obtained at $\Omega = 0$ and just below its OPO threshold, i.e. $g \rightarrow \gamma_a$. The variance is then equal to $V_{t|max}^{a\pm} = 1 - \eta_{esc}$. It is now clear that the losses coming from imperfect coatings of the resonator mirrors and intra-cavity nonlinear crystal together with its absorption have a dramatic effect on the escape efficiency, and thus on the squeezing generated. Note that equa. 5.10 describes the minimum uncertainty state, i.e. $V_t^{a+}V_t^{a-} = 1$, only when $\eta_{esc} = 1$. The uncertainty of the state is further degraded when the squeezed beam experiences loss towards the homodyne detection (HD) system and by a non-perfect HD efficiency. The minimum uncertainty states will play an important role in generating EPR entanglement as will be shown in chapter 7.

As we already detailed, the best squeezing is obtained at frequency $\Omega = 0$. However, observing squeezing at frequencies closed to 0 Hz is practically impossible due to low frequency sources of noise such as acoustic noise, mechanical noise and laser relaxation oscillation noise. Note that this limitation can be overcome by looking at very high frequencies, corresponding to integer multiples of the free spectral range of the OPA cavity, as detailed in chapter 6. Typical frequency spectra of a back-seeded (through the input coupler of reflectivity η_{ic}) OPA cavity are shown in fig. 5.2 a), where we used experimental parameters specified in table 5.1. Here we assume the OPA to be operating in the deamplification regime, so the spectra correspond to the squeezed amplitude quadrature. Reasonable amount of squeezing is still generated at frequencies below the resonator decay rate γ_a .

So far we have assumed an ideal OPA with all input fields being in coherent or vacuum states. We can see from equa. 5.10 that squeezing is also strongly dependant on the variance of the input seed field, i.e. V_{ic}^{a+} in this case, so even though this noise gets deamplified and squeezed in an OPA as well, it still couples an additional noise

Parameters	PPKTP	MgO:LiNbO ₃
Cavity round-trip path length d	275 mm	80 mm
Input coupler transmissivity at fundamental η_{ic}^a	0.0005	0.001
Output coupler transmissivity at fundamental η_{oc}^a	0.1	0.04
Intra-cavity loss at fundamental $1 - \eta_t^a$	0.0095	0.0075
Cavity decay rate γ_a	1.2×10^8	1.8×10^8
Input coupler transmissivity at SH η_{ic}^b	0.95	0.90
Escape efficiency η_{esc}	0.910	0.825
Total detection efficiency for TEM ₀₀ mode	0.865	0.900
Total detection efficiency for TEM ₁₀ mode	0.850	0.875
Nonlinear interaction strength Λ	1100×10^{-4}	2550×10^{-4} 2340×10^{-4}
Intra-cavity power at fundamental $\hbar\omega_a \alpha ^2$	0	1 mW
Focusing parameter ξ	2.56	0.85

Table 5.1: Parameters used for theoretical simulations of the PPKTP and MgO:LiNbO₃ OPAs. The nonlinear interaction strength Λ is given for an OPA operation in the fundamental mode and the two values for MgO:LiNbO₃ correspond respectively to OPA₁ and OPA₂.

into the squeezed field and degrade the overall squeezing. Therefore we require the seed field to be at the QNL to avoid this effect. The variance of the squeezed field is also affected by noise of the pump beam coupled in via the nonlinear interaction. This effect can be, however, minimized by seeding the OPA with a sufficiently low power, so that $|\alpha|^2 \rightarrow 0$, and hence the variance of the pump beam V_{ic}^{b+} is uncoupled from the field spectra. Figs. 5.2 a) and b) show the noise contamination of the squeezed field by the seed and pump fields, respectively, displayed as a function of frequency Ω and the nonlinear gain g . Note that both of the noise sources mentioned are avoided in a bow-tie type OPA producing a squeezed vacuum state, detailed in sec. 5.2.

5.1.3 Squeezing trace

The squeezed states were analyzed throughout this thesis in a HD system, introduced in sec. 3.1.2, except for the measurements of squeezing at very high frequencies, where we employed the self-homodyne detection [47] from technical reasons, see chapter 6. HD provides a phase-sensitive measurement of the squeezed quadratures of the light field, where the quadrature to be analyzed is selected by the phase difference ϕ_{LO} between the signal field and the LO field. By sweeping ϕ_{LO} we thus measure variance $V_t^{a\phi}$, which can be obtained similarly to the OPA field spectra given by equa. 5.10 by performing all the calculations with an arbitrary quadrature operator \hat{X}^ϕ . So for an arbitrary phase, the variance of the transmitted field through the OPA is given by

$$V_t^{a\phi} = V_t^{a+} \cos^2 \phi + V_t^{a-} \sin^2 \phi. \quad (5.11)$$

It is interesting to investigate the behavior of the phase sensitive variance, when changing experimental parameters such as the nonlinear gain and detection efficiency of the HD system. Here we will assume an OPA operating in the deamplification regime, so squeezing will be observed in the amplitude quadrature. Fig. 5.3 shows the calculated

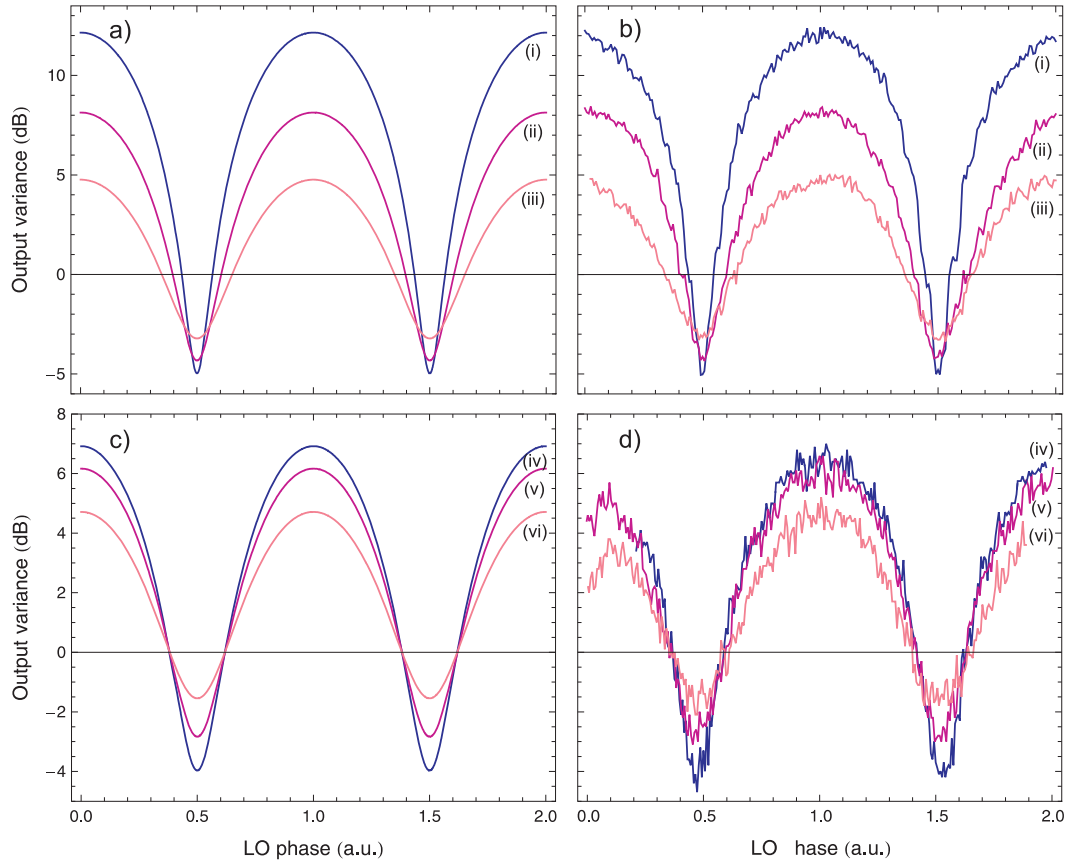


Figure 5.3: Squeezing traces analyzed in a homodyne detector with swept local oscillator phase: a) and b) are the calculated and measured traces, respectively, for the PPKTP OPA for three different values of the nonlinear gain (i) $g = 0.7 \gamma_a$, (ii) $g = 0.52 \gamma_a$, (iii) $g = 0.335 \gamma_a$, at the detection frequency $\Omega/2\pi = 3.8$ MHz; c) and d) are the calculated and measured traces, respectively, for the MgO:LiNbO₃ OPA for three different values of optical attenuation (iv) 0 dB, (v) 1 dB and (vi) 3 dB, at the detection frequency $\Omega/2\pi = 4.3$ MHz and nonlinear gain $g = 0.45 \gamma_a$. Calculations are based on the experimental parameters detailed in table 5.1.

and measured³ squeezing traces under different conditions: a) and b) when changing the nonlinear gain, c) and d) when increasing attenuation of the squeezed beam exiting the OPA, and subsequently analyzed in a HD system. When increasing the nonlinear gain, we can see that the squeezing trace becomes sharper in the squeezed quadrature and more flat in the anti-squeezed quadrature, and we find that as we generate more squeezing, the ratio s_1/s_2 calculated from the zero points of the squeezing trace as shown in inset of fig. 5.4 is a decreasing function of the nonlinear gain. On the other hand, if the squeezed beam is attenuated and analyzed in a HD system, the ratio s_1/s_2 is conserved and only the amount of squeezing and anti-squeezing is changed. This feature can be used for a quick prediction of the measured variance and for estimation of losses in the system, even directly from the screen of a spectrum analyzer. This means that by measuring the ratio s_1/s_2 , which is a measure of how strongly squeezed is the state, one can directly refer to the expected values of the output variance as shown in fig. 5.4.

This technique only works if we can assume that sweeping of the LO phase compared to the phase of the signal field is a linear function of time. However, there

³The gain and attenuation measurements were performed with the PPKTP OPA (sec. 5.2) and the MgO:LiNbO₃ OPA (sec. 7.3), respectively. Parameters used for the calculations are summarized in table 5.1 and correspond to real experimental parameters.

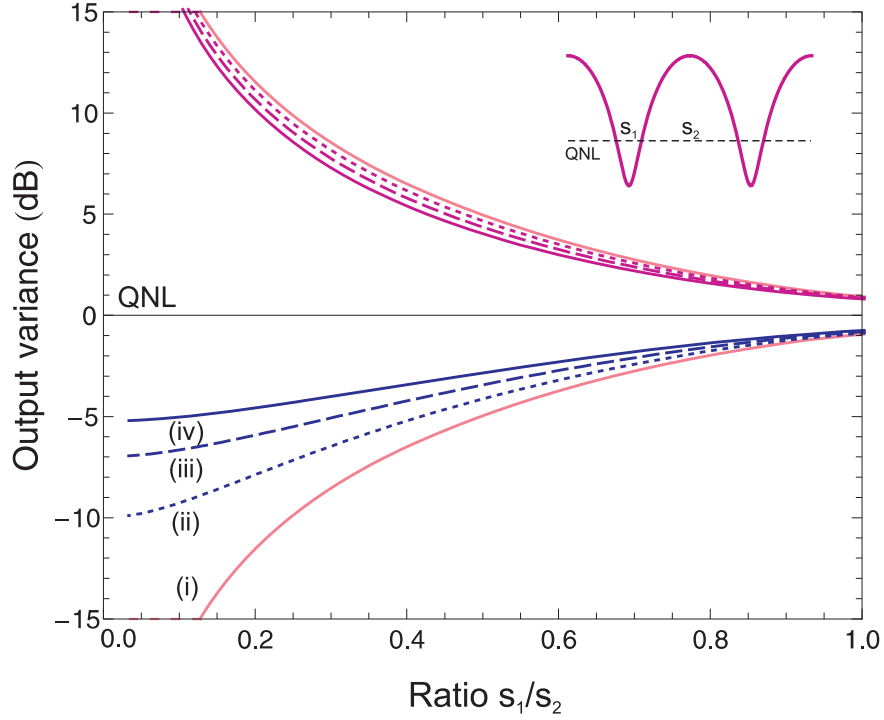


Figure 5.4: Output variance as a function of the ratio s_1/s_2 for (i) perfect squeezing assuming $\eta_{esc}\eta_{tot} = 1$, and the same state analyzed with the detection efficiency (ii) 0.9, (iii) 0.8 and (iv) 0.7.

might be a nonlinear ramp of the PZT actuator, which can cause scaling problems and hence inaccuracy in investigating the ratio s_1/s_2 . This technique also requires all the input fields to be at QNL at the detection frequency, which is often the case in real experiments. The main complication in using this technique might be a phase jitter of the interacting fields if present in the system, which, as will be shown in sec. 5.2.4, will cause shaking the squeezing ellipse faster than the resolution bandwidth of the spectrum analyzer, and hence the measurement of squeezing is averaged with the anti-squeezing noise.

5.2 Generation of squeezed vacuum states

5.2.1 Experimental setup

The experimental setup used to generate squeezed vacuum states is shown in fig. 5.5. The laser source, described in detail in sec. 3.4, is the dual output solid-state monolithic ring-cavity laser based on Nd:YAG laser material with an internal frequency doubler (Diabolo). The fundamental beam exiting the laser is split into two parts, one part is used as a locking beam for the OPA cavity as shown in the schematics, and the other part is first filtered through the mode cleaning cavity (MCC), described in sec. 3.5, and used in the system for alignment purposes and as a LO beam. The function of the MCC is to filter the intensity and frequency noise of the laser above the cavity bandwidth, and to define a high quality spatial mode. The bandwidth of the cavity is 1.8 MHz and the output field is quantum noise limited above 7 MHz, as shown in fig. 3.10. We operated the MCC also as a mode transferring device for generating TEM₁₀ fundamental mode using a flip plate, see sec. 3.6. This method is used if we require the TEM₁₀ operation of the system. The MCC is locked on resonance using the PDH

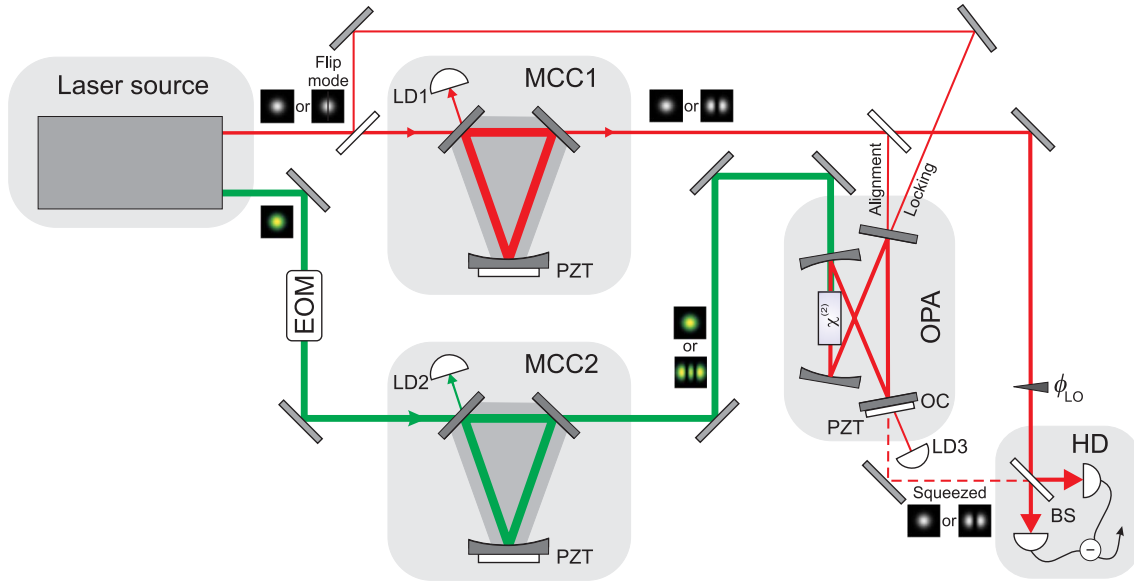


Figure 5.5: Schematics of the experimental setup used to generate vacuum squeezing in the TEM_{00} and TEM_{10} modes utilizing the PPKTP OPA. MCC: mode cleaning (transferring) cavity; OPA: optical parametric amplifier; HD: homodyne detection; EOM: electro-optic modulator; LD: locking detector; PZT: piezo ceramic transducer; OC: output coupler; BS: 50/50 beam splitter.

technique (sec. 3.3.1) by employing the phase modulation frequency of 18.72 MHz and detecting the reflected field from the MCC. The transmission of the cavity for the TEM_{00} and TEM_{10} modes is 95 % and 60 %, respectively. The fundamental field in the desired mode is then used as a LO beam for the HD system and for alignment of the OPA cavity.

OPA cavity

The OPA shown in fig. 5.6 is based on a periodically poled KTP as a nonlinear material. The crystal is placed in a bow-tie cavity resonant for the seed frequency to enhance the nonlinear interaction. The advantage of using PPKTP material is besides its high nonlinearity also a large temperature bandwidth, which ensures the same phase-matching condition for the nonlinear interaction, even if the mode volume inside the crystal heats up due to the absorption of the SH pump field. Therefore it was not necessary to adjust the temperature of the crystal for each new pump power as is usual for e.g. LiNbO_3 material, see sec. 7.4.1. The PPKTP crystal of dimensions $10 \times 2 \times 0.5 \text{ mm}^3$ and the poling period of $\Lambda_{qpm} = 8.958 \text{ }\mu\text{m}$ (Raicol Crystals Ltd.) is housed in a temperature stabilized oven, and its temperature can be controlled within 0.1°C via a Peltier element. Both its surfaces are antireflection coated at the fundamental and SH wavelengths.

The OPA cavity has an optical round trip path length of 275 mm, and is formed by two concave mirrors of radius of curvature 25 mm (high reflecting at fundamental and with transmission 95% for the SH field) and two plane mirrors, from which one is the input coupler of transmission $\eta_{ic} = 0.0005$ and the other one output coupler (OC) of $\eta_{oc} = 0.1$. The cavity forms a beam waist of radius of approximately $19 \text{ }\mu\text{m}$ between the two curved mirrors. This is almost an optimum beam waist for a fundamental mode operation in order to satisfy the Boyd-Kleinman condition, see sec. 4.2.2. The length of the cavity is controlled by a ring PZT actuator with diameter 1/2 inch and of thickness 9 mm, in the same way as the MCC. The PZT is mounted in a specially

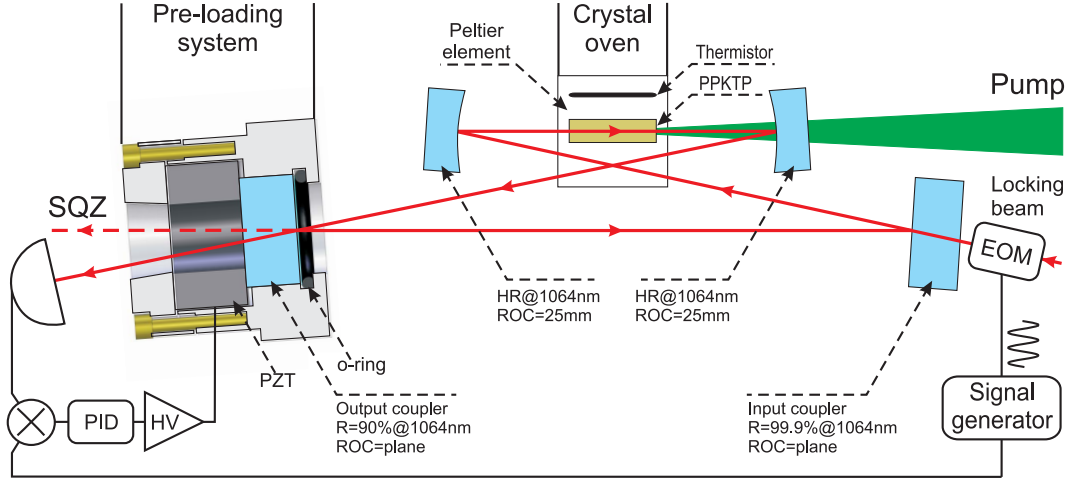


Figure 5.6: Schematics of a bow-tie cavity OPA based on a PPKTP nonlinear material.

designed pre-loaded system together with OC, which is pushed by the PZT against a rubber o-ring. As we already discussed in sec. 3.5 the effect of the pre-loading is simply to increase the spring constant and damping coefficient of the PZT. Careful design of this pre-loaded mount results in rather high resonance frequency of 55 kHz, which increases mechanical stability of the OPA and thus reduce the phase jitter in the system. The whole OPA cavity is built into a solid block of aluminium and enclosed by a plastic cover in order to reduce thermal fluctuations and sound vibrations. The OPA cavity is locked on resonance by detecting the transmitted locking field on detector LD₃ and employing the PDH locking technique. The generated error signal is then fed back to the cavity through a PZT actuator. Here we used the same modulation signal of 18.72 MHz as for MCC as this modulation gets easily transmitted through this rather low finesse cavity ($F = 57$). The frequency bandwidth of the cavity is $\gamma_a/2\pi = 19$ MHz and the free spectral range is 1.1 GHz.

The locking field is actually counter-propagating in the OPA relative to the squeezed beam. This means that this cavity can be locked even without a seed field incident on the input coupler, and in effect we can generate vacuum squeezed states, which was the purpose of this experiment. The power of the locking beam was minimized in order to avoid any contamination of the vacuum squeezed field by the noise on the locking beam, but still keeping the lock robust. By measuring the output power from the OPA, we inferred the intra-cavity power to be less than 1 mW for the locking beam. Assuming AR coating of the PPKTP crystal to reflect 0.2% of incident light on each of its surfaces into the squeezed counter propagating mode, we can consider $|\alpha|^2 \rightarrow 0$. The seed field denoted alignment beam in fig. 5.5 is used to align the pump beam with the OPA intra-cavity mode in order to maximize the nonlinear interaction. For measuring vacuum squeezing, we block this alignment beam, pump the OPA with the SH field, and by sweeping the LO phase we measure the amplitude and phase quadratures of a squeezed state. The spatial profile of the LO beam corresponds to the TEM_{n0} mode of the squeezed beam, so such a HD selectively extracts information from the squeezed beam contained in the TEM_{n0} component.

Green mode cleaning cavity

As we will see in the following it is very important to remove excess noise from the pump field. In particular, the amplitude noise is a source of phase jitter and degrades the measurement of squeezing. For cleaning the pump beam, we implemented a MCC

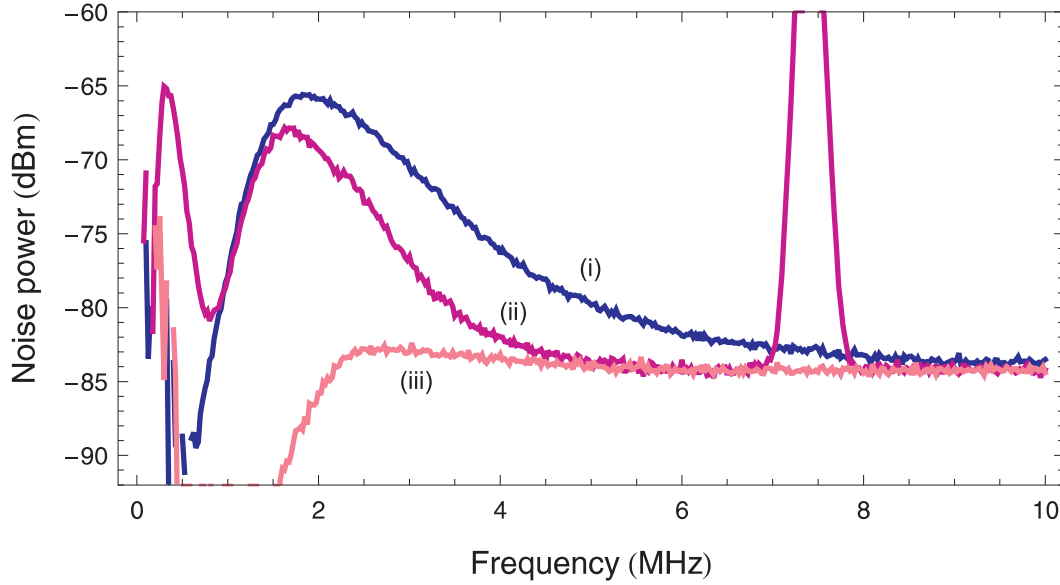


Figure 5.7: Amplitude frequency spectra of a 3.5 mW SH field (i) before and (ii) after transmission through the SH field MCC; trace (iii) is the QNL. The measurements are corrected for the electronic noise which was approximately 8 dB below the QNL. RBW: 300 kHz, VBW: 300 Hz.

cavity into the experiment. This cavity has the same mechanical design as the infrared MCC and we use the same locking technique. There is actually modulation at the frequency of 12 MHz on the pump beam, which comes from the locking modulation of the internal intra-cavity doubler in the laser, but this cannot be used for locking due to huge amplitude modulation. We therefore use an external electro-optic modulator (EOM) to place sidebands at frequency of 19.5 MHz onto the pump beam, and lock the cavity on the reflected field via the PDH technique. The two plane input and output couplers are of reflectivities 99.175%, and together with the curved back HR mirror of the radius of curvature 100 cm form a ring cavity of calculated finesse 368. This corresponds well to the measured value of 325. The cavity linewidth was estimated to be $\delta l = 2$ MHz, and the pump field is at QNL above 5 MHz. The frequency spectra for the SH field before and after filtering by the green MCC are shown in fig. 5.7. The peak at 7.5 MHz is a result of beating of the EOM modulation frequency and the laser internal frequency doubler locking signal.

5.2.2 Regenerative gain

The SH beam exiting the green MCC is carefully mode-matched into the OPA cavity. For the alignment we seeded the locked OPA with the alignment beam as shown in fig. 5.5 and optimized the classical gain of the OPA. Below threshold the seed is either amplified or deamplified depending on the relative phase between the pump and the seed fields. Such a measurement is shown in fig. 5.8, where we measured the regenerative gain of the OPA as a function of pump power at various conditions, i.e. OPA operating at the TEM_{00} or TEM_{10} mode and pumped by the TEM_{00} or TEM_{20} SH mode with optimized phase-matching temperature for the particular higher-order nonlinear interaction [69]. We found that for the best nonlinear interaction, the TEM_{00} pump mode always has to be aligned with the cavity axis and mode-matched into the TEM_{00} fundamental mode. When operating the OPA at higher-order modes, we simply leave the alignment unchanged and switch only the interacting fundamental and/or SH modes, and optimize the phase-matching temperature.

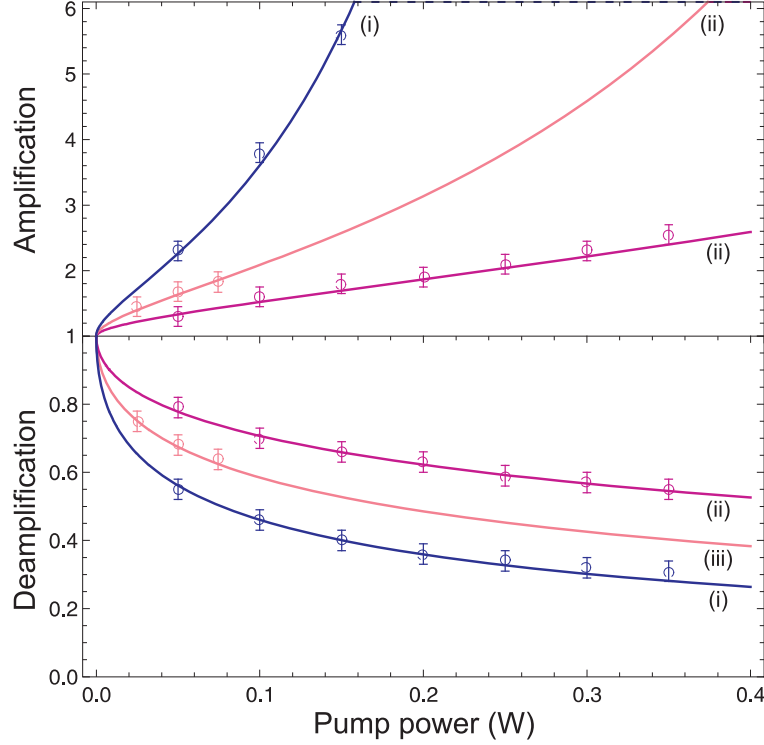


Figure 5.8: Measurements of the regenerative gain (circles) of the PPKTP OPA as a function of pump power and theoretically predicted gain (full lines) for (i) OPA operating at the TEM_{00} mode and pumped by SH field also at the TEM_{00} mode; (ii) and (iii) OPA operating at the TEM_{10} mode and pumped by SH TEM_{00} mode and SH TEM_{20} mode, respectively. The modeled curves are based on the experimental parameters given in table 5.1 and the nonlinear strength Λ is (i) 1100×10^{-4} , (ii) 460×10^{-4} and (iii) 715×10^{-4} .

In the case of $\text{TEM}_{00}^a\text{-TEM}_{00}^b$ interaction, where the superscripts a and b refer to fundamental and SH fields respectively, we obtained maximum amplification of 80 and deamplification of 0.31 at 0.35 W of pump power. This was the maximum pump power available for the experiment. The deamplification of 0.31 indicates that the system is close to the OPO threshold, for which the deamplification is predicted to be 0.25. The measured data were fitted with the parameter $\Lambda_{ppktp}^{00}=1100 \times 10^{-4}$ and the OPO threshold has been estimated to be 0.45 W. This relatively high value results from high decay rate γ_a of the cavity, which is caused by high OC transmission $\eta_{oc}=0.1$. For the $\text{TEM}_{10}^a\text{-TEM}_{00}^b$ operation, we see much lower nonlinear interaction with maximum amplification of 2.55 and deamplification 0.55 again at the pump power of 0.35 W. That is what we expect from theory anyway. Solving equa. 4.12 for the experimental focusing parameter $\xi=2.56$ and decomposing the field into the SH components, we find by optimizing the phase-mismatch the conversion efficiency of the $\text{TEM}_{10}^a\text{-TEM}_{00}^b$ process to be $\eta_{sh}^{10}=18\%$, which results in the interaction strength $\Lambda_{ppktp}^{10}=460 \times 10^{-4}$. This value is used for fitting the data in fig. 5.8, and we find the OPO threshold to be 2.8 W. One can see that this process is pretty inefficient, and we do not expect to observe as high a degree of squeezing as for the $\text{TEM}_{00}^a\text{-TEM}_{00}^b$ interaction.

In order to achieve higher nonlinear gain, we considered also the $\text{TEM}_{10}^a\text{-TEM}_{20}^b$ operation, for which theory predicts up to 50% conversion efficiency under optimized experimental conditions. For our experiment this efficiency was estimated to be $\eta_{sh}^{20}=42\%$, so the measured data were fitted with $\Lambda_{ppktp}^{20}=715 \times 10^{-4}$, and the OPO threshold was estimated to be 1.05 W. We can see from the graph an excellent agreement between the measured data and the predicted nonlinear interaction. The higher nonlinear gain also

predicts squeezing to be stronger than with a TEM_{00} pump mode. For this experiment only 75 mW of pump power at the TEM_{20} mode was available, as the mode was generated by misaligning the incident TEM_{00} beam into the green MCC. This technique results at the most in 25% transmission for this particular mode. In sec. 3.6.2, we proposed an optimized generation of the TEM_{20} mode from the TEM_{00} mode using a specially designed flip plate, which together with proper mode-matching can result in up to 78% efficiency.

5.2.3 TEM_{00} and TEM_{10} squeezing generation

The output fields of the OPA were analyzed in a homodyne detector as described in sec. 3.1.2. Each field was interfered with a bright LO field of the same spatial mode as the analyzed field on a 50/50 beamsplitter (BS). The measured visibilities ν_{vis} were 98.5% and 97.5% for the TEM_{00} and TEM_{10} modes, respectively. The homodyne efficiency for the higher-order modes was always lower than for the case of fundamental modes. This is due to larger spatial extension of the modes, which might be clipping on optical components on the way towards the HD system. Another feature is the additional transverse degree of freedom, which can cause e.g. a rotation of the H-G mode when the beam is not perfectly centered when propagates through a lens. The two BS output fields were detected on a pair of balanced photodiodes with the quantum efficiency $\eta_{det} = 90\%$. The difference of the two resulting photocurrents is analyzed in a spectrum analyzer, and scanning the phase of the LO beam allows the measurement of the amplitude and phase quadratures of the OPA output. Currently an attempt is being made to lock the squeezing quadrature using the quantum noise locking technique [86]. The normalization of the observed variance is done by blocking the OPA output so that only the vacuum fluctuations were detected by HD. Experimental vacuum squeezing traces for the TEM_{00} and TEM_{10} modes are shown in fig. 5.9, where we used 350 mW of SH power in the fundamental mode for pumping the OPA. The phase matching temperatures are for the two modes $T_{pm}^{00} = 27^\circ\text{C}$ and $T_{pm}^{10} = 23.3^\circ\text{C}$, respectively. We observed at the best -5.5 dB of squeezing and +12.0 dB of antisqueezing in the TEM_{00} mode, and -3.1 dB of squeezing and +4.3 dB of antisqueezing in the TEM_{10} mode, after correction for the electronic noise. This is quite far from the minimum uncertainty as predicted from the theory for a lossless OPA system.

Estimating the total detection efficiency $\eta_{tot}^{00} = 0.865$ and $\eta_{tot}^{10} = 0.850$ for the two modes, where $\eta_{tot} = \nu_{vis}^2 \eta_{det} \eta_{opt}$ and assuming $\eta_{opt} = 0.99$, we can infer on the amount of squeezing and antisqueezing just after the OC of the OPA. These are -7.7 dB and +12.6 dB for the TEM_{00} mode and -4.0 dB and +4.8 dB for the TEM_{10} mode. Taking the escape efficiency of the OPA cavity $\eta_{esc} = 0.91$, we find the variances of the state generated inside the OPA being -10.6 dB and +13.0 dB for the TEM_{00} mode and -4.7 dB and +5.1 dB for the TEM_{10} mode. These values are however, not minimum uncertainty and we still require an additional inefficiency of 0.96 somewhere in the OPA system to correct the variances for. This unknown inefficiency could have origin in the escape efficiency η_{esc} , which has been calculated from the listed specifications of the components provided by manufacturers. In the following calculations, we will put this unknown inefficiency on the account of the total detection efficiency η_{tot} .

Figs. 5.10 a) and b) show measurements and theoretically predicted variances of the vacuum squeezed states in the TEM_{00} and TEM_{10} modes, respectively, as a function of pump power. In the case of the TEM_{00} mode, we demonstrate here measurements of vacuum squeezing when pumping the OPA with the SH field before and after filtering in the green MCC. We can see an improvement in squeezing by almost 1 dB just only

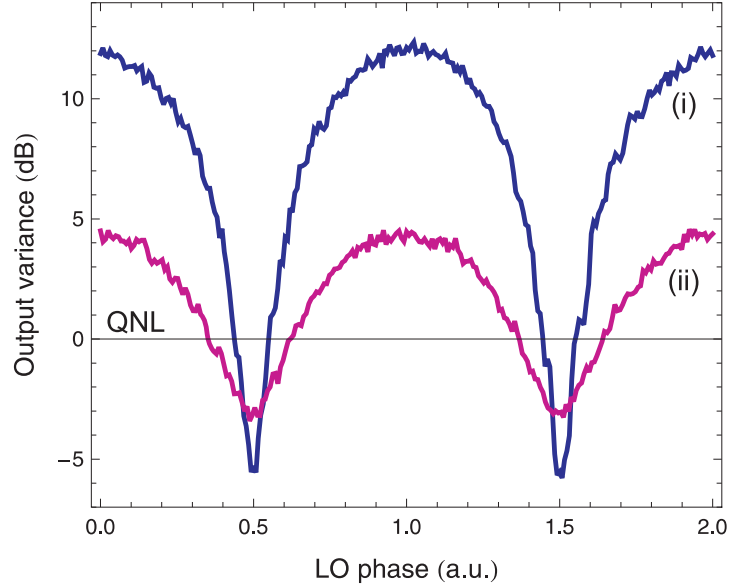


Figure 5.9: Measurements of squeezing traces of (i) TEM_{00} and (ii) TEM_{10} modes, when pumped by 350 mW of SH power in the TEM_{00} mode. The measurements are corrected for electronic noise, which was 14 dBm below the QNL. Detection frequency: 4 MHz; RBW: 300 kHz; VBW: 300 Hz; sweep time: 2 s.

by cleaning the pump field from an excess noise⁴. Both measurements were performed at the same phase-matching temperature and under the same pumping conditions, i.e. we obtained the same regenerative gain for the two measurements. The data points (i) show the measurements of the output variance, when we pump the OPA with the SH field delivered directly from the laser. By increasing the pump power, we generate states of higher degree of squeezing as we expect from theory. However, at a certain pump power, in this case at around 250 mW, squeezing clamps and with further increase of pump power the amount of squeezing even slightly decreases and we do not see any improvement anymore, even though antisqueezing still raises. By implementing into the setup the green MCC, we can see a significant improvement in squeezing by almost 1 dB, and the amount of squeezing still increases with increasing pump power, see data points (ii). Antisqueezing data points follow the measurements generated with the noisy pump thought, which indicates that we truly operate the system with the same regenerative gain. These measurements were fitted with the experimental parameters given in table 5.1, and with the interaction strength $\Lambda_{ppkt}^{00} = 1100 \times 10^{-4}$ used to fit the regenerative gain measurements, see the trace (iii). However, we can see a disagreement between the theoretically predicted curve and the measured data, which is especially significant for antisqueezing results. By introducing into the model any additional unknown loss, which was modeled even as a function of pump power, there is no way one can explain such squeezing and antisqueezing evolution. Based on these results, one can exclude from the model the green induced infrared absorption (GRIIRA) [87], which is a common feature for LiNbO_3 nonlinear material, whereby can cause degradation of squeezing generation.

The measurements suggest that for higher pump powers, the nonlinear strength is not as big as we would conclude from the measurements of regenerative gain. By fitting each data point (ii) only via the nonlinear strength Λ , and assuming all the other parameters including loss to be unchanged, we found Λ to be a decreasing function of

⁴The amplitude noise of the pump field before and after filtering in the green MCC is shown in fig. 5.7.

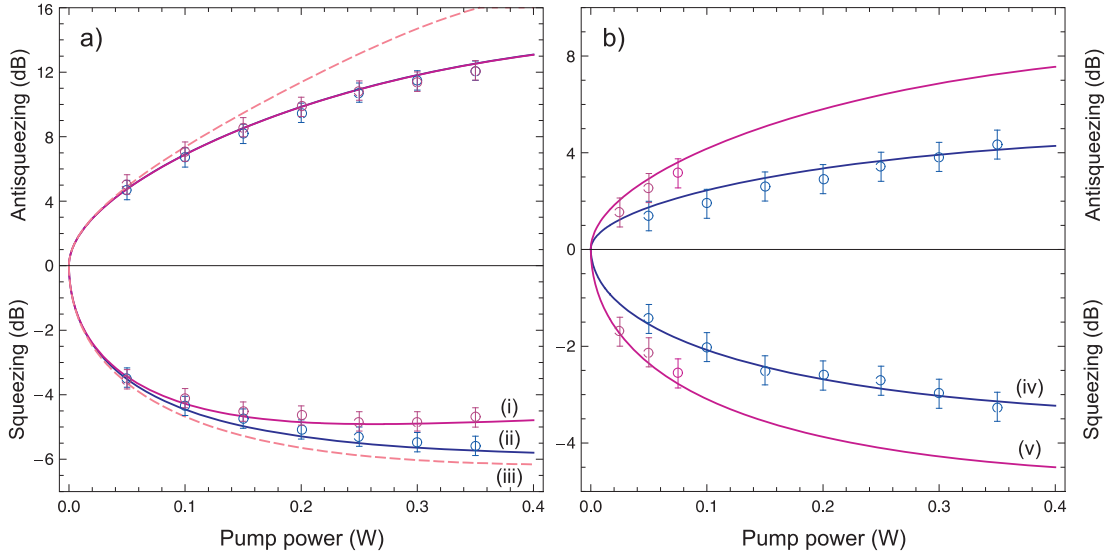


Figure 5.10: Measurements (circles) and theoretically predicted variances (full lines) of the vacuum squeezed states generated by the PPKTP OPA as a function of pump power. a) shows TEM₀₀ squeezing for the OPA pumped with the SH field delivered directly from the laser, trace (i), and pumped with SH field filtered in the MCC, trace (ii). Here we consider the decrease of the squeezing nonlinear strength with increasing pump power. This is to be compared with a predicted variance, which would result from the fundamental theory, trace (iii). b) shows TEM₁₀ squeezing for the OPA pumped by a filtered SH field being in (iv) TEM₀₀ mode and (v) TEM₂₀ mode.

pump power, i.e. for our experiment $\Lambda_{sqz}^{00} = \Lambda_{ppktp}^{00} (1 - 0.5 \times P_{sh})$. Here the pump power P_{sh} is in units of W. By assuming such a squeezing nonlinear strength, the measurements with filtered pump were easily fitted both in squeezing and antisqueezing as shown by trace (ii). Recall that the nonlinear strength for the regenerative gain is still of value $\Lambda_{ppktp}^{00} = 1100 \times 10^{-4}$, used to fit the gain measurements shown in fig. 5.8. This is really a weird result. Note that both the gain and squeezing measurements were taken at the same phase-matching temperatures and in parallel during one experimental run, so we can exclude from arguments an alignment drift or mode matching issues. This feature has to be further investigated.

Going back to the measurements taken with the noisy pump (just directly delivered by the laser), we introduced into the model the effect of pump excess noise, which is the only different parameter between the two squeezing experiments. However, direct coupling of the pump noise into the squeezed field via the nonlinear interaction cannot be considered in the case of vacuum squeezing, as the coupling is interposed via the fundamental intra-cavity field $|\alpha|^2$, which in our experiment is negligible as detailed in sec. 5.2.1. Hence we can see that the pump excess noise has on vacuum squeezing generation more technical inside, and basically introduce into the system a phase jitter. If the phase jitter, i.e. variations in the relative phase of LO and the squeezed beam, is faster than the time required for the spectrum analyzer to gather a single pixel of information, then that point will not be exact measurement of the noise at quadrature phase angle ϕ , but rather measurement of noise averaged over some range of angles $\phi \pm \delta\phi$. In effect, the observed amount of squeezing is reduced and this is due to averaging the squeezed quadrature noise measurement with the noise contained in the antisqueezed quadrature. Introducing such an effect into the model, where we generate 100 random angles $\delta\phi$ in the range $|\delta\phi| < \delta\phi_{max}$, and averaging these results, we can easily fit the measured data points (i) with $\delta\phi_{max} = 6^\circ$, as shown in fig. 5.10 a). From here it is evident that the excess noise of the pump field plays an important role

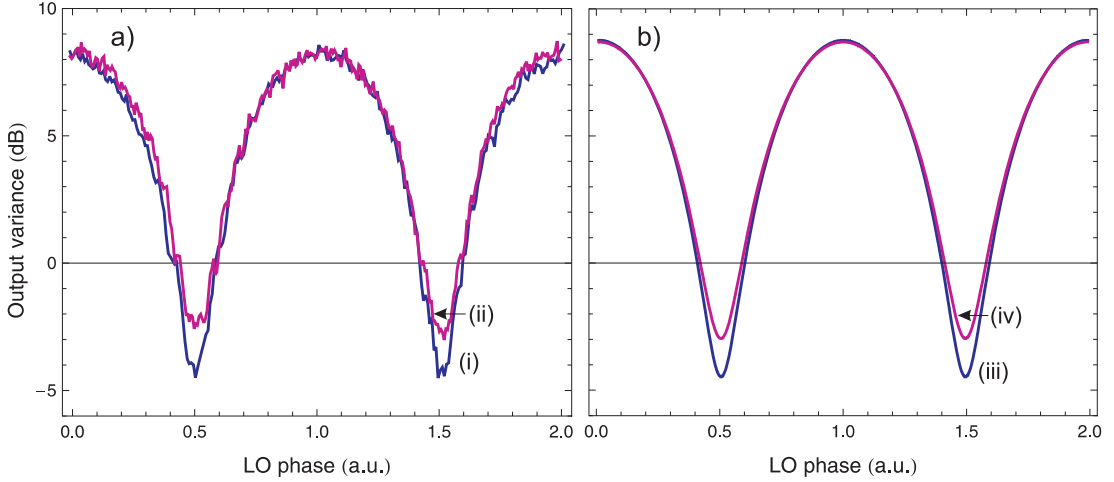


Figure 5.11: Degradation of squeezing by an excess amplitude noise of the pump field. a) measurements of squeezing traces for the case of no excess noise (i) and when placing 6 dB of the amplitude noise onto the pump field (ii), in reference to the spectra shown in fig. 5.7. b) theoretically predicted traces assuming no excess noise (iii) and considering the phase jitter model with $\delta\phi_{max} = 15^\circ$ (iv).

in squeezing generation, and comes as a technical limiting factor, which will be more significant in generating bright squeezing. Further study of the influence of the pump noise on squeezing generation follows in the next section.

The measurements of TEM_{10} squeezing are shown in fig. 5.10 b). These were performed with a pump field filtered in the green MCC, and are shown for pump being in (iv) TEM_{00} mode and (v) TEM_{20} mode. In the later case, by using 75 mW of power, we observed -2.6 dB of squeezing at the TEM_{10} mode. This justifies that using pump of the TEM_{20} spatial profile is a very promising pumping scheme. In this case the nonlinear process can be up to 50% efficient when compared to the nonlinear interaction of fundamental modes. Both measurements were fitted again using the same parameters as in the case of TEM_{00} squeezing except of the squeezing nonlinear strength Λ_{sqz} , and assuming no presence of the phase jitter in the system. Taking again the same nonlinear efficiencies as for the gain measurements, we can define the squeezing nonlinear strengths for the two processes to be $\Lambda_{sqz}^{n0} = \sqrt{\eta_{sh}^{n0}} \Lambda_{sqz}^{00}$, and using these coefficients in the theoretical model, we find again a very good agreement between the measured data and the modeled variances. The trace (v) shows a very promising improvement towards an efficient TEM_{10} squeezing generation. We expect to generate more than -4 dB of squeezing when pumped by 0.3 W of power being in the TEM_{20} mode. This is the limit of the current setup assuming maximum 78% efficiency for optimized TEM_{00} to TEM_{20} conversion in a MCC, see sec. 3.6.2.

5.2.4 Influence of the pump noise on squeezing generation

In order to have more understanding about the influence of the amplitude and phase pump noise on squeezing generation, we inserted into the filtered pump beam an electro-optic modulator (EOM), which we used to place an excess broad-band noise onto the pump beam. We operated both the OPA and the pump field in TEM_{00} modes and pumped the OPA with 150 mW of SH pump power. Squeezing was observed at 6 MHz detection frequency, where the pump beam is at QNL. We found that by introducing a phase noise onto the pump beam (of power up to 6 dB in reference to the QNL of the pump spectra shown in fig. 5.7), there is no change in squeezing generation. Then

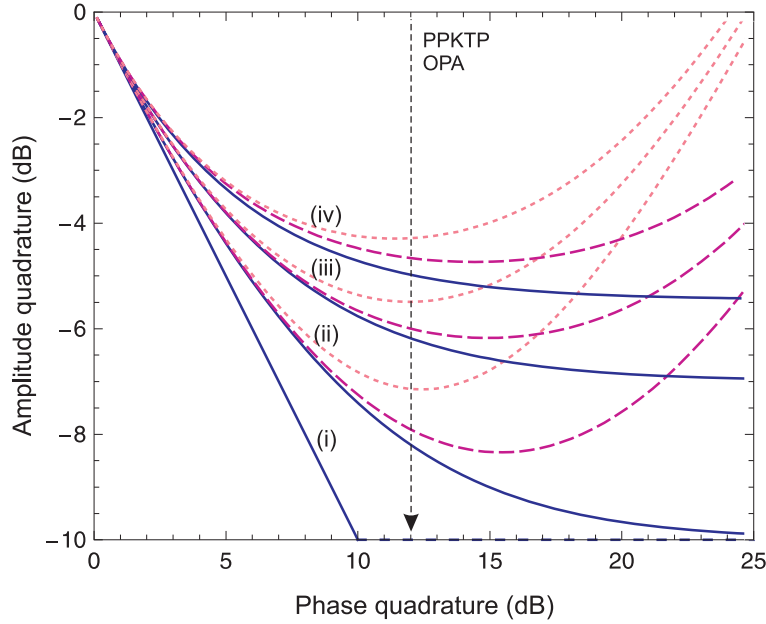


Figure 5.12: Predicted measured squeezing (amplitude quadrature) as a function of antisqueezing (phase quadrature) for an ideal system, trace (i), and for a system of overall efficiency (ii) $\eta_{esc}\eta_{tot} = 0.9$, (iii) $\eta_{esc}\eta_{tot} = 0.8$ and (iv) $\eta_{esc}\eta_{tot} = 0.7$, and for the case of no phase jitter (solid lines), phase jitter of maximum angle variance $\delta\phi_{max} = 2.5^\circ$ (dashed lines) and phase jitter of $\delta\phi_{max} = 5^\circ$ (dotted lines).

we switched the EOM into an amplitude modulator using a quarter wave-plate and a polarizing BS, as detailed in sec. 2.3.1. By introducing an amplitude broad-band noise onto the pump field, we can see a clear degradation of squeezing as shown in fig. 5.11 a). The squeezing trace (i) is the pure measurement of the variance with no excess noise on the pump beam. However, by increasing the amplitude noise of the pump field by 6 dB, we can see a clear decrease in squeezing by almost 2 dB, see the trace (ii). Using the phase jitter model detailed above, we can obtain such an effect for $\delta\phi_{max} = 15^\circ$, as shown in fig. 5.11 b). This is a relatively high value of the phase jitter, but has been used only because of relatively low degree of squeezing of the vacuum state used to demonstrate this effect experimentally.

The phase angle resolution becomes more and more acute with larger squeezing. This can be seen in fig. 5.12, showing the predicted measured squeezing (amplitude quadrature) as a function of antisqueezing (phase quadrature). For a real lossy system, the observed squeezing is an increasing function of antisqueezing (or rather an increasing function of the nonlinear gain), but at a certain gain the squeezing clamps and keeps almost constant with a further increase of antisqueezing. If we consider a phase jitter in the system, squeezing and antisqueezing increases with increasing nonlinear gain, but on the other hand increasingly larger amounts of noise are coupled into the measurement of the squeezed variance. This in effect decreases the amount of observed squeezing. The effect is more significant for states of higher degrees of squeezing and puts a limit on the amount of squeezing observed. We can see that the phase jitter can cause even decrease of the observed squeezing after reaching an optimal squeezing value, which is given by experimental parameters such as the loss and the OPA gain. Such a behavior has been seen experimentally as detailed in sec. 5.2.3. Current status of our PPKTP experiment can be approximately represented by the solid line (iii), as the overall efficiency of the system is $\eta_{esc}\eta_{tot} = 0.78$. We can see that it is mainly the efficiency of the used detectors with $\eta_{det} = 0.90$ and the intra-cavity loss $\eta_l = 0.0095$, which limits us from reaching -7 dB to -8 dB of squeezing.

5.2.5 Optimizing the output coupler transmission

For demonstration of spatial entanglement, which is the topic of chapter 7, and for experiments within quantum imaging in general, we require nonclassical states of light with high degree of squeezing in the TEM_{10} mode. As we could see in the previous section, the best squeezing achievable in this mode is with our current setup -3.1 dB. An important engineering task is to design a correct OPA output coupler of transmission η_{oc} , as this can significantly improve generation of the squeezed states. This has to be designed for a particular interaction strength Λ , to ensure a high enhancement of the nonlinear interaction and the same time high escape efficiency of the OPA cavity.

We used for optimizing η_{oc} the complete model of the OPA with parameters given in table 5.1, including the effect of decreasing the squeezing nonlinear strength with pump power, as detailed in sec. 5.2.3. We also considered all the input fields including the SH pump to be at QNL. We assume here an optimized focusing parameter ξ for the two cases of pumping the OPA operating in the TEM_{10} mode, with pump field being in the TEM_{00} mode and the TEM_{20} mode, see sec. 4.2.4. Recall that these pumping schemes result respectively in conversion efficiencies of $\eta_{sh}^{00} = 22\%$ and $\eta_{sh}^{20} = 50\%$, when normalized to the best conversion efficiency for the fundamental mode interaction. In this model, we assume also a limitation of the pump power available for the experiment in either TEM_{00} or TEM_{20} mode.

Figs. 5.13 a) and b) show the squeezed variance in the TEM_{10} mode as a function of the output coupler transmission, considering the pump field being in the TEM_{00} mode and the TEM_{20} mode, respectively. We expect to observe in the current setup the highest degree of squeezing in the TEM_{10} mode by utilizing an OC with $\eta_{oc} = 0.05$ in the case of the TEM_{00} pump, and with $\eta_{oc} = 0.065$ in the case of the TEM_{20} pump. Here we considered the SH field of 0.3 W optical power in the desired mode. This results in a predicted achievable squeezing of -4.4 dB and -5.2 dB for the two pump modes, respectively. As can be seen, our setup with $\eta_{oc} = 0.1$ is almost perfectly optimized for the fundamental mode interaction, using 0.3 W of pump power.

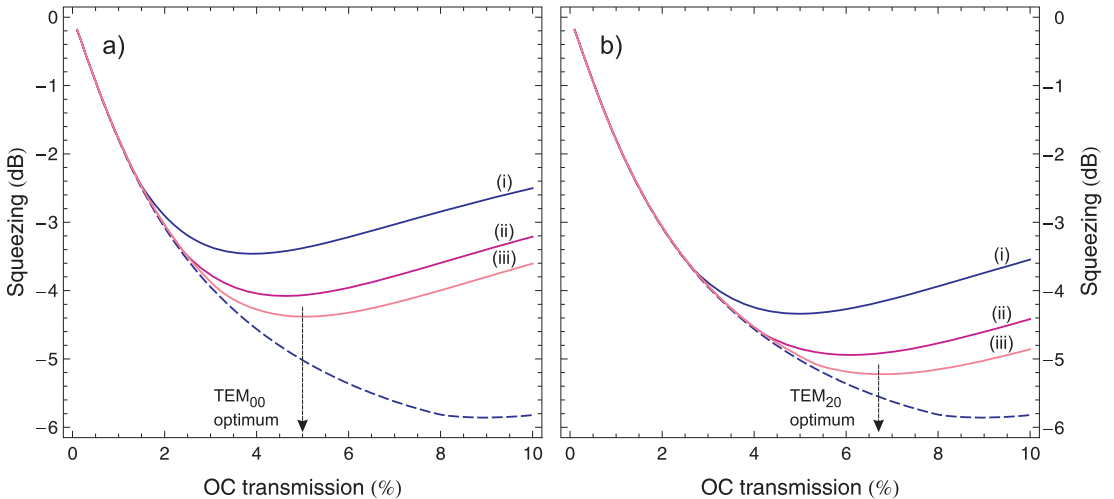


Figure 5.13: Optimization of the squeezed variance in the TEM_{10} mode in terms of the output coupler transmission, considering the pump field being in a) TEM_{00} mode and b) TEM_{20} mode. We assume here a limitation of the pump power available for the experiment in either TEM_{00} or TEM_{20} mode, represented by curve (i) for 0.1 W, (ii) for 0.2 W and (iii) for 0.3 W of optical power. The dashed line shows TEM_{00} squeezing to be almost perfectly optimized for 0.3 W of TEM_{00} pump power, using the output coupler of $\eta_{oc} = 0.1$.

5.3 Summary

In summary, we demonstrated the generation of vacuum squeezed light in the TEM_{00} and TEM_{10} modes utilizing a bow-tie OPA, based on a PPKTP nonlinear material. We measured the level of squeezing of the best -5.5 dB in the TEM_{00} mode and -3.1 dB in the TEM_{10} spatial mode, after correction for the electronic noise. The reported results were measured by scanning the local oscillator phase, and we make an attempt for locking the vacuum squeezed quadrature. We found that a broad-band excess amplitude noise present on the pump field has a strong influence on the squeezing production. By implementing a mode cleaning cavity into the system, in order to filter the broad-band high-frequency amplitude noise of the pump field, we significantly enhanced the squeezing generation. As the pump noise is not directly coupled with the vacuum squeezed field due to its zero intra-cavity coherent amplitude, we conclude that the pump amplitude noise has on production of squeezing, in general, more technical inside, and basically introduces into the system phase jitter. This effect gets more significant with higher degrees of squeezing. On the other hand, production of the vacuum squeezed light is robust against the pump phase noise.

We tested a new pumping scheme for an OPA operating in the TEM_{10} mode, and this involves a pump field of the TEM_{20} spatial profile. As expected from theory, this scheme promises higher nonlinear efficiency than in the case of the TEM_{00} pump, and for an optimized focusing parameter can be up to 50% efficient, when compared to the nonlinear interaction of fundamental modes. Using 75 mW of the TEM_{20} pump power, we observed -2.6 dB of squeezing in the TEM_{10} mode. We expect to generate more than -4 dB of vacuum squeezing in the current setup when pumping by 0.3 W of power, which is a limit of the laser assuming maximum 78% efficiency for transferring the TEM_{00} pump mode into the TEM_{20} mode in an optical cavity. Moreover, by optimizing the output coupler transmission, we could achieve up to -5.2 dB of noise suppression in the TEM_{10} mode. These results are very important when designing a new generation of OPAs operating in higher-order modes. We will use a pair of OPAs operating in the TEM_{10} spatial mode for demonstrating position-momentum entanglement, detailed in chapter 7.

Chapter 6

High-frequency squeezing

This work has been published in Optics Express, vol. 15, no. 9, pp. 5310 (2007)

Observation of a comb of optical squeezing over many gigahertz of bandwidth

R.J. Senior¹, G.N. Milford², J. Janousek¹, A.E. Dunlop², K. Wagner¹,
H-A. Bachor¹, T.C. Ralph³, E.H. Huntington², and C.C. Harb²

¹*Centre for Quantum-Atom Optics, Faculty of Science, The Australian National University,
Canberra, ACT, 0200 Australia*

²*Centre for Quantum Computer Technology, School of Information Technology and Electrical
Engineering, University College, The University of New South Wales, Canberra, ACT, 2600*

³*Centre for Quantum Computer Technology, Department of Physics, The University of Queensland,
St Lucia QLD 4072 Australia*

Abstract: We experimentally demonstrate the generation of optical squeezing at multiple longitudinal modes and transverse Hermite-Gauss modes of an optical parametric amplifier. We present measurements of approximately 3 dB squeezing at baseband, 1.7 GHz, 3.4 GHz and 5.1 GHz which correspond to the first, second and third resonances of the amplifier. We show that both the magnitude and the bandwidth of the squeezing at the higher longitudinal modes is greater than can be observed at baseband. The squeezing observed is the highest frequency squeezing reported to date.

Introduction

There have been numerous proposals for future technologies based on the unique properties of isolated quantum systems. These include quantum key distribution [88, 89], ultra-high precision sensing [90, 91] and even quantum computers [92]. In real applications the functional specifications that emerge are low noise, high bandwidth and the ability to encode information into multiple degrees of freedom. Since quantum optics promises to meet these specifications, it is seen as a strong contender as the platform for a number of these quantum technologies. Key resources required by quantum optical systems are non-classical states of light, which are commonly generated via non-linear optical processes. One such process is parametric down conversion (PDC), in which

a high energy pump photon is converted into two lower energy photons, via a second order nonlinear interaction [34]. PDC is the underlying nonlinear process in optical parametric amplifiers (OPA), devices that are widely used in quantum optics experiments as sources of entangled photon pairs in discrete variable systems [93] and as sources of squeezing in continuous variable systems [3]. Entangled photon pairs exhibit stronger than classical correlations, and squeezed light exhibits noise fluctuations that are smaller than the quantum noise limit (QNL).

Cavity enhancement of PDC, which has been widely used to increase the strength of the nonlinear process, leads to spectral filtering of the down converted output. Multi-mode behavior in cavity enhanced PDC has been observed in the discrete variable domain [94] and cavity enhancement has been identified in continuous variables since the early work of Wu *et. al.* [3]. Recent theoretical predictions have suggested that squeezed states should exist at all higher-order longitudinal and transverse modes of a sub-threshold OPA [95]. However until recently it was not possible to observe squeezing at the higher-order longitudinal modes due to the limited bandwidth of sub-shot noise limited photodetectors. Advances in engineering design techniques for microwave photo-receivers have removed this limitation [96].

In this paper we report the first observation of squeezing spectra in four longitudinal cavity modes: baseband; 1.7 GHz; 3.4 GHz; and 5.1 GHz; and simultaneously two transverse modes: the TEM₀₀ and TEM₁₀ modes. Squeezing of microwaves has been observed in the very high frequency (VHF) band [97], however to the authors' knowledge we report here the widest optical squeezing bandwidth.

Experimental Setup

Squeezed light is produced using an OPA operating below threshold, see fig. 6.1. The OPA is pumped with 532 nm light from a frequency-doubled diode-pumped Nd:YAG laser operating at 1064 nm. The OPA crystal has dimensions $2 \times 2.5 \times 6.5$ mm³ and is made from bulk LiNbO₃ which is 7% doped with MgO and phase-matched at 60°C. The OPA cavity is linear and is formed by the rear surface of the crystal (radius of curvature = 8 mm, high reflector at 532 nm, R=99.9% at 1064 nm) and an external mirror (radius of curvature = 75 mm, R=13% at 532 nm and R=96% at 1064 nm). The front surface of the crystal has a radius of curvature of 8 mm and is anti-reflection coated at both 1064 nm and 532 nm. The optical path length (OPL) of the OPA cavity is approximately 90 mm giving an FSR of 1.7 GHz.

The OPA is seeded with either a TEM₀₀ or TEM₁₀ mode at 1064 nm, with oscillation threshold at 200 mW and 350 mW pump power respectively. The system is operated as a deamplifier with gains of 0.3 and 0.45 for the TEM₀₀ and TEM₁₀ modes respectively. Due to the fact that the system is operating in deamplification mode lower gain values produce greater deamplification. When operated as a squeezer, the OPA is seeded with 5 mW incident on the greater than 99.9% reflecting surface.

The spatial mode of the seed and the local oscillator determine which spatial mode of the squeezed beam will be observed and is controlled by a mode transfer cavity (MTC) (see fig. 6.1). The MTC can couple energy from the TEM₀₀ spatial mode of the incoming beam to higher-order modes resonant in the cavity by misaligning the input beam. The output of the MTC is used to seed the OPA from the rear surface and as the local oscillator in subsequent measurements. The squeezed light was detected on a single detector after being interfered with a strong local oscillator on a 90/10 beam splitter, resulting in 90% of the squeezed light and 10% of the local oscillator light reaching the detector. The local oscillator power after the 90/10 beam splitter was

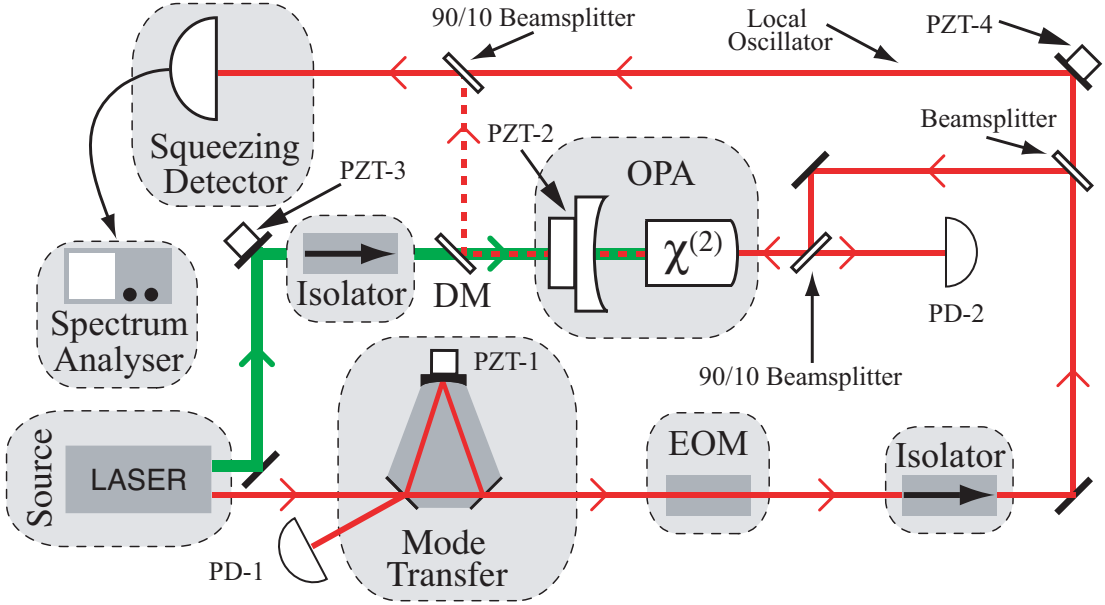


Figure 6.1: Schematic of the experimental setup. Photodetector PD-1 detects the 12 MHz phase modulated signal emitted by the laser and generates an error signal which is sent to a mirror on a piezo-electric transducer PZT-1 to lock the mode transfer cavity (MTC). The electro-optic modulator (EOM) is used to impose 1 MHz and 16 MHz phase modulated signals on the transmitted MTC beam. These two signals are detected on PD-2 which then is used to derive error signals that are sent to PZT-2 and PZT-3 to lock the OPA cavity to the seed and to lock the OPA to de-amplification. The Pound-Drever-Hall locking technique [49] is used in all the locking loops. The local oscillator (LO) phase is swept using PZT-4 with respect to the phase of the squeezing to observe the amplitude and phase quadratures.

7 mW for TEM_{00} , and 4.2 mW for TEM_{10} . The quantum noise level calibration was achieved by direct measurement of the local oscillator at the appropriate photocurrent.

This is a non-standard way to perform the measurements. There are two disadvantages to using this technique, the first being that the observable squeezing is reduced by the 10% lost at the beam splitter and the second being that the noise floor of the measurement is set by the noise of the local oscillator. The latter is of no consequence here because the local oscillator is shot noise limited at microwave frequencies. Although this technique reduces the observed squeezing, the advantage is that it does not require a pair of balanced detectors and broadband subtracting circuitry as needed for homodyne detection. Improved levels of observed squeezing are expected with the future use of a balanced homodyne arrangement. Balanced receivers with appropriate bandwidth are available commercially for the telecommunications market, however the sensitivity is not yet appropriate for the detection of squeezing.

Two different detectors were used to make the measurements. For baseband measurements, photodetectors have been developed in-house using lumped element design methods with readily available photodiodes and electronic components [98]. In particular, the baseband squeezing measurements were taken using a 500 μm diameter InGaAs photodiode with quantum efficiency of more than 95% using an AD829 amplifier in transimpedance mode. This detector had greater than 10 dB clearance between electronic noise and quantum noise from DC and 30 MHz. Note that the locking detectors for both the MTC and the OPA were of a lumped element design using 1 mm InGaAs photodiodes and LMH6624 amplifiers in transimpedance mode.

Higher bandwidth photodetectors require consideration of transmission-line effects that otherwise limit the utility of the lumped-element approach at microwave frequencies [99]. In [96] we describe such a photodetector that consists of a reverse-biased *pin* InGaAs photodiode, a microwave bandwidth amplifier and an inter-connecting matching network. This matching network achieves a broad-band power match between the AC shot noise power developed by the photodiode and the amplifier's 50 Ω input impedance. The photodetector is constructed as a microstrip circuit allowing close integration of the photodiode and associated bias circuitry, microstrip matching network and amplifier components (Mini-Circuits ERA MMIC [100]). Careful management of technical noise sources and circuit layout achieved a quantum efficiency of more than 92% and approximately 3 dB separation between electronic noise and quantum noise from 1.5 GHz to approximately 6 GHz, see [96] for more details.

Theory

A brief summary of the theoretical predictions for the outputs of the OPA is provided in this section, more details may be found in references [101, 95]. Of interest here are the variances of the output amplitude and phase quadrature fluctuations normalized to the QNL as a function of Fourier frequency. The variance in the amplitude quadrature is denoted $V_{out}^+(\Omega)$, and the variance in the phase quadrature is denoted $V_{out}^-(\Omega)$ where Ω is the Fourier frequency, i.e. the difference frequency between the optical carrier and the sidebands. The output variances are

$$V_{out}^{\pm}(\Omega) = \left| \frac{(\gamma \pm \chi)^2 - \left(\frac{1-e^{i\Omega\tau}}{\tau}\right)^2}{\left(\gamma - \frac{1-e^{i\Omega\tau}}{\tau}\right)^2 - \chi^2} \right|^2 V_{in}^{\pm}(\Omega), \quad (6.1)$$

where the cavity decay rate is $\gamma = \eta_{oc}/\tau$ and it is assumed to be set only by the transmission η_{oc} of the output coupling mirror and the cavity round trip time τ . The nonlinear frequency conversion rate is χ and the down conversion bandwidth of the crystal is taken to be large compared to the Fourier frequencies of interest. The nonlinear frequency conversion rate is $\chi = 2\beta_{in}\chi^{(2)}$ where $\chi^{(2)}$ is the second-order coefficient of nonlinearity for the nonlinear material and β_{in} is the amplitude of the pump field (assumed to be real without loss of generality). Equa. 6.1 describes the frequency and phase dependent amplification (amplitude quadrature variance) or deamplification (phase quadrature variance) of the noise of the seed. Minima in the squeezing spectrum are separated in frequency by the cavity free-spectral range (FSR) and occur at Fourier frequencies of $\Omega = m\Omega_{FSR} = 2\pi m/\tau$ for $m = 0, 1, 2, \dots$ within the downconversion bandwidth. Note that the resonance at $m = 0$ is the baseband squeezing spectrum. The downconversion bandwidth in a bulk nonlinear material of length L is estimated to be $10c/nL$ (c is the speed of light in vacuum, n is the refractive index of the material) [102]. Therefore, we estimate an upper bound of $m \approx 60$ for the crystals described herein.

The theory as it stands does not account for losses, which are modeled by a single beam splitter placed after the OPA output using the standard beam splitter equation [67]. The total loss in the system comprises terms due to:

- 1 intra-cavity loss of the OPA plus escape efficiency of output coupling, $(23 \pm 3)\%$;
- 2 optical losses between the OPA and the detection beam splitter, $(6 \pm 1)\%$;
- 3 the quantum efficiency of the photodetector, worst case $(8 \pm 2)\%$;

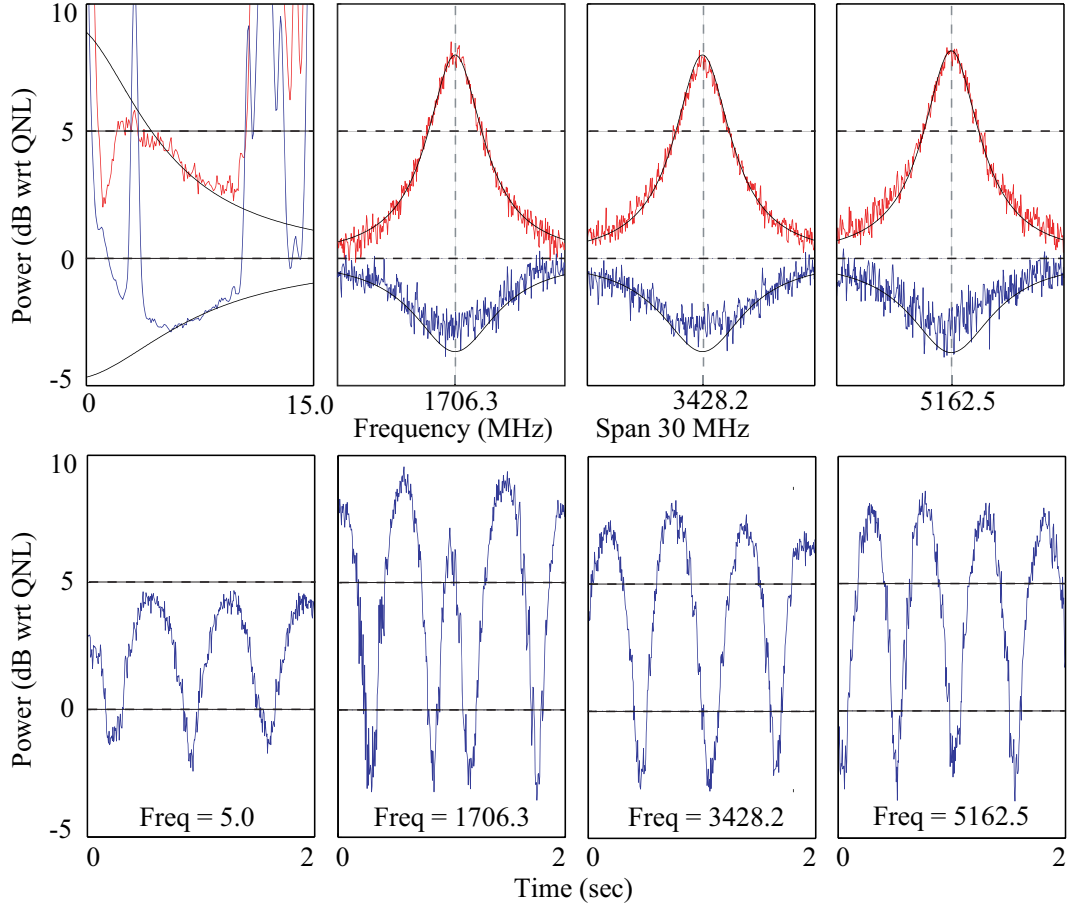


Figure 6.2: TEM₀₀ mode power spectrum of squeezing, normalized to the quantum noise limit. Upper traces show frequency measurements and theoretical predictions over a 15 MHz span at baseband, and 30 MHz span at the first, second and third FSRs; lower traces show zero span spectra as a function of sweeping the LO phase over a 2 second period. Zero span measurements are shown relative to the quantum noise level for the amplitude quadrature. The measurement resolution bandwidth is 1 MHz and video bandwidth is 1 kHz for the high frequency results. Note that the baseband results show excess technical noise due to the imposed locking modulation signals.

4 non-ideal overlap of the local oscillator with the squeezed beam, $(7 \pm 2)\%$; and

5 loss of squeezing at the 90/10 detection beam splitter, $(10 \pm 0.1)\%$.

The estimates indicated for each form of loss lead to a lower bound on the total system loss of $(54 \pm 4)\%$.

Experimental Results

Figs. 6.2 and 6.3 show measurements of squeezing at baseband as well as the first, second and third FSRs of the OPA for both TEM₀₀ and TEM₁₀. On average the observed TEM₀₀ squeezing at baseband is approximately 2.5 dB and 3 dB at the higher resonances. Similarly, the observed TEM₁₀ squeezing at baseband is approximately 2 dB and 2.5 dB at the higher resonances. Note that the shape of the squeezing is dictated by the linewidth of the cavity and thus the profile of squeezing at higher FSRs is symmetric and the bandwidth is twice that of the baseband spectrum.

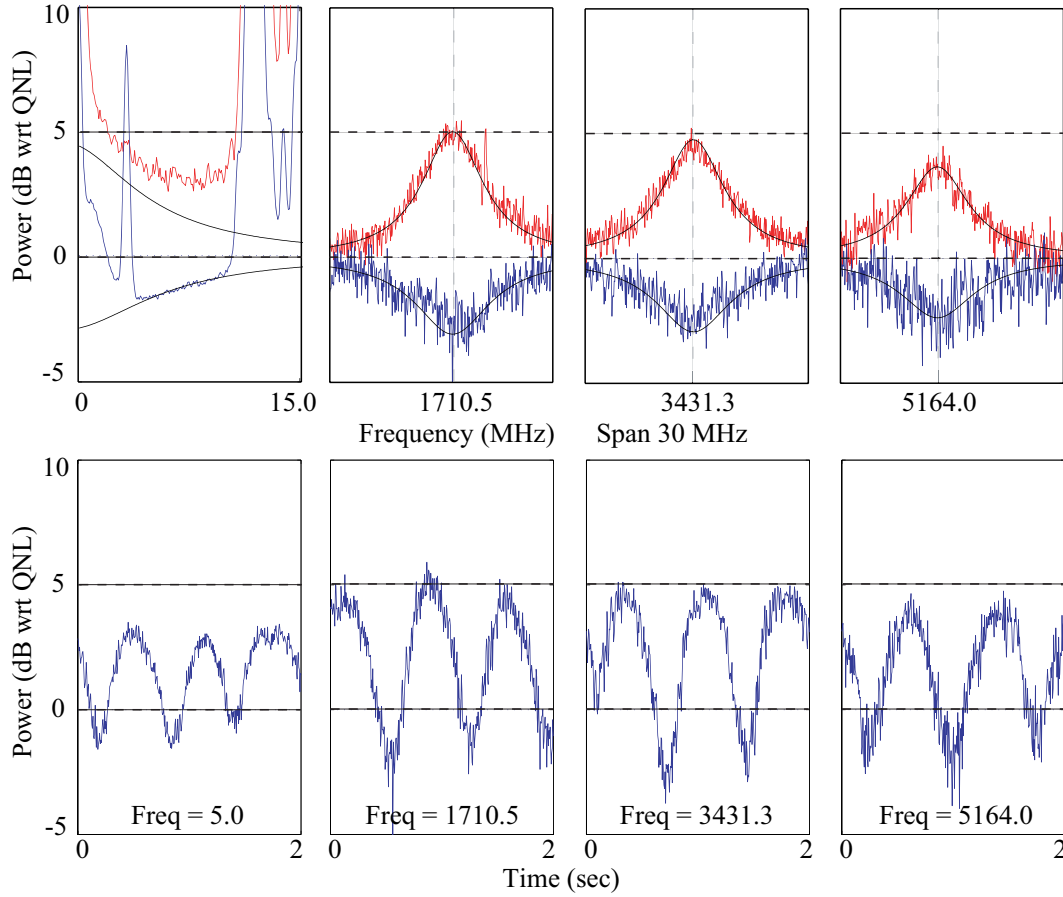


Figure 6.3: TEM_{10} mode power spectrum of squeezing, normalized to the quantum noise limit. Upper traces show frequency measurements and theoretical predictions over a 15 MHz span at baseband, and 30 MHz span at the first, second and third FSRs; lower traces show zero span spectra as a function of sweeping the LO phase over a 2 second period. Zero span measurements are shown relative to the quantum noise level for the amplitude quadrature. The measurement resolution bandwidth is 1 MHz and video bandwidth is 1 kHz for the high frequency results. Note that the baseband results show excess technical noise due to the imposed locking modulation signals.

Overlaid on the upper traces of these figures are theoretical predictions of the output spectra of the OPA cavity assuming that the seed is quantum noise limited in both quadratures and at all frequencies. The theory curves were fitted to the measured results using: τ , which determines the frequency at which maximum squeezing is observed; χ , which determines the magnitude of squeezing; γ , which determines the width of the squeezing spectrum; and the total losses in the experiment, which determine the degree to which the squeezing is degraded and the anti-squeezing is attenuated. Table 6.1 shows the parameters used for each simulation.

Intuitively, one would expect that the magnitude of the squeezing should be identical at all resonances. This intuition arises from the expectation that deamplification should be identical at each cavity resonance, which is indeed observed experimentally. However the input noise at baseband is very different to the input noise at higher frequencies and hence the output noise at baseband, which is simply deamplified input noise, is very different to the output noise at higher frequencies. At low frequencies, laser noise and technical noise from the locking loops are dominant and act to corrupt the baseband squeezing. The large oscillations observed in the spectrum of the baseband measurements are from laser noise that is present from the modulations used to

Spatial Mode	Frequency	τ (GHz ⁻¹)	χ/γ	Losses
TEM ₀₀	Baseband	0.5	0.32	47 %
	1st FSR	0.586	0.32	57 %
	2nd FSR	0.58337	0.32	57 %
	3rd FSR	0.58111	0.325	57 %
TEM ₁₀	Baseband	0.55	0.17	45 %
	1st FSR	0.5844	0.2	50 %
	2nd FSR	0.58295	0.19	50 %
	3rd FSR	0.58117	0.15	50 %

Table 6.1: Parameters used to fit the theoretical simulations to the measured high frequency squeezing results.

lock the seed light to the OPA cavity. The modulations occur at the imposed modulation frequencies as well as the intermodulation beat frequencies.

By contrast, the seed at the higher longitudinal modes is free of technical noise that is often present at baseband. It therefore follows that the squeezing is expected to be of the same magnitude at all higher resonances and stronger at higher resonances than at baseband. This is consistent with the observations and reinforced by noting the strong agreement between measurement and theory based on a QNL seed at higher resonances and the strong disagreement at baseband. Note that the presence of the seed field produce a squeezed output that is bright in comparison to the vacuum, where as the squeezing at the higher free spectral ranges is not contaminated by the seed light and is truly a squeezed vacuum.

It is observed that there is less squeezing for the TEM₁₀ mode than observed for the TEM₀₀. This is because the OPA is pumped with the second harmonic of the seed beam at 532 nm in the TEM₀₀ spatial mode. This pumping scheme is optimal when generating a TEM₀₀ squeezed beam but results in reduced squeezing in comparison to TEM₁₀. This effect is described in detail in Lassen *et. al.* [69] and accounted for in equa. 6.1 by a reduction in the value of χ .

An interesting feature of our spectra is that the minima for the TEM₀₀ (1706.3 MHz, 3428.2 MHz and 5162.5 MHz) and TEM₁₀ (1710.5 MHz, 3431.3 MHz and 5164.0 MHz) modes do not occur at the same frequencies, nor are successive minima separated by the same frequency spacing. The frequency of the first minimum of the TEM₀₀ mode implies that the OPL of the OPA cavity is 87.7 mm compared to 87.9 mm inferred from the first minimum of the TEM₁₀ mode. Each of the subsequent minima in the squeezing for the TEM₀₀ mode imply that the OPL of the cavity successively shortens by 300 μ m. Differences in the inferred OPL are not insignificant compared to the total OPL of the cavity. This effect requires further investigation.

Baseband squeezing has been observed at very low frequencies at the cost of considerable technical effort [71, 103], leading to the potential to observe very low frequency signals with a squeezed noise floor. However, squeezing produced at higher FSR's can be observed without the requirement of eliminating very low frequency technical noise.

Acknowledgments - This work was supported by the Australian Research Council Centre of Excellence scheme.

Conclusion

In conclusion, we have shown the only reported measurement of squeezed light at microwave sideband frequencies. Such optical states might be used to produce 'multiplexed entanglement' for quantum communications applications. Moreover we have observed squeezing in higher-order transverse modes, which provides additional degrees of freedom for the quantum systems.

Part III

Spatial entanglement

Chapter 7

Theory and experimental realization of spatial entanglement

Contents

7.1	Entangled states	83
7.1.1	Continuous variable entanglement	83
7.1.2	Inseparability criterion	85
7.1.3	EPR paradox criterion	86
7.2	Displacement and tilt	87
7.2.1	Classical description	87
7.2.2	Quantum operators	89
7.2.3	Heisenberg inequality relation	90
7.2.4	Spatial entanglement	90
7.3	Experimental setup	92
7.3.1	The squeezing sources	95
7.3.2	Generation of position and momentum squeezed states	97
7.3.3	Generation and detection of entangled states	100
7.4	Experimental results	101
7.4.1	Regenerative gain and squeezing	101
7.4.2	Measurements of the position-squeezed states	104
7.4.3	Measurements of entanglement	105
7.4.4	Characterization of the entangled states	107
7.4.5	Summary	111

Quantum optics also allows production of the so-called entangled beams or EPR-beams. Entangled beams give us the opportunity to investigate fundamental quantum properties of twin light beams, such as non-locality and entanglement. These quantum properties are presently seen as fundamental to future technological applications such as quantum communication and quantum computing. The output of two squeezed laser beams, operating on the same mode, can be combined to produce pairs of entangled modes. This is well established for the Gaussian beam and has been used in many applications, such as dense coding [104, 105] and teleportation [106]. We can now extend this to spatial systems, where the entangled properties are, for example, displacement

and tilt, and hence position and momentum, of a bright laser beam. Such an experiment would verify the original concept of position-momentum entanglement proposed by Einstein, Podolsky and Rosen [28], referred here to spatial entanglement.

First we focus on the basic theory of quadrature entanglement of optical fields in the continuous variable regime and its production. In real experiments we need some method by which we can characterize the strength of entanglement. We adopted two commonly used methods to characterize the strength of entanglement, the inseparability criterion and the EPR paradox criterion. Both criteria considered here have strong physical significance and are described in the following. We introduce basic optical operations related to physical parameters of a Gaussian beam - displacement and tilt, and the quantum operators to which they are linked are introduced - position and momentum operators. The understanding of these parameters at the quantum level allows us to measure them with an increased accuracy even below the quantum noise limit. The fact that position and momentum observables of a TEM₀₀ beam do not commute allows the generation of EPR states, i.e. states entangled in position and momentum, even in the continuous variable regime. The concept of spatial entanglement is introduced.

Then we detail the experimental setup used to generate a pair of spatially entangled beams. The concept is based on the position-squeezed beams, which are generated by a lossless combination of an amplitude-squeezed TEM₁₀ beam with a coherent TEM₀₀ carrier beam in a mode combiner. The bright carrier beam makes a reference in the system for position and momentum. Spatial entanglement can be then generated by interfering such a multi-mode spatially squeezed field on a 50/50 beamsplitter with another amplitude-squeezed TEM₁₀ beam, which in effect creates a pair of spatially entangled beams. Finally, the experimental results are presented showing strong correlations between the two fields in the frequency range 3.2 – 4.2 MHz. These results show the first demonstration of entanglement between position and momentum of a bright optical beam in the continuous variable regime as originally considered by Einstein, Podolsky and Rosen. This system has a potential to demonstrate quantum imaging protocols such as spatial teleportation and dense coding as well.

This work has been published in:

- *Experimental realization of spatial entanglement for bright optical beams*
J. Janousek, V. Delaubert, K. Wagner, H. Zou, C.C. Harb, P.K. Lam, and H.-A. Bachor
- Oral presentation, AQIS 2007, Kyoto, Japan
- Oral presentation IF2-2-TUE, CLEO/IQEC 2007, Munich, Germany
- Poster WC0654, AIP 2006, Brisbane, Australia
- *Tools for spatial multi-mode quantum information: modulation, detection and quantum correlations*
M. Lassen, V. Delaubert, J. Janousek, K. Wagner, H.-A. Bachor, P.K. Lam, N. Treps, P. Buchhave, C. Fabre, and C.C. Harb
Phys. Rev. Lett. 98, 083602 (2007)
- *Entangling the spatial properties of laser beams*
J. Janousek, K. Wagner, V. Delaubert, H. Zou, C.C. Harb, N. Treps, P.K. Lam, and H.-A. Bachor
To be submitted to Nature Physics (2008)

7.1 Entangled states

Entanglement is certainly the most intriguing feature of quantum mechanics. Its theoretical as well as experimental implications are at the core of all quantum information protocols. The concept of entanglement was first introduced by Einstein, Podolsky, and Rosen in 1935 [28]. They used this concept to propose that either quantum mechanics was incomplete or local realism was false. They demonstrated that an apparent violation of the Heisenberg inequality could be achieved between the position and momentum observables of a pair of particles. This apparent violation has since been termed the EPR paradox. Demonstration of the EPR paradox relies on quantum correlations between a pair of non-commuting observables, so that measurement of either observable in subsystem x allows the inference of that variable in subsystem y to better than the quantum noise limit (QNL).

Recently, entanglement has been shown to be an enabling technology in quantum information protocols such as quantum teleportation [106], dense coding [104, 105] and quantum computation [107], which has stimulated further investigation into its properties. In the following we will focus first on the quadrature entanglement of optical fields in the continuous variable regime [73, 108], which has been extensively investigated since the first experiment of optical entanglement by Ou. et al. in 1992, involving a non-degenerate OPA [74]. The signature of quadrature entanglement is strong correlations and anticorrelations between the two entangled beams in both the amplitude and phase quadratures.

Note that theoretically any pair of conjugate observables can be used to generate entangled beams. Quadrature entanglement has already been extended to polarization entanglement in the continuous variable regime using the feature that the Stokes parameters accounting for the polarization states do not commute [109, 110]. We will also extend this notion to entanglement of position and momentum (x - p) for bright optical beams which was originally considered by Einstein, Podolsky, and Rosen; position-momentum entanglement, or rather, *spatial entanglement* will be introduced and experimentally demonstrated in sec. 7.2.4.

7.1.1 Continuous variable entanglement

The generation of optical quadrature entanglement can be obtained directly out of a nonlinear device such as an OPO [111, 112], or by a combination of two quadrature squeezed beams with orthogonal squeezing on a 50/50 beamsplitter (BS) [74, 76, 108, 113, 114]. The latter technique requires two amplitude or phase squeezed beams to be interfered in-quadrature in the BS plane, or alternatively an amplitude squeezed beam and a phase squeezed beam to be combined in-phase in the BS plane. A simple scheme for the generation of quadrature entanglement is shown in fig. 7.1.

The two input fields denoted with the indexes 1 and 2 are incident on the BS, and their amplitude and phase quadratures are described respectively by X_i^+ and X_i^- , $i = 1, 2$. We adopted in this thesis the generation of quadrature entanglement by interfering two amplitude squeezed beams on the BS in-quadrature, i.e. $\Delta^2 \hat{X}_1^+ < 1$ and $\Delta^2 \hat{X}_2^+ < 1$ with $\phi_{ent} = \pi/2$ being their relative phase shift, and this will be assumed in the following mathematical definitions. The coherent amplitudes of the two states are $\alpha_1 = \langle \hat{X}_1/2 \rangle$ and $\alpha_2 = \langle \hat{X}_2/2 \rangle$, and we assume their intensities to be equal. The frequency domain amplitude and phase quadratures of the output beams x and y can be expressed as [38]

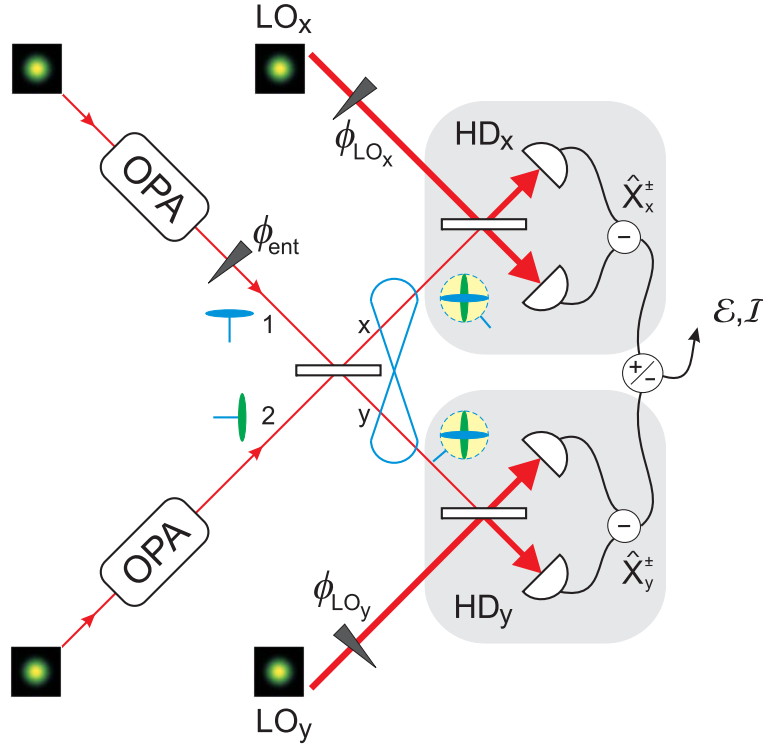


Figure 7.1: Schematics of the quadrature entanglement experiment. Two amplitude squeezed beams are combined on a 50/50 BS in quadrature, i.e. $\phi_{ent} = \pi/2$. Properties of each of the entangled beams x and y are analyzed by HD with LO fields being in the same transverse mode as the analyzed fields. The detected signals yield either the degree of EPR paradox \mathcal{E} or the degree of inseparability \mathcal{I} , used to characterize the entangled state.

$$\hat{X}_x^\pm = \frac{1}{2}(\pm \hat{X}_1^+ + \hat{X}_2^+ + \hat{X}_1^- \mp \hat{X}_2^-), \quad (7.1)$$

$$\hat{X}_y^\pm = \frac{1}{2}(\hat{X}_1^+ \pm \hat{X}_2^+ \mp \hat{X}_1^- + \hat{X}_2^-). \quad (7.2)$$

In the limit of perfect squeezing of the two beams, i.e. $\Delta^2 \hat{X}_1^+ \rightarrow 0$ and $\Delta^2 \hat{X}_2^+ \rightarrow 0$, the variances of the sum of amplitude fluctuations and the difference of phase fluctuations between both beams approach zero, which means that an amplitude quadrature measurement on beam x would provide an exact prediction of the amplitude quadrature of beam y , and vice versa. However, both variables cannot be measured simultaneously. This is a demonstration of the EPR paradox in exactly the manner proposed in the seminal paper of Einstein *et al.* [28]. Representation of ideal EPR states is shown in fig. 7.2 a). Observation of either quadrature on an entangled beam shows a noisy state, but a comparison of the two entangled beams shows correlations in the phase quadrature, i.e. $\delta \hat{X}_x^- = \delta \hat{X}_y^-$, and anti-correlations in the amplitude quadrature, i.e. $\delta \hat{X}_x^+ = -\delta \hat{X}_y^+$, as shown respectively in figs. 7.2 b) and c). Analysis of entanglement in the physically realistic regime, where we deal with finite squeezing, is however more complex, and will be investigated in the following.

In real experiments, we need a tool to characterize the strength of entanglement. Discrete variable entanglement can be fully characterized by a density matrix of finite dimension (usually 4×4). In contrast, complete characterization of continuous variable entanglement would require a density matrix of infinite size. Moreover the density matrix does not immediately provide a measure of whether beams x and y are entangled,

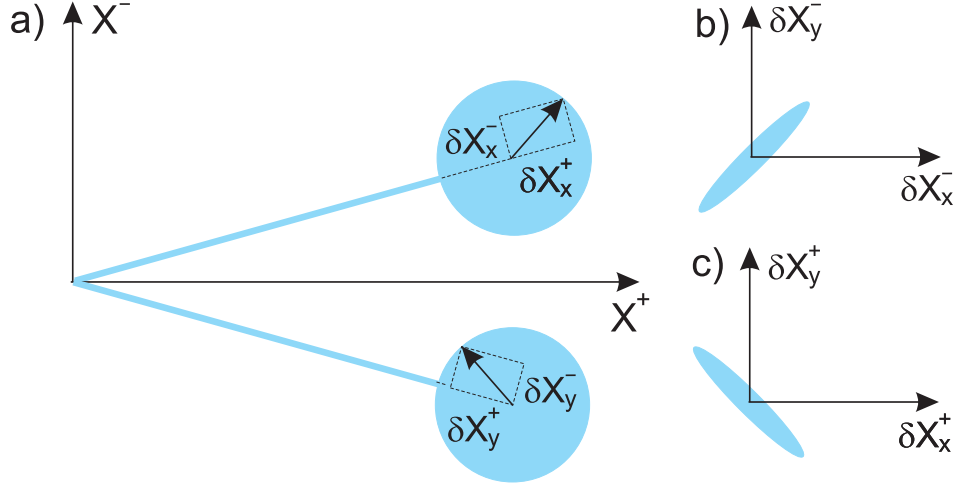


Figure 7.2: a) Representation of ideal EPR states in Fresnel plane with b) phase quadratures being correlated with the other part of the entangled state, whereas c) the fluctuations on their amplitude quadratures are anti-correlated.

or how strongly they are entangled. However, for states with Gaussian statistics, well defined characterization techniques do exist. For characterizing the entangled states in our experiments we utilized two criteria commonly used in the entanglement community: the inseparability criterion proposed by Duan *et al.* [115] and the EPR paradox criterion proposed by Reid and Drummond [116]. Both criteria considered here have strong physical significance, as they have a straightforward dependence on the strength of the quantum resources used to generate entanglement, and are commonly used to gauge the strength of entanglement in experiments. We therefore refer to both criteria as measures of the strength of entanglement.

7.1.2 Inseparability criterion

The inseparability criterion quantifies entanglement of a quantum state. To provide a direct measure of the strength of entanglement we define here the degree of inseparability, which for the case of two amplitude squeezed beams combined on a 50/50 BS is given by [38]

$$\mathcal{I} = \sqrt{\Delta^2 \hat{X}_{x\pm y}^+ \Delta^2 \hat{X}_{x\pm y}^-}, \quad (7.3)$$

where $\Delta^2 \hat{O}_{x\pm y}$ is the minimum of the variance of the sum or difference of the operator \hat{O} between beams x and y normalized to the two beam quantum noise limit, i.e. $\Delta^2 \hat{O}_{x\pm y} = \min\langle(\delta\hat{O}_x \pm \delta\hat{O}_y)^2\rangle/2$. The inseparability criterion $\mathcal{I} = 1$ corresponds to the situation of two incident coherent beams. If $\mathcal{I} < 1$, two incident beams are said inseparable. Note that the best possible entanglement is obtained for two perfectly squeezed beams for which $\mathcal{I} = 0$.

It is interesting to focus on the effect of decoherence in the form of optical loss on the inseparability criteria. For entanglement generated from a pair of uncorrelated squeezed beams, with equal optical loss for beams x and y , the inseparability criterion \mathcal{I} can be expressed as a function of the overall detection efficiency η_{tot} as [38]

$$\mathcal{I} = \eta_{tot} \Delta^2 \hat{X}^+ + (1 - \eta_{tot}), \quad (7.4)$$

where $\Delta^2 \hat{X}^+$ refers to the amplitude quadrature noise variance of both input beams 1 and 2 assuming they are equally squeezed, i.e. $\Delta^2 \hat{X}_1^+ = \Delta^2 \hat{X}_2^+$. Equa. 7.4 shows

that as long as the two beams used to generate entanglement are squeezed, whatever this level is and even when η_{tot} approaches zero, \mathcal{I} remains below unity meaning that the output beams are always entangled according to this criterion. Entanglement is then robust against losses at least in the sense that loss alone cannot transform an inseparable state into a separable one. These results are compared with the EPR paradox criterion in fig. 7.3.

7.1.3 EPR paradox criterion

This criterion quantifies the degree of EPR paradox of a state, which is slightly more restrictive than the general concept of entanglement or inseparability. It is derived from the ability of a state to produce an apparent violation of Heisenberg inequalities between two conjugate variables, similarly to what Einstein, Podolsky, and Rosen showed in 1935 between the position and momentum observables of a pair of particles [28]. This apparent violation has since been termed the EPR paradox. It relies on the fact that measurement of either observable in subsystem x allows the inference of that variable in subsystem y to better than the QNL, even if the two beams are far apart from each other. Between the amplitude and phase quadratures of a pair of optical beams this is quantified by the product of conditional variances [116], and the degree of EPR paradox \mathcal{E} is then defined as

$$\mathcal{E} = \Delta^2 \hat{X}_{x|y}^+ \Delta^2 \hat{X}_{x|y}^-, \quad (7.5)$$

where the EPR paradox is demonstrated for $\mathcal{E} < 1$. The quadrature conditional variances $\Delta^2 \hat{X}_{x|y}^\pm$ are given by

$$\Delta^2 \hat{X}_{x|y}^\pm = \Delta^2 \hat{X}_x^\pm - \frac{|\langle \delta \hat{X}_x^\pm \delta \hat{X}_y^\pm \rangle|^2}{\Delta^2 \hat{X}_y^\pm}, \quad (7.6)$$

where the product $\langle \delta \hat{X}_x^\pm \delta \hat{X}_y^\pm \rangle$ can be quantified from measurements of the amplitude and phase variances of the individual entangled beams and the measurements of the amplitude and phase quadrature sum and difference variances as

$$\langle \delta \hat{X}_x^\pm \delta \hat{X}_y^\pm \rangle = \pm \Delta^2 \hat{X}_{x\pm y}^\pm \mp \frac{1}{2} (\Delta^2 \hat{X}_x^\pm + \Delta^2 \hat{X}_y^\pm). \quad (7.7)$$

Assuming identical noise properties for the two beams incident on the entanglement BS, i.e. $\Delta^2 \hat{X}_1^+ = \Delta^2 \hat{X}_2^+ = \Delta^2 \hat{X}^+$ and $\Delta^2 \hat{X}_1^- = \Delta^2 \hat{X}_2^- = \Delta^2 \hat{X}^-$, and assuming an identical detection efficiency η_{tot} for the two beams, the effect of optical loss on the degree of EPR paradox is given by [25]

$$\mathcal{E} = 4 \left(1 - \eta_{tot} + \frac{2\eta_{tot} - 1 + \eta_{tot}^2 (\Delta^2 \hat{X}^+ + \Delta^2 \hat{X}^- - 1)}{\eta_{tot} (\Delta^2 \hat{X}^+ + \Delta^2 \hat{X}^- - 2) + 2} \right)^2. \quad (7.8)$$

The degree of EPR paradox is thus directly related to optical losses, to the amount of squeezing, and also to the minimum uncertainty of the input states, as we will emphasize later on. Dependence of the degree of inseparability \mathcal{I} and the degree of EPR paradox \mathcal{E} on the total detection efficiency η_{tot} is shown in fig. 7.3, where we compare the two criteria in terms of squeezing and minimum uncertainty of the input states. In the case of minimum uncertainty input states for which $\Delta^2 \hat{X}^+ + \Delta^2 \hat{X}^- = 1$, see fig. 7.3 a), the degree of EPR paradox is $\mathcal{E} = 1$ when $\eta_{tot} = 0.5$ independently of the level of squeezing. This defines a boundary such that if $\eta_{tot} > 0.5$, the EPR paradox criterion is satisfied for any level of squeezing, and if $\eta_{tot} < 0.5$, it can never be

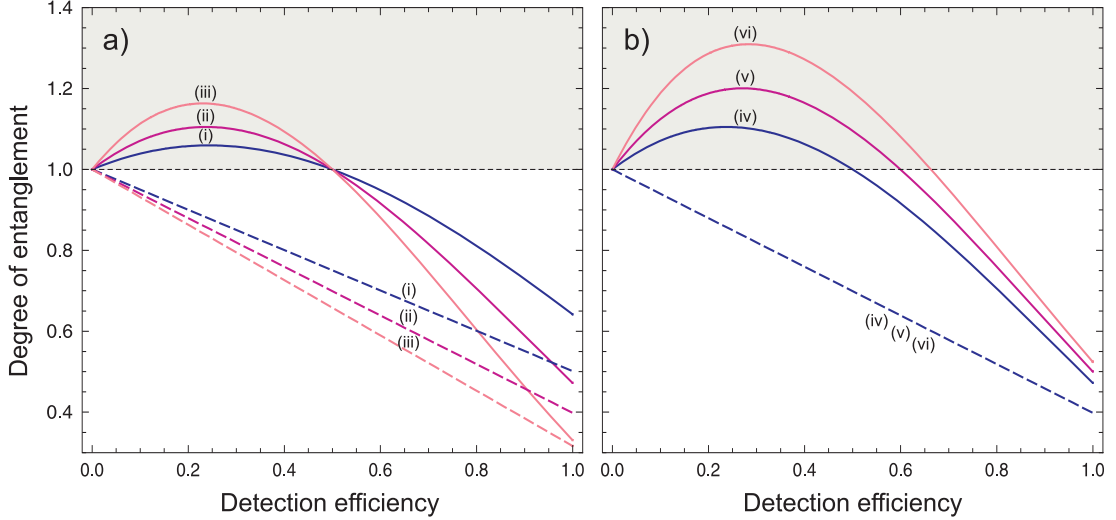


Figure 7.3: EPR paradox criterion (full lines) and inseparability criterion (dashed lines) as a function of detection efficiency η_{tot} for a) minimum uncertainty input states and b) non-minimum uncertainty input states. The two criteria are shown for the following squeezing/antisqueezing values (in dB): (i) -3/3, (ii) -4/4, (iii) -5/5, (iv) -4/4, (v) -4/5, (vi) -4/6.

satisfied. This is a striking contrast to the inseparability criterion which, as we showed earlier, is satisfied for any level of squeezing and any detection efficiency. This different behavior is based on the fact that optical and detection loss changes the purity of entanglement for which only the EPR paradox is sensitive to. Satisfaction of the EPR paradox criterion is a sufficient but not necessary condition for entanglement between two beams.

For input states being not the minimum uncertainty, i.e. $\Delta^2 \hat{X}^+ \Delta^2 \hat{X}^- > 1$, see fig. 7.3 b), the inseparability criterion is clearly independent of this property. On the other hand the EPR paradox criterion is very sensitive whether the input states are minimum uncertainty or not. The boundary below which the EPR paradox is satisfied is highly dependent on the minimum uncertainty of the input states, and in this case the observation of EPR paradox requires very low losses.

7.2 Displacement and tilt

It has been shown in reference [17] that simple optical images, such as the displacement and tilt of a Gaussian beam, can be simply described with Hermite-Gauss (H-G) modes, see sec. 2.5. Here we will introduce these basic optical operations, and present the quantum operators to which they are related. The understanding of these parameters at the quantum level allows one to measure them with an increased level of accuracy even below the QNL [18, 19, 20]. Note that the simple optical images could also possibly lead to parallel quantum information applications in the transverse plane [117].

7.2.1 Classical description

Here we will assume displacement and tilt of a laser beam of TEM₀₀ spatial distribution, as shown in fig. 7.4, which is relevant to this thesis, but the analysis can be in principle extended to any higher-order H-G mode [25]. For simplicity, the description will be done in one dimension, i.e. along x axis, but an identical set of variables could be similarly defined along the other orthogonal direction of the transverse plane. A displacement

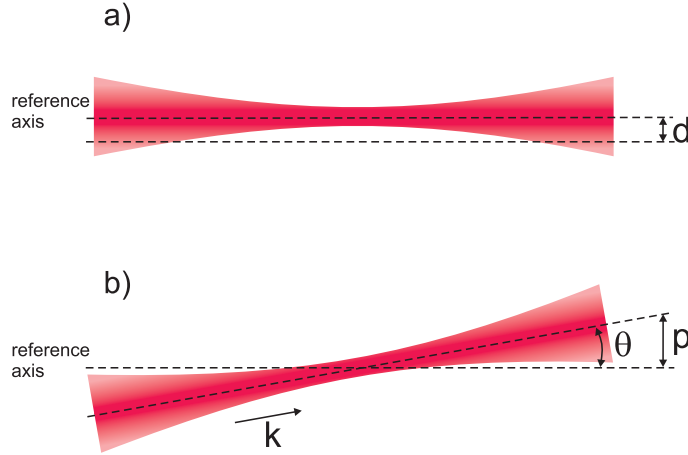


Figure 7.4: a) Displacement and b) tilt of a TEM₀₀ Gaussian beam relative to the propagation axis.

corresponds to a beam translation by distance d along the transverse direction x in reference to the propagation axis z of a non-displaced beam, whereas a tilt is defined as an angular displacement by an angle θ from the propagation axis. In this description, we assume the displacement d to be much smaller than the beam waist radius w_0 , i.e. $d \ll w_0$, and we also use the paraxial approximation, i.e. assume that the tilt of the beam is small so $\theta < \lambda/w_0 \ll 1$. In this case the displaced and/or tilted TEM₀₀ field can be expressed as

$$\mathcal{E}_{d,p}(x) = \mathcal{E}_0 \sqrt{\bar{n}} \left[u_0(x) + \left(\frac{d}{w_0} + i \frac{w_0 p}{2} \right) u_1(x) \right], \quad (7.9)$$

where $\mathcal{E}_0 \sqrt{\bar{n}}$ is the amplitude of the incident TEM₀₀ field containing \bar{n} photons; the expressions for $u_n(x)$ of the two H-G modes are given by equas. 2.34 and 2.35. The transverse momentum of the beam p is defined in the limit of small angles as $p = 2\pi\theta/\lambda$. Note that all transverse modes defined here need a reference frame, which is provided by the axis of the detection device. Displacement and tilt are thus measured relative to this reference.

We can see from equa. 7.9 that the information about magnitude of displacement or tilt of the TEM₀₀ beam can be extracted by measuring the real or imaginary component, respectively, of the TEM₁₀ field hereby generated. In other words, the information about displacement is contained in the *in-phase* amplitude of the TEM₁₀ mode relative to the *carrier* TEM₀₀ mode, and similarly the tilt information is contained in the *in-quadrature* amplitude of the TEM₁₀ mode relative to the carrier field. A change in position is more clearly identified with decreasing beam waist w_0 and in the near field of the beam waist. On the other hand, a change in tilt is more identified for this case in the far field (this situation corresponds to having a large beam waist in the near field). It has been shown both theoretically and experimentally [23] that the optimal detection method for a displacement and/or tilt measurement is just the homodyne detection (HD), see sec. 3.1.2, whose local oscillator (LO) is a bright TEM₁₀ beam.

Displacement and tilt of other beam profiles can be similarly analyzed. In the more general case, the transverse beam profile carrying the displacement or tilt information is always orthogonal to the carrier field, and the two quantities are carried by the same transverse mode only in the case of the TEM₀₀ displacement and/or tilt operation.

7.2.2 Quantum operators

Quantum mechanical description of displacement and tilt of a laser beam can be written similarly to equa. 7.9 just by replacing the displacement d and tilt of the beam expressed in terms of p with their quantum counterpart, the position operator \hat{x} and the momentum operator \hat{p} , respectively. Such a multi-mode beam can be identified with a general form of a beam containing an infinite number of modes, i.e. $\hat{\mathcal{E}}(x) = \mathcal{E}_0 \sum_{n=0}^{\infty} [u_n(x)\hat{a}_n + u_n^*(x)\hat{a}_n^\dagger]$, where only the two modes u_0 and u_1 are non-vacuum modes. By expressing the modal creation and annihilation operators in terms of modal quadrature operators denoted for clarity $\hat{X}^{n0\pm}$, we can work out the position and momentum operators to be respectively

$$\hat{x} = \frac{w_0}{2\sqrt{n}} \hat{X}^{10+}, \quad (7.10)$$

$$\hat{p} = \frac{1}{w_0\sqrt{n}} \hat{X}^{10-}. \quad (7.11)$$

We can see that position and momentum are linked to the amplitude and phase quadratures of the TEM₁₀ mode component of the field, where the quadratures are defined relative to the TEM₀₀ carrier field phase. The minimum measurement of the two quantities is limited by the variance of the TEM₁₀ mode at the particular quadrature. In the case of coherent illumination, the minimum measurable displacement and tilt is then $d_{qnl} = \frac{w_0}{2\sqrt{n}}$ and $p_{qnl} = \frac{1}{w_0\sqrt{n}}$, respectively¹ [20, 118]. In order to perform measurements of these quantities beyond the QNL, we are required to fill in the TEM₁₀ mode with a squeezed light. Depending on the phase between the TEM₁₀ squeezed field and the TEM₀₀ carrier field, one can then selectively measure displacement or tilt below the QNL [19, 18, 20]. It is now convenient to introduce the position and momentum squeezed states [27], which are basically multi-mode states of light consisting of a bright TEM₀₀ carrier field and a TEM₁₀ squeezed field with a fixed phase relation between the two fields. Having amplitude squeezed light in the TEM₁₀ mode, which is relevant to our experiments, we can generate position and momentum squeezed states, as shown in fig. 7.5, by mixing the amplitude squeezed field and the carrier field respectively in-phase and in-quadrature, i.e. having 0 and $\pi/2$ relative phase between the two fields. Similarly we can use the phase squeezed light and having respectively $\pi/2$ and 0 relative phase between the two fields.

It can be also shown [27] that position and momentum are conjugate observables satisfying the following commutation relation

$$[\hat{x}, \hat{p}] = \frac{i}{n}, \quad (7.12)$$

and this is the important property allowing us to demonstrate spatial entanglement, or rather entanglement between the two observables \hat{x} and \hat{p} . Another consequence of this relation is that measuring the displacement below the QNL will result in an excess noise on the conjugate observable, and vice versa. To give an example, using a -3 dB of squeezing in the appropriate component of the beam for a displacement measurement results in a noise power reduction by a factor of 2. The enhanced minimum measurable displacement is then $1/\sqrt{2}d_{qnl}$, whereas the measurement of the conjugate variable, the momentum in this case, is degraded at least by a factor of $\sqrt{2}$, which would be the case if the detection mode is filled with the minimum uncertainty state.

¹To give an example, having 1 mW of power at the wavelength 1 μm and beam waist 100 μm , the quantum noise limit for the displacement and tilt measurement is respectively 0.2 nm and 7 nrad, assuming the detection interval 1/RBW, where RBW is the resolution bandwidth of 100 kHz.

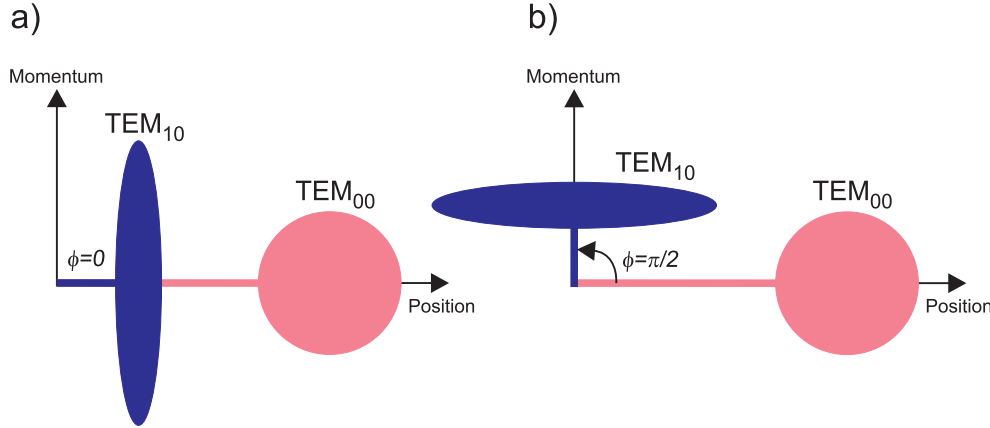


Figure 7.5: Representation of a) position squeezed state and b) momentum squeezed state in the position-momentum Fresnel diagram. Here we assume amplitude squeezed light in the TEM_{10} mode mixed with a bright TEM_{00} carrier field. As the two fields are part of the same multi-mode beam, their relative phase is very important as it determines whether the state is position or momentum squeezed.

7.2.3 Heisenberg inequality relation

The commutation relation 7.12 is similar to the position-momentum commutation relation for a single photon apart from the factor $1/\bar{n}$, which is related to the precision with which one can measure the beam position and momentum. The Heisenberg inequality relation is then written as

$$\Delta^2 \hat{x} \Delta^2 \hat{p} \geq \frac{1}{4\bar{n}}. \quad (7.13)$$

The factor $1/\bar{n}$ is related to the fact that sensitivity of the beam position and beam momentum scales with $\sqrt{\bar{n}}$, as shown respectively in equas. 7.10 and 7.11. When the number of detected photons is small, measurements of beam position and momentum are highly uncertain². However, assuming a bright coherent beam, the product $1/\bar{n}$ becomes zero so that even without using sources of squeezed light, x and p can be known simultaneously with very high precision.

7.2.4 Spatial entanglement

As we already detailed in previous section, the concept of entanglement was first introduced by Einstein, Podolsky, and Rosen in 1935 [28]. They originally demonstrated that an apparent violation of the Heisenberg inequality could be achieved between the position and momentum ($x - p$) observables of a pair of particles. The states realizing the EPR paradox, i.e. having quantum correlations between its position and momentum, are referred to as *EPR states*. EPR states have already been experimentally demonstrated in the discrete regime with atoms [119, 120], or using photon pairs in the regime of few incident photons, where quantum correlations were observed between the near field and the far field corresponding to the position and momentum observables of photon pairs [121]. However, to date no such states have been generated with optical beams in the continuous variable regime as originally considered by Einstein, Podolsky and Rosen.

²This has direct consequences on the resolution of optical images at low photon flux, i.e. one can obtain a good image resolution only if \bar{n} is large enough.

The aim of the work presented in this section is to generalize the former continuous variable quadrature entanglement experiments [74, 108, 122] to the spatial domain, similarly to what has been done in the polarization domain [109, 110, 112, 123, 124], in order to produce entanglement of position and momentum conjugate observables. This theoretical proposition using two bright optical beams was first introduced by M.T.L. Hsu *et al.* in 2005 [27], and was termed spatial entanglement of bright optical beams. By spatial entanglement they referred to entanglement of spatial observables, namely position and momentum, involving a complete detection of the beams in the transverse plane. This has to be distinguished from previous use of this term, where it referred to quadrature entanglement between restricted spatial areas of optical images [125, 126, 127], or local areas of a Bose-Einstein condensate [128].

The fact that position and momentum observables of a TEM₀₀ beam do not commute, expressed by the Heisenberg inequality relation 7.13, allows the generation of EPR states even in the continuous variable regime. Entanglement can be then generated by mixing two beams, each containing two components - a bright TEM₀₀ mode and a dim vacuum-squeezed TEM₁₀ mode - on a 50/50 BS, similarly to the previous experiments involving quadrature entanglement generation [74, 108, 122]. In the following, we will assume the particular case of the orthogonal combination of two position-squeezed beams, as defined earlier in this section. However, it is easy to show that all the results still hold for any situation including also momentum-squeezed beams as long as the relative phases ϕ_1 and ϕ_2 between the dim squeezed TEM₁₀ and bright coherent TEM₀₀ components are identical, and that both squeezed TEM₁₀ components interfere in-quadrature on the entanglement BS, i.e. $\phi_{ent} = \pi/2$, as shown in fig. 7.6.

For position squeezed states, only the TEM₁₀ mode is occupied by a vacuum squeezed mode, and all other modes are occupied by vacuum fluctuations. Knowing that both beams are combined in-quadrature on the 50/50 BS, we can find out the two entangled fields using the BS equations 3.2 and 3.3, and to demonstrate the existence of entanglement, we seek quantum correlation and anti-correlation between the position and momentum quantum noise operators. The position fluctuation operators corresponding to beams x and y are given respectively by [27]

$$\delta\hat{x}_x = \frac{w_0}{2\sqrt{2\bar{n}}}(\delta\hat{X}_1^{10+} + \delta\hat{X}_2^{10-}) = \frac{1}{\sqrt{2}}\left(\delta\hat{x}_1 + \frac{w_0^2}{2}\delta\hat{p}_2\right), \quad (7.14)$$

$$\delta\hat{x}_y = \frac{w_0}{2\sqrt{2\bar{n}}}(\delta\hat{X}_1^{10+} - \delta\hat{X}_2^{10-}) = \frac{1}{\sqrt{2}}\left(\delta\hat{x}_1 - \frac{w_0^2}{2}\delta\hat{p}_2\right), \quad (7.15)$$

and the momentum fluctuation operators are given by

$$\delta\hat{p}_x = \frac{1}{w_0\sqrt{\bar{n}}}(\delta\hat{X}_1^{10-} + \delta\hat{X}_2^{10+}) = \frac{1}{\sqrt{2}}\left(\delta\hat{p}_1 + \frac{2}{w_0^2}\delta\hat{x}_2\right), \quad (7.16)$$

$$\delta\hat{p}_y = \frac{1}{w_0\sqrt{\bar{n}}}(\delta\hat{X}_1^{10-} - \delta\hat{X}_2^{10+}) = \frac{1}{\sqrt{2}}\left(\delta\hat{p}_1 - \frac{2}{w_0^2}\delta\hat{x}_2\right), \quad (7.17)$$

where \bar{n} is the number of photons detected in each of the two position squeezed beams during the measurement time (taken to be equal for the two input beams). This is actually the same as number of photons detected in each of the entangled beams assuming a perfect 50/50 entanglement BS. In our case, where the two input beams are position squeezed, the sign difference between the position noise operators in equas. 7.14 and 7.15 as well as that between the momentum noise operators in equas. 7.16 and 7.17 are signatures of correlation and anti-correlation for $\delta\hat{x}$ and $\delta\hat{p}$. It is not surprising to find here a direct link with the inseparability criterion introduced in sec. 7.1. In the case, where two beams are perfectly interchangeable and have symmetrical fluctuations in

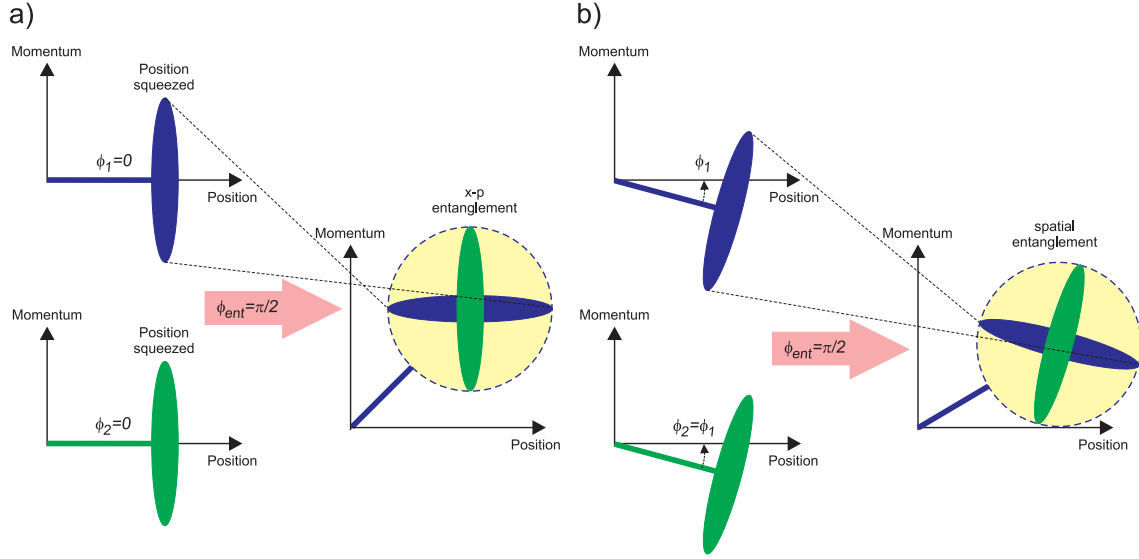


Figure 7.6: Fresnel representation of a) x-p entanglement generated by orthogonal combination of two position squeezed beams, and b) spatial entanglement in a more general case of any orthogonal combination of two beams with non-zero relative phase between the squeezed TEM₁₀ field and the TEM₀₀ carrier field. Similarly to the definition used in fig. 7.5, the horizontal axis of the Fresnel diagram corresponds here to the TEM₀₀ phase reference and therefore designates the position axis; the vertical axis refers to the momentum of the beam.

the amplitude and phase quadratures, the inseparability criterion has been generalized and normalized to a product form given by [73, 108, 109, 129]

$$\mathcal{I}(\hat{x}, \hat{p}) = \sqrt{\frac{\langle (\hat{x}_x + \hat{x}_y)^2 \rangle \langle (\hat{p}_x - \hat{p}_y)^2 \rangle}{|\langle [\hat{x}, \hat{p}] \rangle|^2}}. \quad (7.18)$$

By using observables $\delta\hat{x}$ and $\delta\hat{p}$ given by equas. 7.14-7.17 as well as the commutation relation equa. 7.13, the inseparability criterion for beams x and y can be found as [27]

$$\mathcal{I}(\delta\hat{x}, \delta\hat{p}) = \frac{4\bar{n}}{w_0^2} \sqrt{\langle \delta\hat{x}_1^2 \rangle \langle \delta\hat{x}_2^2 \rangle} = \sqrt{\langle (\delta\hat{X}_1^{10+})^2 \rangle \langle (\delta\hat{X}_2^{10+})^2 \rangle} < 1, \quad (7.19)$$

where we have chosen to combine two position squeezed beams, i.e. $\langle (\delta\hat{X}_1^{10+})^2 \rangle < 1$ and $\langle (\delta\hat{X}_2^{10+})^2 \rangle$, resulting in creation of position noise anti-correlations and momentum noise correlations, and in this case $\mathcal{I}(\delta\hat{x}, \delta\hat{p}) < 1$. Thus we have demonstrated that continuous-variable EPR entanglement between the position and momentum observables of two continuous-wave beams can be achieved. This is what we propose to demonstrate experimentally in the following.

7.3 Experimental setup

In sec. 7.1.1, we introduced methods for characterizing the continuous variable entangled states using the inseparability and EPR paradox criteria. In the following, we will describe methods used in our experiment to generate a pair of entangled beams in position and momentum, i.e. spatially entangled beams. We then present the experimental results showing strong nonclassical correlations between the two position-momentum entangled fields in the frequency range 3.2 – 4.2 MHz.

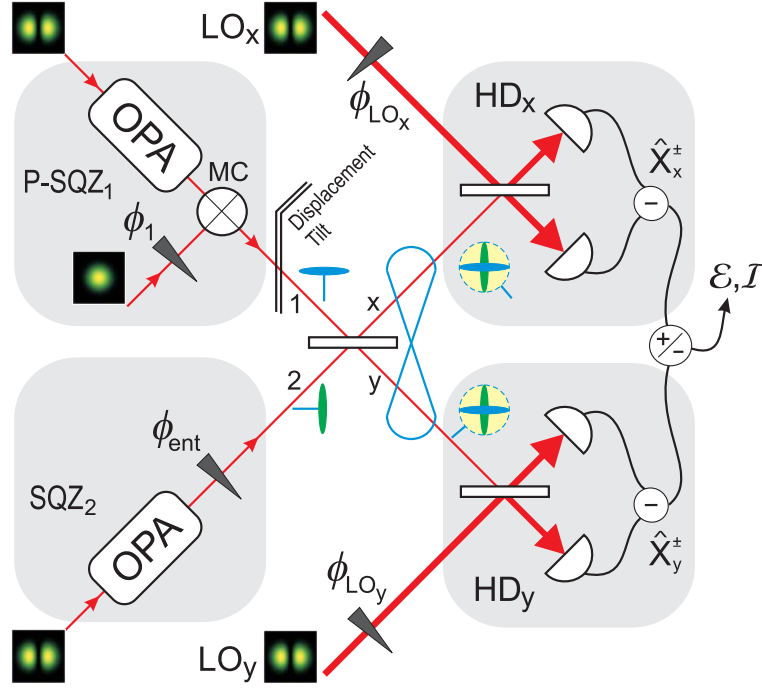


Figure 7.7: Scheme for position-momentum entanglement for a bright TEM_{00} carrier field generated by mixing a position-squeezed beam (P-SQZ) with a dim amplitude squeezed beam (SQZ) on a 50/50 beamsplitter (BS). OPA: optical parametric amplifier; MC: mode combiner, HD: homodyne detection; LO: local oscillator.

A simple scheme for generating spatial entanglement is shown in fig. 7.7 and is based, as we already detailed, on the concept of position-squeezed beams, first introduced in ref. [17]. The squeezing sources used for entanglement generation were based on the $\text{MgO}:\text{LiNbO}_3$ nonlinear material, the same nonlinear medium we used for demonstrating high frequency squeezing in chapter 6. For demonstrating spatial entanglement we built two identical OPAs capable of delivering a constant -3.2 dB of squeezing in the TEM_{10} mode. The original proposal of spatial entanglement by Hsu *et al.* [27] considered two position-squeezed beams to be combined on the entanglement BS. This would result in the possibility of encoding the displacement and/or tilt information on either beam 1 or 2 or both of them the same time, acting as independent channels. This information from the two independent channels would be then entangled in the beams x and y .

However, as such a scheme is very complex and requires twice as many locking loops, we considered in our experiment for simplicity only one position-squeezed beam to be combined with a dim amplitude squeezed beam on a 50/50 BS. This scheme still works as we have the reference beam (TEM_{00} carrier) in the system, but limits us to encoding an information only into this particular beam. This can be also seen from equas. 7.14, 7.15 and 7.16, 7.17 where the position and momentum fluctuation operators depend only on the amplitude and phase quadrature operators of the squeezed TEM_{10} component of the two input fields. The number of photons \bar{n} detected in each of the two entangled beams during the measurement time (with the carrier field present) only scales the problem.

The position squeezed beam was generated either by a lossless combination of a dim amplitude squeezed TEM_{10} beam with a coherent TEM_{00} carrier beam in a Mach-Zehnder interferometer (MZI) or using a partially transmitting BS; both of these techniques are described in detail later in this section. Entanglement was then gener-

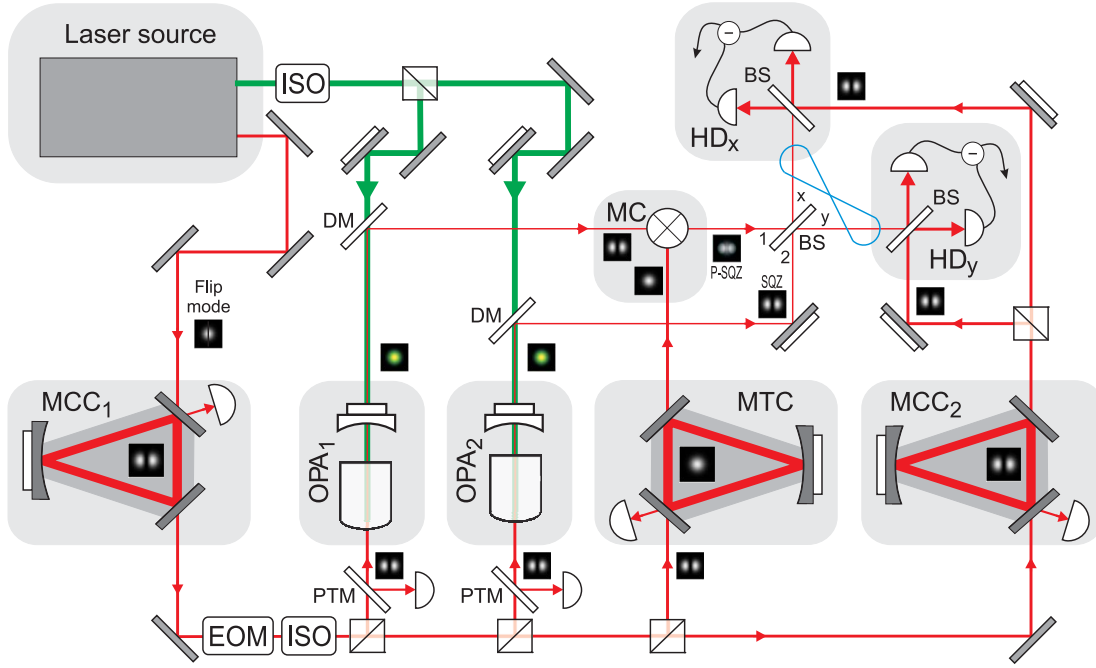


Figure 7.8: Schematics of the experimental setup used to demonstrate spatial entanglement. A position-squeezed beam is generated in a mode combiner (MC) by mixing the TEM_{10} squeezed field exiting the OPA_1 with a TEM_{00} carrier field. This position-squeezed beam is then interfered with the TEM_{10} squeezed field exiting the OPA_2 on a 50/50 beamsplitter (BS) in order to generate a pair of entangled beams x and y . The entangled fields are analyzed in homodyne detection systems (HD). OPA: optical parametric amplifier; MCC: mode cleaning cavity; MTC: mode transferring cavity; MC: mode combiner, HD: homodyne detection; LO: local oscillator; EOM: electro-optic modulator; ISO: optical isolator; DM: dichroic mirror; PTM: partially transmitting mirror.

ated by mixing the position squeezed beam with the dim amplitude squeezed beam on a 50/50 BS locked in-quadrature, so we effectively mixed two orthogonal squeezed states as required for entanglement generation. The entangled beams were analyzed with two homodyne detection (HD) systems with their spatial profiles being in the TEM_{10} mode, in order to access the entangled information about position and momentum of the bright TEM_{00} carrier beam. Amplitude and phase quadratures are accessible for both beams depending on the relative phase of the LO beam and the analyzed field. The appropriate combination of both HD signals then yields the degree of EPR paradox \mathcal{E} or the degree of inseparability \mathcal{I} . In the following, we will describe in detail each of these building blocks used at the end to demonstrate spatial entanglement.

Demonstration of spatial entanglement is a very complex task and involves a lot of locking loops, used to keep all the fields with a fixed relative phase. Schematics of the experimental setup is shown in fig. 7.8, the detailed scheme of the spatial entanglement experiment can be found in appendix A.1. The laser used to drive the experiment is again the dual output solid-state monolithic ring-cavity laser based on Nd:YAG with an internal frequency doubler (Diabolo), with its infrared output phase-modulated (PM) at the frequency 12 MHz, see sec. 3.4. For filtering the intensity and frequency noise of the fundamental laser field, and for defining a pure Gaussian spatial mode, we employed a high finesse mode cleaning cavity (MCC_1), described in detail in sec. 3.5. The MCC_1 was also used as a mode transferring device for generating TEM_{10} fundamental mode using a flip plate exactly in the same way as in the case of the PPKTP squeezing experiment, see sec. 5.2.1. The internal modulation frequency at 12 MHz was then used for locking the MCC_1 using the PDH technique, detailed in sec. 3.3.1.

As the experiment involves a lot of locking loops to be controlled, we used an external electro-optic modulator (EOM) to impose 14.3 MHz and 21.3 MHz PM signals on the transmitted beam through the MCC_1 . The 14.3 MHz signal was used to derive error signals to lock the two OPA cavities to the seed field, and for locking two additional high finesse cavities in the system: MCC_2 , which was used for improving the spatial profile of the LO beam in order to obtain high visibilities in the HD systems; and MTC, which was operating as a mode transferring cavity for converting the TEM_{10} mode back to the TEM_{00} mode. This field was used as the carrier beam for generating the position-squeezed beam. The 21.3 MHz signal was used to lock the OPAs to deamplification and hence to generate dim amplitude-squeezed fields. To avoid the back reflected light from the system from reaching the MCC_1 (this could influence the lock stability), we placed into the beam path an optical isolator (ISO) providing 40 dB of isolation from reflective elements. The fundamental field was then used as a seed for both OPAs, as a LO beam for the HD systems and finally after the mode conversion as a carrier field.

7.3.1 The squeezing sources

The pair of OPAs used to generate the amplitude-squeezed states in the TEM_{10} mode were hemilithic cavities of identical design, shown in fig. 7.9. Each of the OPAs consists of a $2 \times 2.5 \times 6.5 \text{ mm}^3$ bulk LiNbO_3 type I nonlinear crystal, which is 7 % doped with MgO , and an output coupler (OC) with 94% reflectivity at 1064 nm and 10% reflectivity at 532 nm. The OC has the radius of curvature 25 mm. Both facets of the $\text{MgO}:\text{LiNbO}_3$ crystal were polished to have 8 mm radius of curvature. The back surface was coated for high reflectance for both the fundamental and second-harmonic (SH) field ($R > 99.9\%$ at 1064 nm), the front crystal surface was anti-reflection coated for both wavelengths ($R < 0.1\%$ at 1064 nm). The crystal material has internal loss of approximately 0.1% at 1064 nm and 4% at 532 nm. The crystal was placed in a temperature stabilized oven, which was heated constantly to temperature of around 60°C using resistors built in the oven base. The fine tuning of the crystal temperature was achieved by a Peltier element, to which the crystal was attached, in order to satisfy the phase-matching condition and so maximize the nonlinear interaction. As we already detailed, $\text{MgO}:\text{LiNbO}_3$ material has significantly smaller temperature bandwidth then the PPKTP crystal, which requires much more precise control of the phase-matching temperature. The power to the Peltier element was delivered by a temperature controller, which monitored the crystal housing temperature with a thermistor.

The OC was placed 23 mm from the front surface of the crystal, forming $24 \mu\text{m}$ waist for the 1064 nm light within the crystal. For controlling the length of the cavity, we used a 9 mm thick ring PZT actuator, which was housed together with the OC mirror in the same pre-loading system we used for the PPKTP squeezer, see sec. 5.2.1. Using the pre-loading system we enhanced the PZT bandwidth to 55 kHz, which results in a very good stability of the OPA. Each of our OPAs was seeded with the TEM_{10} field through the back of the $\text{MgO}:\text{LiNbO}_3$ crystal. Detecting the reflected field (we used a 90/10 BS as one of the steering mirrors, as shown in fig. 7.8, which allowed detection of the reflected field from the OPA without using any sophisticated scheme involving a Faraday rotator) from the back surface of the $\text{MgO}:\text{LiNbO}_3$ crystal, and de-modulating the resulting photocurrent at 14.3 MHz provided a PDH type error signal. The error signal was used to control the length of the OPA cavity and lock the OPA to the TEM_{10} mode. The power of the seed field was minimized in order to avoid contamination of the squeezed field by the excess noise of the seed, but still keeping the OPA stably locked, and at the same time having a sufficient power for implementing various locks in the system, i.e. for locking the relative phase between

7.3.2 Generation of position and momentum squeezed states

In this experiment, the position squeezed beam was generated either by a lossless combination of a vacuum amplitude squeezed TEM_{10} beam with a coherent TEM_{00} carrier beam in a MZI, or using a partially transmitting BS. Another option is using an optical cavity, for more details see e.g. reference [25]. As we already detailed, the bright carrier beam provides the reference for position and momentum of, in this case, the OPA_1 squeezed field. The carrier field was generated by the MTC, which converts the TEM_{10} mode into the TEM_{00} mode by misaligning the incident field into the cavity, similarly what we discussed in sec. 3.6.1. In fact the MTC is of identical design as the MCC_1 and MCC_2 used in the experiment. The carrier field was sent to a mode combiner and mixed with the dim TEM_{10} squeezed field.

The correct scheme for generating the position-squeezed beam would be to combine a bright carrier field with the TEM_{10} squeezed vacuum. This, however, is not experimentally feasible as we need to lock the relative phase between the two fields, and this puts a requirement on the squeezed state to have a small coherent amplitude. The power of the carrier beam was set to be 10 times stronger than the power of the dim squeezed (deamplified) field, i.e. $P_{\text{car}} = 91 \mu\text{W}$ versus $P_{\text{sqz}} = 9 \mu\text{W}$, assuming deamplification of the OPA seed in the nonlinear process by factor of 0.5.

Beam splitter

The most simple scheme for combining two different H-G modes is obviously the one using a simple BS, as shown in fig. 7.10 a). As the H-G modes of different orders are orthogonal, they do not significantly interfere on the BS and simply reflect or transmit through the BS. As we are interested in combining the two modes, we can effectively use only one output of the BS and the other one is lost. Moreover, when one of the input states of a particular mode is a squeezed state, it is obvious here that the action of the BS will be to add vacuum fluctuations into the squeezed state. The contamination of the squeezed field with vacuum noise can be avoided by choosing a BS with a high reflection for the squeezed field, but this results in a huge loss of the second beam to be combined. Anyway, we used such a technique of combining higher-order modes for the final spatial entanglement experiment, just only because of the modulation-free locking of the two incident fields, as this does not introduce any excess noise into the squeezed field.

Alignment of such a mode combiner is relatively easy. We first switched both the input beams of the partially transmitting BS into the same TEM_{00} spatial mode, which has been done by locking the MCC_1 , MTC and OPA_1 into this particular mode. Experimentally, we typically achieved 99.5% visibility. Then the MCC_1 and OPA_1 was switched back to the TEM_{10} mode, and as the propagation axis of the output beam exiting a cavity is defined by its cavity axis, we still keep a perfect alignment between the two fields. Generation of position squeezed beams requires to lock the relative phase between both input beams. For this task, we used the spatial mode locking technique [25, 48], by detecting the field from the unused port of the BS on a split-detector. The fact is that both beams are not orthogonal anymore with respect to split detection, as both beams interfere on each half of the overall beam. Note that such an interference signal cannot be generated with a normal bucket detector. When the two fields are in-phase in the plane of the split-detector, the optical phase of the TEM_{10} mode is advanced by $\pi/2$ on one side of the TEM_{10} pattern and $-\pi/2$ on the other, relative to the TEM_{00} mode. As the carrier drifts away, the phase of the TEM_{00} mode will shift relative to the two halves of the TEM_{10} mode. The error signal is therefore obtained by

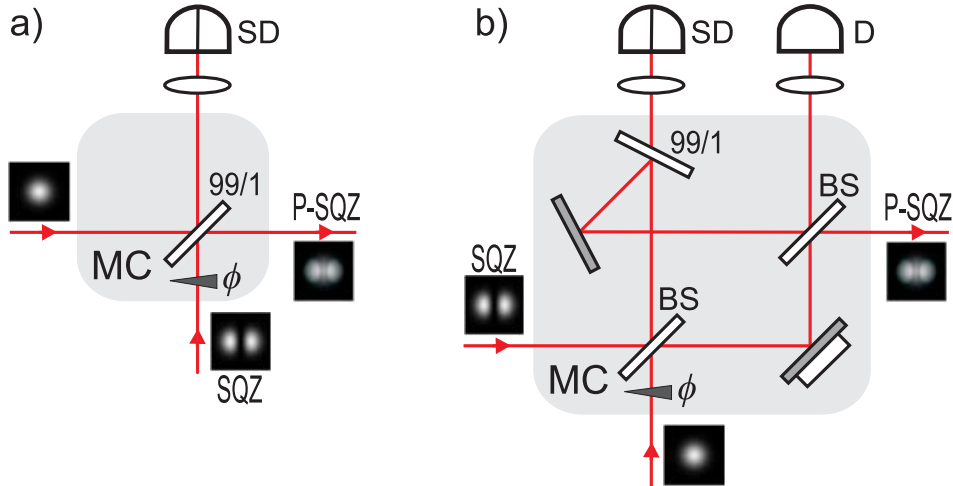


Figure 7.10: Schematics of a) beamsplitter mode combiner and b) nonsymmetric Mach-Zehnder interferometer mode combiner. A position-squeezed beam (P-SQZ) is generated by mixing a TEM_{00} carrier field with a dim TEM_{10} amplitude squeezed beam. D: locking detector; SD: split-detector.

detecting the interference between the TEM_{10} and TEM_{00} modes on the split-detector as shown in fig. 7.11 a). Fig. 7.11 b) explains, how the intensities of the field on left and right hand half of the detector vary as the phase of the carrier drifts away. The error signal is found by subtracting the DC photocurrents of the two detector halves of the split detector.

In principle, if the two components would be well collimated so that the Gouy phase shift between the two different fields is zero within the length of the experiment, and if we would lock the two components on the split-detector without using any focusing optics, we can obtain zero relative phase between the two fields within the experiment. In this case such a multi-mode beam is a perfect position-squeezed state as shown in fig. 7.6 a). However, in reality the size of the split detector is much smaller than the beam waist of the collimated fields, and one needs to use focusing optics for mode-matching the two fields into the split-detector. In this case, the two components will experience a different Gouy phase shift on the way from the focusing lens to the split-detector plane. As this technique allows to lock the two fields in-phase only in the split-detector plane, this results in a non-zero relative phase between the two collimated fields within the length of the experiment. This corresponds to the general case of a spatial-squeezed state as shown in fig. 7.6 b). If we would use for generating spatial entanglement two position-squeezed states³ as originally considered by Hsu *et al.* [27], one need to make sure that the two corresponding split-detectors are equally positioned from the focusing optics (of the same focal lengths) so that the relative phases between the components of beams 1 and 2 are equal, i.e. $\phi_1 = \phi_2$. The advantage of using only one position-squeezed beam in the system is that it is no longer necessary to perform such a complicated adjustment of the two split-detectors. We just require to lock phases of the two components of the position-squeezed state within the measurement time window, whatever the relative phase between the two fields is.

³In the following, we will use the term position-squeezed beam for simplicity, even if the relative phase between the TEM_{00} and TEM_{10} components is not necessarily zero.

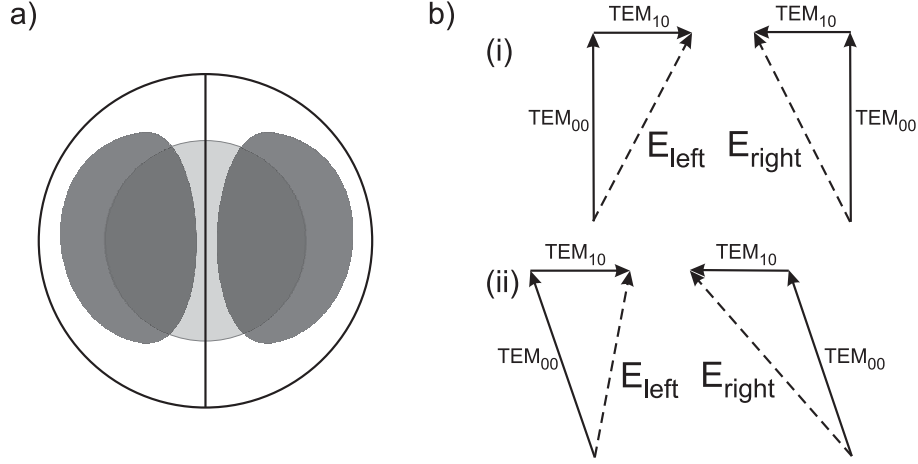


Figure 7.11: Split-detector locking: a) the pattern of the TEM_{00} mode and TEM_{10} mode on the split-detector; b) the interference of the fields when (i) both fields are in-phase in the split-detector plane and (ii) slightly out of phase in the split-detector plane [48].

Nonsymmetric Mach-Zehnder interferometer

A more promising scheme for combining beams, whose transverse profiles have opposite parity, is a nonsymmetric MZI [20] shown in fig. 7.10 b). Such a device allows a lossless combination of a TEM_{00} beam, whose profile is even with respect to the transverse axis, with a TEM_{10} beam, whose profile is odd. The presence of an odd number of mirrors in the interferometer insures an additional π phase shift only for odd modes between both arms of the nonsymmetric MZI. This asymmetry has an effect that the two opposite parity modes entering the nonsymmetric MZI via the two input ports interfere constructively on the same output port and without experiencing any losses. The integrality of the bright TEM_{00} carrier beam and the squeezed TEM_{10} field is thus preserved at the output of the MZI. This is due to the presence of the extra mirror. In the case of a common symmetric MZI, the two beams would have been re-separated at the output of the interferometer.

In order to maximize the MZI stability, the interferometer needs to be as small as possible with arms of comparable length. The best operation is achieved with collimated beams, for which a small discrepancy in the arm lengths has no critical consequences on the mode matching of the beams on the second BS of the interferometer. Experimentally, the interferometer was aligned on the squeezed TEM_{10} beam as we want to minimize losses on this particular beam, with fringe visibility of 98%. For locking the MZI, we used the dither locking technique as introduced in sec. 3.3.2, by looking at the error signal from the unused port of the interferometer. The aim is to lock the MZI to a dark fringe, leaving all the intensity in the other output port. We modulated field in one arm of the interferometer via an accidental resonance of the PZT actuator, the same actuator used to control the phase difference between both arms. Typically the modulation frequency using a PZT is around 1 MHz, in our case we got the best error signal at 373.6 kHz. The error signal is then obtained by mixing down the detected field at the modulation frequency, and this was fed back via a PID controller and a high voltage amplifier to the PZT of the interferometer.

The carrier beam was aligned on the first BS of the interferometer and locked using the split-detector exactly in the same way as in the case of the BS combiner detailed earlier. The error signal was extracted from the MZI via a partially transmitting mirror

in one of the arms of the interferometer. Its transmission could be tuned by changing the angle of incidence of the beam, so we were able to extract only 1% of the light incident on the mirror. This power was still enough for generating the spatial-mode locking signal on the split-detector, and the same time did not introduce a huge loss onto the squeezed beam. In overall, the efficiency of the MZI was 97%. As we already detailed, we avoided using the nonsymmetric MZI in the final spatial entanglement experiment, as the squeezed beam gains an excess amplitude and phase noise in the detection frequency window due to beating of the MZI locking signal with other modulation frequencies used in the experiment, their higher harmonics and cross-beats.

7.3.3 Generation and detection of entangled states

Both non-classical beams were combined on a 50/50 entanglement BS. The alignment was done with TEM_{10} fields only, and we achieved the fringe visibility of 98%. In order to generate either quadrature entanglement (carrier beam is blocked) or spatial entanglement (one or both of the TEM_{10} squeezed fields are mixed with the TEM_{00} carrier field), we need to lock the relative phase of the two interacting fields on the entanglement BS exactly to $\phi_{ent} = \pi/2$. This was done using DC locking with the error signal being difference between the sum of HD detectors, i.e. $[D_1 + D_2] - [D_3 + D_4]$. In practise, this lock actively balances power in the two entangled beams. It is important to note that the entanglement error signal will be centered on zero only if the power of both LO beams, both squeezed beams and the power of the carrier beam are carefully matched.

The entangled fields are analyzed in the homodyne detectors HD_x and HD_y with bright LO beams of the TEM_{10} spatial profile. The LO beams were prior to HD spatially filtered in the MCC_2 , and we typically achieved visibilities of 96.5% between the analyzed and LO beams. The power of each of the LO beams was set to 3 mW in order to be large enough relative to the power of the squeezed and carrier beams (respectively at least 100 times and 10 times larger), but the same time small enough not to saturate individual homodyne detectors. These detectors were built in-house at the ANU and are based on ETX500 photodiodes with quantum efficiency of $95 \pm 3\%$.

To characterize entanglement, we need to successively measure correlations and anti-correlations between the HD signals, when the homodyne systems are locked respectively to the phase and amplitude quadratures over the detection time window. Detection of the amplitude quadrature requires locking the homodyne system to a dark - or bright - fringe [47], which means that the power on the homodyne BSs needs to be maximally asymmetric. Locking to a turning point of the homodyne system is therefore analogous to locking to a cavity resonance. Similarly to the case of MZI detailed earlier, we used the dither locking technique, by applying a high frequency phase modulation on the same PZT actuator that is used to lock the homodyne system. The mechanics of the PZT-mirror mounts gave accidental resonances at 359 kHz and 368 kHz for the homodyne systems HD_x and HD_y , respectively. Mixing down the AC subtracted signals of the two HDs, i.e. $D_1 - D_2$ and $D_3 - D_4$, at the appropriate modulation frequency then gives the error signals used to lock both homodyne systems to the amplitude quadrature.

When the detection is perfectly locked to the amplitude quadrature, the phase modulation will not be seen in the subtracted signal, giving a zero in the demodulation signal. If the detection phase drifts, the demodulation of the subtracted photocurrents gives a positive or negative voltage depending on the direction of the drift, therefore

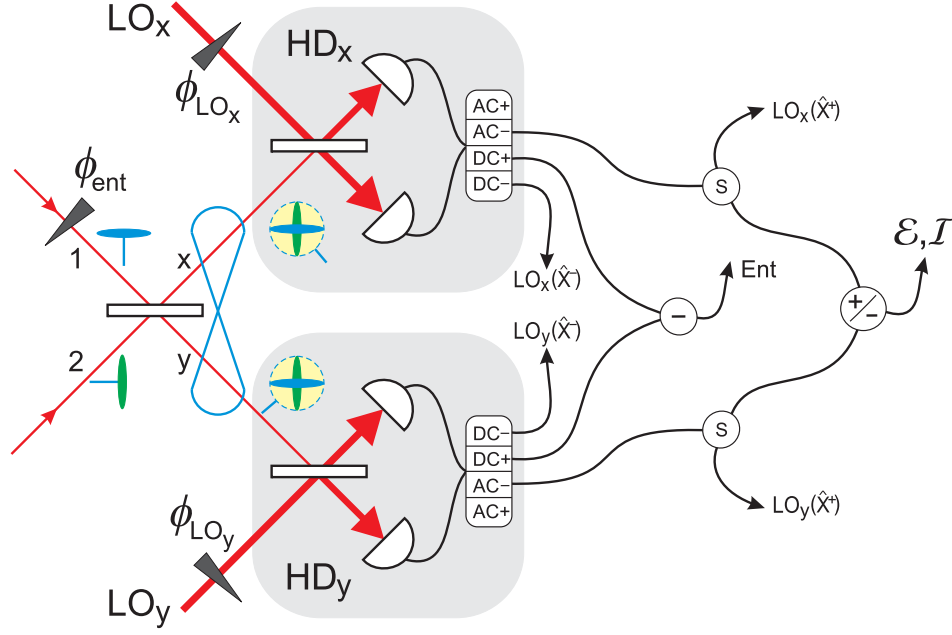


Figure 7.12: Electronic layout of the HD systems used to lock the system to produce a pair of entangled fields, and to perform measurements of their properties, i.e. $\Delta^2 \hat{X}_x^\pm$, $\Delta^2 \hat{X}_y^\pm$ and $\Delta^2 \hat{X}_{x\pm y}^\pm$. Using sum and differences of the homodyne AC and DC signals, we can monitor the relative phase ϕ_{ent} between the two beams incident on the entanglement BS, and the relative phases ϕ_{LO_x} and ϕ_{LO_y} between the individual entangled fields with their corresponding LO beam. This provides a measurement on either the amplitude or phase quadrature.

providing a zero-crossing error signal. For the phase quadrature measurements, we require to lock both HD systems to a half-fringe. The error signals can be here directly generated via the subtraction of the DC photocurrents of the two HDs, i.e. $D_1 - D_2$ and $D_3 - D_4$. The summary of all the locking signals and signals used for measurements of quantum correlations between the two entangled beams is given in fig. 7.12.

7.4 Experimental results

7.4.1 Regenerative gain and squeezing

Before performing the entanglement measurements, we first analyzed both of our squeezing sources operating in the TEM_{10} mode in terms of classical gain and quadrature variance. A plot of observed gain of both OPAs versus pump power is shown in fig. 7.13. The maximum gain/deamplification achieved with 0.2 W of pump power is 3.7/0.45 and 3.2/0.43 for OPA₁ and OPA₂, respectively. In general, we can see that the OPA₁ is more efficient than the OPA₂, and by fitting the measured data, we estimated values of the nonlinear strength (defined in sec. 5.1) to be respectively $\Lambda_{ln,1} = 1200 \times 10^{-4}$ and $\Lambda_{ln,2} = 1100 \times 10^{-4}$. Their difference might be caused by imperfect mode-matching of the pump beam into the active volume of the nonlinear crystal. Besides that, these values are almost 2.5 times higher, i.e. the MgO:LiNbO₃ OPAs are 1.6 times more efficient, than in the case of the PPKTP squeezer detailed in sec. 5.2.1, where the nonlinear strength for the TEM_{10} operation was estimated to be $\Lambda_{ppktp}^{10} = 470 \times 10^{-4}$. In fact, for a 532 nm pumped OPA the effective nonlinear coefficient is higher for the PPKTP material, $d_{ppktp} = 10.7$ pm/V, than the one of the MgO:LiNbO₃ material, $d_{ln} = 5.3$ pm/V. Such a difference in the nonlinear strengths arises from the fact that the LN OPAs were well optimized for the TEM_{00} pump profile in terms of focusing

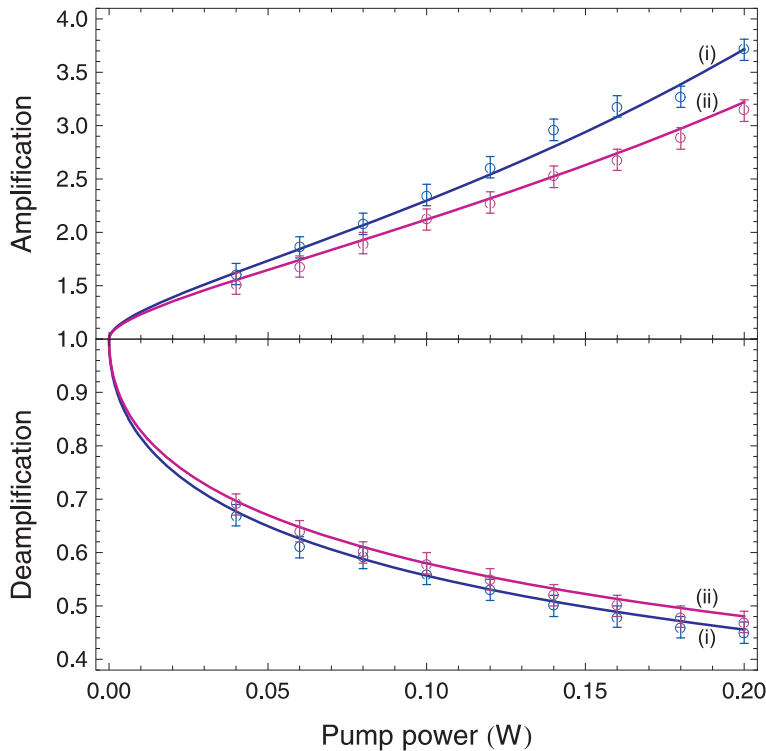


Figure 7.13: Measurements of regenerative gain of the MgO:LiNbO₃ OPAs as a function of pump power (circles), and theoretically predicted gain (full lines) for (i) OPA₁ and (ii) OPA₂. Both OPAs are operating in the TEM₁₀ mode and pumped by SH field in the TEM₀₀ mode. The simulated curves are based on the experimental parameters given in table 5.1, with the nonlinear strengths $\Lambda_{ln,1} = 1200 \times 10^{-4}$ and $\Lambda_{ln,2} = 1100 \times 10^{-4}$.

parameter ξ , as discussed in the generalized Boyd-Kleinman theory for higher-order mode nonlinear interaction (see sec. 4.2.2). Another thing is that the MgO:LiNbO₃ crystal was actually double-passed by the pump field as one side of the crystal was coated for high reflection at the pump frequency, what results in a larger interaction length of the nonlinear process. When increasing pump power, it is always important to optimize the phase-matching temperature of the OPA crystal due to the 4% absorption of radiation at 532 nm, which has an effect of heating the mode volume inside the crystal. The optimum phase-matching temperatures were found for the two OPAs to be $T_1=61.45^\circ$ and $T_2=59.60^\circ$ at 200 mW of pump power (this is 0.2° less than would be the phase-matching temperature in the case of low pump power).

Measurements of locked squeezing, in this case OPA₁ operating in the TEM₀₀ and TEM₁₀ modes, are shown in fig. 7.14. We observed -4.76 ± 0.19 dB of squeezing and 8.19 ± 0.11 dB of antisqueezing in the TEM₀₀ mode using 80 mW of pump power. Note that the amplification and deamplification was in this case 9.30 and 0.31, respectively, with the OPO threshold of 220 mW. However, for generating spatial entanglement, we aim for the best squeezing and minimum uncertainty of the states in the TEM₁₀ mode. For this operation, we observed at the best -3.68 ± 0.17 dB of squeezing and 5.01 ± 0.10 dB of antisqueezing when pumping the OPA with 160 mW of pump power. Corresponding gain is shown in fig. 7.13. Each spectrum analyzer trace was taken with the sweep time of 2 s, the resolution bandwidth RBW=100 kHz and the video bandwidth VBW=300 Hz. The reported mean values and variances of squeezing and antisqueezing were calculated from the measurements in the frequency window 3.2 – 4.2 MHz. The huge peak at 5 MHz corresponds to beating of the modulation frequencies used in the system with the 12 MHz internal laser modulation frequency.

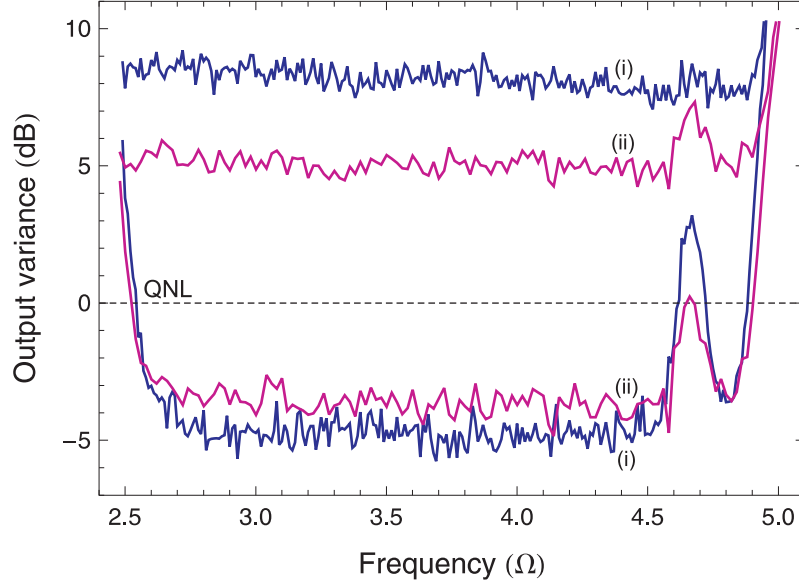


Figure 7.14: Measurements of locked squeezing and antisqueezing spectra produced by OPA₁ (i) operating in the TEM₀₀ spatial mode using 80 mW of TEM₀₀ pump power, and (ii) operating in the TEM₁₀ spatial mode using 160 mW of TEM₀₀ pump power. The measurements are corrected for electronic noise, which was 10 dBm below the QNL. RBW: 100 kHz; VBW: 300 Hz; sweep time: 2 s.

This is then beating with the LO_x modulation frequency and creates the small peak at frequency 4.67 MHz. We can see that each modulation frequency present in the system is introducing an excess noise into the detection frequency window, therefore for taking the final entanglement measurements with the carrier field, we rather avoided using the MZI combiner, which involves an additional modulation frequency. Thus we preferably used for combining the OPA₁ TEM₁₀ squeezed field with the TEM₀₀ carrier field a modulation-free locking scheme involving a simple BS, as discussed in sec. 7.3.2.

In order to find the optimum values of pump power at which the spatially entangled beams will be generated (we require strongly squeezed states in the TEM₁₀ mode, the best with identical squeezing and antisqueezing properties for both OPAs, and both states being closest to minimum uncertainty), we performed measurements of the output variance versus the pump power, as shown in fig. 7.15. At each new pump power, we always locked the corresponding LO beam either in-phase or in-quadrature with the dim squeezed beam, and performed respectively the measurements of squeezing and antisqueezing. The data points correspond to the mean values calculated from the measurements in the frequency range 3.2 – 4.2 MHz, with error bars showing their variances. We found again a very good agreement between the measured data and theoretically predicted traces of the output variance for both OPAs. We used in the model the experimental parameters given in table 5.1, with the squeezing nonlinear strength being $\Lambda_{sqz,i} = \Lambda_{ln,i}(1 - 0.5 \times P_{sh})$, similarly what we used for fitting the output variance data in the case of the PPKTP squeezer detailed in sec. 5.2.3. Notice that at high pump powers, the measured data does not follow the modeled traces, and this is due to difficulties to lock an OPA properly to deamplification. This results in a reduced gain, and thus to lower values of squeezing and antisqueezing measurements. We found that the best operating point for our OPAs in terms of generated squeezing and stability of the lock to deamplification will be to pump the OPAs with the following powers: $P_1 = 130$ mW and $P_2 = 180$ mW. At this pump powers, we achieved similar noise properties of the two squeezing sources, i.e. -3.2 dB of squeezing and 5.1 dB of antisqueezing for both OPAs.

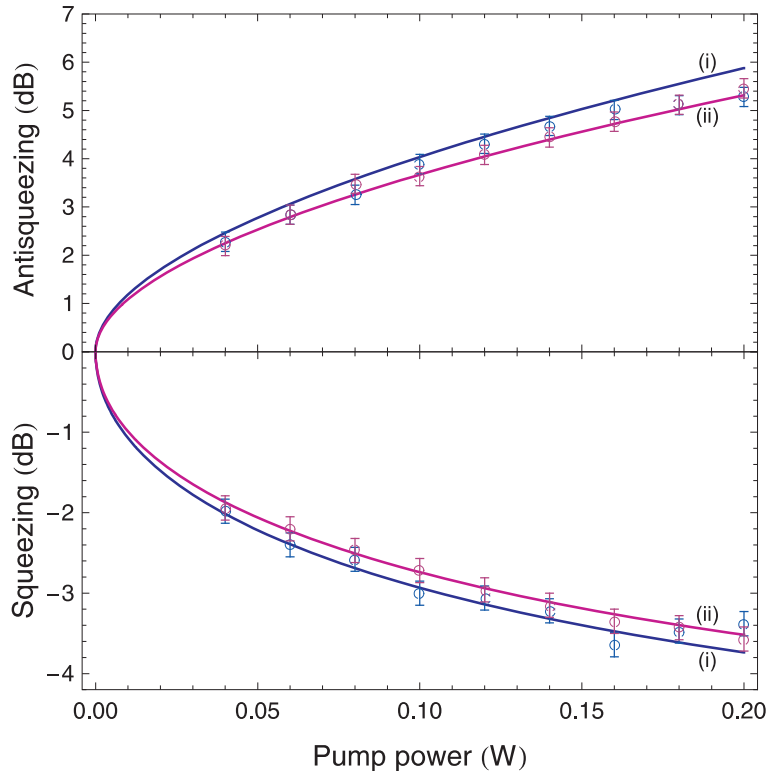


Figure 7.15: Measurements (circles) and theoretically predicted variances (full lines) of the TEM_{10} squeezed states generated by (i) OPA_1 and (ii) OPA_2 , as a function of pump power. Parameters used to fit the measured data are the same as detailed in caption of fig. 7.13, and the squeezing nonlinear strength is $\Lambda_{sqz,i} = \Lambda_{ln,i}(1 - 0.5 \times P_{sh})$. The reported mean values and variances were calculated from measurements of locked spectra in the frequency window 3.2 – 4.2 MHz.

7.4.2 Measurements of the position-squeezed states

The next step towards the experimental realization of spatial entanglement involves generation of the position-squeezed state as detailed in sec. 7.3.2. Here we used for combining the TEM_{10} squeezed field and the TEM_{00} carrier field a nonsymmetric MZI. When measuring the nonclassical properties of the position-squeezed state, we do not expect any modification to the correlations between the measured signals on the HD detectors compared to the experiment, which does not involve any carrier field. Indeed, the carrier's TEM_{00} mode is orthogonal to the TEM_{10} mode of the LO and should not therefore modify the nonclassical properties lying in the TEM_{10} component of the multi-mode field. Such a measurement⁴ normalized to the shot noise is shown in fig. 7.16 a). As we expected, the measurements of the squeezing spectra show that mixing the TEM_{10} squeezed beam with the TEM_{00} carrier field in the MZI has no influence on the amount of squeezing observed, i.e. the detection of the position-squeezed beam gives identical noise reduction below the QNL, when compared to a detection of the squeezed TEM_{10} field. As shown in fig. 7.16 b), the only difference is equal increase in noise power of all traces due to the contribution of noise of the carrier beam, whose power as stated earlier is not totally negligible relative to the LO power. The absence of cross-

⁴This measurement was performed just to prove the basic concept of position-squeezed beams, and was taken prior to redesigning our squeezing sources and all the locking loops in the system for the final spatial entanglement experiment. At that stage of the experiment, we were able to generate only -2.5 dB of locked squeezing in the TEM_{10} mode as shown in fig. 7.16. Thus the noise traces do not correspond to our actual squeezing results reported in this section. Further technical details on this experiment can be found in reference [25].

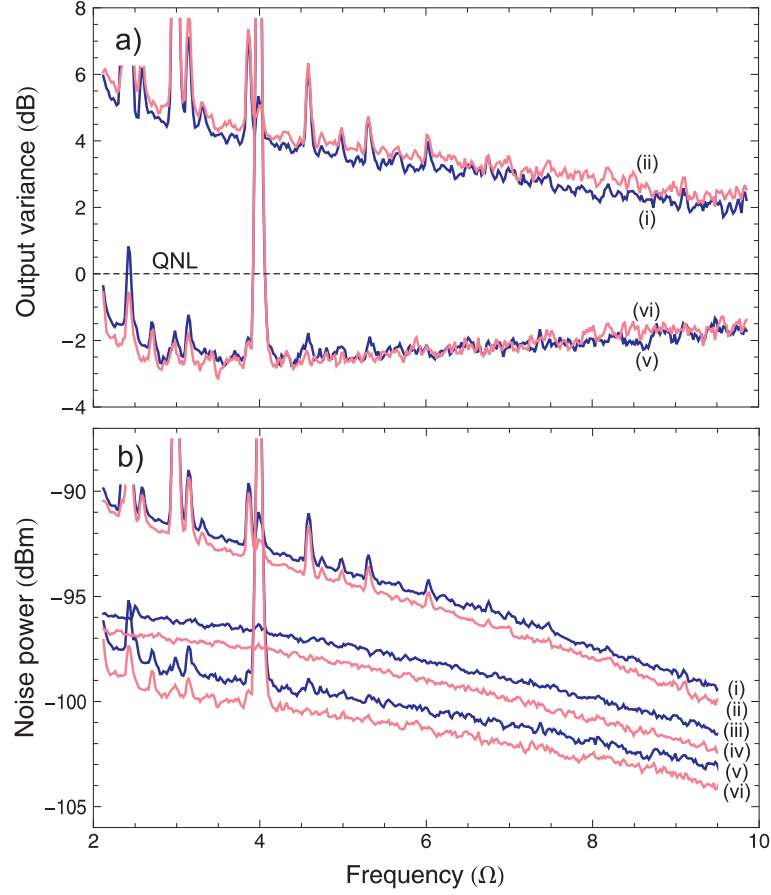


Figure 7.16: Squeezing and antisqueezing noise spectra of a multi-mode position-squeezed beam, compared to a TEM_{10} squeezed beam: a) normalized to the QNL; b) directly recorded spectrum analyzer traces. The presence of the carrier beam is not modifying the quantum properties of the TEM_{10} component of the multi-mode beam. (i) antisqueezing, (iii) shot noise and (v) squeezing spectra of the position-squeezed beam; (ii) antisqueezing, (iv) shot noise and (vi) squeezing spectra of the TEM_{10} squeezed beam. RBW: 300 Hz; VBW: 30 Hz; sweep time: 2 s.

talk between the orthogonal modes shows the quality of our experiment. Any drop in the fringe visibility would indeed couple some of the noise of the TEM_{00} carrier into the squeezed TEM_{10} component, and hence reduce the observed amount of squeezing. The presented results prove that spatial entanglement using a position-squeezed beam is feasible.

7.4.3 Measurements of entanglement

As expected from theory, after combining the TEM_{10} squeezed field and the position-squeezed field on a 50/50 entanglement BS and locking their relative phase to $\pi/2$, the two entangled fields should be noisy, i.e. well above the QNL, at its both amplitude and phase quadratures. Measured spectra of their amplitude and phase quadrature variances are shown in fig. 7.17 a). All traces are greater than the QNL, which is a necessary prerequisite for entanglement. However, assuming a symmetric arrangement of the experiment, i.e. having identical noise properties of the two squeezed fields, locking their relative phase exactly to $\pi/2$ on the entanglement BS and having identical HD efficiencies for analyzing the two fields, we would expect to observe identical spectra of the two entangled beams x and y at both amplitude and phase quadratures, as predicted by equas. 7.1 and 7.2. This is certainly not the case in our experiment.

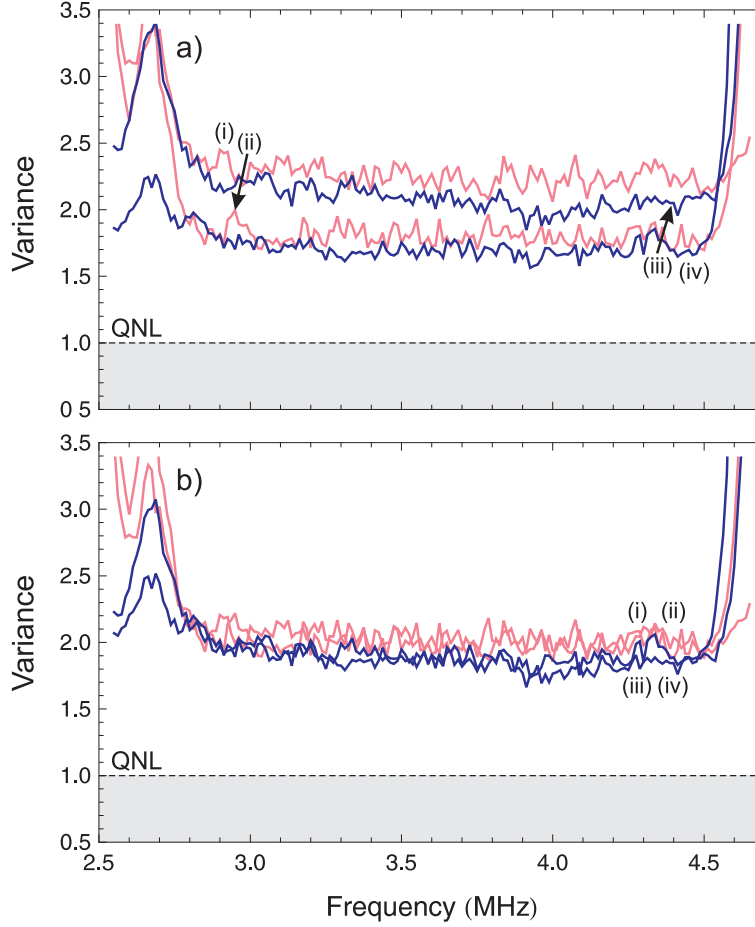


Figure 7.17: Measured frequency spectra of the amplitude and phase quadrature variances of the individual entangled fields x and y , normalized to the QNL. a) measured data, b) data corrected for the asymmetry 0.45 : 0.55. (i) $\Delta^2 \hat{X}_x^+$, (ii) $\Delta^2 \hat{X}_y^+$, (iii) $\Delta^2 \hat{X}_x^-$ and (iv) $\Delta^2 \hat{X}_y^-$.

We can see that the noise properties in the amplitude and phase quadratures of a particular beam are very similar, i.e. $\Delta^2 \hat{X}_x^+ \approx \Delta^2 \hat{X}_x^-$ and $\Delta^2 \hat{X}_y^+ \approx \Delta^2 \hat{X}_y^-$, however these spectra are distinctively different between the two entangled fields x and y , i.e. $\Delta^2 \hat{X}_x^+ \neq \Delta^2 \hat{X}_y^+$ and $\Delta^2 \hat{X}_x^- \neq \Delta^2 \hat{X}_y^-$. Clearly, the symmetry arrangement of the experiment was broken. As we showed earlier, both of the squeezing sources are very similar in their noise properties, thus one can exclude this argument in the following discussion. Considering different efficiencies of the two HD systems used to analyze the entangled fields, one would need to assume an unknown loss, or rather inefficiency, of around 20% experienced by one of the entangled fields, i.e. beam y in this case, in order to lift up the noise traces $\Delta^2 \hat{X}_y^+$ and $\Delta^2 \hat{X}_y^-$ towards the appropriate noise traces of the entangled beam x . This is certainly not the case. A reasonable explanation might be that the asymmetric behavior has an origin in an improper lock of the relative phase between the two squeezed fields.

Regardless the fact that the entangled beams are asymmetric, we analyzed the correlations between the beams x and y . As we already detailed, the characterization of entanglement requires to successively measure correlations and anti-correlations between the HD signals, when the homodyne systems are locked respectively to phase and amplitude quadratures. This involves the measurements of $\Delta^2 \hat{X}_{x \pm y}^\pm$, as explained in sec. 7.1.1. Spectra for $\Delta^2 \hat{X}_{x \pm y}^\pm$ were obtained by taking the minimum of the sum and difference variances between the HD systems x and y , with both homodynes locked to either the amplitude or phase quadrature. For the incident amplitude-squeezed

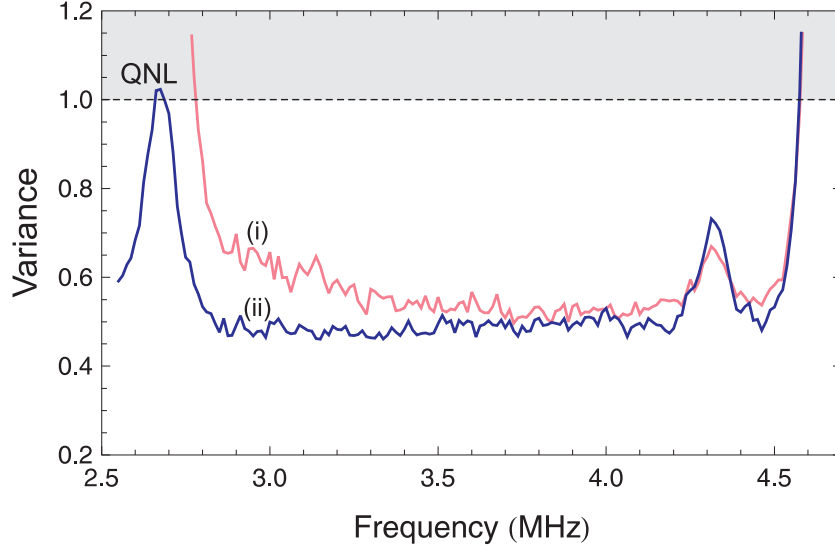


Figure 7.18: Measured frequency spectra of the minimum of amplitude and phase quadrature sum and difference variances between the position-momentum entangled beams x and y . These measurements correspond for the case of an amplitude-squeezed TEM₁₀ beam and a position-squeezed beam combined on the entanglement BS to measurements of (i) $\Delta^2 \hat{X}_{x+y}^+$ and (ii) $\Delta^2 \hat{X}_{x-y}^-$. The spectra were normalized to the QNL.

and position-squeezed beams, where we expect the anti-correlations to occur in the amplitude quadrature and correlations in the phase quadrature, these minima then correspond to measurements of $\Delta^2 \hat{X}_{x+y}^+$ and $\Delta^2 \hat{X}_{x-y}^-$. The spectra were normalized to the shot noise scaled by the combined power of the two LOs and the carrier field (the power of the dim squeezed fields does not contribute to the shot noise), and these are shown in fig. 7.18. This noise reduction below the QNL is the signature that the two beams generated after the entanglement BS are indeed entangled. In the small frequency range between 3.7 – 4.0 MHz, both variances almost overlap as expected from theory, however below 3.7 MHz the amplitude quadrature sum variance experiences an excess noise. This effect has an origin in the relaxation oscillation of the laser [38]. As the measurement of $\Delta^2 \hat{X}_{x+y}^+$ is obtained by summing the amplitude quadrature photo-currents from HD_x and HD_y, the contribution from the relaxation oscillation was therefore also summed. In the measurement of $\Delta^2 \hat{X}_{x-y}^-$, this effect was canceled by subtracting the phase quadrature photo-currents.

7.4.4 Characterization of the entangled states

Let us now quantify entanglement produced between the amplitude and phase quadratures with the two most commonly used criteria presented in sec. 7.1.1. The degree of inseparability can be directly determined using equa. 7.3 from the amplitude and phase quadrature sum and difference variance spectra shown in fig. 7.18. These results together with the theoretically predicted curve calculated from the model, assuming a symmetric system with both squeezing sources delivering -3.2 dB of amplitude squeezed light in the TEM₁₀ mode and having the visibility of 98% when mixing the two squeezed fields on the entanglement BS, are presented in fig. 7.21. We achieved the degree of inseparability $\mathcal{I} = 0.51 \pm 0.01$ in the frequency range 3.2 – 4.2 MHz, which very well agrees with the model and proves that the two beams x and y are highly entangled.

In order to characterize the entangled states in terms of the EPR paradox criterion, we need to quantify the amplitude and phase quadrature conditional variances between

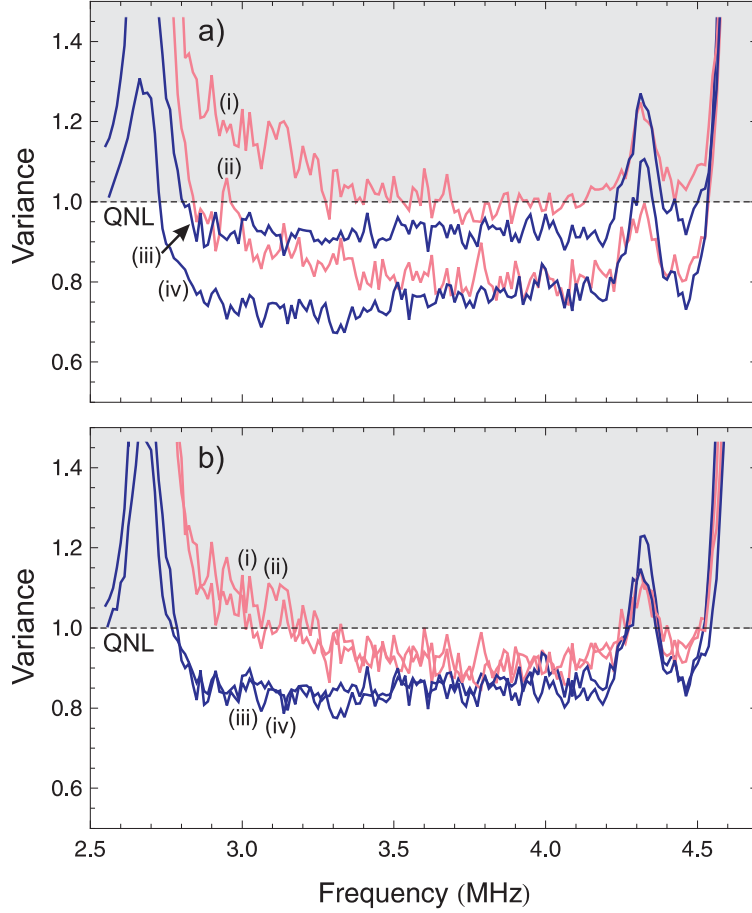


Figure 7.19: Frequency spectra of the amplitude and phase quadrature conditional variances of the beam x (y) given a measurement of that properties on the beam y (x). a) directly calculated from the measurements of $\Delta^2 \hat{X}_{x\pm y}^\pm$, $\Delta^2 \hat{X}_x^\pm$ and $\Delta^2 \hat{X}_y^\pm$; b) calculated from the measurements of $\Delta^2 \hat{X}_{x\pm y}^\pm$ and the measurements of $\Delta^2 \hat{X}_x^\pm$ and $\Delta^2 \hat{X}_y^\pm$ corrected for the asymmetry 0.45 : 0.55. (i) $\Delta^2 \hat{X}_{x|y}^+$, (ii) $\Delta^2 \hat{X}_{y|x}^+$, (iii) $\Delta^2 \hat{X}_{x|y}^-$, (iv) $\Delta^2 \hat{X}_{y|x}^-$.

the beams x and y . This can be easily done using equa. 7.6, where the term in the nominator can be easily calculated using equa. 7.7 from the measurements of the amplitude and phase quadrature sum and difference variances, i.e. $\Delta^2 \hat{X}_{x+y}^\pm$ and $\Delta^2 \hat{X}_{x-y}^\pm$, and the amplitude and phase variances of the individual position-momentum entangled beams, i.e. $\Delta^2 \hat{X}_x^\pm$ and $\Delta^2 \hat{X}_y^\pm$. The conditional variance measures the uncertainty of one variable, e.g. \hat{X}_x^+ , given knowledge of another variable, e.g. \hat{X}_y^+ . By looking at the two homodynes individually, we should be thus able to infer the properties, i.e. position or momentum, of the beam x from the measurements performed on the beam y , or the other way around, infer the properties of the beam y from the measurements performed on the beam x . The two pairs of conditional variances $\Delta^2 \hat{X}_{x|y}^\pm$ and $\Delta^2 \hat{X}_{y|x}^\pm$ calculated from our results are shown in fig. 7.19 a). Notice that the conditional variances $\Delta^2 \hat{X}_{x|y}^\pm$ do not correspond to the second pair $\Delta^2 \hat{X}_{y|x}^\pm$ as we would expect in an ideal case. This could be explained by a systematic asymmetry in our experiment as detailed earlier.

As expressed by equa. 7.5, taking the product of the amplitude and phase quadrature conditional variances yields the degree of EPR paradox. As shown in fig. 7.20 a), we obtained two distinctively different frequency spectra of the EPR paradox criterion, depending on which beam, i.e. x or y , you perform the measurement of a certain quantity, and to which beam, i.e. y or x , you infer this quantity. Estimating the mean values

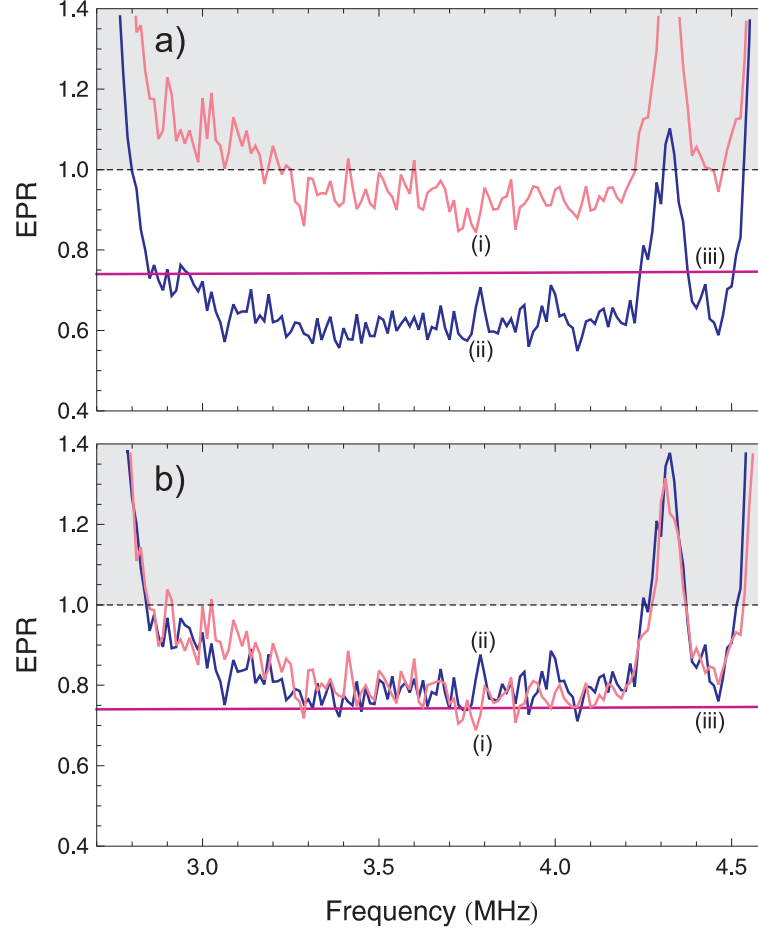


Figure 7.20: Frequency spectra of the degree of EPR paradox between position and momentum of the entangled beams x and y . a) and b) refer respectively to the uncorrected and corrected results as detailed in caption of fig. 7.19. (i) $\mathcal{E}_{x|y} = \Delta^2 \hat{X}_{x|y}^+ \Delta^2 \hat{X}_{x|y}^-$, (ii) $\mathcal{E}_{y|x} = \Delta^2 \hat{X}_{y|x}^+ \Delta^2 \hat{X}_{y|x}^-$, (iii) spectra expected from our model.

and variances from the two presented frequency spectra of the EPR paradox criterion in the frequency range 3.2–4.2 MHz then gives $\mathcal{E}_{x|y} = 0.93 \pm 0.01$ and $\mathcal{E}_{y|x} = 0.62 \pm 0.01$ for the two situations discussed. These results, however, do not correspond to the expected degree of EPR paradox estimated by the model, which predicts the value of $\mathcal{E}_{th} = 0.74$ as shown in fig. 7.20 a). In the model, we again assumed a symmetric system with squeezed states of -3.2 dB of squeezing and 5.1 dB of antisqueezing to be mixed on the entanglement BS with the visibility of 98%. Regardless the distinctively different results of the degree of EPR paradox criterion for the two situations, the presented results demonstrate entanglement between position and momentum of the two nonclassical fields x and y .

Looking back on the frequency spectra of the conditional variances of the amplitude and phase quadratures of the two entangled beams, shown in fig. 7.19 a), we can see that the pairs of conditional variances $\Delta^2 \hat{X}_{x|y}^\pm$ and $\Delta^2 \hat{X}_{y|x}^\pm$ have very similar features, and in fact the pairs of traces are only shifted from each other, indicating that their distinct difference might be caused by an improper estimation in the final stage of post-processing. This is justified by the fact that the frequency spectra of the amplitude and phase quadrature sum and difference variances, i.e. $\Delta^2 \hat{X}_{x+y}^+$ and $\Delta^2 \hat{X}_{x-y}^-$, shown in fig. 7.18, are almost overlapping out of the region of the relaxation oscillation noise, i.e. in the frequency range 3.7–4.1 MHz, before the signals are contaminated again with an excess noise having an origin in cross-beat of the modulation frequencies used in the

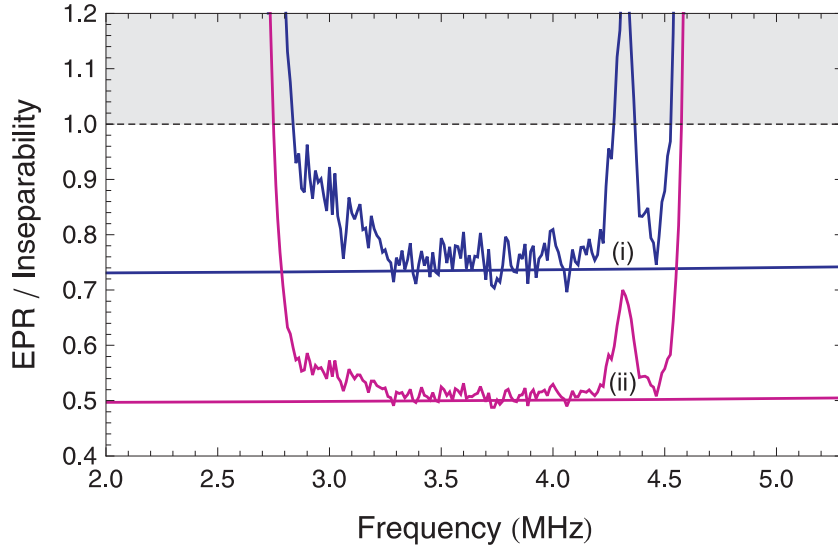


Figure 7.21: Frequency spectra of the degree of (i) inseparability \mathcal{I} , and (ii) EPR paradox \mathcal{E} , between position and momentum of the entangled beams x and y . The full lines show the theoretically predicted spectra.

system. This all indicates that all of the measurements of the variance of the photocurrents were taken correctly, i.e. the two squeezed fields incident on the entanglement BS were locked properly with $\pi/2$ being their relative phase shift, except for the final stage of the experiment involving measurements of the amplitude and phase quadrature variances of the two entangled beams x and y , shown in fig. 7.17 a), where the two squeezed fields could be locked not exactly to the right point. This would result in an asymmetric distribution of the interfered fields into the two outputs of the entanglement BS, which in effect would increase the noise power of the beam x , resulting in a decrease of noise power of the beam y , or vice versa.

Assuming this is the case, we post-processed the amplitude and phase quadrature variances of both entangled beams in order to match their power, see fig. 7.17 b). Based on these estimations, we conclude that the power was distributed into the two BS outputs with ratio 0.45 : 0.55. We calculated again the conditional variances $\Delta^2 \hat{X}_{x|y}^\pm$ and $\Delta^2 \hat{X}_{y|x}^\pm$ using the modified amplitude and phase quadrature variances, and we find an excellent agreement between the two pairs of conditional variances, as shown in fig. 7.19 b). Using these results, we can directly quantify the EPR paradox criteria, as shown in fig. 7.20 b), giving values of $\mathcal{E}_{x|y} = 0.79 \pm 0.01$ and $\mathcal{E}_{y|x} = 0.78 \pm 0.01$ for the two cases, depending on which beam we look at and to which beam we infer these properties. The reported EPR values very well correspond to the model, which as we already stated predicts the value of $\mathcal{E}_{th} = 0.74$.

7.4.5 Summary

In summary, we demonstrated the concept of spatial entanglement experimentally by building a unique apparatus for the generation of a pair of beams entangled in position and momentum. This experiment involves two identical squeezing sources operating in the TEM_{10} mode. We generated a position-squeezed beam by mixing one of the TEM_{10} squeezed fields with a bright TEM_{00} carrier field, which makes in the system a reference for position and momentum. Mixing this multi-mode spatially squeezed beam with the other TEM_{10} squeezed field on a 50/50 beamsplitter and locking their relative phase to $\phi_{ent} = \pi/2$ then allows to entangle an information about position and momentum of the bright reference beam into the pair of the entanglement BS output beams.

We characterized the strength of entanglement using the inseparability criterion and the EPR paradox criterion, and we measured their degrees in the frequency range 3.2 – 4.2 MHz to be $\mathcal{I} = 0.51 \pm 0.01$ and $\mathcal{E} = 0.78 \pm 0.01$, respectively. The presented results summarized in fig. 7.21 show the first demonstration of entanglement between position and momentum of a bright optical beam in the continuous variable regime, as originally considered by Einstein, Podolsky and Rosen. Moreover, this system allows demonstration of quantum imaging protocols such as spatial teleportation and dense coding. We could also demonstrate using this setup the capability of a quantum communication system with several degrees of freedom by encoding and detecting modulation onto squeezing into different degrees of freedom. This gives us also the opportunity to explore techniques for the modulation, transmission and detection of complex quantum states.

Chapter 8

Conclusions and outlook

This thesis investigated spatial quantum optical techniques, which have a potential to be used for ultra-sensitive measurements beyond the QNL, and in applications within the fields of quantum communication and quantum information processing. For investigating the basics of the spatial quantum effects, we require a multi-mode squeezed light, where the light beam displays nonclassical spatial properties in the transverse direction. Such a source of squeezed spatial light can be based on OPAs, widely used in quantum optics experiments for generating amplitude or phase squeezed light. The first attempt for achieving the goal is to generate squeezing in the higher-order Hermite-Gauss modes, which form an optimum basis for measurements of displacement and tilt of a laser beam. This requires understanding of mode coupling between the different transverse modes in a nonlinear device, in our case via the second-order nonlinear interaction.

In chapter 4, we demonstrated the multi-mode SHG in a QPM nonlinear device, namely in a PPKTP nonlinear crystal. The results show that transverse mode coupling of the interacting fields can be understood in terms of mode overlaps, and that the ratio between the generated SH components can be experimentally adjusted via the focusing parameter and crystal temperature. We can use these results in reverse to optimize a spatial profile of the pump field for an efficient down-conversion process of an OPA operating in higher-order modes. We found that for an OPA operating in the TEM_{n0} mode, the optimum pumping scheme is achieved utilizing a pump beam of TEM_{2n0} spatial profile, and the highest nonlinear gain occurs for the focusing parameter $\xi = 2.84$ and at the same phase-matching temperature as for the fundamental mode operation. In particular, the nonlinear conversion can be for a TEM_{10} OPA up to 50% efficient using a TEM_{20} pump, and in the case of a TEM_{20} OPA this process can be up to 37.5% efficient using a TEM_{40} pump, relative to the conversion efficiency achieved with fundamental modes. If we desire to use a TEM_{00} pump for an OPA operating in the TEM_{10} spatial mode, the maximum conversion efficiency is 22%, and is obtained for rather low focusing parameter $\xi = 1.8$ and at lower phase-matching temperatures.

In chapter 5, we demonstrated the generation of vacuum squeezed light in the TEM_{00} and TEM_{10} modes utilizing a bow-tie OPA, based on a PPKTP nonlinear material. We measured the level of squeezing of the best -5.5 dB in the TEM_{00} mode and -3.1 dB in the TEM_{10} spatial mode, after correction for the electronic noise. The reported results were measured by scanning the local oscillator phase, and we make an attempt for locking the vacuum squeezed quadrature. We found that a broad-band excess amplitude noise present on the pump field has a strong influence on the squeezing production. We significantly enhanced the squeezing generation by spectral filtering

the pump field from the excess amplitude noise in a mode cleaning cavity. As the pump noise is not directly coupled in the bow-tie OPA with the vacuum squeezed field due to its zero intra-cavity coherent amplitude, we conclude that the pump amplitude noise has on production of squeezing, in general, more technical inside and basically introduces into the system phase jitter. This effect gets more significant with higher degrees of squeezing. On the other hand, production of the vacuum squeezed light is robust against the pump phase noise.

We tested a new pumping scheme for an OPA operating in the TEM_{10} mode, and this involves a pump field of the TEM_{20} spatial profile. As expected from theory, this scheme promises higher nonlinear efficiency than in the case of the TEM_{00} pump, and for an optimized focusing parameter can be up to 50% efficient, when compared to the nonlinear interaction of fundamental modes. Using 75 mW of TEM_{20} pump power, we observed -2.6 dB of squeezing in the TEM_{10} mode. We expect to generate more than -4 dB of vacuum squeezing in the current setup when pumping by 0.3 W of power, which is a limit of the laser assuming maximum 78% efficiency for transferring the TEM_{00} pump field into the TEM_{20} mode in an optical cavity. Moreover, by optimizing the output coupler transmission, we could achieve up to -5.2 dB of noise suppression in the TEM_{10} mode. These results are very important when designing a new generation of OPAs operating in higher-order modes.

In chapter 6, we experimentally demonstrated the generation of optical squeezing in multiple longitudinal modes and transverse Hermite-Gauss modes of an optical parametric amplifier. We presented measurements of approximately -3 dB of squeezing at baseband, 1.7 GHz, 3.4 GHz and 5.1 GHz, which correspond to the first, second and third resonances of the amplifier. Such optical states might be used to produce 'multiplexed entanglement' for quantum communications applications. Moreover we observed squeezing in higher-order transverse modes, which provides additional degrees of freedom for the quantum systems. We showed that both the magnitude and the bandwidth of the squeezing in the higher longitudinal modes are greater than can be observed at baseband, which is affected by low frequency technical noise. The squeezing observed is the highest frequency squeezing reported to date.

In chapter 7, we experimentally demonstrated the generation of spatial entanglement for bright optical beams. We built a unique apparatus for the generation of a pair of beams entangled in position and momentum. This experiment involves two identical squeezing sources operating in the TEM_{10} mode. We generated a position-squeezed beam by mixing one of the TEM_{10} squeezed fields with a bright TEM_{00} carrier field, which makes a reference in the system for position and momentum. Mixing this multi-mode spatially squeezed beam with the other TEM_{10} squeezed field on a 50/50 beamsplitter then allows to entangle an information about position and momentum of the bright reference beam into the pair of output beams.

We characterized the strength of entanglement using the inseparability criterion and the EPR paradox criterion, and we measured their degrees in the frequency range 3.2 – 4.2 MHz to be $\mathcal{I} = 0.51 \pm 0.01$ and $\mathcal{E} = 0.78 \pm 0.01$, respectively. The presented results show the first demonstration of entanglement between position and momentum of a bright optical beam in the continuous variable regime as originally considered by Einstein, Podolsky and Rosen. Moreover, this system allows demonstration of quantum imaging protocols such as spatial teleportation and dense coding. We could also demonstrate using this setup the capability of a quantum communication system with several degrees of freedom by encoding and detecting modulation onto squeezing into different degrees of freedom. This gives us also the opportunity to explore techniques for the modulation, transmission and detection of complex quantum states.

Appendix A

Spatial entanglement setup

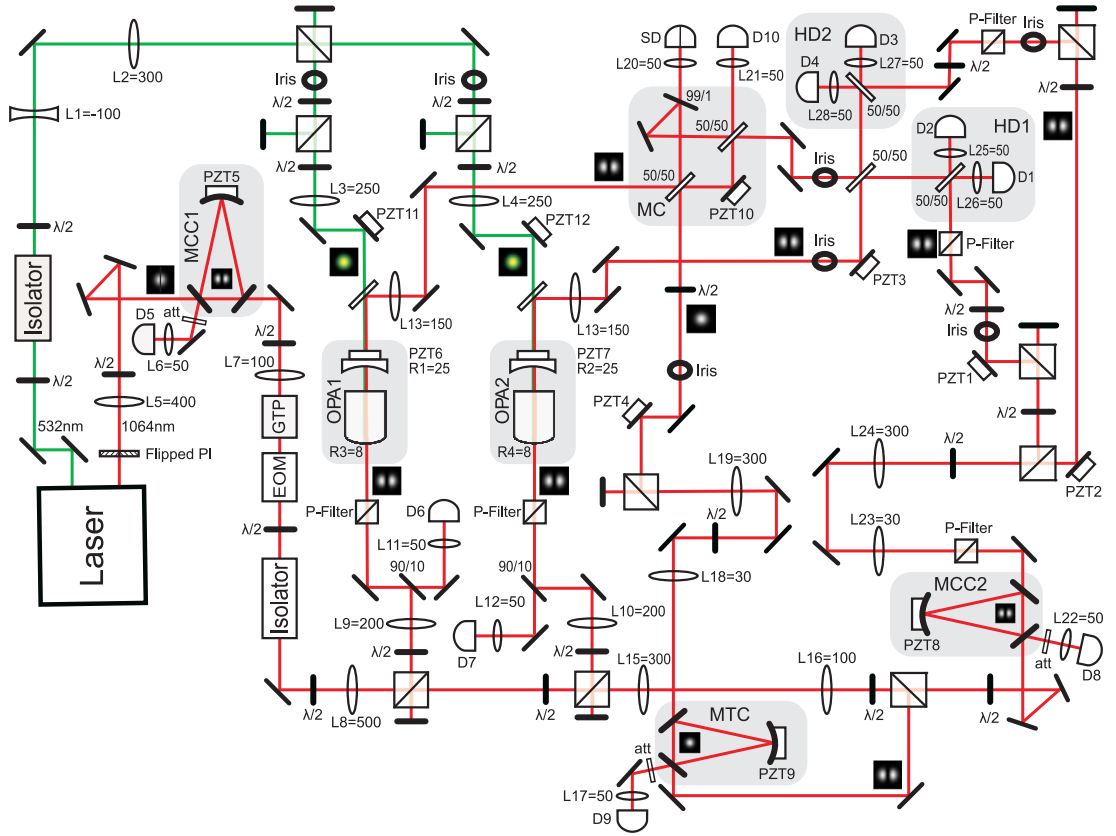


Figure A.1: Detailed schematics of the experimental setup used to demonstrate spatial entanglement. EOM: electro-optic modulator, GTP: Glan Thompson polarizer, HD: homodyne detection system, MC: mode combiner, MCC: mode cleaning cavity, MTC: mode transferring cavity, OPA: optical parametric amplifier, PZT: piezo ceramic transducer, D: detector, SD: split detector, L: lens, R: radius of curvature.

Appendix B

Picture gallery

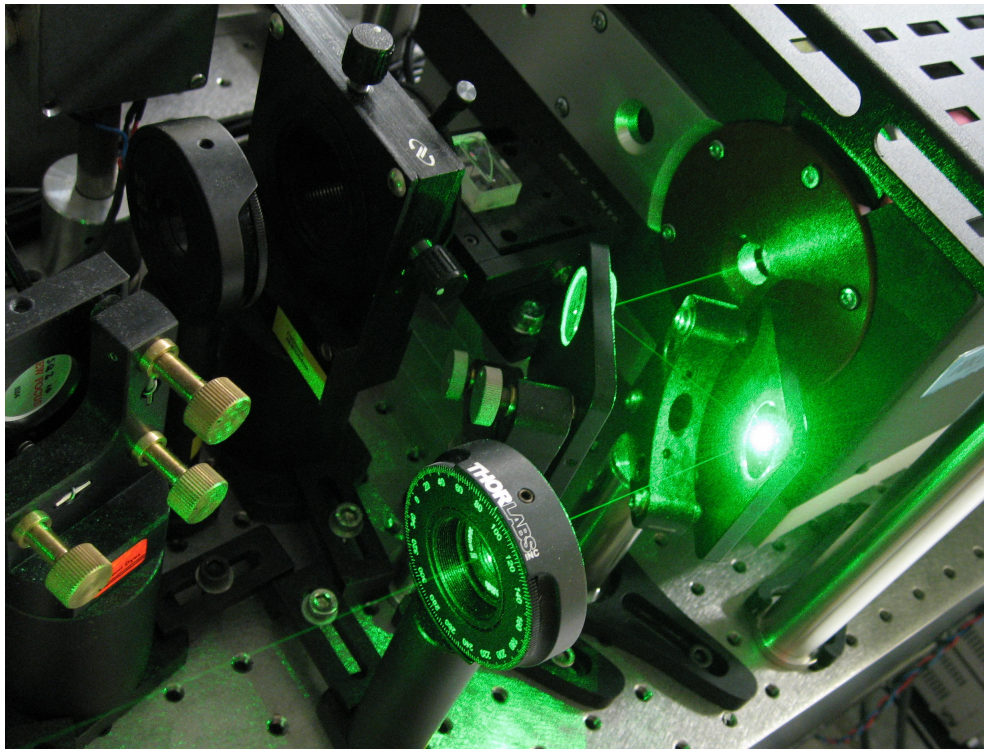


Figure B.1: Diabolo laser - dual output solid-state monolithic ring-cavity laser based on Nd:YAG material with an internal frequency doubler.

DTU

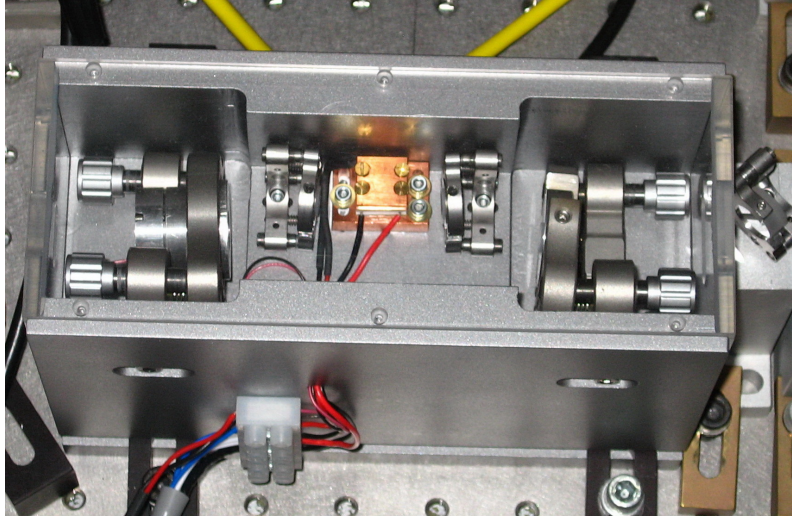


Figure B.2: Bow-tie cavity OPA based on a PPKTP nonlinear material.

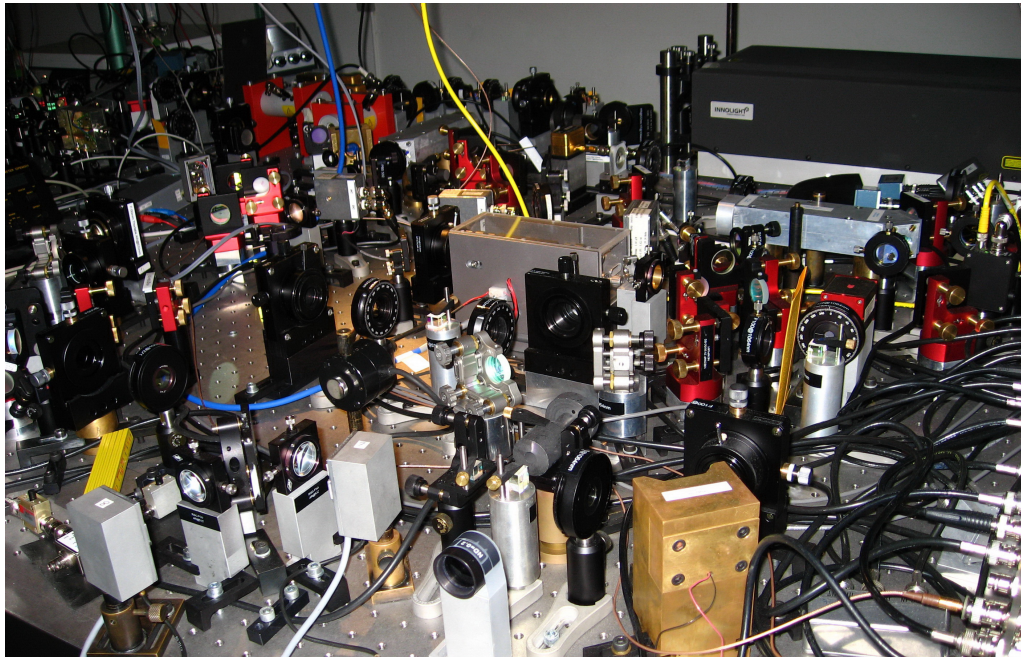


Figure B.3: Experimental setup for generation of vacuum squeezing in the TEM_{00} and TEM_{10} spatial modes utilizing a PPKTP OPA.

ANU

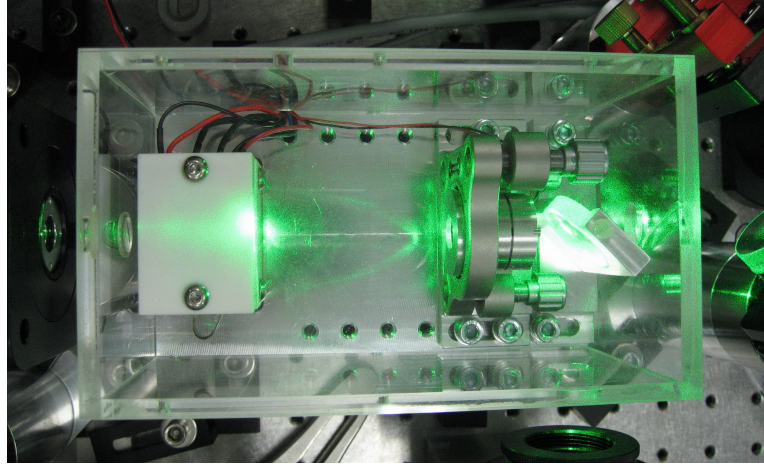


Figure B.4: $\text{MgO}:\text{LiNbO}_3$ based OPA serving as a TEM_{10} squeezing source for the spatial entanglement experiment.

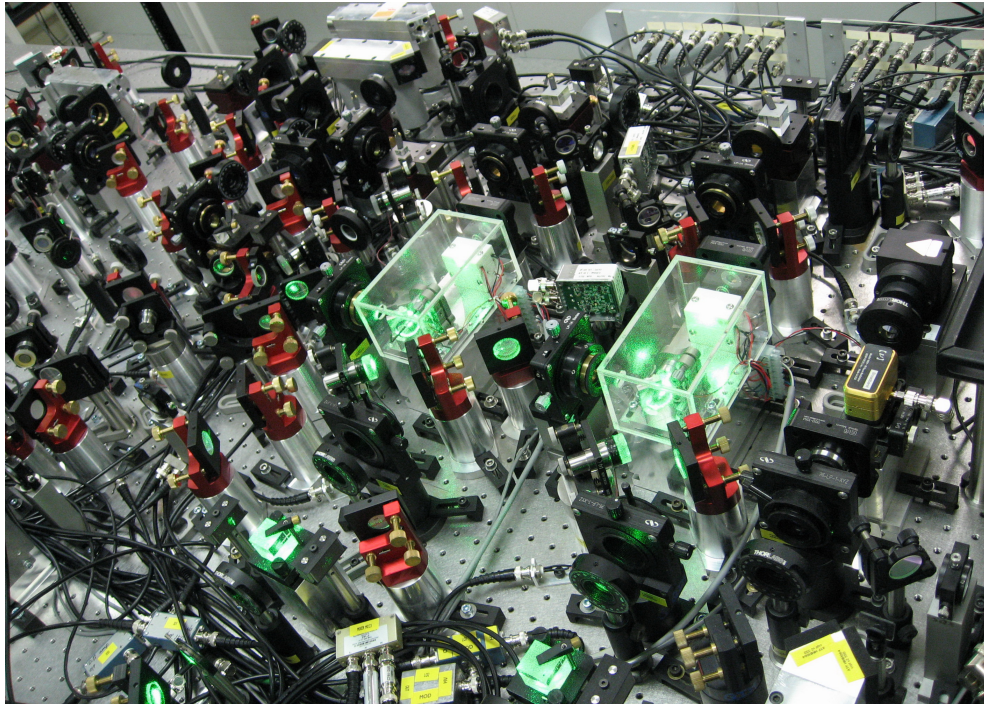


Figure B.5: Experimental setup used to generate a pair of entangled beams in position and momentum.

References

- [1] T. H. Maiman. Stimulated optical radiation in ruby. *Nature*, 187:493, (1960).
- [2] Lord Rayleigh. Collected optics papers of lord rayleigh, philos. mag. 261, 403, 477 (1879). *Opt. Soc. Am. A*, page 117, (1994).
- [3] L. A. Wu, H. J. Kimble, J. Hall, and H. Wu. Generation of squeezed states by parametric down conversion. *Phys. Rev. Lett.*, 57:2520, (1986).
- [4] L. A. Wu, M. Xiao, and H. J. Kimble. Squeezed states of light from an optical parametric oscillator. *J. Opt. Soc. Am. B*, 4:1465, (1987).
- [5] P. Kurz, R. Paschotta, K. Fiedler, A. Sizmann, G. Leuchs, and J. Mlynek. Squeezing by second-harmonic generation in a monolithic resonator. *Appl. Phys. B*, 55:216, (1992).
- [6] J. Heersink, V. Josse, G. Leuchs, and U. L. Andersen. Spatial entanglement of a free bosonic field. *Opt. Lett.*, 30:1192, (2005).
- [7] K. Bergman and H. A. Haus. Squeezing in fibers with optical pulses. *Opt. Lett.*, 16:663, (1991).
- [8] P. K. Lam, T. Ralph, B. Buchler, D. McClelland, H.-A. Bachor, and J. Gao. Optimization and transfer of vacuum squeezing from an optical parametric oscillator. *J. Opt. B: Q. Semiclass. Opt.*, 1:469, (1999).
- [9] S. Suzuki, H. Yonezawa, F. Kannari, M. Sasaki, and A. Furusawa. 7 db quadrature squeezing at 860 nm with periodically poled ktiopo₄. *Appl. Phys. Lett.*, 89:061116, (2006).
- [10] Y. Takeno, M. Yukawa, H. Yonezawa, and A. Furusawa. Observation of -9 db quadrature squeezing with improvement of phase stability in homodyne measurement. *quant-ph*, page 0702139, (2007).
- [11] H. Vahlbruch, M. Mehmet, N. Lastzka, B. Hage, S. Chelkowski, A. Franzen, S. Gossler, K. Danzmann, and R. Schnabel. Observation of squeezed light with 10 db quantum noise reduction. *quant-ph*, page 0706.1431v1, (2007).
- [12] E. S. Polzik, J. Carri, and H. J. Kimble. Spectroscopy with squeezed light. *Phys. Rev. Lett.*, 68:3020, (1992).
- [13] P. H. Souto Ribeiro, C. Schwob, A. Maitre, and C. Fabre. Sub-shotnoise high-sensitivity spectroscopy with optical parametric oscillator twin beams. *Opt. Lett.*, 22:1893, (1997).
- [14] K. McKenzie, D. A. Shaddock, D. E. McClelland, B. C. Buchler, and P. K. Lam. Experimental demonstration of a qqueezing-enhanced power-recycled michelson

- interferometer for gravitational wave detection. *Phys. Rev. Lett.*, 88:231102, (2002).
- [15] L. A. Lugiato, A. Gatti, H. Ritsch, I. Marzoli, and G. L. Oppo. Quantum images in nonlinear optics. *J. Mod. Opt.*, 44:1899, (1997).
- [16] L. A. Lugiato and P. Grangier. Improving quantum noise reduction with spatially multimode squeezed light. *J. Opt. Soc. Am. B*, 14:225, (1997).
- [17] V. Delaubert, N. Treps, C. C. Harb, P. K. Lam, and H-A. Bachor. Quantum measurements of spatial conjugate variables: Displacement and tilt of a gaussian beam. *Opt. Lett.*, 31:1537, (2006).
- [18] N. Treps, N. Grosse, W. P. Bowen, C. Fabre, H-A. Bachor, and P. K. Lam. A quantum laser pointer. *Science*, 301:940, (2003).
- [19] N. Treps, U. Andersen, B. Buchler, P. K. Lam, A. Maitre, H-A. Bachor, and C. Fabre. Surpassing the standard quantum limit for optical imaging using non-classical multimode light. *Phys. Rev. Lett.*, 88:203601, (2002).
- [20] N. Treps, N. Grosse, W. Bowen, M. T. L. Hsu, A. Maitre, C. Fabre, H-A. Bachor, and P. K. Lam. Nano-displacement measurements using spatially multimode squeezed light. *J. Opt. B: Q. Semiclass. Opt.*, 6:664, (2004).
- [21] B. Willke et al. The geo 600 gravitational wave detector. *Class. Quantum Grav.*, 19:1377, (2002).
- [22] C. A. J. Putman, K. O. van der Werf, B. G. de Grooth, N. F. van Hulst, F. B. Segerink, and J. Greve. Atomic force microscope with integrated optical microscope for biological applications. *Rev. Sci. Instrum.*, 63:1914, (1992).
- [23] V. Delaubert, N. Treps, M. Lassen, C. C. Harb, C. Fabre, P. K. Lam, and H-A. Bachor. Tem_{10} homodyne detection as an optimal small displacement and tilt measurements scheme. *Phys. Rev. A*, 74:053823, (2006).
- [24] V. Delaubert, M. Lassen, D. R. N. Pulford, H.-A. Bachor, and C. C. Harb. Spatial mode discrimination using second harmonic generation. *Optics Express*, 15:5815, (2007).
- [25] V. Delaubert. Imagerie quantique a petit nombre de modes transverses. *PhD Thesis (Laboratoire Kastler Brossel, Universite Pierre et Marie Curie, Paris 2007)*.
- [26] M. Lassen, V. Delaubert, J. Janousek, K. Wagner, H.-A. Bachor, P. K. Lam, N. Treps, P. Buchhave, C. Fabre, and C. C. Harb. Tools for spatial multi-mode quantum information: modulation, detection and quantum correlations. *Phys. Rev. Lett.*, 98:083602, (2007).
- [27] M. T. L. Hsu, W. P. Bowen, N. Treps, and P. K. Lam. Continuous-variable spatial entanglement for bright optical beams. *Phys. Rev. A*, 72:013802, (2005).
- [28] A. Einstein, B. Podolsky, and N. Rosen. Can quantum-mechanical description of physical reality be considered complete? *Phys. Rev.*, 47:777, (1935).
- [29] M. O. Scully and M. S. Zubairy. Quantum optics. *Cambridge University Press, UK*, (1997).
- [30] W. Heisenberg. Über den anschaulichen inhalt der quantentheoretischen kinematik und mechanik. *Zeitschrift für Physik*, 43:172, (1927).

- [31] B. Yurke. Use of cavities in squeezed light generation. *Phys. Rev. A*, 20:408, (1984).
- [32] L. A. Lugiato, G. Strini, and F. de Martini. Squeezed states in second-harmonic generation. *Opt. Lett.*, 8:256, (1983).
- [33] L. Mandel. Opt. comm. *Science*, 42:437, (1982).
- [34] R. W. Boyd. Nonlinear optics. *Academic Press*, (1992).
- [35] L. Brillouin. Diffusion of light and x-rays by a transparent homogeneous body. *Ann. Phys.*, 17:88, (1922).
- [36] P. Debye and F. W. Sears. On the scattering of light by supersonic waves. *Proc. Nat. Acad. Sci.*, 18:409, (1932).
- [37] R. Lucas and P. Biquard. Optical properties of solid and liquid medias subjected to high-frequency elastic vibrations. *Journal Phys.*, 71:464, (1932).
- [38] W. P. Bowen. Experiments towards a quantum information network with squeezed light and entanglement. *PhD Thesis (Australian National University, Canberra 2003)*.
- [39] E. P. Wigner. On the quantum correction for thermodynamic equilibrium. *Phys. Rev.*, 40:749, (1932).
- [40] U. Leonhardt. Measuring the quantum state of light. *Cambridge university press, Cambridge*, (1997).
- [41] C. W. Gardiner and M. J. Collett. Input and output in damped quantum systems: Quantum stochastic differential equations and the master equation. *Phys. Rev. A*, 31:3761, (1985).
- [42] A. E. Siegman. Lasers. *University Science, Mill Valley California*, (1986).
- [43] R. W. Boyd. Intuitive explanation of the phase anomaly of focused light beams. *J. Opt. Soc. Am.*, 70:877, (1980).
- [44] H. Kogelnik. Coupling and conversion coefficients for optical modes. *Proceedings of the Symposium on Quasi-Optics*, (1964).
- [45] E. Morrison, B. Meers, D. Robertson, and H. Ward. Automatic alignment of optical interferometers. *Appl. Opt.*, 33:5041, (1994).
- [46] M. T. L. Hsu, V. Delaubert, P. K. Lam, and W. P. Bowen. Optimum small optical beam displacement measurement. *J. Opt. B : Q. Semiclass. Opt.*, 6:495, (2004).
- [47] H. A. Bachor and T. C. Ralph. A guide to experiments in quantum optics. *Wiley-VCH*, (2003).
- [48] B. C. Buchler. Electro-optic control of quantum measurements. *PhD Thesis (Australian National University, Canberra 2001)*.
- [49] R. W. P. Drever, J. L. Hall, F. V. Kowalski, J. Hough, G. M. Ford, A. J. Munley, and H. Ward. Laser phase and frequency stabilization using an optical resonator. *Appl. Phys. B*, 31:97, (1983).
- [50] Innolight GmbH. Diabolo laser. <http://www.innolight.de>.

- [51] J. Arlt, K. Dholakia, L. Allen, and M.J. Padgett. The production of multi-ringed laguerre-gaussian modes by computer-generated holograms. *J. Mod. Opt.*, 45:1231, (1998).
- [52] M. Lassen. Investigation of spatial quantum optical effects with applications in quantum information and biophotonics. *PhD Thesis (Technical University of Denmark, Lyngby 2007)*.
- [53] V. Delaubert, D. A. Shaddock, P. K. Lam, B. C. Buchler, H-A. Bachor, and D. E. McClelland. Generation of a phase-flipped gaussian mode for optical measurements. *J. Opt. A*, 4:393, (2002).
- [54] P. A. Franken, A. E. Hill, C. W. Peters, and G. Weinreich. Generation of optical harmonics. *Phys. Rev. Lett.*, 7:4, (1961).
- [55] L. H. Yu, L. DiMauro, A. Doyuran, W. S. Graves, E. D. Johnson, R. Heese, S. Krinsky, H. Loos, J. B. Murphy, G. Rakowsky, J. Rose, T. Shaftan, B. Sheehy, J. Skaritka, X. J. Wang, and Z. Wu. First ultraviolet high-gain harmonic-generation free-electron laser. *Phys. Rev. Lett.*, 91:074801, (2003).
- [56] C. K. N. Patel. Optical harmonic generation in the infrared using a co₂ laser. *Phys. Rev. Lett.*, 16:613, (1966).
- [57] S. Paschotta, J. Schiller, and J. Mlynek. Efficient continuous-wave frequency doubling of 1.06 μm with a monolithic mgo:linbo₃ resonator. *Opt. Lett.*, 19:1325, (1994).
- [58] T. C. Ralph, M. S. Taubman, A. G. White, D. E. McClelland, and H.-A. Bachor. Squeezed light from second-harmonic generation: Experiment versus theory. *Opt. Lett.*, 20:1316, (1995).
- [59] D. K. Serkland, P. Kumar, M. A. Arbore, and M. M. Fejer. Amplitude squeezing by means of quasi-phase-matched second-harmonic generation in a lithium niobate waveguide. *Opt. Lett.*, 22:1497, (1997).
- [60] N. Grosse, W. P. Bowen, K. McKenzie, and P. K. Lam. Harmonic entanglement with second-order nonlinearity. *Phys. Rev. Lett.*, 96:063601, (2006).
- [61] G. D. Boyd and D. A. Kleinman. Parametric interaction of focused gaussian beams. *J. Appl. Phys.*, 39:3597, (1968).
- [62] J. A. Armstrong, N. Bloembergen, J. Ducuing, and P. S. Pershan. Interactions between light waves in a nonlinear dielectric. *Phys. Rev.*, 127:1918, (1962).
- [63] K. Fradkin, A. Arie, A. Skliar, and G. Rosenman. Tunable midinfrared source by difference frequency generation in bulk periodically poled ktiopo₄. *Appl. Phys. Lett.*, 74:914, (1999).
- [64] J. D. Bierlein and H. Vanherzeele. Potassium titanyl phosphate: properties and new applications. *J. Opt. Soc. Am. B*, 6:622, (1989).
- [65] S. Emanuelli and A. Arie. Temperature-dependent dispersion equations for ktiopo₄ and ktioaso₄. *Appl. Opt.*, 42:6661, (2003).
- [66] P. Scotto, P. Colet, and M. San Miguel. All-optical image processing with cavity type ii second-harmonic generation. *Opt. Lett.*, 28:1695, (2003).
- [67] D. F. Walls and G. J. Milburn. Quantum optics. *Springer-Verlag, Berlin*, (1995).

- [68] N. Lastzka and R. Schnabel. The gouy phase shift in nonlinear interactions of waves. *Opt. Exp.*, 15:7211, (2007).
- [69] M. Lassen, V. Delaubert, C. C. Harb, N. Treps, P. K. Lam, and H.-A. Bachor. Generation of squeezing in higher order hermite-gaussian modes with an optical parametric amplifier. *J. Eur. Opt. Soc. Rapid. Pub.*, 1:06003, (2006).
- [70] R. R. Slusher, L. W. Hollberg, B. Yurke, J. C. Mertz, and J. F. Valley. Observation of squeezed states generated by four-wave mixing in an optical cavity. *Phys. Rev. Lett.*, 55, (1985).
- [71] K. McKenzie, N. Grosse, W. Bowen, S. Whitcomb, M. Gray, D. McClelland, and P. K. Lam. Squeezing in the audio gravitational-wave detection band. *Phys. Rev. Lett.*, 93:161105, (2004).
- [72] R. J. Senior, G. N. Milford, J. Janousek, A. E. Dunlop, K. Wagner, H.-A. Bachor, T. C. Ralph, E. H. Huntington, and C. C. Harb. Observation of a comb of optical squeezing over many gigahertz of bandwidth. *Opt. Exp.*, 15:5310, (2007).
- [73] W. P. Bowen, R. Schnabel, P. K. Lam, and T. C. Ralph. A characterization of continuous variable entanglement. *Phys. Rev. A*, 69:012304, (2004).
- [74] Z. Y. Ou, S. F. Pereira, H. J. Kimble, and K. C. Peng. Realization of the einstein-podolsky-rosen paradox for continuous variables. *Phys. Rev. Lett.*, 68:3663, (1992).
- [75] C. Schori, J. L. Sorensen, and E. S. Polzik. Narrow-band frequency tunable light source of continuous quadrature entanglement. *Phys. Rev. A*, 66:033802, (2002).
- [76] Ch. Silberhorn, P. K. Lam, O. Weiss, F. Koenig, N. Korolkova, and G. Leuchs. Generation of continuous variable einstein-podolsky-rosen entanglement via the kerr nonlinearity in an optical fiber. *Phys. Rev. Lett.*, 86:4267, (2001).
- [77] P. Zoller *et al.* Quantum information processing and communication - strategic report on current status, visions and goals for research in europe. *Eur. Phys. J. D*, 36:203, (2005).
- [78] A. Furusawa, J. L. Sorensen, S. L. Braunstein, C. A. Fuchs, H. J. Kimble, and E. S. Polzik. Unconditional quantum teleportation. *Science*, 282:706, (1998).
- [79] J. Jing, J. Zhang, Y. Yan, F. Zhao, C. Xie, and K. Peng. Experimental demonstration of tripartite entanglement and controlled dense coding for continuous variables. *Phys. Rev. Lett.*, 90:167903, (2003).
- [80] A. M. Lance, T. Symul, W. P. Bowen, B. C. Sanders, and P. K. Lam. Tripartite quantum state sharing. *Phys. Rev. Lett.*, 92:177903, (2004).
- [81] V. Delaubert, N. Treps, G. Bo, and C. Fabre. Optical storage of high-density information beyond the diffraction limit: A quantum study. *Phys. Rev. A*, 73:013820, (2006).
- [82] M. Kolobov and C. Fabre. Quantum limits on optical resolution. *Phys. Rev. Lett.*, 85:3789, (2000).
- [83] I. Sokolov, M. Kolobov, A. Gatti, and L. Lugiato. Quantum holographic teleportation. *Opt. Comm.*, 193:175, (2001).

- [84] G. J. Milburn and D. F. Walls. Squeezed states and intensity fluctuations. *Phys. Rev. A*, 27:392, (1983).
- [85] H. M. Wiseman, M. S. Taubman, and H-A. Bachor. Feedback-enhanced squeezing in second harmonic generation. *Phys. Rev. A*, 51:3227, (1995).
- [86] K. McKenzie, N. Grosse, W. Bowen, S. Whitcomb, M. Gray, D. McClelland, and P. K. Lam. Quantum noise locking. *J. Opt. B: Quantum Semiclass. Opt.*, 7:421, (2005).
- [87] Y. Furukawa, A. Alexandrovski, R. Route, M. Fejer, and G. Foulon. Green-induced infrared absorption in mgo doped linbo₃. *Appl. Phys. Lett.*, 78:1970, (2001).
- [88] N. Gisin, G. Ribordy, W. Tittel, and H. Zbinden. Quantum cryptography. *Rev. Mod. Phys.*, 74:145–195, (2002).
- [89] F. Grosshans, G. Van Assche, J. Wenger, R. Brouri, N. J. Cerf, and P. Grangier. Quantum key distribution using gaussian-modulated coherent states. *Nature*, 421:238, (2003).
- [90] C. M. Caves. Quantum-mechanical noise in an interferometer. *Phys. Rev. D*, 23:1693, (1981).
- [91] B. J. Meers and K. A. Strain. Modulation, signal, and quantum noise in interferometers. *Phys. Rev. A*, 44:4693, (1991).
- [92] M. Nielsen and I. Chuang. Quantum computation and quantum information. *Cambridge University Press, Cambridge, UK*, (2000).
- [93] P. G. Kwiat, K. Mattle, H. Weinfurter, and A. Zeilinger. New high-intensity source of polarization-entangled photon pairs. *Phys. Rev. Lett.*, 75:4337, (1995).
- [94] Y. J. Lu and Z. Y. Ou. Optical parametric oscillator far below threshold: Experiment versus theory. *Phys. Rev. A*, 62:033804, (2000).
- [95] A. E. Dunlop, E. H. Huntington, C. C. Harb, and T. C. Ralph. Generation of a frequency comb of squeezing in an optical parametric oscillator. *Phys. Rev. A*, 73:013817, (2006).
- [96] G. N. Milford, C. C. Harb, and E. H. Huntington. Shot noise limited, microwave bandwidth photodetector design. *Rev. Sci. Instrum.*, 77:114701, (2006).
- [97] B. Yurke, P. G. Kaminsky, and R. E. Miller. Observation of 4.2-k equilibrium-noise squeezing via a josephson-parametric amplifier. *Phys. Rev. Lett.*, 60:764, (1988).
- [98] M. B. Gray, D. A. Shaddock, C. C. Harb, and H.-A. Bachor. Photodetector designs for low-noise, broadband, and high-power applications. *Rev. Sci. Instrum.*, 69:3755, (1998).
- [99] G. Gonzalez. Microwave transistor amplifiers: Analysis and design. (1996).
- [100] Mini-Circuits. *www.mini-circuits.com*.
- [101] C. Fabre and S. Reynaud. Quantum noise in optical systems: A semiclassical approach.

- [102] M. G. Raymer, J. Noh, K. Banaszek, and I. A. Walmsley. Pure-state single-photon wave-packet generation by parametric down-conversion in a distributed microcavity. *Phys. Rev. A*, 72:023825, (2005).
- [103] H. Vahlbruch, S. Chelkowski, B. Hage, A. Franzen, K. Danzmann, and R. Schnabel. Demonstration of a squeezed-light-enhanced power- and signal-recycled michelson interferometer. *Phys. Rev. Lett.*, 95:211102, (2005).
- [104] C. H. Bennett and S. J. Wiesner. Communication via one- and two-particle operators on einstein-podolsky-rosen states. *Phys. Rev. Lett.*, 69:2881, (1992).
- [105] T. C. Ralph and E. H. Huntington. Unconditional continuous-variable dense coding. *Phys. Rev. A*, 66:042321, (2002).
- [106] C. H. Bennett, G. Brassard, C. Crepeau, R. Jozsa, A. Peres, and W. K. Wootters. Teleporting an unknown quantum state via dual classical and einstein-podolsky-rosen channels. *Phys. Rev. Lett.*, 70:1895, (1993).
- [107] D. P. DiVincenzo. Quantum computation. *Science*, 270:255, (1995).
- [108] W. P. Bowen, R. Schnabel, P. K. Lam, and T. C. Ralph. An experimental investigation of criteria for continuous variable entanglement. *Phys. Rev. Lett.*, 90:043601, (2003).
- [109] W. P. Bowen, N. Treps, R. Schnabel, and P. K. Lam. Experimental demonstration of continuous variable polarization entanglement. *Phys. Rev. Lett.*, 89:253601, (2002).
- [110] N. Korolkova, G. Leuchs, R. Loudon, T. C. Ralph, and C. Silberhorn. Polarization squeezing and continuous-variable polarization entanglement. *Phys. Rev. A*, 65:052306, (2002).
- [111] J. Laurat, G. Keller, J. A. Oliveira-Huguenin, C. Fabre, T. Coudreau, A. Serafini, G. Adesso, and F. Illuminati. Entanglement of two-mode gaussian states: characterization and experimental production and manipulation. *J. Opt. B*, 7:577, (2005).
- [112] J. Laurat, G. Keller, C. Fabre, and T. Coudreau. Generation of two-color polarization-entangled optical beams with a self-phase-locked two-crystal optical parametric oscillator. *Phys. Rev. A*, 73:012333, (2006).
- [113] Y. Zhang, H. Wang, X. Li, J. Jing, C. Xie, and K. Peng. Experimental generation of bright two-mode quadrature squeezed light from a narrow-band nondegenerate optical parametric amplifier. *Phys. Rev. A*, 62:023813, (2000).
- [114] J. Laurat, T. Coudreau, G. Keller, N. Treps, and C. Fabre. Compact source of einstein-podolsky-rosen entanglement and squeezing at very low noise frequencies. *Phys. Rev. A*, 70:042315, (2004).
- [115] L.-M. Duan, G. Giedke, J. I. Cirac, and P. Zoller. Inseparability criterion for continuous variable systems. *Phys. Rev. Lett.*, 84:2722, (2000).
- [116] M. D. Reid and P. D. Drummond. Quantum correlations of phase in nondegenerate parametric oscillation. *Phys. Rev. Lett.*, 60:2731, (1988).
- [117] C. M. Caves and P. D. Drummond. Quantum limits on bosonic communication rates. *Rev. Mod. Phys.*, 66:481, (1994).

- [118] C. Fabre, J. B. Fouet, and A. Maitre. Quantum limits in the measurement of very small displacements in optical images. *Opt. Lett.*, 25:76, (2000).
- [119] A. S. Parkins and H. J. Kimble. Position-momentum einstein-podolsky-rosen state of distantly separated trapped atoms. *Phys. Rev. A*, 61:052104, (2000).
- [120] H. de Riedmatten, J. Laurat, C. W. Chou, E. W. Schomburg, D. Felinto, and H. J. Kimble. Direct measurement of decoherence for entanglement between a photon and stored atomic excitation. *Phys. Rev. Lett.*, 97:113603, (2006).
- [121] J. C. Howell, R. S. Bennink, S. J. Bentley, and R. W. Boyd. Realization of the einstein-podolsky-rosen paradox using momentum-and position-entangled photons from spontaneous parametric down conversion. *Phys. Rev. Lett.*, 92:210403, (2004).
- [122] J. Jing, S. Feng, R. Bloomer, and O. Pfister. Experimental continuous-variable entanglement from a phase-difference-locked optical parametric oscillator. *quant-ph*, page 0604134, (2006).
- [123] R. Zambrini, A. Gatti, L. A. Lugiato, and M. San Miguel. Polarization quantum properties in a type-ii optical parametric oscillator below threshold. *Phys. Rev. A*, 68:063809, (2003).
- [124] V. Josse, A. Dantan, A. Bramati, M. Pinard, and E. Giacobino. Continuous variable entanglement using cold atoms. *Phys. Rev. Lett.*, 92:123601, (2004).
- [125] A. Gatti, E. Brambilla, L. A. Lugiato, and M. I. Kolobov. Quantum entangled images. *Phys. Rev. Lett.*, 83:1763, (1999).
- [126] P. Navez, E. Brambilla, A. Gatti, and L. A. Lugiato. Spatial entanglement of twin quantum images. *Phys. Rev. A*, 65:013813, (2001).
- [127] A. Gatti, E. Brambilla, and L. A. Lugiato. Entangled imaging and wave-particle duality: from the microscopic to the macroscopic realm. *Phys. Rev. Lett.*, 90:133603, (2003).
- [128] L. Heaney, J. Anders, and V. Vedral. Spatial entanglement of a free bosonic field. *quant-ph*, page 0607069, (2006).
- [129] S. Mancini, V. Giovannetti, D. Vitali, and P. Tombesi. Entangling macroscopic oscillators exploiting radiation pressure. *Phys. Rev. Lett.*, 88:120401, (2002).